Studies on Interactions of Transition Metals with Leucine and Isoleucine using Spectroscopic and Electrochemical Techniques

A

Dissertation
for the Partial Fulfillment of the Requirements
for the Award of the Degree of
Doctor of Philosophy
in Chemistry

Submitted

By

Md. Mahmudul Hasan
Registration no. 86
Session 2016-2017

Physical Chemistry Research Laboratory
Department of Chemistry
Dhaka University
February, 2020

UNIVERSITY OF DHAKA
DEPARTMENT OF CHEMISTRY
Dhaka-1000, Bangladesh

Dr. M. Q. Ehsan
Professor

Tel: 9661900-59/4880
FAX: (880-2)-8615583
E-mail: mqehsan@yahoo.com

Certificate

This is to certify that the thesis entitled "*Studies on Interactions of Transition Metals with Leucine and Isoleucine using Spectroscopic and Electrochemical Techniques*" is the record of the research done by Mr. Md. Mahmudul Hasan, registration no. 86/2016-2017, research scholar, Department of Chemistry, Dhaka University, under my guidance for the award of Doctor of Philosophy in Physical Chemistry and that this thesis has not previously formed the basis for the award of any degree, diploma or other similar title to the candidate.

This is also to certify that the thesis represents the independent work of the candidate.

Md. Qamrul Ehsan

Dedicated

To

My Little Angel (Daughter)

Muntaqa Hasan

ACKNOWLEDGEMENT

It brings me great pleasure for an opportunity to work and submit my dissertation on “Studies on Interactions of Transition Metals with Leucine and Isoleucine using Spectroscopic and Electrochemical Techniques”. Foremost, I am grateful to the Almighty Allah for the wisdom he bestowed upon me, the strength, patience of my mind and good health in order to finish this research. Working as a PhD student was a dream as well as challenging experience to me. In all these years, many people were instrumental directly or indirectly to overcome the challenges facing my dream. It was hardly possible for me to thrive in my doctoral work without the precious support of these personalities. Here is a small tribute to all those people.

I would like to thank the Department of Chemistry, University of Dhaka for permitting and offering the opportunity to work as a PhD researcher in the “Oxford of the East”.

I am highly indebted to my respected supervisor, Dr. Md. Qamrul Ehsan, Professor, Department of Chemistry, University of Dhaka, for introducing me in the world of research. His expertise, constructive guidance, cheerful enthusiasm and ever-friendly nature accelerate me to complete my research work in a respectable manner.

I extend my profound gratitude and indebtedness to Dr. Pradip Kumar Bakshi, Professor, Department of Chemistry, University of Dhaka, for his valuable suggestions to write the thesis book. Thank you so much for your precious time to look over each word of my thesis book.

I wish to acknowledge the services rendered by the Laboratory of Organic Structural Chemistry (Prof. Shinmyozu laboratory), Department of Molecular Chemistry, Graduate School of Sciences & IMCE, Kyushu University, Japan.

I would like to offer my heartiest thanks to the Chairman, Bangladesh Council of Scientific and Industrial Research, for permitting me to perform the thermal analysis as the requirements of my study.

I immensely grateful to Wazed Miah Science Research Center, Jahangirnagar University, Bangladesh for permitting me to carry out the NMR analysis which plays an important part of my research work.

I would like to extend sincere gratitude to Mohammad A. Halim, PhD, CEO, and The Red-Green Research Centre. The theoretical calculations would not be possible without the help of his team.

I am thankful to my course teachers for doing their responsible job to complete my theoretical part as the requirements of my study. I am grateful to Dr. Abdul Jabbar, Professor, Department of Chemistry, University of Dhaka for his inspiration and cordial help in discussing different electrochemical techniques to complete my thesis.

My special thanks to Hossain Mohammad Naseem Akhtar, PhD, Ex research fellow of this laboratory for his advises and encouragement during my research. Thanks goes to Md. Elius Hossain, Associate Professor, Bangladesh University of Engineering and Technology (BUET), for his assistance.

I express my heartiest thanks to the entire laboratory attendant and technicians of Department of Chemistry especially Halim bhai, Sreekesh bhai, Jahangir bhai, Atiq bhai, Farid bhai, Harun bhai for their help and co-operation during my research work.

Last but not the least it is a great pleasure for me to express deepest love to my family for their support in this long journey. Their inspiration in all my ups and downs was beyond description.

Md. Mahmudul Hasan
Department of Chemistry
University of Dhaka

ABSTRACT

The redox behavior of the metal ions, Cu(II), Zn(II) and Cd(II) in absence and presence of the two isomeric ligand leucine and isoleucine were studied in aqueous medium using cyclic voltammetry. It was found that the redox process of the respective metal ions is quasi-reversible and some chemical reaction also occurs at the electrode surface while electron transfers. The study also supports that maximum interaction of the metal ion occurs at 1:2 mole ratio with the anionic form of the ligand.

Chronoamperometry and chronocoulometry were also performed to further investigate the electrochemical process. The result showed that after interaction the spike height is decreased, indicating towards a decrease in rate of electrolysis. The charge at τ is also decreased when ligand is mixed with the metal ion, which indicates that interaction occurs between metal ion and the ligand. The observations from the Anson plot indicate that adsorption of reactant or product occurs at the electrode surface in all cases.

The solid products obtained from the reaction of the metal ions, Co(II), Ni(II), Cu(II), Zn(II), Cd(II) and Hg(II) with anionic ligand were characterized by different analytical methods. Both leucine and isoleucine forms 1:2 complexes with metal ion, which is confirmed by the elemental and metal analysis. Thermal analysis ensures that the Co and Ni complex of both leucine and isoleucine contains two molecules of crystalline water. The Cu complex of isoleucine contains one molecule and the Zn complex of isoleucine contains half molecule of crystalline water. The other complexes do not contain any water of crystallization. The compounds have high melting temperature and are mostly insoluble in the common solvents. But the Ni-leucine, Co-isoleucine, Ni-isoleucine and Cu-isoleucine complexes are soluble in methanol.

The bonding nature of the complexes was characterized by spectroscopic study. IR spectral data of the complexes indicate that the metal-ligand bonding occurs through nitrogen atom of NH_2 group and oxygen atom of COO^- group. The shifting of the absorption bands, appearing of d-d transitions and charge transfer bands in the UV-Visible absorption spectrum also indicates the probability of forming M←L coordination bonds in the complexes. The UV-Visible diffuse reflectance spectral analysis shows that all the complexes have lower band gap energy, indicating their good conducting behavior. The nuclear magnetic resonance (NMR) spectral analysis demonstrated that the peaks overlap with each other. A peak for

-COOH proton appears in the ligand but in the complex it is not seen. This may be due to complexation of ligand with the metal ion.

The Differential Scanning Calorimetry (DSC) curve of the complexes is sharp endothermic. Therefore, the weight changes monitored by thermogravimetry involved absorption of energy. Magnetic susceptibility data of the complexes conclude that all of them are high spin paramagnetic complex excluding Zn, Cd and Hg complexes which are diamagnetic.

Density functional theory (DFT) has been employed in calculating the equilibrium geometries and vibrational frequencies of the complexes at B3LYP level of theory using 6-31G(d) and SDD basis sets. In addition, frontier molecular orbital and time-dependent density functional theory (TD-DFT) calculations are performed with CAM-B3LYP/6-31+G(d,p) and B3LYP/SDD level of theories. DFT calculation confirms that Co, Ni and Cu complexes form square planar structure whereas Zn, Cd and Hg adopt distorted tetrahedral structure. Cation-binding energy, enthalpy and Gibbs free energy values indicate that the complexes are thermodynamically stable. UV–Visible and TD-DFT studies reveal that these complexes demonstrate representative charge transfer and d–d transitions bands. The experimental IR vibrational frequencies and the absorption properties are very consistent with the calculated values. The HOMO-LUMO gap of the complexes is decreased from the parent ligand indicating that metal has a noticeable effect on the frontier molecular orbital energies.

CONTENT

CHAPTER 1 INTRODUCTION

CHAPTER 2 STUDY OF METAL – LIGAND INTERACTION IN SOLUTION

CHAPTER 3 STUDY OF METAL-LIGAND INTERACTION IN SOLID STATE

CHAPTER 4 SUMMARY

REFERENCES

INTRODUCTION

1.1 General background

The phrase “we are what we eat” is frequently used to signify that the compositions of our bodies is dependent in large measure on what we have consumed. The many chemical elements in the human body occur mainly in the form of water, proteins, fats, mineral salts and carbohydrates. Each human body is built up from food containing these five constituents and vitamins as well.

Proteins are made of carbon, hydrogen, oxygen and nitrogen. Some proteins also contain sulfur and phosphorus. They are particularly important as nitrogenous substances and are necessary for growth and development of the body, for body maintenance and the repair and replacement of damaged tissues, to produce metabolic and digestive enzymes, as an essential constituent of certain hormones [1].

Proteins are the most abundant biological macromolecules occurring in cells. The fundamental component of protein is the polypeptide chain composed of amino acids residues. Twenty different amino acids are involved in protein synthesis. They are classified as essential and non-essential types. When taken up into the human body from the diet, the 20 standard amino acids either are used to synthesize proteins, other biomolecules, or are oxidized to urea and carbon dioxide as a source of energy [2,3].

Transition metals such as Fe, Cu, Zn, Ni, Co, Mn have important biological functions and their activity depends on the ability to form complexes with biological molecules. Iron is the most important metal ion used in hemoglobin for oxygen transport and as an active site for many metalloenzymes in animals. Chronic diarrhoea can be a sign of zinc deficiency, and diarrhoea can lead to excessive zinc losses and zinc deficiency when dietary zinc is inadequate. Copper is essential to all living organisms as a trace dietary mineral because it is a key constituent of the respiratory enzyme complex cytochrome c oxidase. In humans, copper is found mainly in the liver, muscle, and bone. Copper is absorbed in the gut, then transported to the liver bound to albumin. After processing in the liver, copper is distributed to other tissues in a second phase, which involves the protein ceruloplasmin, carrying the majority of copper in blood. Ceruloplasmin also carries the copper that is excreted in milk, and is particularly well-absorbed as a copper source. Cobalt is the active center of a group of coenzymes called cobalamins. Vitamin B_{12}, the best-known example of the type, is an essential vitamin for all animals. Cobalt in inorganic form is also a micronutrient for bacteria, algae and fungi [1,4].

All metal ions which have gained access to the human system in sufficient amount and are not easily excreted or toxic to an extent; therefore can damage specific organs, affect central nervous system or interfere enzymatic process. Thus chelating agents are used in medicine for the formation of soluble, easily excretable metal chelates. Amino acids are well known among the chelating agents. Again the metal ions can be present as complexes. Metal complexes of amino acids are important in the biological system, for both nutritive and catalytic chemical reactions. In animals, free amino acids play an important role in the complexation of metal ions. The toxicity of such ions is decreased by chelation. Metals are often transported as amino acid complexes, which are generally governed by complex equilibria. The binding of metal ions changes the pK values of amino acids, which can in turn be used for activation. As well as occurring in biological systems, metal complexes can actually be used as drugs. The best example here is *cis*-platin, the name given to *cis*-$[PtCl_2(NH_3)_2]$, which is used in cancer chemotherapy [5]. This is a very simple complex, though there is one drawback: it has a certain degree of toxicity itself.

Leucine and isoleucine are two important isomeric essential amino acids in humans. Both are important for protein synthesis and many metabolic functions. They are used in assisting wound healing, stimulating immune function, promoting secretion of several hormones, synthesis of hemoglobin and regulating blood sugar and energy levels. Leucine also prevents breakdown of muscle proteins after trauma or severe stress [2,3].

Leucine **Isoleucine**

Fig. 1.1: Structure of leucine (2-amino-4-methylpentanoic acid) and isoleucine (2-amino-3-methylpentanoic acid)

Leucine and isoleucine both contains an amino (-NH_2) group and a carboxylic acid (-COOH) group in the same carbon which makes them very strong ligand (chelating agent) to coordinate with metal ions.

The above considerations together with the significant role of metal ions in the biological processes, systematic study of interactions of amino acids with metals is necessary. In this communication leucine and isoleucine complexes of some transition metals namely Co(II), Ni(II), Cu(II), Zn(II), Cd(II), Hg(II) are prepared and characterized by spectroscopic and electrochemical techniques.

1.2 Biological importance of metal and metal complexes

Metal ions play very significant role in biological systems as micronutrients. Many metals are essential for living organisms. They are vital components of blood, bones, teeth, body pigments, nerves, some proteins and enzymes. The coloring pigments which impact color to the plants and flowers contains ions like Cu(II), Fe(II), Co(II) etc. Metals in living bodies are mostly coordinated to their chemical species in it, to name some of the most important ones; we have hemoglobin in the red blood corpuscles, which is an iron complex of porphyrin. The iron becomes coordinated to oxygen in the lungs to form oxyhemoglobin, which is carried through the circulatory systems to all body regenerated. The green part of plant have green pigments called chlorophyll, which is a catalyst for the process of photosynthesis by which the plant produce food for glucose from carbon dioxide and water.

$$CO_2 + H_2O \xrightarrow[hv]{\text{Chlorophyll}} \text{Glucose}$$

Chlorophyll contains Mg as the central metal atom in a ring like structure similar to hemoglobin. Many proteins have metal ions, such as Ca(II), Mg(II) and Zn(II) coordinated to them and are called metalloproteins. For example, calcium cacinate is present in blood. Among the vitally important biochemical processes which are influenced by the metal ions are:

(i) Transmission of the nerve pulses in the animal bodies
(ii) Maintenance of the osmotic pressure in the animal and plant bodies\
(iii) In activation of enzymes
(iv) Polymerization of protein sub-units
(v) The binding of RNA to ribosome

(vi) Ion exchange in bones and other semisolid system

(vii) Phosphoryl group transfer and phosphate binding by divalent Ca, Mg, Mn

(viii) Development of effective control over various concentrations of essential components and to check concentrations of toxic substances in the body system to avoid malignancy of the cell and many other functions.

Manganese: Manganese is a trace element distribute throughout the body tissues and fluids. The bone, kidney, liver, pancreas and pituitary tissues contain more manganese than others. Several manganese containing metalloproteins have been discovered. Two enzymes pyruvate carboxylase and superoxide dismutase have been isolated from chicken liver mitochondria and appear to occur in other animal tissue mitochondria as well. Pyruvate carboxylase is involved in the synthesis of carbohydrates while superoxide dismutase is necessary for the protection of cells from high levels of oxygen radical [4].

Iron: Iron is the most common transition metal in biology. Iron is an essential element for most life on Earth, including human beings by participating in a wide variety of metabolic processes, including oxygen transport, DNA synthesis, and electron transport. Most of the iron (about 75%) in the body is present in the red blood cells, mainly as a component of haemoglobin. Much of the rest is present in the myoglobin, a compound occurring mainly in muscles, and as storage iron or ferritin, mainly in the liver, spleen and bone marrow. Additional tiny quantities are found binding protein in the blood plasma and in respiratory enzymes. The main vital function of iron is in the transfer of oxygen at various sites in the body. Haemoglobin is the pigment in the erythrocytes that carries oxygen from the lungs to the tissues. Myoglobin in skeletal and heart muscle accepts the oxygen from the haemoglobin. Once the oxygen is delivered the iron (as part of haemoglobin) binds the carbon dioxide which is then transported back to the lung from where it gets exhaled. When red blood cells die, their iron is released and carried by transferrin to the bone marrow and to other organs such as the liver and spleen. In the bone marrow, iron is stored and used as needed to make new red blood cells. Iron is also involved in the conversion of blood sugar to energy. Metabolic energy is crucial for athletes since it allows muscles to work at their optimum during exercise or when competing. The production of enzymes (which play a vital role in the production of new cells, amino acids, hormones and neurotransmitters) also depends on iron, this aspect becomes crucial during the recovery process from illnesses or following strenuous exercise or competing. The end result of iron deficiency is anemia [1,4,6,8].

Cobalt: Vitamin B_{12} is the name generally used for a group of related cobalt-containing compounds, also known as cobalamins, of which cyano cobalamin and hydroxocobalamin are the principal forms in clinical use. Vitamin B_{12}, occurs in the body mainly as methylcobalamine (Mecobalamin) and adenosylcobalamin (cobamamide) and hydroxocobalamin. Mecobalamin and cobamamide act as coenzymes in the nucleic acid synthesis. Vitamin B_{12} substances bind to intrinsic factor, a glycoprotein secreted by the gastric mucosa, and are the actively absorbed from the gastrointestinal tract. Vitamin B_{12} is extensively bound to specific plasma proteins called transcobalamins. Vitamin B_{12} is stored in the liver excreted in the bile. Hydroxocobalamin combines with cyanide to form cyano cobalamin, and thus may be used as an antidote to cyanide toxicity. Hydroxocobalamin is reported to be effective in controlling cyanide toxicity due to nitroprusside infusion and after exposure to inhaled combustion products in residential fires [1,4,8].

Nickel: Nickel compounds that possess similar elemental compositions but vary in physicochemical properties can elicit markedly different biological effects. The crystalline nickel sulfides and oxides that slowly dissolve in body fluids and readily enter cells by phagocytosis tend to be most active in producing morphological transformation of SHE cells in vitro and stimulating erythrocytosis and carcinogenesis following administration to rats. Although water-soluble nickel salts have not been shown to initiate carcinogenesis in rodents, the soluble nickel salts are evidently effective as cancer promoters following initiation of tumor genesis by aromatic hydrocarbons and nitrosoamines. Growing evidence suggests that the Ni(III)/Ni(II) redox-couple facilitates oxygen free-radical reactions, which may represent one of the molecular mechanisms for genotoxicity and carcinogenicity of nickel compounds [1,4,8].

Copper: Copper is required for many diverse functions such as melamin pigment formation, electron transport, phospholipid synthesis, collagen synthesis and integrity of myelin sheath. Copper is a constituent of several enzymes. Copper plays an important role in the catalytic activity of enzymes like cytochrome oxides which undergoes cyclic Cu(II)-Cu(I) transitions as they participate in carrying electrons to oxygen. Copper is also present in the active group of an important enzyme, Lysol oxides, which makes the cross linkage between peptide chains in collagen and elastin. Ferroxidase I (ceruloplasmin) and ferroxidase II are involved in the oxidation of ferrous to ferric ion. Dopamine-hydroxylase present in adrenal medulla is a copper enzyme which converts dopamine to norepinephrine by adding oxygen to the beta carbon atom. Melanocytes and melanoma tissues of human beings contain copper containing enzyme called tyrosinase which is responsible for melamin formation. Copper influences iron absorption and metabolism of iron from liver and other tissue stores. Copper containing water soluble proteins have been separated from brain tissue. The cerebrocuprein is one of these proteins which contain 3% copper. Other copper containing proteins are erythrocuprein occur in RBC and hepatocuprein occur in liver. In adults the copper content in whole blood is something over 100 µg per 100 mL. Copper appears to be involved in young erythrocytes formation and any deficiency of copper results anemia. In animals, if copper is given in place of iron in liver and spleen hemoglobin synthesis is rapid. Any deficiency of copper would results metabolic disorder [1,4,8,9].

Zinc: Zinc is an essential element in human nutrition. Most of the zinc in the body is in the skeleton, but other tissues (such as skin and hair) and some organs (particularly the prostate) have relatively high concentrations. Zinc is essential for the function of a large number of metalloenzymes including carbonic anhydrase, carboxypeptidase, phosphatases, dehydrogenases and transaminases. Zinc ion also involved in the biochemical processes which regulate protein and nucleic acid synthesis and turnover. Zinc is essential for the preservation of ribosomal tertiary structure. In zinc deficiency, ribosomes tend to unfold. Unfolded ribosomes do not function as templates for protein synthesis. Therefore, synthesis of enzymes such as DNA polymerase, thymine kinase and proline hydroxylase is decreased. Nucleic acid synthesis is impaired, cell replication is inhibited and growth fails. Zinc appears to be involved in the stabilization of plasma insulin. The plasma insulin concentration is low on zinc deficient diet. Chronic diarrhoea can be a sign of zinc deficiency, and diarrhoea can lead to excessive zinc losses and zinc deficiency when dietary zinc is inadequate. Zinc supplements have been shown to reduce the incidence, intensity, or duration of acute diarrhoea in children in developing countries. Growth retardation, loss of appetite and reduced food intake has been observed in zinc deficiency [1,4,7,8].

1.3 Toxicity of metals

One of the most serious problems, facing the world today is the contamination of the environment by toxic metals. One area of particular interest is the detection of heavy metals and metalloids in environmental matrices, complexation with chelating agents to reduce the degree of toxicity, characterization and the elucidation of their pathways through various environmental compartments. Focalizing on their degree of toxicity metal and metalloid ions can be divided into three groups. The metal or metalloids of the first group are toxic at all concentrations and have no known biological functions; this group includes lead, cadmium and mercury. The ions of the second group include arsenic, bismuth, indium, antimony and thallium; they also have no known biological functions, but are less toxic. However, they are still toxic if present in more than trace concentration (ppm level). The final groups includes essential trace metals or metalloids such as, zinc, copper, nickel, cobalt, manganese, iron, selenium which are required for various biochemical and physiological processes are toxic above certain concentrations.

Manganese: Manganese toxicity produces profound neurological disturbances similar to those of Parkinson's disease [1,4]. In this condition, metabolism of biogenic amines appears to be abnormal and seems to be linked to manganese metabolism. The successful treatment of Parkinsonism with L-dopa also seems to involve changes in manganese metabolism.

Cadmium: Cadmium is used in a wide range of manufacturing processes and cadmium poisoning presents a recognized industrial hazard. Inhalation of cadmium fumes during welding procedures may not produce symptoms until 12 to 36 hours have passed and these symptoms include respiratory distress leading to pulmonary edema; kidney toxicity is also a feature of acute cadmium poisoning. Ingestion of cadmium or its salts has the additional hazard of severe gastrointestinal effects. Cadmium has a long biological half-life and accumulates in body tissues, particularly the liver and kidneys. Chelation therapy is not generally recommended for cadmium poisoning, although sodium calcium edentate has been used following acute ingestion. Chronic exposure to cadmium results in progressive renal impairment and other effects. An increased incidence of cancer of the prostate has been reported in subjects exposed to high levels of cadmium but evidence is not conclusive. Cadmium sulphate has been used topically in some countries for the treatment of skin and scalp conditions. Cadmium sulphate has been included in some preparations for the treatment of eye irritation [1,4].

Mercury: Mercury was an important constituent of drugs for centuries as an ingredient in many diuretics, antibacterials, antiseptics, skin ointments, and laxatives. The use of mercury in medicinal preparations has dramatically decreased due to the toxic effects that it has in the human body, such as nausea, vomiting, abdominal pain, bloody diarrhoea, kidney damage, and death. Mercury readily forms covalent bonds with sulfur, and it is this property that accounts for most of the biological properties of the metal. When the sulfur is in the form of sulfhydryl groups, divalent mercury replaces the hydrogen atom to form mercaptides, X-Hg-SR and $Hg(SR)_2$, where X is an electronegative radical and R is a protein. Organic mercurials form mercaptides of the type RHg-SR'. Mercurials even in low concentrations are capable of inactivating sulfhydryl enzymes and thus interfering with cellular metabolism and function. Mercury also combines with other ligands of physiological importance, such as phosphoryl, carboxyl, amide, and amine groups. Organic mercurial compounds produce similar toxic effects to inorganic compounds, but they have a more selective action on the CNS that has proved difficult to treat. The degree of toxicity varies with the different groups of organic mercurial's; those used as preservatives or disinfectants. Methyl mercury is notorious for its toxicity; there have been cases of fetal neurotoxicity during outbreaks of methyl mercury poisoning. Chronic mercury poisoning may results from inhalation of mercury vapor, skin contact with mercury or mercury compounds, or ingestion of mercury salts over prolonged periods. The kidneys are one of the primary sites for the accumulation of mercury in the body. All forms of mercury may be toxic to the kidney although the inorganic forms are the most nephrotoxic. In severe cases of mercury poisoning chelation therapy may be required to facilitate the removal of mercury from the body. Chelating agents that may be used include dimercaprol, penicillamine, succimer, or unithiol. Some mercury salts are effective parasiticides and fungicides. Organic mercurial's such as phenyl mercuric acetate, borate and nitrate are also used as preservatives. Other mercury salts that have been used for their antibacterial activity include mercuric chloride, yellow mercuric oxide, and mercurous chloride. Some mercury compounds have been used in homeopathic medicine [1,4].

Lead: Lead poisoning (plumbism) may be due to inorganic or organic lead and may be acute or, more often, chronic. It has followed exposure to a wide range of compounds and objects from which lead may be absorbed following ingestion or inhalation. Children are often victims of accidental poisoning and may be vulnerable to chronic exposure to lead from environmental pollution. Over a period of time lead accumulates in the body and it is distributed in the soft tissues, with higher concentrations in the liver and kidneys. In the blood it is associated with the erythrocytes. It is also deposited in calcified bone, hair and teeth. Lead crosses the placental barrier. It is excreted in the faces, urine and sweat and also appears in breast milk. Acute effects of lead poisoning include abdominal pain, diarrhoea, vomiting, hypotension, muscle weakness, fatigue, abnormal liver function and acute interstitial nephritis. Encephalopathy may occur and is more common in children. There may also be kidney damage and impairment of mental function. Children with elevated lead concentrations may be symptomatic apart from intellectual deficits and behavioral disorders.

Organic lead poisoning produces mainly CNS symptoms; there can be gastrointestinal and cardiovascular effects, and renal and hepatic damage. Lead is absorbed from the gastrointestinal tract. It is also absorbed by the lungs from dust particles or fumes. Inorganic lead is not absorbed through intact skin, but organic lead compounds may be absorbed rapidly. Lead forms chelate with chelating agents. Children with blood lead concentration 250 nanograms/mL may require chelation therapy (e.g. sodium calcium edentate has been widely used as a means of assessing the need for therapy) [1,4].

1.4 Leucine and isoleucine

Leucine (leu) and isoleucine (ile) both are essential amino acid used in the biosynthesis of proteins. Both are α-amino acid, meaning they contains a α-amino group (which is in the protonated $-NH_3^+$ form under biological conditions), a α-carboxylic acid group (which is in the deprotonated $-COO^-$ form under biological conditions), and a hydrocarbon side chain, making them a non polar aliphatic amino acid. They are essential in humans, meaning the body cannot synthesize them and must be obtained from the diet.

1.4.1 Food sources and dietary needs: High Leucine and isoleucine foods include concentrated whey, soy, pea protein, beef, fish, chicken, chicken egg, almonds, oats, lentils, corn, cow milk, beans, cheese, pork, nuts, seafood, spinach, asparagus, lettuce (red leaf), squash, cauliflower, broccoli etc. The recommended daily intake for leucine is 39 mg per kilogram of body weight or 17.7 mg per pound. A person weighting 70 kg (~154 pounds) should consume around 2730 mg of leucine per day [10].

1.4.2 Pharmacology: Leucine is a dietary amino acid with the capacity to directly stimulate myofibrillar muscle protein sysnthesis. This effect of leucine arises results from its role as an activator of the mechanistic target of rapamycin (mTOR), a serine-threonine protein kinase that regulates protein biosynthesis and cell growth. Leucine metabolism occurs in many tissues in the human body. However, most dietary leucine is metabolized within the liver, adipose tissue and muscle tissue. Adipose and muscle tissue use leucine in the formation of sterols and other compounds [2,3].

1.4.3 Toxicity: Leucine toxicity, as seen in decompensate maple syrup urine disease, causes delirium and neurologic compromise, and can be life-threatening. A high intake of leucine may cause or exacerbate symptoms of pellagra in people with low niacin status because it interferes with the conversion of L-tryptophan to niacin. Leucine at a dose exceeding

500 mg/kg/d was observed with hyperammonemia. As such, unofficially, a tolerable upper intake level (UL) for leucine in healthy adult men can be suggested at 500 mg/kg/d or 35 g/d under acute dietary conditions [2,3].

1.5 Literature review

Cyclic voltammetry (CV) and differential pulse voltammetry (DPV) were performed with a glassy carbon electrode (GCE) modified with polyglutamic acid (PGA) on the three dihydroxybenzene isomers, catechol (CT), hydroquinone (HQ) and resorcinol (RS) [11]. At bare GCE, these isomers exhibited voltammogram with highly overlapped redox peaks that impeded their simultaneous detection in binary and ternary mixtures. On the contrary, at PGA modified GCE binary and ternary mixtures of the dihydroxybenzene isomers showed well-resolved redox peaks in both CV and DPV experiments. The resolving ability of PGA modified GCE proves its potential to the exploited as an electrochemical sensor for the simultaneous detection of these isomers.

Electrochemical behavior of catechol (CT), hydroquinone (HQ) and resorcinol (RS) was investigated in KCl, acetate buffer and phosphate buffer at glassy carbon electrode using cyclic voltammetry [12]. The results implied that the glassy carbon electrode exhibited a synergistic and excellent electro catalytic effect on the redox behaviors of the benzenediols. CT and HQ showed one pair of redox peaks in acetate and phosphate buffer but two pairs of redox peaks in KCl. In all cases the redox process was quasireversible. RS behaves almost irreversibly in all three electrolytic medium. The electrochemical process in all the isomers was diffusion controlled.

The redox behavior of Zn^{2+} ion and its electrochemical nature when interacts with the pharmaceutical drug metronidazole was investigated by G. J. Islam *et al.* [13]. Cyclic voltammetric (CV), chronoamperometric (CA) and chronocoulometric (CC) technique was applied for the research. The redox process of the metal ion was found as a combination of diffusion and adsorption controlled.

The redox behavior of Cu^{2+} ion and its electrochemical nature when interacts with the pharmaceutical drug metronidazole was investigated by G. J. Islam *et al.* [14]. Cyclic voltammetric (CV), chronoamperometric (CA) and chronocoulometric (CC) technique was applied for the research. The redox process of the metal ion was found as a combination of diffusion and adsorption controlled.

Rahman *et al.* investigated the interaction of Fe(III) with niacin and pyridoxine by UV-Visible spectrophotometry and cyclic voltammetry [15]. The metal to ligand ratio for Fe(III)-niacin system was found to be approximately 1:3 and in Fe(III)-pyridoxine system it was 1:1. The redox properties of uncoordinated Fe(III)/Fe(II) system is reversible at platinum electrode and in presence of the ligands the system was found to be quasi-reversible in nature. In all cases the system was diffusion controlled.

Hasan *et al.* studied the redox behavior of Cd(II) and interaction of Cd(II) with cyclic amino acid, proline, in KCl, $NaClO_4$ and acetate buffer of different pH [16]. The cyclic voltammogram showed that the system is two electron transfer process and quasi-reversible. The heterogeneous charge transfer rate constant, Tafel slope is also reported.

Hossain *et al.* studied the redox behavior of Zn(II) and interaction of Zn(II) with aspartic acid in KCl, $NaClO_4$ and acetate buffer of different pH [17]. The cyclic voltammogram showed that the system is two electron transfer process and quasi-reversible. The heterogeneous charge transfer rate constant, Tafel slope is also reported.

Electrochemical investigation for the complexation of iron (Fe) with ascorbic acid (AA) in aqueous medium was carried out by cyclic voltammetry, chronocoulometry and differential pulse voltammetry [18]. It has been established from Job's plot that Fe-AA complex is formed with 1:1 ratio. The active centre of AA for complexation to Fe is calculated by MOPAC (Semi empirical computation, molecular orbital package-PM3) computation. The stability constant of Fe-AA complex was determined by anodic striping voltammetry. The Fe-AA complex was successfully utilized to detect and qualitatively determine trace amount of AA.

The detailed redox behavior of copper-saccharin (Cu-Sac) complex was examined using the cyclic voltammertic technique [19]. It was found that the adsorption process suppresses the Faradic process of the complex. The effect of the introduction of the secondary ligand, 1, 10-phenanthroline (phen), pyridine (py) and bipyridine (bp) on the redox behavior of the Cu-Sac complex was studied where these ligands contributed on the charge transfer kinetics of the complex. The heterogeneous charge transfer rate constants were reported.

The redox behavior of manganese system in Mn-Sac and Mn-Sac-Phen complexes were studied using cyclic voltametric technique at glassy carbon electrode (GCE) in KCl electrolyte [20]. The CV of Mn-Sac solution is more or less similar to that of uncoordinated Mn. The presence of secondary ligand phenanthroline changes the CV of Mn system largely compared to those of uncoordimated Mn and Mn-Sac. The redox system was irreversible in mn-Sac and quasi-reversible in Mn-Sac-phenanthroline complex.

The electrochemical redox behavior of Fe(II)/Fe(III) systems formed during the oxidation of complexes $[Fe(C_7H_4NO_3S)_2(H_2O)_4].2H_2O$ (Fe-Sac) and $[Fe(C_7H_4NO_3S)_2(C_{12}H_8N_2)].2H_2O$ (Fe-Sac-Phen) have been investigated using cyclic voltammetry in the aqueous medium [21]. One pair of well defined cathodic and anodic peaks appeared for the transfer of single electron in the Fe-Sac complex. The electrode process was found irreversible. In the presence of secondary ligand, 1,10-phenanthroline (Fe-Sac-phen complex), the redox behavior was quasi-reversible. The effect of pH on the redox behavior of iron system was studied in acetate buffer.

The electrochemical redox behavior of Mn(II)/Mn(IV) system at different environment have been investigated using cyclic voltammetry [22]. Two pairs of well defined cathodic and anodic peaks appeared for transfer of two electrons in two separate steps. The electrode process was diffusion controlled. The effect of pH on the redox system was also studied.

Electrochemical redox behavior of Fe-Vit B_6 complex was investigated in HEPES buffer in the pH range 5.1-13.1 using cyclic voltammetry [23]. Well defined anodic and cathodic peaks were observed in the voltammogram at pH 13.1. At pH 8.0, only one cathodic peak and at pH 5.1, only one anodic peak was found. At all the pH values, the system was deviated from reversible behavior.

Electrochemical oxidation of iodide and bromide has been studied in the presence of benzoylacetone in dilute acetic acid medium using cyclic voltammetry at carbon electrodes [24]. At graphite paste and glassy carbon electrodes the iodide/iodine and bromide/bromine systems showed reversible redox reaction involving transfer of two electrons. In presence of benzoylacetone the oxidized product iodine/bromine, undergone chemical reaction to produce halo-derivatives. So, the process provides a route of electrochemical synthesis of 2-iodo and 2-bromobenzoylacetone in an undivided cell.

Cyclic voltametric (CV) studies of Cu-aspartic acid complex were carried out at glassy carbon electrode in acetate buffer medium [25]. Widely separated cathodic and anodic pair of peaks was observed in the potential window -1050 to 1000 mV. The electrode process was diffusion controlled.

Pervaiz *et al.* synthesized amino acid derivative Schiff base by reaction of leucine with salicyldehyde in basic medium [26]. The Schiff base was used as a ligand which was reacted with Co, Mn, Cu and Cd metals in order to form the stable complexes. The synthesized ligand and metals complexes were characterized by elemental and different spectroscopic tools i.e. FTIR, Mass spectrometry and NMR. All compounds including ligand and complexes were also engaged with different bacterial (*Escheria coli*, *Staphylococcus aureus*, *Bacillus subbtilis*) and fungal strains (*Alternaria alternate*, *Aspergillus flavus* and *Aspergillus niger*) in order to check the inhibitory action of titled compounds. The results showed that the metal complexes have greater antimicrobial activities than ligand.

The synthesis and structural characterization of cobalt (II) complexes of amino acid Schiff bases was prepared from salicylaldehyde and three amino acid (valine, leucine and isoleucine) in basic medium [27]. The metal complexes was synthesized by treating an ethanolic solution of the ligand with appropriate amount of metal salts [1:2] [M:L] ratio. The synthesized Schiff bases and their metal complexes have been investigated on the bases of elemental chemical analysis, FTIR, electronic spectral, H NMR, ^{13}C NMR, MS, molar conductance and magnetic susceptibility measurements. The electronic spectrum of the metal complexes and their magnetic susceptibility measurements suggest octahedral structures are the probable coordination geometries for the isolated complexes. The Schiff bases and their metal complexes were preliminary scanned against various strains of microbes to study their biological effect.

Amino acid Schiff bases with ester function $K(Rleu)\cdot 2H_2O$ (1), $K(Rile)\cdot 2H_2O$ (2), $K(Rhis)\cdot H_2O$ (3) (Rleu, Rile and Rhis represent the Schiff base of DL-leucine, L-isoleucine and L-histidine, and ethyl-α-ketocyclopentylcarboxylate) were synthesized by A. Angoso *et al.* [28]. Compounds 1, 2 and 3 were characterized by H NMR spectroscopy. The copper(II) complexes, $Cu(Rleu')\cdot H_2O$ (4), $Cu[Rile']\cdot H_2O$ (5) and $Cu(Rhis')\cdot 2H_2O$ (6), were obtained with the N-deprotonated Schiff bases (Rleu′, Rile′ and Rhis′). The COO^- stretching bands in their IR spectra suggest that the carboxylate acts as a monodentate group when binding with copper. The temperature dependence of the susceptibility for 6 may be fit to the Curie-Weiss expression χ = O.32/(T-26.2) emu mol^{-1} K^{-1} The dehydration process of 6 leads to the anhydrous compound, enthalpy (53±2 kJ mol^{-1}) and activation energy (82±5 kJ mol^{-1}).

V. J. Tonoyan *et al.* reported that salicylidene-D,L-tyrosine ethyl ester and $Cu(II)(SalTyrOEt)_2$ were synthesized, characterized, and chain-breaking antioxidant and prooxidant reactivities determined in a 2,2′-azoisobutyronitrile initiated linoleic acid peroxidation reaction [29]. Kinetics of oxygen consumption were found to be comparable to the antioxidant reactivity of 2,6-ditertiary-butyl-4-hydroxytoluene, due to efficient removal of linoleic acid peroxyl radical with the formation of linoleic acid hydroperoxide, LOOH, and correlate with the presence of tyrosyl phenolic OH groups. Copper in Cu(II)(SalTyrOEt)$_2$ accounts for prooxidant reactivity, catalyzing removal of LOOH, except at low concentrations when its antioxidant properties dominate. It is concluded that Cu(II)(SalTyrOEt)$_2$ is a unique antioxidant with prooxidant reactivity.

G. S. Grigoryan *et al.* studied the catalytic activity of Co(II) ion and isoleucine complex on decay of cumene hydroperoxide in aqueous solution [30]. They presents the results of a study of catalytic decomposition of ROOH under the influence of $[\text{Co·Ile}]^+$ complex with composition 1:1, which is formed in the system Co^{2+} + Ile + ROOH + H_2O, and kinetic parameters of the reaction at the temperature range 323–353 K. Amino acid (Ac) and metal ions M(II) do not cause decomposition of ROOH separately, which occurs at their jointly presence in the reaction solution with the formation of complexes $[\text{MAc}]^+$ in alkaline medium. Because of catalytic action of the formed complex on ROOH the latter decomposes into oxygen and corresponding alcohol.

Mixed ligand Th(IV) complexes of the type $[M(Q)_2LNO_3.H_2O]$ have been synthesized using 8-hydroxyquinoline (HQ) as a primary ligand and N- and/or O- donor amino acids (HL) such as L-alanine, L-phenylalanine, L-serine and L-tyrosine as secondary ligands [31]. The electrical conductance studies of the complexes in DMF at 10^{-3} M concentration indicate their non-electrolytic nature. Room temperature magnetic susceptibility measurements revealed diamagnetic nature of the complexes. Electronic absorption spectra of the complexes show intra-ligand and charge transfer transitions, respectively. The thermal analysis data of the complexes indicate the presence of a coordinated water molecule. The tube dilution method has been used to study the antibacterial activity of the complexes against the pathogenic bacteria *S. aureus* and *E. coli*. The results have been compared against those of control tetracycline, which was screened simultaneously and indicate mild antibacterial activity of the complexes. The representative complex has been screened for cytotoxicity (IC_{50}) studies against *Ehrlich ascites* cells and *Daltons lymphoma ascites* cells and shows low cytotoxic activity.

Mixed ligand Ni(II) complexes of the type [M(Q)(L).2H_2O] have been synthesized by using 8-hydroxyquinoline (HQ) as a primary ligand and N- and/or O- donor amino acids (HL) such as L-serine, L-isoleucine, L-proline, 4-hydroxy-L-proline and L-threonine as secondary ligands [32]. The metal complexes have been characterized on the basis of elemental analysis, electrical conductance, room temperature magnetic susceptibility measurements, spectral and thermal studies. The electrical conductance studies of the complexes in methanol at 10^{-3} M concentration indicate their non-electrolytic nature. Room temperature magnetic susceptibility measurements revealed paramagnetic nature of the complexes. Electronic absorption spectra of the complexes show intra-ligand, charge transfer and d-d transitions, respectively. The thermal analysis data of the complexes indicate the presence of coordinated water molecules. Tube dilution method has been used to study the antibacterial activity of the complexes against the pathogenic bacteria *C. diphtheriae, S. aureus* and *C. albicans*. The results have been compared with those of control tetracycline, which was screened simultaneously and indicated mild antibacterial activity of the complexes.

Farid khan *et al.* reported the voltammetric reduction of Zn(II) using L-lysine, L-ornithine, L-threonine, L-serine, L-phenylglycine, L-phenylalanine, L-glutamic acid, L-aspartic acid and vitamin B_7 (biotin) at pH 7.30 ± 0.01 and I = 1.0 M $NaClO_4$ at 25 and 35 °C [33]. The nature of the current voltage curves was quasireversible and diffusion-controlled. Zn^{2+} formed 1 : 1 : 1, 1 : 1 : 2 and 1 : 2 : 1 complexes with these drugs as confirmed by the Schaap and McMaster method. The sequence of the stability constant of L-lysine < L-ornithine < L-threonine < L-serine < L-phenylglycine < L-phenylalanine < L-glutamic acid < L-aspartic acid complexes can be explained on the basis of the size, basicity and steric hindrance of ligands. The values of the stability constant (log β) varied from 2.13 to 11.37 and confirm that these drugs, i. e. L-amino acids or in combination with vitamin B_7 or their complexes, could be used against Zn^{2+} toxicity. The thermodynamic parameters such as enthalpy (ΔH), free energy (ΔG) and entropy change (ΔS) are also reported. The kinetic parameters viz. the transfer coefficient (α), degree of irreversibility (λ), diffusion coefficient (D) and standard rate constant (k) were calculated. The values of α confirmed the symmetric nature of the ‘activated complex’ between oxidants and reluctant in response to the applied potential between the dropping mercury electrode and solution interface.

Six ternary α-amino acid copper(II) complexes of the general formula [Cu(AA)(B)(H_2O)](X) (1–6), where AA is L-leu = L-leucine (1–3) or L-ile = L-isoleucine (4–6), B is a N,N-donor heterocyclic base, viz. 2,20-bipyridine (bpy, 1, 4), 1,10-phenanthroline (phen, 2, 5) and dipyrido [3,2:20,30-f] quinoxaline (dpq, 3, 6) and X = ClO_4^- / NO_3^- have been synthesized, characterized, and their DNA binding and cleavage activity studied [34]. The bpy and dpq complexes of L-ile (4,6) have been structurally characterized by X-ray crystallography. The complexes show a distorted square-pyramidal (4 + 1) CuN_3O_2 coordination geometry. The one-electron paramagnetic complexes display a d–d band near 600 nm in water and show a cyclic voltammetric response due to a Cu(II)/Cu(I) couple near -0.1 V (vs. SCE) in DMF-0.1 M TBAP. All complexes are 1:1 electrolytes. Binding interactions of the complexes with calf thymus DNA (CTDNA) have been investigated by absorption, emission, viscosity and DNA melting studies. The phen and dpq complexes are avid binders to the calf thymus DNA, giving an order: (3,6) (dpq) > (2,5) (phen) (1,4) (bpy). The bpy complexes do not show any apparent binding to the DNA and hence show poor DNA cleavage activity. The phen and dpq complexes (2,3,5,6) show efficient oxidative cleavage of pUC19 supercoiled DNA (SC-DNA) in the presence of the reducing agent 3-mercaptopropionic acid (MPA) involving hydroxyl radical (OH) species, as evidenced from the control data showing inhibition of DNA cleavage in the presence of OH radical quenchers, viz. DMSO, mannitol, KI and catalase.

Voltammetric technique was used to study the binary and ternary complexes of cadmium with L-amino acids and vitamin-C (L-ascorbic acid) at pH = 7.30 ± 0.01, $\mu = 1.0$ M KNO_3 at 25ºC and 35ºC by F. Khan *et al* [35]. Cd (II) formed 1:1:1, 1:1:2 and 1:2:1 complexes with L-lysine, L-ornithine, L-threonine, L-serine, L-phenylglycine, L-phenylalanine, L-glutamic acid and L-aspartic acid used as primary ligands and L-ascorbic acid used as secondary ligand. The trend of stability constant of complexes was Llysine < L-ornithine < L-threonine < L-serine < L-phenylglycine < L-phenylalanine < L-glutamic acid < L-aspartic acid which can be explained on the basis of size, basicity and steric hindrance of ligands. The values of stability constant (log β) varied from 2.23 to 11.33 confirm that these drugs i.e. L-amino acids or in combination with L-ascorbic acid or their complexes could be used against Cd(II) toxicity. The study has been carried out at 35ºC also to determine the thermodynamic parameters such as enthalpy change (ΔH), Free energy change (ΔG) and entropy change (ΔS) respectively.

Fatma M. Elzawawy determined the stoichiometric stability constants for La(III) and Y(III) L-serine complexes by potentiometric methods at different ionic strengths adjusted with $NaClO_4$ and at different temperatures [36]. The overall changes in free energy (ΔG^o), enthalpy

(ΔH^o) and entropy (ΔS^o) during the protonation of L-serine and that accompanying the complex formation with the metal ions have been evaluated.

S. S. Khaloo and his coworkers investigated the electrochemical behavior of cysteine at a chemically modified electrode prepared by incorporating cobalt(II) phthalocyanine [Co(II)Pc] into carbon paste matrix by cyclic voltammetry and potentiometry [37]. The modified electrode showed high electrocatalytic activity toward cysteine; the overpotential for the oxidation of cysteine was decreased by more than 100 mV, and the corresponding peak current increased significantly. The electrocatalytic process was highly dependent on the pH of the supporting electrolyte. The peak currents decreased when the pH was raised to 6 and totally disappeared at pH $\geq$ 7, resulting from the autocatalytic oxidation of cysteine by Co(II)Pc at the electrode surface. Therefore, at pH values of 6 to 8, the modified electrode was used as a potentiometric sensor for quantitative measurement of cysteine in the presence of oxygen in air saturated solutions. In fact, the Co(II)Pc/Co(I)Pc couple acts as a suitable mediator for indirect oxidation of cysteine by dissolved oxygen at approximately neutral pH values. Under the optimized conditions, the potentiometric response of the modified electrode was linear against the concentration of cysteine in the range of 0.6 μM to 2 mM. The limit of detection was found to be 0.5 μM. The potentiometric response time was $\leq$15 s. The electrode showed long term stability; the standard deviation of the slope obtained after repeated calibration during a period of two months was 2.8% (n = 7). Application of the electrode in a recovery experiment for the determination of cysteine added to a synthetic serum sample is described.

A copper complex of isoleucine, molecular formula $Cu(C_6H_{12}NO_2)_2$, is synthesized in water-ethanol medium and characterized by elemental analysis, FTIR, UV-Visible spectroscopy, thermogravimetric analysis (TGA), reflectance analysis, conductivity measurement and theoretical structure determination [38]. The complex is soluble in methanol and decomposed before melting. The conductivity measurement concluded that this complex is weak electrolyte. Optimized structure of the synthesized $Cu(C_6H_{12}NO_2)_2$ complex is square planar calculated by DFT level of theory.

Metal complexes of the essential amino acids leucine and methionine, $[M(L.H_2O)_2]$, [where L = leucine and methionine), M = Co^{2+}, Ni^{2+}, Cu^{2+}, Zn^{2+}, Cd^{2+}], have been prepared from the reaction of chloride salt of transition metal with sodium salt of the amino acid [39]. The complexes have been characterized by means of infrared spectrum and atomic absorption analysis. The IR spectrum and atomic absorption analysis showed that amino acids act as bidentate ligands. IR spectroscopy confirms the ligand coordination to the metal ions through carboxyl and amine groups. The prepared complexes show poor solubility in water and in the common organic solvents.

The stability constants of Cu^{2+}, Mn^{2+} and UO_2^{2+} complexes with isoleucine were determined by paper electrophoretic technique [40]. Present method is based upon the migration of a spot of the metal ions on a paper strip at different pH’s of background electrolyte. A graph of pH against mobility gives information about the binary complexes and permit to calculate their stability constants. The first and second stability constants of [Cu(II) – isoleucine], [Mn(II) – isoleucine] and [UO_2(II) – isoleucine] complexes were found to be (8.41±0.07; 6.43±0.03), (3.87±0.11; 2.61±0.06) and (7.91±0.13; 5.73±0.04) for Cu(II), Mn(II) and UO_2(II) complexes, respectively at ionic strength 0.1 Mol/L and a temperature of 35^0C.

The dissociation of L-serine orthophosphate (H_3L) and its complexation reactions with calcium(II) and magnesium(II) have been studied by potentiometric titration at 37 ^{0}C in the 0.15 $molL^{-1}$ potassium nitrate medium and (with the exception of calcium(II) complexation) in the 0.15 $molL^{-1}$ tetraethylammonium bromide medium [41]. A least squares interpretation of the data has yielded dissociation constants for H_3L and equilibrium constants for the formation of the 1:1 metal-ion complexes MH_2L^+, MHL, and ML^-. In addition the dimeric species $H_5L_2^-$, $MH_3L_2^-$, and $M_2H_2L_2$ are consistent with the data and equilibrium constants for their formation have been determined.

The binary and ternary metal complexes of Cu(II) and Ni(II) with some amino acids (leucine, isoleucine and serine) as primary ligand and pyrophosphate (PP), adenosine-5´-triphosphate (ATP), as secondary ligand have been studied potentiometrically at 35°C and a constant ionic strength (1.0 mol dm^{-3} KNO_3) [42]. The formation of various binary and ternary complexes has been inferred from the corresponding titration curves. The Irving and Rossotti titration technique has been applied to determine the formation constants corresponding to various complexation equilibria.

A new series of potential ligands N-[benzoylaminothioxomethyl]-amino acid (HL) were prepared by the reaction of benzoylisothiocyanate with various amino acids namely histidine, alanine, phenylalanine, serine and cystene [43]. The ligands were characterized by IR, UV-Vis and NMR spectra. The $ML_2.nH_2O$ complexes of these ligands [M = Cu(II), Co(II), Ni(II)] were isolated and have been characterized by UV-Vis and IR spectrum.

The heat effects of complex formation between nickel(II), cobalt(II), cadmium(II), and zinc(II) ions and L-serine in aqueous solution over the ionic strength range 0.25–0.75 (background electrolyte KNO_3) were determined calorimetrically at 298.15 K [44]. The heats of dilution of solutions of metal nitrates with solutions of the background electrolyte were measured under identical conditions for the introduction of the corresponding corrections. The thermodynamic characteristics of complex formation between 3*d* transition metals and L-serine were calculated. The results were analyzed using the Herny theory. The complex-forming ability of transition metals in reactions with the ligand was characterized with the use of the Irving-Williams series.

The preparation of platinum(II) complexes containing L-serine using $K_2[PtCl_4]$ and KI as raw materials was undertaken [45]. The *cis–trans* isomer ratio of the complexes in the reaction mixture differed significantly depending on whether KI was present or absent in the reaction mixture. One of the two [Pt(L-ser-*N*,*O*)$_2$] complexes (L-ser = L-serinate anion) prepared using KI crystallizes in the monoclinic space group $P2_12_12_1$ with unit cell dimensions a = 8.710(2) Å, b = 9.773(3) Å, c = 11.355(3) Å, Z = 4. The crystal data revealed that this complex has a *cis* configuration. The other [Pt(L-ser-*N*,*O*)$_2$] complex also crystallizes in the monoclinic space group $P2_12_12_1$ with unit cell dimensions a = 7.0190(9) Å, b = 7.7445(6) Å, c = 20.946(2) Å, Z = 4. The crystal data revealed that this complex has a *trans* configuration. The ^{195}Pt NMR chemical shifts of *trans*-[Pt(L-ser-*N*,*O*)$_2$] and *cis*-[Pt(L-ser-*N*,*O*)$_2$] complexes are −1632 and −1832 ppm, respectively. ^{195}Pt NMR and HPLC measurements were conducted to monitor the reactions of the two [Pt(L-ser-*N*,*O*)$_2$] complexes with HCl. Both ^{195}Pt NMR and HPLC showed that the reactivity's of *cis*- and *trans*-[Pt(L-ser-*N*,*O*)$_2$] toward HCl are different: coordinated carboxyl oxygen atoms of *trans*-[Pt(L-ser-*N*,*O*)$_2$] were detached faster than those for *cis*-[Pt(L-ser-*N*,*O*)$_2$].

A series of metal(II) complexes have been synthesized by the reaction of chloride salts of magnesium, calcium, iron, cobalt, copper and zinc with amino acids, DL-alanine, L-glutamic acid and leucine [46]. Complex formation occurred at the proximal sites of the carboxyl moiety and the alpha amino nitrogen by 1:2 stoichiometric reactions which were also confirmed by elemental analysis and FTIR data. The metal complexes of DL-alanine and

L-glutamic acid are water soluble while metal-leucine complex has solubility in DMSO. The purposed structures of complexes were confirmed by H NMR studies.

The solid complexes $[Co(C_6H_{10}NO_2S)_2]$, $[Ni(C_6H_{10}NO_2S)_2]$, $[Cu(C_6H_{10}NO_2S)_2]$ and $[Fe(C_6H_{10}NO_2S)_2]$ were obtained from the reaction of cobalt(II), nickel(II), copper(II) and iron(II) salts with the potassium salt of the amino acid deoxyalliin (S-allyl-L-cysteine) [47]. Electronic absorption spectra of the complexes are typical of octahedral structures. Infrared spectroscopy confirms the ligand coordination to the metal ions through (COO^-) and (NH_2) groups. EPR spectrum of the Cu(II) complex indicates a slight distortion of its octahedral symmetry. Mössbauer parameters permitted to identify the presence of iron(II) and iron(III) species in the same sample, both of octahedral geometry. Thermal decomposition of the complexes lead to the formation of CoO, NiO, CuO and Fe_2O_3 as final products. The compounds show poor solubility in water and in the common organic solvents. Based on the chemical and spectroscopic results the following schematic structure for the complexes is proposed.

A series of complexes of Cu(II) with essential amino acids have been prepared with formula $[M(L)_2]^{2+}$ (where L = L-asparginine, L-histidine, L-lysine). The complexes were synthesized and characterized by elemental chemical analysis, electronic and infrared spectrum. IR spectroscopy confirms the ligand coordination to the metal ions through carboxyl and amine groups [48].

Unsymmetrical mixed ligand metal complexes of Hg(II) and UO_2(II) with 2,3 dihydroxypyridine (DHP) and amino acids glycine (gly), alanine (ala), valine (val) and leucine (leu) have been synthesized [49]. All synthesized complexes were characterized by analytical and spectral studies i.e. elemental analysis, electronic, IR and thermal (TGA, DTA, DSC) spectral studies. On the basis of characterization data UO_2(II) complexes possessed six coordinated octahedral geometry while Hg(II) complexes possessed four coordinated tetrahedral geometry. *In vitro* antifungal activity of the complexes was examined against the fungi *F. moniliformae and R. solani* by using food poison technique.

Synthesis and identification of some metal complexes of three amino acid namely glycine, alanine and valine was done by Obaid and his coworkers [50]. The complexes were prepared by reacting the three amino acids with the metal(II) chloride by using 50% ethanolic solution and 50% distilled water in the molar ratio [1:1:1:1] (M:Gly:Ala:Val). The prepared complexes identified by using physical properties, flame atomic absorption and conductivity measurements, in addition, mass, FTIR and UV-Visible spectrum as well magnetic moment data. The general formula of the complexes is Na[M(Gly)(Ala)(Val)].H_2O where M(II) represent Cu(II), Zn(II), Cd(II) and Hg(II). The Co(II) complex has the formula [Co(Ala)(Val)(OH_2)$_2$] and the Ni(II) complex has the formula Na[Ni(Ala)(Val)Cl].H_2O. Each of the glycine, alanine and valine behave as a bidentate ligand which is coordinated through the oxygen atom of the carboxyl group ($-COO^-$) and the nitrogen atom of the amino group ($-NH_2$). The suggest geometry of the metal(II) complexes to be octahedral except the Ni(II) complex is square pyramid geometry. The antibacterial and antifungal activity of the products were also studied.

Metal(II) coordination compounds of glycine and phenylalanine were synthesized and characterized using infrared and electronic spectroscopic, and magnetic susceptibility measurements [51]. The complexes were tested for antimicrobial activity against *Bacillus subtilis*, *Staphylococcus aureus*, *Methicillin* Resistant *Staphy-lococcus aureus* (MRSA), *Escherichia coli, Pseudo-monas aeruginosa, Proteus vulgaris* and *Candida albicans*. The stoichiometric reaction between the metal(II) ions and ligands in molar ratio M:L (1:3) [where M = Mn, Co, Ni, Cu and Cd; L = glycine, phenylalanine] resulted in the formation of five-coordinate square pyramidal dinuclear geometry for both copper complexes and six-coordinate octahedral geometry for the other complexes. The spectroscopic and magnetic moment data suggested that the ligands coordinated via both their amino and carboxylate ion moieties. The complexes demonstrated better activities against one or more of the tested microbes than acriflavine, the standard drug used.

Using potentiometric titrations, UV-Vis, IR and speciation diagrams, it appeared that the simplest amino acid Glycine (Gly) is not reacting in a simple manner at all with the copper metal ion (Cu^{2+}) in aqueous solutions at 25°C [52]. The potentiometric measurements indicated that Cu^{2+} released a net of two protons ($2H^+$) into the solution. Free Gly released one proton (H^+) into the solution from the single ammonium group. On the other hand, when Glycine hydrochloride (Gly.HCl) was used instead of free Gly, both the carboxylate and the ammonium groups released their protons. Upon the reaction of Cu^{2+} with Gly.HCl in any molar ratio, a net of four protons or more were released into the solution; one H^+ from the carboxylic acid group, the second from the ammonium group and the additional two protons from the Cu^{2+}-aqua ligands. The proposed solution species are in a good agreement with what has been shown in the literature.

Palladium(II) complexes with Schiff bases ligands derived from salicylaldehyde and amino acids (Ala, Gly, Met, Ser, Val) have been synthesized and characterized by FTIR, UV-Vis and H-NMR spectroscopy [53]. The electrospray mass spectrometry (ES-MS) spectrometry confirms the formation of palladium(II) complexes in 1/2 (M/L) molar ratio. All the Pd(II) complexes $[Pd(SalAla)_2]Cl_2$, $[Pd(SalGly)_2]Cl_2$, $[Pd(SalMet)_2]Cl_2$, $[Pd(SalSer)_2]Cl_2$, $[Pd(SalVal)_2]Cl_2$; have shown antibacterial activity against Gram-positive bacteria *Staphylococcus aureus* and Gram-negative bacteria *Escherichia coli*.

The antibacterial properties of differently copper and cobalt amino acids complexes on agar plates were investigated in the present study [54]. The antibacterial activity of amino acid complexes was evaluated against on three bacteria strains (*Escherichia coli, Bacillus cereus, Micrococcus luteu*s). Generally, the amino acids complexes were mainly active against gram-positive organisms, species like *Micrococcus luteus* being the most susceptible strain tested. It was registered a moderate antibacterial activity against *Bacillus cereus*. The microorganisms *Escherichia coli*, which are already known to be multi-resistant to drugs, were also resistant to the amino acids complexes but also to the free salts tested. *Escherichia coli* were susceptible only to the $CoCl_2$ and copper complex with phenylalanine. The complexes with leucine and histidine seem to be more active than the parent free ligand against one or more bacterial species. Moderate activity was registered in the case of complexes with methionine and phenylalanine. From the complexes tested less efficient antibacterial activity was noted in the case of complexes with lysine and valine. These results show that cobalt and copper complexes have an antibacterial activity and suggest their potential application as antibacterial agents.

Metal complexes of N-phthaloyl glycine with Cu(II), Ag(I), Cd(II), Hg(II), and Pb(II) have been prepared in aqueous methanolic solution [55]. The complexes have been characterized by elemental analysis, thermogravimetric analysis (TG, DTG), and mass, infrared and H-NMR spectrum. Infrared spectrum were detected concerning, the final residual of the thermal decomposition of all the N-phthaloyl glycine complexes. N-phthaloyl glycine (Gly) molecule coordinated to the metal ions through its carboxylic group.

The interactions of transition metals cobalt(II) and nickel(II) ions with the amino acids L-threonine (L-thr), L-proline (L-pro) and L-lysine (L-lys) in aqueous solution have been studied by using visible spectroscopic method [56]. On addition of amino acids to the aqueous solution of the metal ions, a change in the visible spectrum is observed due to the replacement of the water molecules from the coordination sphere of the aquo-complex $[M(H_2O)_6]^{2+}$ by the amino acid molecules. $[M(H_2O)_6]^{2+} + L = [M(H_2O)_5L]^{2+} + H_2O$ (where M = Co(II) and Ni(II); L = L-threonine, L-proline and L-lysine). The equilibrium constants and the change of Gibbs free energy ΔG^o of the water exchange process at room temperature have been determined. For Ni(II)-H_2O-amino acid systems the equilibrium constants have been determined for five variable temperatures (318-298 K) and the corresponding thermodynamic parameters ΔG^o, ΔH^o and ΔS^o have been calculated.

Synthesis of vanadium(V) complex containing L-phenylalanine and synthesis of vanadium(V) complex with aspartic acid is discussed [57]. The complexes are obtained as coloured microcrystalline products. These newly synthesized complexes are insoluble in aqueous medium and in organic solvents. The complexes are air stable. The presences of ligands such as peroxide (O_2^{2-}), phenylalanine ($C_9H_{11}NO_2$), aspartic acid ($C_4H_7NO_4$) are confirmed from qualitative tests in the respective complexes.

Seven novel metal complexes of the second-generation quinolone antibacterial agent enrofloxacin with Mn^{2+}, Fe^{3+}, Co^{2+}, Ni^{2+}, Zn^{2+}, Cd^{2+} and UO_2^{2+} have been prepared and characterized with physicochemical methods and infrared, UV-Vis and nuclear magnetic resonance spectroscopies [58]. In the resultant complexes, enrofloxacine acts as a bidentate deprotonated ligand bound to the metal through the pyridine oxygen and one carboxylate oxygen. The central metal atoms are six coordinate with slightly distorted octahedral geometry. Molecular modeling calculations have been performed in order to propose a model for the structure of Mn^{2+}, Fe^{3+} and UO_2^{2+} complexes. The antimicrobial activity of the complexes has been tested on three different microorganisms. The complexes exhibit better or equal inhibition in comparison to free enrofloxacin.

Some transition metal complexes of phenylalanine of general formula $[M(C_9H_{10}NO_2)_2]$; where M = Mn(II), Co(II), Ni(II), Cu(II) and Zn(II) were prepared in aqueous medium and characterized by spectroscopic, thermo-gravimetric (TG) and magnetic susceptibility analysis [59]. Density functional theory (DFT) has been employed calculating the equilibrium geometries and vibrational frequencies of those complexes at B3LYP level of theory using 6-31G(d) and SDD basis sets. In addition, frontier molecular orbital and time-dependent density functional theory (TD-DFT) calculations are performed with CAM-B3LYP/6-31+G(d,p) and B3LYP/SDD level of theories. DFT calculation confirms that Mn, Co, Ni and Cu complexes form square planar structure whereas Zn adopts distorted tetrahedral geometry.

The metal–oxygen bonds in the optimized geometry of all complexes are shorter compared to the metal–nitrogen bonds which is consistent with a previous study. Cation-binding energy, enthalpy and Gibbs free energy indicates that these complexes are thermodynamically stable. UV–Vis and TD-DFT studies reveal that these complexes demonstrate representative metal-to-ligand charge transfer (MLCT) and d–d transitions bands.

Complex of iron(III) with saccharine, $[Fe(C_7H_4O_3SN)_2Cl]$ has been prepared in aqueous medium [60]. The IR and electronic spectral analysis suggested that two saccharine molecules were attached to the metal ion through N atom and there was no chemically coordinated water or crystalline water in the complex molecule. The complex was paramagnetic. The cyclic voltammertic study indicated a quasi-reversible electron transfer process due to the presence of iron in the compound.

Ehsan *et al.* showed that, tris(2-aminoethyl)amine, tren, was reacted with Co(II), Ni(II), Cu(II) and Zn(II) in presence of ammonia and in presence of 4,4’-bipyridyl separately in the aqueous medium [61]. In all preparations ClO_4^- ion was added as counter ion to get the solid product. The general formulae of the prepared complexes are $[M(tren)(NH_3)](ClO_4)_2$ and $[M(tren)(C_{10}H_8N_2)](ClO_4)_2$. Elemental analysis, IR, UV-Visible spectral analysis has been used to characterize the compounds. They also reported d-values from powder photographs. Molecular modeling of the compounds gives idea about the structures. Bonding pattern of all the compounds indicate slightly distorted trigonal bipyramidal geometry. Because of steric hindrance of three five membered rings within metal and the ligand, tren, the equatorial plane of the trigonal bipyramid is inclined towards the tripodal ligand.

Ehsan *et al.* reported that, pyridoxine or Vitamin B_6 reacts with Fe(III), Mo(VI), Cd(II), Hg(II) and U(VI) in aqueous medium to produce solid stable compounds [62]. The compounds were characterized by using elemental analysis data and IR and UV-Visible spectroscopic techniques. Conductance behavior of the aqueous solution and the thermal decomposition nature of the complexes were also studied.

Ehsan and his coworkers prepared solid complexes by reacting tripodal ligand, tren with Ag(I), Cd(II), Hg(II), Zr(IV) and U(VI) in ethanol medium [63]. Ag(I) and Cd(II) formed simple five coordinated compounds and others produced double salt like compounds. The bonding pattern of the compounds was assigned on the basis of IR and UV-Visible spectral analysis. The molecular model suggested spherically symmetrical trigonal bipyramidal Ag and Hg-compounds, slightly distorted trigonal bipyramidal Cd-compound and slightly distorted octahedral U-compound.

Mixed ligand complexes of saccharin and 4, 4-bipyridyl with Co(II), Ni(II), Cu(II) and Zn(II) were synthesized in the aqueous medium [64]. Elemental analysis, IR and UV-Vis spectral analysis were used to characterize the compounds. From powder photographs d-values were reported. Molecular modeling of the compounds suggested slightly distorted octahedral geometry.

A copper complex of the logand β-N-oxalyl-α,β-diamino propionic acid, (ODAP), was synthesized in aqueous medium [65]. The empirical formula $[Cu(C_5H_6N_2O_5).2H_2O]$ has been suggested by elemental data. The bonding nature has been assigned by UV-visible and IR spectral analysis. The d-values from powder diffraction photograph were reported. A distorted octahedral geometry was suggested by molecular model. A diffusion controlled redox process of the metal ion was confirmed by cyclic Voltammertic analysis.

Ehsan *et al.* has showed that pyridoxine or Vitamin B_6 after neutralization with calculated amount of base ($NaHCO_3$) react with Mn(II), Co(II), Ni(II), Cu(II) and Zn(II) ions in aqueous medium to produce complexes [66]. The Cu-complex is different from the others in its chemical composition, solubility, precipitation process, and also in its IR and UV-Visible spectrum.

Metal aspartates of general formula $M(C_4H_5NO_4).xH_2O$ where M = Ni, Cu, Zn, Cd reacts with 2, 2′-bipyridyl in the aqueous medium to produce mixed ligand complexes of stoichiometry $M(C_4H_5NO_4)(C_{10}H_8N_2).xH_2O$ [67]. The compositions of the complexes were confirmed by comparing the elemental analysis data. From the IR spectral analysis it was found that the bonding pattern of the metal aspartates remains same even in the presence of secondary ligand 2, 2 bipyridyl. Thermal and conductivity properties were also studied.

Tris(2-aminoethyl)amine, tren, has been reacted with Cr(III) and Fe(III) in ethanol [68]. The complexes were characterized by elemental analysis data, IR and UV-Visible spectral analysis data.

Isothiocyanato complexes of first row transition metals with quadridentate tripodal ligand, tris(2-aminoethyl)amine, tren, were prepared and characterized by elemental and spectroscopic analysis [69]. The empirical formulae of the complexes were

[M(tren)(NCS)](SCN), where M = Mn(II), Cu(II), Ni(II) and Zn(II). In Co-compound, chloride ion remains as counter ion. The SCN^- ion bonded to metal through the N atom. X-ray powder pattern of the complexes were also studied.

Ehsan *et al.* reported that DL-aspartic acid reacts with Mn(II), Co(II), Ni(II), and Pd(II) to give stable complexes [70]. It forms 1:1 complexes with Co(II) and Ni(II) where both the carboxylic acid group remain deprotonated and 2:1 complexes with Mn(II) and Pd(II) where at least one carboxylic acid group is protonated.

Ehsan prepared mixed ligand complexes, $M(ASP)(L).H_2O$, M= Hg(II) and Pb(II), ASP = DL-aspartic acid, L = 2,2′-bipyridyl and 1,10-phenanthroline [71]. The complexes were characterized by elemental and spectral analysis.

Mixed ligand complexes of Ni(II), Cu(II), Zn(II) and Cd(II) aspartates with 1,10-phenanthroline have been prepared and characterized [72]. The composition of the complexes was confirmed by comparing the analytical data. The complexes were thermally stable. The spectral analysis of the complexes also reported.

Thiamin hydrochloride reacts with mercuric chloride in aqueous solution to produce a crystalline compound having the stoichiometry $Hg_3Cl_8(C_{12}H_{18}N_4OS)$ [73]. The compound crystallizes in the triclinic space group. The crystal structure consists of two structurally different types of mercuric chloride species, $[Hg_2Cl_6]^{2-}$ (dimer) and $[Hg_4Cl_{10}]^{2-}$ (tetramer) and thiaminium cations $[C_{12}H_{18}N_4OS]^{2+}$ (ratio 1:1:2). The thiamin moiety was directly bonded to a Hg atom of the tetramer through the hydroxyl oxygen atom of the thiazolium side chain and additionally to a Hg atom of the dimer through the unprotonated N atom of the pyridinium ring.

EPR and ENDOOR spectrum of the trigonal bipyramidal copper compexes with sulfur and nitrogen donor tripodal ligands were studied in the frozen condition [74]. The results showed that unlike the tbp copper complexes with nitrogen only donor tripodal ligands, the unpaired electron orbital is not d_{z2}, but largely deviated to d_{z2-y2} or d_{z2-x2}, which is rather similar to those of the tetragonal copper complexes.

DL- aspartic acid has been reacted with Cr(III) and Fe(III) in the aqueous medium [75]. The stoichiometry of the compounds were $Cr(C_4H_5NO_4)(OH)$ and $Fe(C_4H_6NO_4)(OH)(NO_3).2H_2O$. The IR spectral studies suggested that in Cr-aspartate both the carboxylic acid groups are in the deprotonated state and participate in bond formation with metal ion and in Fe-aspartate at least one acid group remains in the protonated state. The Fe-aspartate was further reacted with neutral ligands 1,10-phenanthroline and 2,2'-bipyridine to give $Fe(C_4H_6NO_4)(C_{12}H_8N_2)(OH)(NO_3)$ and $Fe(C_4H_5NO_4)(C_{10}H_8N_2)(NO_3)$.

DL- aspartic acid reacts with Zr(IV), Ru(III), Pt(IV) and U(VI) in the aqueous medium and produces complex compounds of stoichiometry $ZrO(C_4H_6NO_4)Cl.2H_2O$, $Ru(C_4H_5NO_4)Cl.2H_2O$, $Pt(C_4H_6NO_4)_2Cl_2.3H_2O$ and $UO_2(C_4H_5NO_4).2H_2O$ [76]. The composition of the complexes were confirmed by elemental analysis and characterized by spectral and thermal analysis.

Ehsan *et al.* synthesized metal complexes of L-glutamic acid of general formula $M(C_5H_7NO_4).2H_2O$, M = Co(II), Ni(II), Cu(II) and Zn(II) in aqueous medium [77]. The compounds were chartacterized by elemental, spectral, thermal, analysis. Both the carboxylic acid group are in the deprotonated state and participate in the bond formation with the metal ion. The d-values of the complexes have also been reported.

Ehsan [78] reported the signals of protons and nitrogens in the ENDOOR spectra of the trigonal bipyramidal copper complexes $[Cu(tren)(NH_3)](ClO_4)_2$ and [Cu(tren)(NCS)](SCN) have successfully separated by taking the ESR spectra of the same sample at two different microwave frequencies and taking ENDOOR spectra at the same positions of ESR spectra. The NH_2 protons in the complexes were identified by the process of deuteration, and tentative assignments of other protons have also been suggested.

Ehsan *et al.* prepared the complexes of L-proline with Cd(II) and Hg(II) in aqueous medium [79]. Elemental analysis suggest the stoichiometry of the compounds as $(C_5H_9NO_2)CdCl_2.H_2O$ and $(C_5H_9NO_2)Hg_2Cl_4$. Spectroscopic and structural analysis suggest that in both compound the ligand remains intact and retains its zwitterion form. The Cd compound crystallizes in the orthorhombic system with space group $P2_12_12_1$ and the Hg compound crystallizes in triclinic system with space group P1.

DL-aspartic acid reacts with Zn(II), Mo(VI), Hg(II) and Pb(II) in aqueous medium to give complexes with stoichiometry $Zn(C_4H_5NO_4).3H_2O$, $(MoO_3)(NH_4)(C_4H_6NO_4)$, $Hg(C_4H_5NO_4).H_2O$, $Pb(C_4H_5NO_4).0.5H_2O$ and $Pb(C_4H_6NO_4)NO_3.2H_2O$ [80]. These complexes have been characterized by elemental analysis and their IR, NMR, UV, thermal and electrolytic properties studied.

Haider *et al.* prepared the complexes of DL-aspartic acid with Cu(II), Cd(II) and Hg(II) in aqueous medium to give complexes of stoichiometry $Cu(C_4H_5NO_4).4½H_2O$, $Cd(C_4H_5NO_4).H_2O$ and $HgCl_2(C_4H_7NO_4).H_2O$ [81]. Spectral and other evidences suggest that both the carboxylate groups in the ligand are deprotonated in the Cu(II) and Cd(II) complexes whereas in the Hg(II) compound the aspartic ligand remains intact in its zweitterionic form.

Several compounds of 8-hydroxy quinoline e.g. $Zr(C_9H_6NO)_4.H_2O$, $RuCl_2(C_9H_6NO).C_9H_7NO$, $HgNO_3(C_9H_6NO)$, $Tl(C_9H_6NO)$ and $UO_2(CH_3COO)_2(C_9H_7NO)_2$ have been prepared and characterized [82]. It was suggested that in some cases 8-hydroxy quinoline is bonded with metals as anionic ligand while in other cases it remains neutral and may either be bonded with metals or remains in the lattice without any direct interaction with metals.

Niacinamide forms metal complexes of general formula $[M(C_6H_6N_2O)_2]Cl_2$; where M = Mn(II), Co(II), Ni(II), Cu(II) and Zn(II) in the aqueous medium [83]. The complexes were formulated by comparing the experimental and calculated data for C, H, N and metal. The UV-Visible, FTIR spectral analysis and thermo gravimetric analysis (TGA) of these complexes have been studied. Magnetic susceptibility values indicate that all complexes except Zn complex are paramagnetic in nature. The redox properties of the metal ions in the Mn, Cu and Zn complexes have been studied by the cyclic voltammetric techniques. In all cases the systems were quasi-reversible.

Cd(II), Hg(II) and Pb(II) were reacted with nicotinamide and nicotinic acid (Vitamin B_3) in the aqueous medium to form 2:1 complex [84]. The solid products obtained were formulated by comparing the experimental and calculated data for C, H, N and metal. The complexes were characterized by UV-Visible and FTIR spectral analysis. The absence of any crystalline or coordinated water in the complexes was confirmed by thermogravimetric analysis. The complexes were weak electrolyte as indicated by the conductance behavior.

Metal complexes of niacin (3-pyridine carboxylic acid) were prepared in the aqueous medium and characterized by different physico-chemical methods [85]. On the basis of the elemental analysis the empirical formula of the complexes have been proposed as $[Fe(C_6H_4NO_2)]Cl_2$, $[Co(C_6H_4NO_2)]Cl$, $[Zn(C_6H_4NO_2)]Cl$, $[Cd(C_6H_4NO_2)]Cl$, and $[Hg(C_6H_4NO_2)]Cl$. IR spectral data indicate that the metal-ligand bonding occurs through nitrogen atom of aromatic ring and oxygen atom of COO^- group. UV-Visible spectrum showed that Fe(III) and Co(II) complexes show d-d electronic transition in addition to $\pi\rightarrow\pi^*$, $n\rightarrow\pi^*$ and $n\rightarrow\sigma^*$ transitions. QSTG analysis data strongly supported the absence of water molecules in the complexes and the weight of the residue corresponds to the respective metal oxides. The redox properties of Zn(II), Cd(II) and Hg(II) in their complexes are studied by cyclic voltammetric techniques. The charge transfer process was not reversible.

Mamun and his coworkers showed that, cystene forms metal complexes of general formula $[M(C_6H_{10}N_2O_4S_2)]$; where M = Mn(II), Co(II), Ni(II), Cu(II), Zn(II), Cd(II), Hg(II) and Pb(II) in the aqueous medium [86]. Before reacting with metal salts the ligand solution was neutralized by $NaHCO_3$ solution. The complexes were formulated by comparing the C, H, N, S and metal analysis data. The prepared complexes were characterized by UV-Visible, FTIR spectral analysis, magnetic susceptibility, cyclic voltammertic analysis.

Some 1:2 metal complexes of DL-methionine were prepared in aqueous medium [87]. The empirical formula of the complexes were proposed as $[(C_5H_{10}NO_2S)_2M]$; where M = Mn(II), Co(II), Ni(II), Cu(II), Zn(II), Cd(II) and Hg(II). The complexes were characterized by magnetic susceptibility data, IR, UV-Visible spectral analysis. The redox behavior of the metal ion the complexes was studied by cyclic voltammetric analysis.

Two compounds were prepared by reacting tris(2-aminoethyl)amine, (tren) with Cu(II) and Zn(II) in the ethanol medium [88]. The empirical formula was proposed as $[Cu(C_6H_{18}N_4)(NO_3)]NO_3$ and $[Zn(C_6H_{18}N_4)(ClO_4)]ClO_4$. IR, UV-Visible spectral analysis was used to characterize the complexes. The d-values were calculated from X-ray powder photographs. Molecular model calculation indicated distorted trigonal bipyramidal structures for the complexes. The cyclic voltammertic analysis gives the redox process of the respective metal ion in the complexes to be diffusion controlled.

Triethylenetetramine was reacted with Cr(III), and Fe(III) in ethanol medium [89]. The solid crystalline complexes were formulated by comparing C, H, N, M analysis data. The complexes were characterized by UV-Visible and IR spectral analysis. The molecular model calculation suggested the *trans* geometry for the complexes.

Triethylenetetramine was reacted with Co(II), Ni(II) and Cu(II) in ethanol medium [90]. In each case the solid crystalline products were precipitated out after adding SCN^- counter ion. The complexes were formulated by comparing C, H, N, M analysis data. The complexes were characterized by UV-Visible and IR spectral analysis. The molecular model calculation suggested the *trans* geometry for the complexes.

1.6 Research plan

The multifunctional activity of many metal complexes has been found to be essential for living organisms. Attempt have been made in the present work to systematically study the leucine and isoleucine complexes of transition metals in order to get greater insight about the amino acid-metal interactions which could help to understand the role of metal ions in the biological processes. Purpose of the present work also included the preparation of metal complexes of leucine and isoleucine in solid phase and to characterize these using different conventional methods and study their various properties in order to establish the nature of metal-amino acid interactions. The present studies are associated with the following areas of interest:

(i) Studies of the metal-ligand interaction electrochemically in solution.

(ii) Synthesis of metal-leucine and metal-isoleucine complexes of some transition metal such as Mn(II), Fe(II), Fe(III), Co(II), Ni(II), Cu(II), Zn(II), Cd(II), Hg(II) and Pb(II).

(iii) Elemental analysis of the complexes to determine their empirical formula.

(iv) Studies of various physical properties such as melting point, solubility etc. of these complexes.

(v) Investigation of spectral properties like IR, UV, NMR to help characterization of the complexes and also to find out various structural features of bonding.

(vi) Thermal analysis of the complexes to determine the mode of decomposition, to understand the bonding nature between the different species of the molecules, composition of the end product and the nature of the water molecule present in the compounds.

(vii) Theoretical studies of the complexes.

(viii) Based on the results obtained from the different studies undertaken in the work, to propose possible structures of the complexes.

(ix) Antimicrobial activity of the complexes.

STUDY OF METAL-LIGAND INTERACTION IN SOLUTION

2.1 Introduction

Electrochemistry is the branch of physical chemistry that studies the relationship between electricity, as a measurable and quantitative phenomenon, and identifiable chemical change, with either electricity considered an outcome of a particular chemical change or vice versa. These reactions involve electric charges moving between electrodes and an electrolyte (or ionic species in a solution). Voltammetry is the branch of electrochemistry which refers to the measurement of current that result from the application of potential. In voltammetry, information about an analyte is obtained by measuring the current as the potential is varied. The analytical data for a voltammertic experiment comes in the form of a voltammogram which plots the current produced by the analyte versus the potential of the working electrode.

Cyclic voltammetry (CV) has become an important and widely used electro analytical technique in many areas of chemistry. It is often used to study a variety of redox processes, to determine the stability of reaction products, the presence of intermediates in redox reactions, electron transfer kinetics and the reversibility of a reaction. CV can also be used to determine the electron stoichiometry of a system, the diffusion coefficient of an analyte, and the formal reduction potential of an analyte, which can be used as an identification tool. In addition, because concentration is proportional to current in a reversible, Nernstian system, the concentration of an unknown solution can be determined by generating a calibration curve of current vs. concentration. In cellular biology it is used to measure the concentrations in living organisms. In organometallic chemistry, it is used to evaluate redox mechanisms.

Chronoamperometry (CA) and chronocoulometry (CC) are the classical electrochemical techniques frequently used in electro analytical chemistry. Applications of this technique include measurement of electrode surface area, diffusion coefficients, concentration, and kinetics of both heterogeneous electron transfer reactions and chemical reactions coupled to electron transfer, adsorption, and the effective time window of an electrochemical cell.

2.2 Experimental

Materials, methods and equipments

The results of any analytical chemistry depend on the purity of chemical used, the calibration of the instruments and the accuracy of the methods applied. Impure chemicals, non calibrated instruments, wrong method does not give the accurate and precise result. So, pure and branded chemicals should be used in analytical process. The instruments should be calibrated before use. The sources of different chemicals, the instruments and brief description of the methods used to study the metal-ligand interaction are described below.

2.2.1 Chemicals: All chemicals, solvents and ligand used in the work were analytical grade obtained from E. Merck of Germany, British Drug House (BDH) of England and Sigma-Aldrich Chemical Co. of USA. Nitrogen gas manufactured by BOL, Bangladesh. Water used in all of the experimental processes was de-ionized.

2.2.2 Methods and equipments: Different electro analytical techniques are used in this work. The theories, experimental setup of the techniques are described on the basis of some standard books and articles [91-99].

2.2.2.1 Cyclic voltammetry: Cyclic voltammetry (CV) is a type of potentiodynamic electrochemical measurement. In a cyclic voltammetry experiment, the working electrode potential is ramped linearly versus time. Unlike in linear sweep voltammetry, after the set potential is reached in a CV experiment, the working electrode's potential is ramped in the opposite direction to return to the initial potential. These cycles of ramps in potential may be repeated as many times as needed. The current at the working electrode is plotted versus the applied voltage (that is, the working electrode's potential) to give the cyclic voltammogram trace. The potential waveform and the resulting voltammogram of such a process are shown in Fig. 2.1. A key feature in understanding CV method is the relationship between the potential applied to an electrode and the resulting current is measured against the applied potential. If the polarizable electrode is at equilibrium with the solution in which it is immerged, it will exhibit a potential invariant with time and related thermodynamically to the composition of the solution.

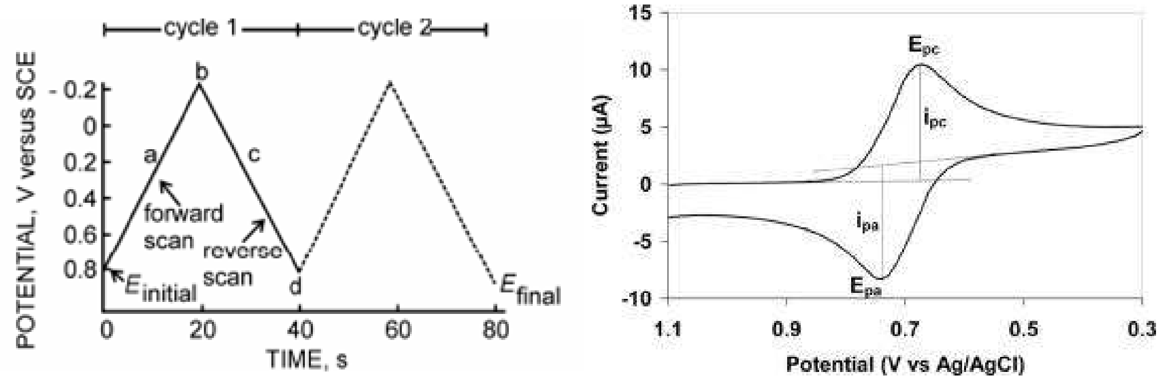

Fig. 2.1: Cyclic voltammetry waveform and voltammogram

An electrochemical system containing species “O” which is capable of being reduced to “R” at the electrode can be represented by the following reversible electrochemical reaction.

$$O \quad + \quad ne \longrightarrow R$$

Nernst equation for the reversible reaction is given by

$$E = E^o - \frac{0.059}{n} \log \frac{C^O s}{C^R s}$$

where, E = Potential applied to the electrode, E_0 = Standard reduction potential of the couple vs reference electrode, n= no. of electrons involved in the redox reaction, C^0_s = Surface concentration of species “O”, C^R_s = Surface concentration of species “R”.

The parameters collected from a cyclic voltammogram is cathodic peak potential ($E_{pc)}$, anodic peak potential (E_{pa}), cathodic peak current (i_{pc}), anodic peak current (i_{pa}).

A redox couple in which both species rapidly exchange electrons with the working electrode is known to be an electrochemically reversible couple. The formal reduction potential E_0 for a reversible reaction is centered between E_{pc} and E_{pa}.

$$E_o = \frac{E_{pc} + E_{pa}}{2}$$

The number (n) of electrons transferred during a reversible reaction is determined from the separation between peak potential. $\Delta E_p = E_{pc} - E_{pa} = 0.059/n$ V

Thus a one electron process exhibits a ΔE_p of 59 mV for a reversible couple. Slow electron transfer reaction or irreversibility of electron transfer reaction increases E_p in excess of 59 mV. In this case the reaction is kinetically controlled. The peak current both (i_{pc} and i_{pa}) for a. reversible reaction can be express by the Randles- Sevcik equation.

$$i_p = 2.69*10^5 n^{2/3} A D^{1/2} C v^{1/2}$$

where, i_p = peak current in ampere, N = electron stoichiomerty, A = area of the electrode in cm^2, D = diffusion co-efficient in $cm^2 s^{-1}$, C = concentration of the species in mol cm^{-3}.

According to the RandlesSevcik equation the peak current is proportional to the square root of scan rate and is directly proportional to the concentration of the electro active species. Since the Randles Sevcik equation is valid for both cathodic and anodic peaks, the ratio of currents is unity for a reversible system.

The heterogeneous charge transfer rate constant, k_f for reversible system can be calculated by using the following equation.

$$i_{pc} = n F A C^O_{ox}$$

where, i_{pc} = cathodic peak current (in ampere) n = number of electron involved in the reaction (electron stoichiomerty), F = Faraday constant (96500 coulombs), A = area of the electrode surface, C^0_{ox} = concentration of the species “O” ($molL^{-1}$) and k_f = charge transfer rate constant (cms^{-1}).

For irreversible systems, the charge transfer rate constant k_f can be calculated by using the following equation.

$$E_{pc} = E_{1/2} - b (0.52 - 1/2 \log b/D - \log k_f + 1/2 \log v$$

where E_{pc} = cathodic peak potential (V), $E_{1/2}$ = half wave potential (V), D = Diffusion coefficient (cm^2s^{-1}), b = Tafel slope = 2.303 $RT/\alpha N_aF$; α = transfer coefficient, N_a = number of electrons involved in the rate determining step, R = molar gas constant = 8.314 $JK^{-1}mol^{-1}$, T = Temperature (K), v = scan rate (Vs^{-1}) and k_f = charge transfer rate constant (cms^{-1}).

$$(E_p)_2 – (E_p)_1 = (2.303RT/ \alpha N_aF) \log \sqrt{(v_1/v_2)}$$

where, $(E_p)_2$ and $(E_p)_1$ are peak potentials at scan rate v_2 and v_1 respectively.

The diffusion coefficient of a system can be calculated by using the expression,

$$i_{pc} = 2.99*10^5\ n\ (\alpha N_a)^{1/2}\ A\ D^{1/2}\ C\ v^{1/2}$$

where i_{pc} = cathodic peak current (ampere), n = total number of electrons involved in the reaction, α = transfer coefficient, N_a = number of electrons involved in the rate determining step, A = area of the electrode surface (cm^2), D = Diffusion coefficient (cm^2s^{-1}), C = concentration of the electro active species (mol L^{-1}) and v = scan rate (Vs^{-1}).

2.2.2.2 Chronoamperometry and chronocoulometry: The electrochemical excitation in both the chronocoulometric and chronoamperometric techniques is a potential step applied suddenly to an electrode. The response of the electrode reaction is a current decay with time. In chronoamperometry the current-time curve is the measured response. In chronocoulometry one measures the integral of the current-time response i.e. the charge-time curve. Because of the basic similarity of the two processes, they are considered together.

In chronoamperometry, a potential step is applied to the working electrode and the resulting current-time response (current response or chronoamperogram) is measured. As mass transport under this condition is solely by diffusion, the i-t curve reflects the change in the concentration gradient in the vicinity of the surface. This involves a gradual expansion of the diffusion layer associated with the depletion of the reactant, and hence decreased slop of the concentration profile as time progresses. The double potential step chronoamperometry experiment is illustrated in Fig. 2.2.

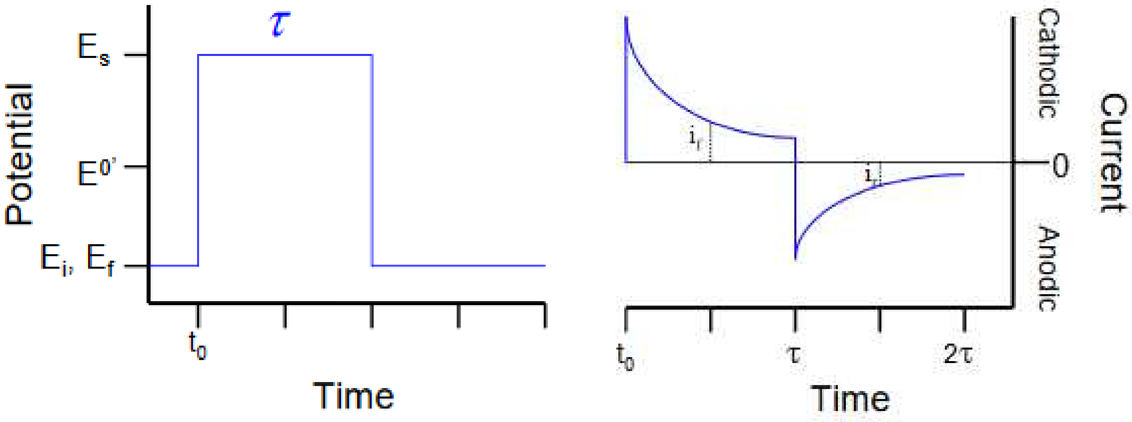

Fig. 2.2: Chronoamperometry potential waveform and the current response

The current decays with time as given by Cottrell equation: $i = nFACD^{½} \pi^{-½} t^{-½}$

where, n = number of electron transferred, F = Faraday's constant, A = electrode area, D = diffusion coefficient, C = concentration of the electro active species.

The chronoamperogram shows a current spike followed by a gradual decay in current. The spike is due to the initial electrolysis of species at the electrode surface and decay is due to the diffusion of species to the electrode surface.

The forward step, i.e the transition from initial potential (E1) to first step potential (E2) at t = 0, is that the electrode must instantly reduce the metal from higher oxidation state to lower one.

$$Mn^{+} + e \rightarrow M^{(n-1)+}$$

For a period τ, it causes a buildup of the reduced product in the region near the electrode. However, in the second phase of the experiment after τ, the potential returns to E1, where only the oxidized form is stable at the electrode. The ionic radical produced by reduction cannot coexist there; hence large anodic current declines in magnitude.

In a chronocoulometry experiment, the total charge (Q) that passes during the time following a potential step is measured as a function of time. Q is obtained by integrating the current, i, during the potential step. For a well behaved system (diffusion only), the charge observed following a potential step to a point significantly more negative (for a reduction) of the E^0, is described by the integrated Cottrell equation, known as the Anson equation.

$$Q_d = 2nFAC_0D_0^{½} \pi^{-½} t^{½}$$

The double potential step chronocoulometry experiment is illustrated in Fig. 2.3 for a diffusion-only redox system. Potential step programs in chronocoulometry are identical to those used in chronoamperometry. The most obvious advantage of recording charge rather than current is that Q increases with time following a potential step, reaching a maximum at the end of the step, where the most meaningful experimental data generally is observed.

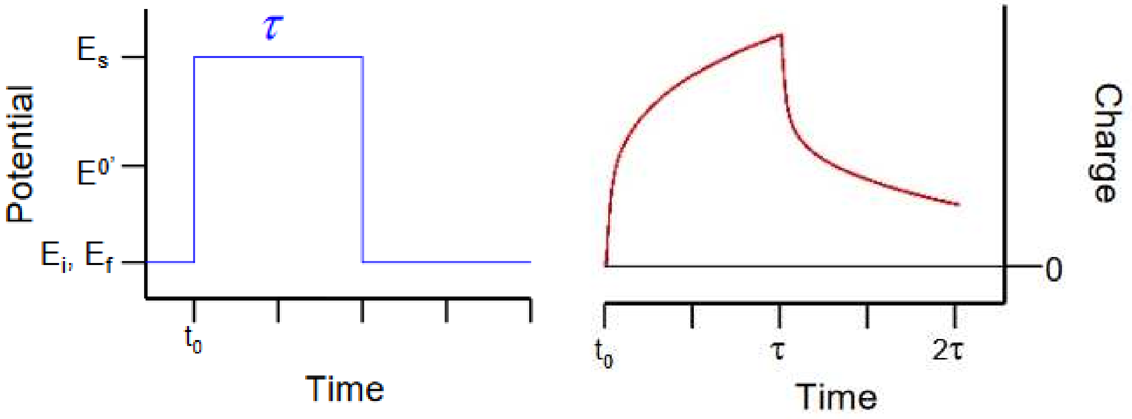

Fig. 2.3: Chronocoulometry potential waveform and the charge response

Signal-to-noise improvements also result as the integration of the current signal tends to "smooth" the random noise contained in the signal. Hence, chronocoulometry is preferred over chronoamperometry for the measurement of electrode area (A) and diffusion coefficients (D).

The enhanced signal observed in chronocoulometry also makes it the better technique for measurement of the kinetics of chemical reactions following electron transfer. In the double potential step experiment illustrated in the previous figure, the reduced form of the redox couple still in the vicinity of the electrode following the forward step can be re-oxidized to the original material during the reverse potential step. As was the case in chronoamperometry, the signal observed in the reverse step is less than that seen in the forward step. The charge for a chemically and electrochemically reversible species on the reverse step is given by

$$Q_r = 2nFAC_0D_0^{½}\,\pi^{-½}[\tau½ + (t-\tau)^{½} - t½]$$

The values for charge measured at a time equal to τ/2 after each step (designated Q_r and Q_f in the Fig. 2.4) for such a system would yield a charge ratio $[Q_r\ (2\tau)\ /\ Q_f\ (\tau)]$ equal to 0.414. Chemical reactions coupled to the electron transfer will cause this ratio to deviate from the theoretical value.

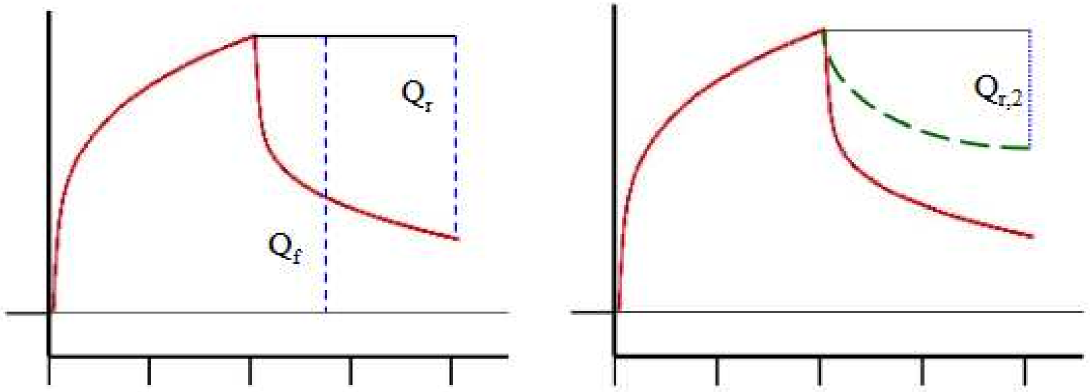

Fig. 2.4: Chronocoulometric charge

For example, if the reduced form of the species produced by the forward potential step decays to an electro-inactive species (Red → P), the charge observed on the reverse potential step ($Q_{r,2}$) will be smaller than that for the uncomplicated case. Values for k, the homogeneous rate constant for the follow-up reaction, can be obtained using working curves derived for varying values of τ.

As was the case in chronoamperometry, a change in the applied potential of the working electrode will always be accompanied by a rearrangement of the ions in the double layer, leading to a contribution to the signal from capacitive current. Since the current is integrated over time in chronocoulometry, the charge due to the capacitive current will still be part of the total at the end of the step. The fact that it takes a very short amount of time after the potential step to charge the double layer does, however, allow the user to easily distinguish between the double layer charge, Q_c, and the charge due to diffusion, Q_d. If the total charge for the forward step, Q_f, equal to ($Q_d + Q_c$), is plotted as a function of $t^{1/2}$ a straight line is obtained for a kinetically uncomplicated system with an intercept equal to Q_c and a slop of 2/100DCAFn2, and a slope of $2nFAC_0D_0^{1/2}\pi^{-1/2}$. This is due to the double layer charging being essentially “instantaneous” following the potential step while the charge arising from diffusion requires time for the electro active component to reach the electrode surface and react.

Perhaps the most important application of the chronocoulometric technique is the determination of surface concentrations of adsorbed electro active species, designated Γ_0. Following a forward potential step of sufficient magnitude, electro active material that is adsorbed to the surface is instantaneously electrolyzed. The charge resulting from this reaction, Q_{ads}, being faradic in nature is given by

$$Q_{ads} = n\ F\ A\ \Gamma_0$$

with Γ_0 having units of mol/cm^2 and other variables their usual meaning. The total charge observed (forward step) is now given by

$$Q_r = Q_d + Q_{ads} + Q_c = 2nFAC_0D_0^{½}\ \pi^{-½}\ t^{½}\ + n\ F\ A\ \Gamma_0 + Qc$$

When adsorbed materials are present, the intercept of the Anson plot becomes the sum of Q_{ads} and Q_c While it is possible to ascertain a value for Q_c and thus Q_{ads} by running a “blank” electrolyte-only experiment, these measurements cannot accurately account for changes brought about by adsorption. A more suitable method for the determination of $Q_{ads.}$

Anson plots (Fig. 2.5) are prepared for both the forward and reverse potential steps, with Q_f vs t½ being plotted for the forward step and Q_r vs $[\tau^{½} + (t-\tau)^{½} - t^{½}]$ for the reverse. For the case where the original material is adsorbed but the electrode product is not, the difference in the intercepts of the two plots directly yields Q_{ads}. Fig. 2.5 shows Anson plots for the forward potential step for a non-adsorbed analyte (left) and for a double-potential step experiment involving a pre-adsorbed material (right).

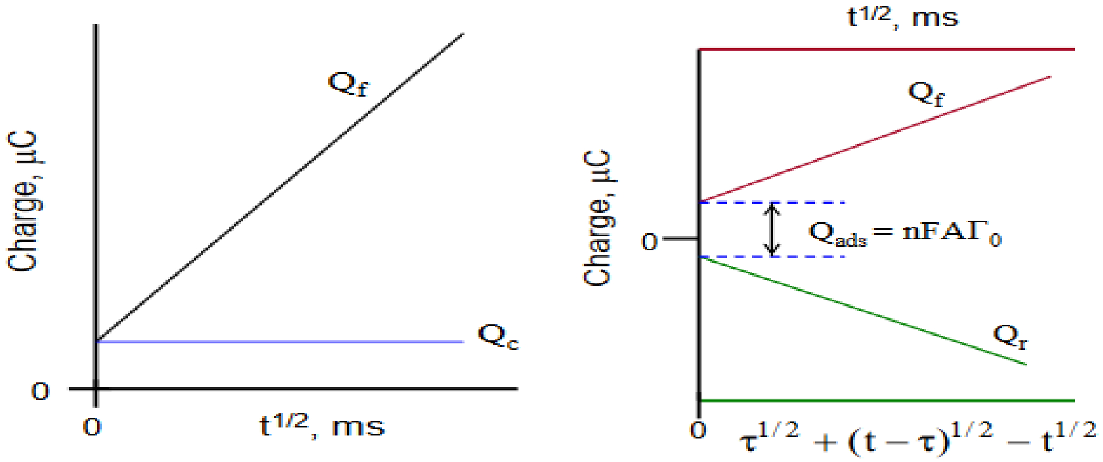

Fig. 2.5: Linear chronocoulometric charge

2.2.2.3: Instrumentation of electrochemical analysis: The electrochemical analysis was studied with a PC controlled electrochemical analyzer made by CH instruments at Department of Chemistry, University of Dhaka, Bangladesh.

The main instrument for voltammetry is the potentiostat, which applies the desired potential to the electrochemical cell (i.e. between a working electrode and a reference electrode), and a current to voltage converter, which measures the resulting current. The current is typically displayed on a recorder as a function of the applied potential. The current required to sustain the electrolysis at the working electrode is provided by the auxiliary electrode (counter electrode).

Fig. 2.6: Computer controlled potentiostat used in electrochemical analysis

The electrodes used in the present study were,

(i) Working electrode is a glassy carbon solid disk electrode.
(ii) Ag/AgCl (standard KCl) electrode as reference electrode.
(iii) Counter electrode is a Pt wire.

Large supporting electrolyte concentrations are necessary to increase solution conductivity. As electron transfers occur at the electrodes, the supporting electrolyte will migrate to balance the charge and complete the electrical circuit. Without the electrolyte available to achieve charge balance, the solution will be resistive to charge transfer. Large supporting electrolyte concentrations are also necessary to limit analyte migration. Movement of the analyte to the electrode surface is controlled by three modes of mass transport namely convection, migration, and diffusion. All theoretical treatments and modeling exclude migration and convection of the analyte. To ensure that these mechanisms of mass transport are minimized, convection is reduced by the absence of stirring or vibrations, and migration is minimized through the use of electrolyte in high concentration. Potassium chloride has become the electrolyte of choice for inorganic electrochemistry experiments performed in inorganic solvents as they fulfill the conditions of electrolyte choice. So, all the solutions in the present studies were prepared in freshly prepared potassium chloride solutions (0.1 M).

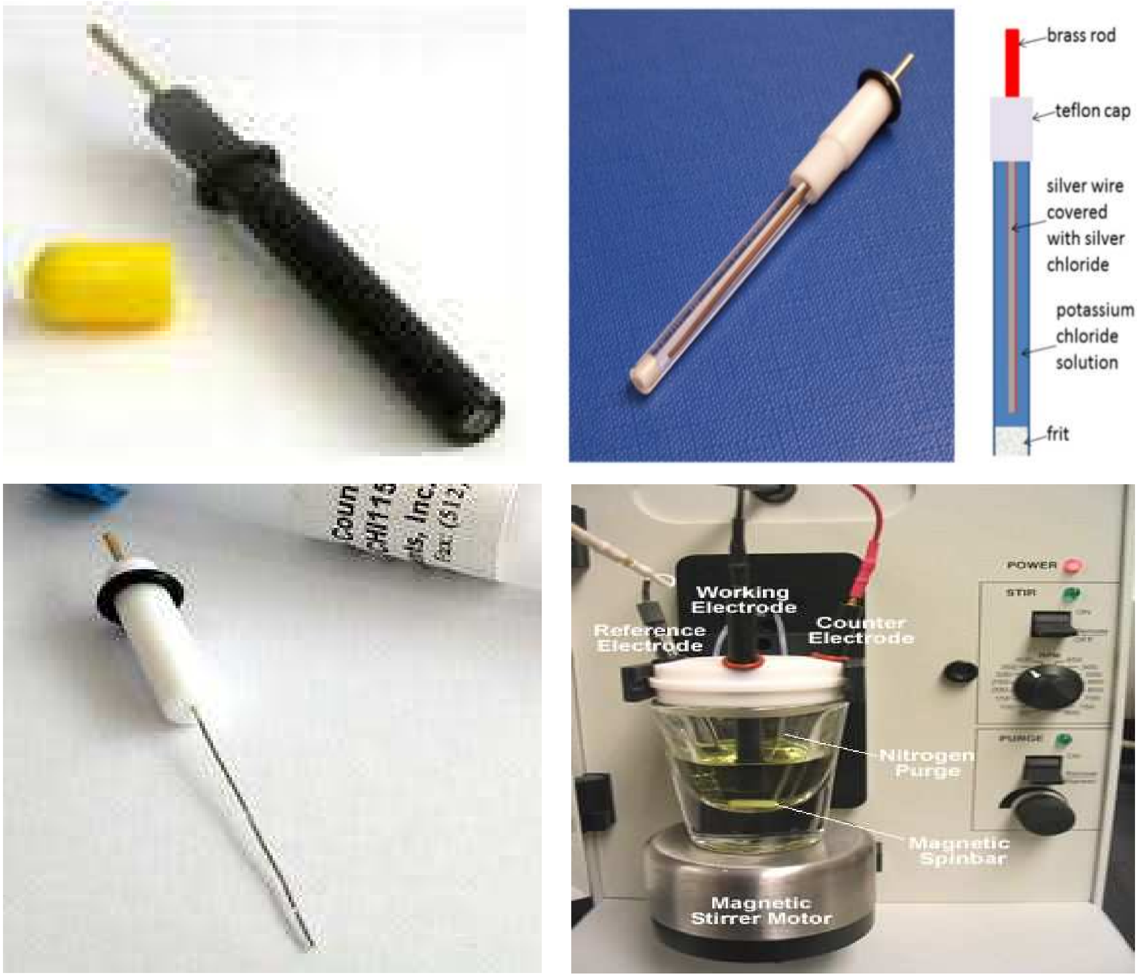

Fig. 2.7: Electrodes and the cell stand used in electrochemical analysis

Since electrodes are capable of adsorbing species during an experiment, the surface of the working electrode was polished with fine alumina powder (0.3 micron or lower) on a wet polishing cloth after every experiment. To do so a part of the cloth was made wet with deionized water and alumina powder was sprinkled on it. The electrode was then polished on this surface by soft pressing the electrode against the polishing surface and then washed with deionized water. At this point, the electrode surface would look like a shiny black mirror. The cell was assembled and filled with 10 mL of the solution to be examined so that the electrodes ware sufficiently immersed. In electrochemical experiments, the presence of oxygen can also alter the electrochemical response of analyte. Oxygen undergoes a reversible one-electron reduction to form the oxygen radical anion (superoxide, O_2•−). To avoid interference from dissolved O_2, all electrolyte solutions were spurge with an inert gas before measurements are taken. This was done by purging an inert gas N_2 through the solution.

2.3 Results and discussions

In the present study, at first the redox behavior of Cu(II), Zn(II) and Cd(II) ion was studied in KCl supporting electrolyte using glassy carbon electrode. Then the redox behavior of the respective metal ion was studied in presence of the ligand. To do so, equal volume of the metal ion and the ligand solution were mixed together and voltammogram of the resultant solution was taken. The background scan was performed to test if all the components of the cells are in good condition before adding the analyte as well as to quantify the capacitive current. The redox behavior of the metal ion in absence and in presence of ligand was discussed and compared.

Chronoamperometry and chronocoulometry has achieved their importance in characterizing the rate of electrolysis and adsorption criteria of a system. The chronoamperometric and chronocoulometric study of the metal ion in absence and in presence of ligand was performed and discussed.

2.3.1 Cyclic voltammertic study of Cu(II) and Cu(II)-ligand interaction in aqueous medium at room temperature

2.3.1.1 Redox behavior of Cu(II)

The redox behavior of $CuCl_2$ in 0.1 M KCl was studied using cyclic voltammertic technique at glassy carbon electrode within the potential window from 0.5 V to -0.5 V. The pH of the solution was found 4.57. A CV of the system is shown in Fig. 2.8. The voltammogram shows two cathodic peaks (c1 and c2) at potential + 0.0126 V and -0.3124 V due to reduction of Cu(II) to Cu(I) and Cu(I) to Cu(0) respectively. Two anodic peaks is observed at potential +0.046 V and +0.246 V due to oxidation of Cu(0) to Cu(I) and Cu(I) to Cu(II) respectively. The electrode reaction may be presented by the following equations:

Cathodic reaction: $Cu(II) + e \rightarrow Cu(I)$

$Cu(I) + e \rightarrow Cu(0)$

Anodic reaction: $Cu(0) - e \rightarrow Cd(I)$

$Cu(I) - e \rightarrow Cd(II)$

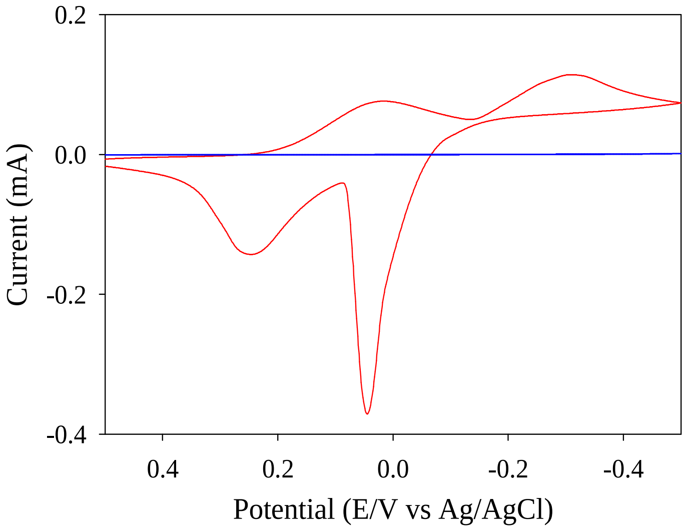

Fig. 2.8: CV of 0.01 M $CuCl_2$ (red) and 0.1 M KCl (blue) at 0.03 Vs^{-1}

The redox behavior of Cu(II) was also studied at different scan rates. Scan rate is defined as the fraction of the potential window analyzed per unit time. The size of the diffusion layer above the electrode surface becomes different depending upon the voltage scan rate used. In a slow voltage scan rate the diffusion layer grows much further from the electrode in comparison to a fast scan. Therefore the scan rate variation is important. The variation of the CV's of $CuCl_2$ at different scan rate is shown in Fig. 2.9. The current-potential data obtained from the voltammogram is tabulated in Table 2.1 and Table 2.2.

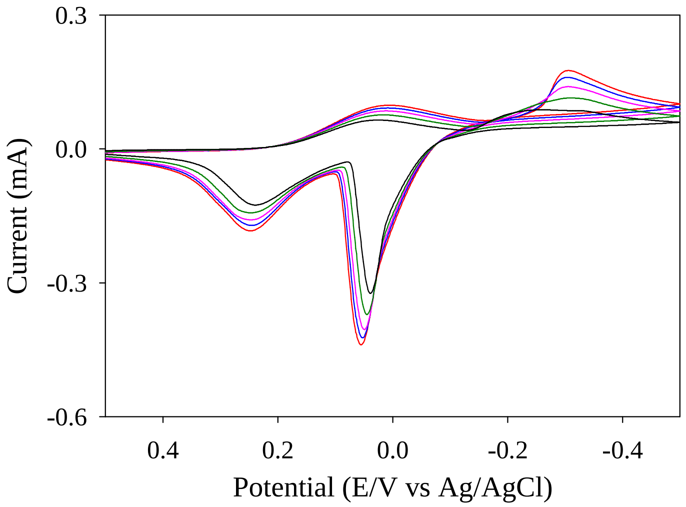

Fig. 2.9: CV's of 0.01 M $CuCl_2$ at different scan rate

Table 2.1: **Current-potential data for 1st peak pair of the voltammogram of Cu(II) at different scan rate**

v Vs^{-1}	$v^{1/2}$ Vs^{-1}	$+ E_{pc}$ Volt	$+ E_{pa}$ Volt	$+ i_{pc}$ mA	$- i_{pa}$ mA	ΔE_p Volt	i_{pa}/i_{pc}
0.02	0.1414	0.0250	0.2376	0.0642	0.1250	0.2126	1.95
0.03	0.1732	0.0126	0.2458	0.0714	0.1464	0.2332	1.59
0.04	0.2000	0.0084	0.2458	0.0832	0.1626	0.2374	1.46
0.05	0.2236	0.0084	0.2458	0.0916	0.1750	0.2374	1.36
0.06	0.2449	0.0042	0.2458	0.0952	0.1809	0.2416	1.33

v = scan rate, $v^{1/2}$ = SQRT of scan rate, E_{pc} = cathodic peak potential, E_{pa} = anodic peak potential, i_{pc} = cathodic peak current, i_{pa} = anodic peak current, ΔE_p = peak potential separation, i_{pa}/i_{pc} = peak current ratio

Table 2.2: **Current-potential data for 2nd peak pair of the voltammogram of Cu(II) at different scan rate**

v Vs^{-1}	$v^{1/2}$ Vs^{-1}	$- E_{pc}$ Volt	$+ E_{pa}$ Volt	$+ i_{pc}$ mA	$- i_{pa}$ mA	ΔE_p Volt	i_{pa}/i_{pc}
0.02	0.1414	0.2624	0.0376	0.0856	0.3249	0.2248	3.79
0.03	0.1732	0.3124	0.0460	0.1143	0.3714	0.2664	3.25
0.04	0.2000	0.3082	0.0500	0.1374	0.4042	0.2582	2.94
0.05	0.2236	0.3082	0.0500	0.1584	0.4208	0.2582	2.66
0.06	0.2449	0.3082	0.0542	0.1761	0.4380	0.2540	2.49

v = scan rate, $v^{1/2}$ = SQRT of scan rate, E_{pc} = cathodic peak potential, E_{pa} = anodic peak potential, i_{pc} = cathodic peak current, i_{pa} = anodic peak current, ΔE_p = peak potential separation, i_{pa}/i_{pc} = peak current ratio

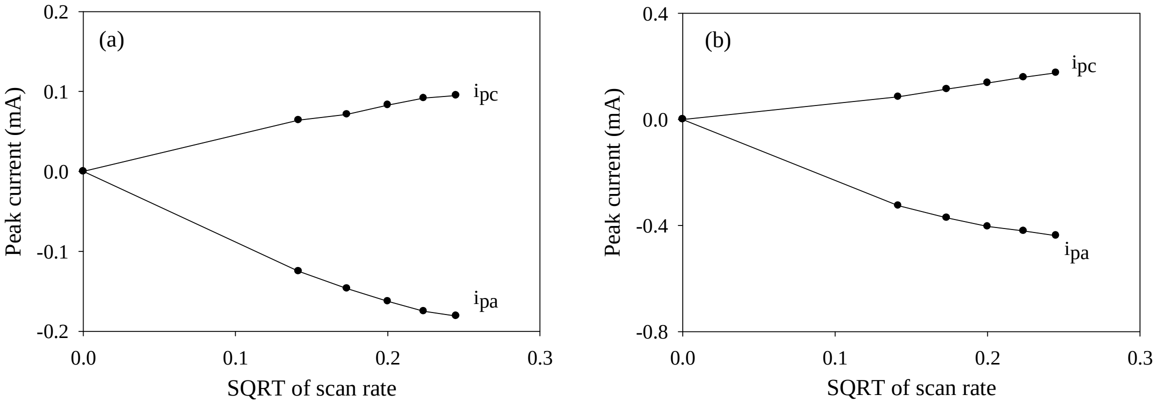

Fig. 2.10: Variation of peak current with SQRT of scan rate for (a) 1st and (b) 2nd peak pair

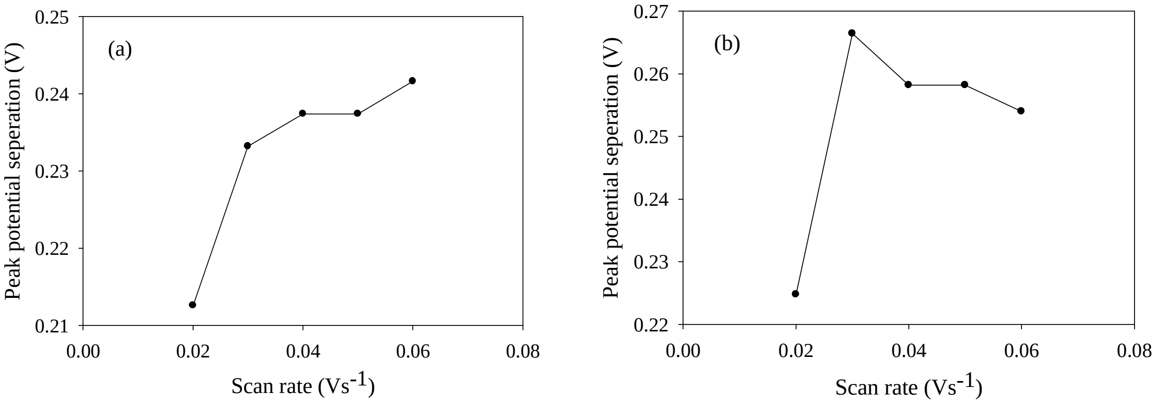

Fig. 2.11: Variation of peak potential separation with scan rate for (a) 1st and (b) 2nd peak pair

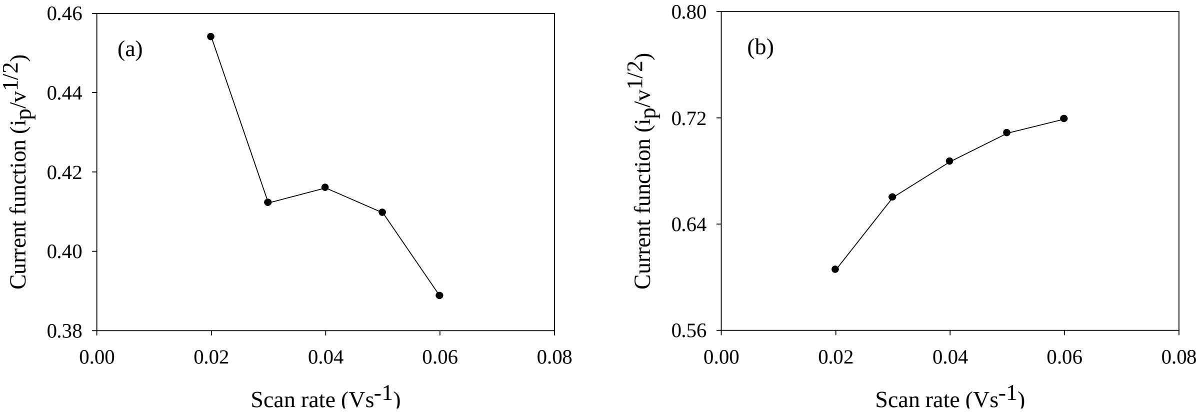

Fig. 2.12: Variation of current function with scan rate for (a) 1st and (b) 2nd peak pair

Some graphical analysis was done on the basis of the current-potential data and is displayed in Fig. 2.10 to Fig. 2.12. The analysis shows with the increase of scan rate peak current for both cathodic and anodic peaks increases. This can be rationalized by considering the size of the diffusion layer and the time taken to record the scan. The voltammogram takes longer to record as the scan rate is decreased. Therefore, the size of the diffusion layer above the electrode surface becomes different depending upon the voltage scan rate. In a slow voltage scan the diffusion layer grows much farther from the electrode in comparison to a fast scan. Consequently, the flux to the electrode surface is considerably smaller at slow scan rate than it is at faster rate. As the current is proportional to the flux towards the electrode, the magnitude of current becomes lower at slow scan rate and higher at higher scan rates.

The peak current changes almost linearly with square root of scan rate. Therefore diffusion of the analyte occurs to the electrode surface. The peak potential separation is much larger. With the increase of scan rate the cathodic peak shifts towards negative potential and the anodic peak shifts towards positive potential. Therefore the peak potential separation increases with scan rate. This is may be due to ohmic drop. The electrolytic solutions have an intrinsic resistance R_{sol} in the electrochemical cell. While some potentiostats can compensate for most of this solution resistance (Rc), there remains a portion of uncompensated resistance (R_u) between the WE and the RE. During electrochemical measurements, the potential that the instrument records may not be the potential experienced by the analyte in solution due to R_u. This phenomenon is called ohmic drop. The current function changes with scan rate. The peak current ratio is greater than unity and changes with scan rate. These facts indicate that the electrode process is quasi-reversible and affected by chemical reactions [91-98].

2.3.1.2 Redox behavior of Cu(II) in presence of leucine

The redox behavior of Cu(II) in presence of zwitterionic leucine (z. leu) in 1:1 mol ratio was studied within the potential window from 0.5 V to -0.5 V. The pH of the mixture was found 3.05 while the pH of z. leu and $CuCl_2$ was 6.45.and 4.57 respectively. Therefore the pH of $CuCl_2$ does changed significantly after mixing with z. leu. The voltammogram of Cu(II) before and after interaction is displayed in Fig. 2.13. The voltammogram shows that the peak potential and peak current changed significantly after mixing z. leu with the metal ion. This may be due to interaction of Cu(II) with z. leu.

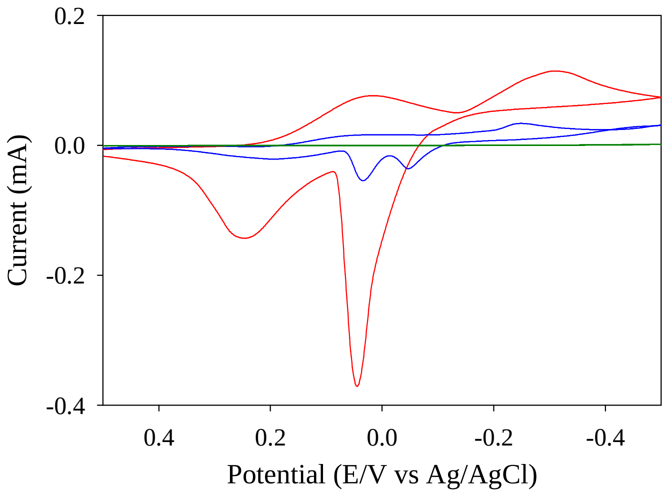

Fig. 2.13: CV's of free Cu(II) (red), Cu(II) in presence of z. leu (blue) and z. leu (green)

The redox behavior of Cu(II) in presence of anionic leucine (a. leu) in 1:1 mol ratio was also studied within the same potential window. The pH of the mixture was found 5.23 while the pH of anionic leucine and $CuCl_2$ was 9.28 and 4.57 respectively. Here, also the pH of the metal ion solution is changed significantly after mixing with anionic ligand. The voltammogram of $CuCl_2$ in absence and in presence of anionic leucine is compared in Fig. 2.14. The voltammogram shows that after mixing ligand to the metal ion solution, both the peak potential and peak current changed. This may be due to interaction of Cu(II) with anionic leucine.

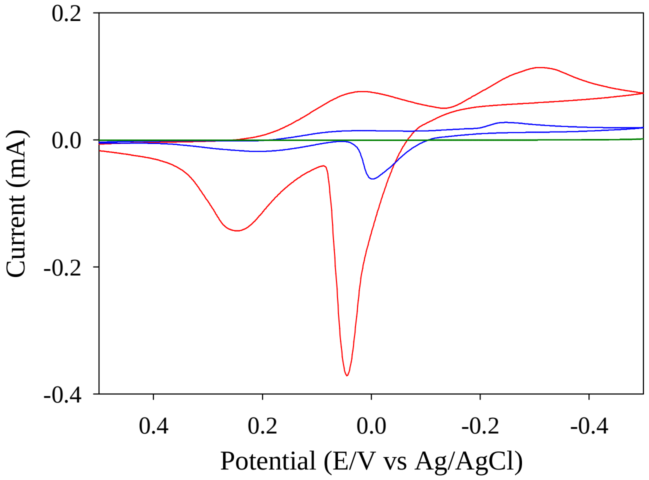

Fig. 2.14: CV's of free Cu(II) (red), Cu(II) in presence of a. leu (blue) and a. leu (green)

The voltammogram of Cu(II)-z. leu and Cu(II)-a. leu system is compared with the CV of free $CuCl_2$ in the Fig. 2.15. From the voltammogram of Cu(II) we see that both the peak potential and peak current has changed after mixing with ligand. So, Cu(II) interacts with both z. leu and a. leu. But since the peak current is minimum, the Cu(II)-anionic leucine interaction may be more pronounce over Cu(II)-zwitterionic leucine interaction.

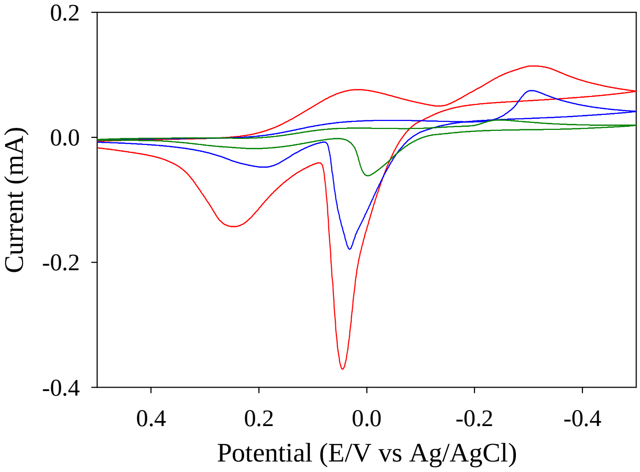

Fig. 2.15: CV's of free Cu(II) (red), Cu(II) in presence of z. leu (blue) and Cu(II) in presence of a. leu (green)

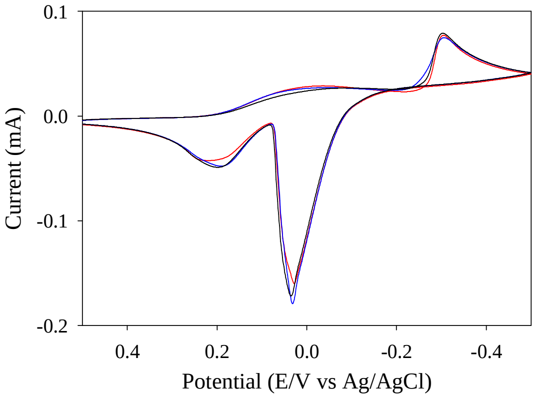

Fig. 2.16: CV's of Cu(II) in presence of z. leu at 1:0.5 (red), 1:1 (blue) and 1:2 (black) mole ratio

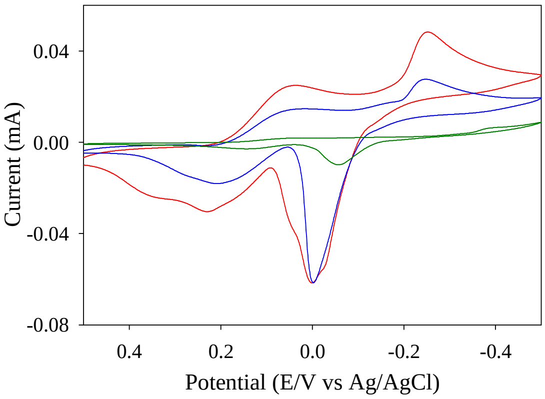

Fig. 2.17: CV's of Cu(II) in presence of a. leu at 1:0.5 (red), 1:1 (blue) and 1:2 (green) mole ratio

The interactions of Cu(II) with both z. leu and a. leu are studied at different mole ratio. The voltammogram are compared in Fig. 2.16 and Fig. 2.17. Since the voltammogram are alike, the variation of mole ratio does not have any effect on the interaction of Cu(II) with z. leu.

But there is a significant difference in the voltammogram of Cu(II)-a. leu system. The peak potential has significantly changed and peak current is minimum during 1:2 interactions. Therefore it can be said that maximum interaction of Cu(II) occurs with anionic leucine in 1:2 mole ratio.

The CV of Cu(II) in presence of anionic leucine was studied at different scan rate. The voltammogram are compared in Fig. 2.18 and the corresponding current-potential data are tabulated in Table 2.3 and Table 2.4. Some graphical analysis was done on the basis of the current-potential data and is displayed in Fig. 2.19 to Fig. 2.21. The analysis shows with the increase of scan rate peak current for both cathodic and anodic peaks increases. In a slow voltage scan the diffusion layer grows much farther from the electrode in comparison to a fast scan. Consequently, the flux to the electrode surface is considerably smaller at slow scan rate than it is at faster rate. As the current is proportional to the flux towards the electrode, the magnitude of current becomes lower at slow scan rate and higher at higher scan rates. Again, the change in peak current with square root of scan rate is almost linear. Therefore the system may be diffusion controlled. The peak potential separation is much larger. With the increase of scan rate the cathodic peak shifts towards negative potential and the anodic peak shifts towards positive potential. Therefore the peak potential separation increases with scan rate. This is may be due to ohmic drop. The current function changes with scan rate. The peak current ratio is greater than unity. These facts indicate that the electrode process is quasi-reversible and associated with some chemical reaction [91-98].

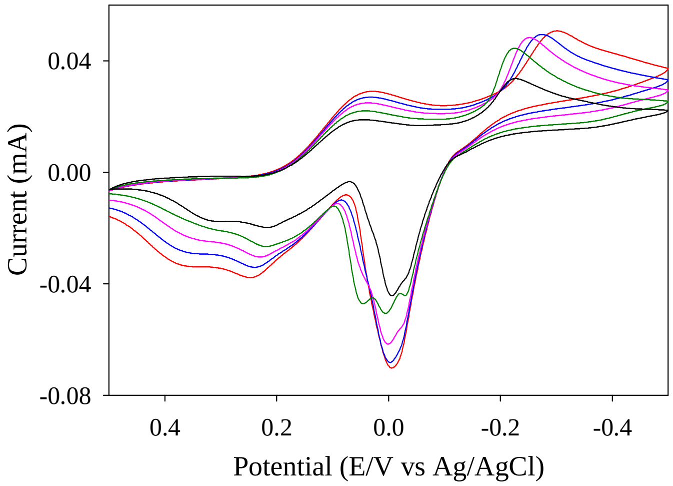

Fig. 2.18: CV's of Cu(II) in presence of anionic leucine at different scan rate

Table 2.3: **Current-potential data for 1st peak pair of the voltammogram of Cu(II) in presence of anionic leucine at different scan rate**

v Vs^{-1}	$v^{1/2}$ Vs^{-1}	$+E_{pc}$ Volt	$+E_{pa}$ Volt	$+i_{pc}$ mA	$-i_{pa}$ mA	ΔE_p Volt	i_{pa}/i_{pc}
0.02	0.1414	0.0416	0.2166	0.0196	0.0160	0.1750	1.225
0.03	0.1732	0.0416	0.2166	0.0234	0.0143	0.1750	1.636
0.04	0.2000	0.0376	0.2292	0.0233	0.0183	0.1916	1.273
0.05	0.2236	0.0334	0.2376	0.0275	0.0242	0.2042	1.136
0.06	0.2449	0.0292	0.2460	0.0300	0.0292	0.2168	1.027

v = scan rate, $v^{1/2}$ = SQRT of scan rate, E_{pc} = cathodic peak potential, E_{pa} = anodic peak potential, i_{pc} = cathodic peak current, i_{pa} = anodic peak current, ΔE_p = peak potential separation, i_{pa}/i_{pc} = peak current ratio

Table 2.4: **Current-potential data for 2nd peak pair of the voltammogram of Cu(II) in presence of anionic leucine at different scan rate**

v Vs^{-1}	$v^{1/2}$ Vs^{-1}	$-E_{pc}$ Volt	$-E_{pa}$ Volt	$+i_{pc}$ mA	$-i_{pa}$ mA	ΔE_p Volt	i_{pa}/i_{pc}
0.02	0.1414	0.225	0.0042	0.0155	0.0482	0.2208	3.11
0.03	0.1732	0.225	0.0042	0.0234	0.0550	0.2208	2.35
0.04	0.2000	0.254	0.0000	0.0266	0.0642	0.2540	2.41
0.05	0.2236	0.275	0.0040	0.0258	0.0733	0.2710	2.84
0.06	0.2449	0.300	0.0082	0.0258	0.0725	0.2918	2.81

v = scan rate, $v^{1/2}$ = SQRT of scan rate, E_{pc} = cathodic peak potential, E_{pa} = anodic peak potential, i_{pc} = cathodic peak current, i_{pa} = anodic peak current, ΔE_p = peak potential separation, i_{pa}/i_{pc} = peak current ratio

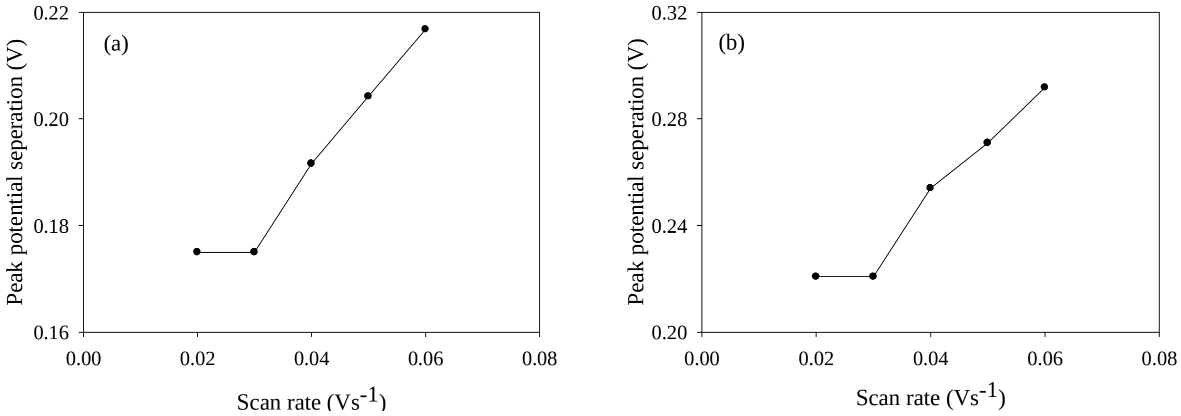

Fig. 2.19: Variation of peak potential separation with scan rate for (a) 1st and (b) 2nd peak pair

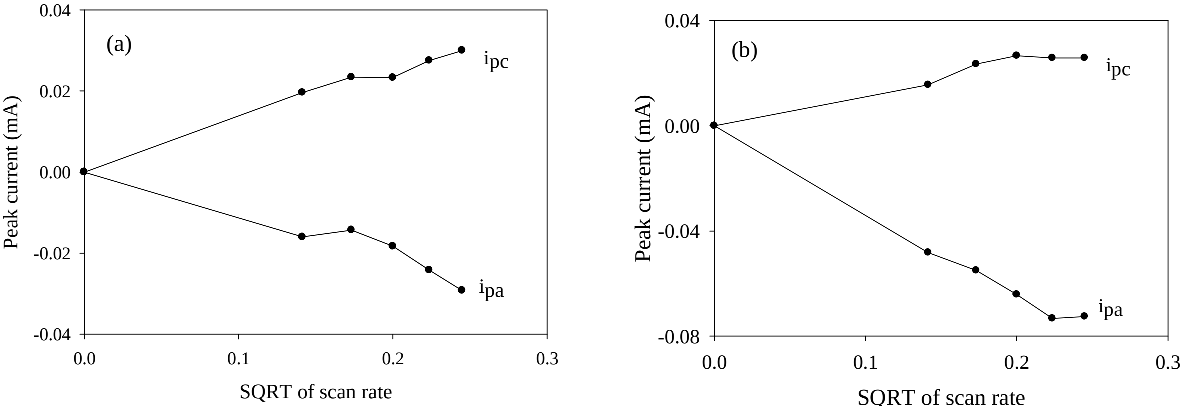

Fig. 2.20: Variation of peak current with SQRT of scan rate for (a) 1st and (b) 2nd peak pair

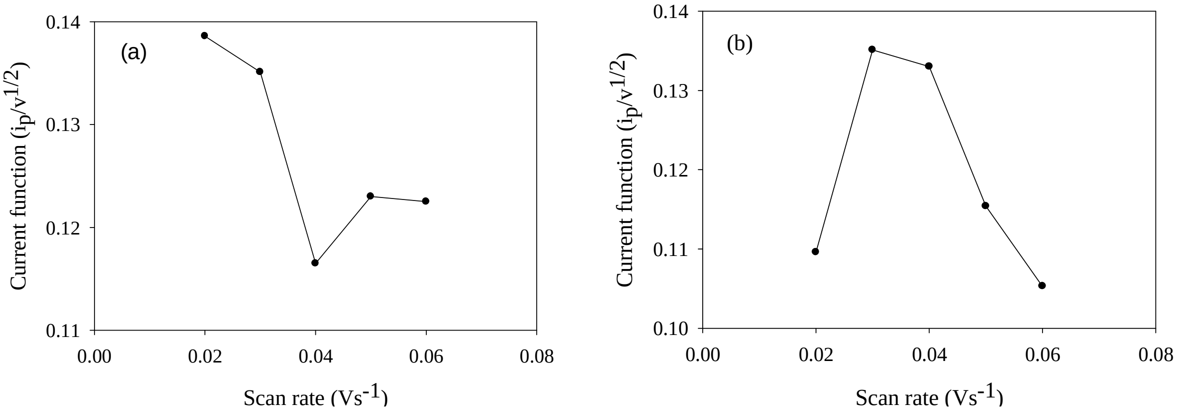

Fig. 2.21: Variation of current function with scan rate for (a) 1st and (b) 2nd peak pair

2.3.1.3 Redox behavior of Cu(II) in presence of isoleucine

The redox behavior of Cu(II) in presence of zwitterionic isoleucine (z. ile) in 1:1 mol ratio was studied within the potential window from 0.5 V to -0.5 V. The pH of the mixture was 3.02 while the pH of z. ile and $CuCl_2$ was 6.20.and 4.57 respectively. Therefore the pH of $CuCl_2$ does changed significantly after mixing with z. ile. The voltammogram of Cu(II) before and after interaction is displayed in Fig. 2.22. The voltammogram shows that although the peak potential not changed significantly but the peak current decreases. This may be due to interaction of Cu(II) with z. ile.

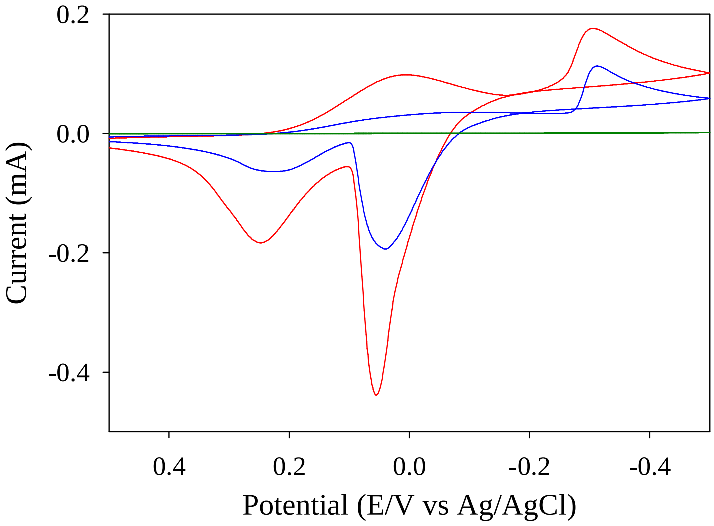

Fig. 2.22: CV’s of free Cu(II) (red), Cu(II) in presence of z. ile (blue) and z. ile (green)

The redox behavior of Cu(II) in presence of anionic isoleucine (a. ile) in 1:1 mol ratio was also studied within the same potential window. The pH of the mixture was found 5.20 while the pH of anionic isoleucine and $CuCl_2$ was 9.14 and 4.57 respectively. Here, the pH of the metal ion solution is changed significantly after mixing with anionic ligand. The voltammogram of $CuCl_2$ in absence and in presence of anionic isoleucine is compared in Fig. 2.23. The voltammogram shows that after mixing ligand to the metal ion solution, both the peak potential and peak current changed. This may be due to interaction of Cu(II) with anionic isoleucine.

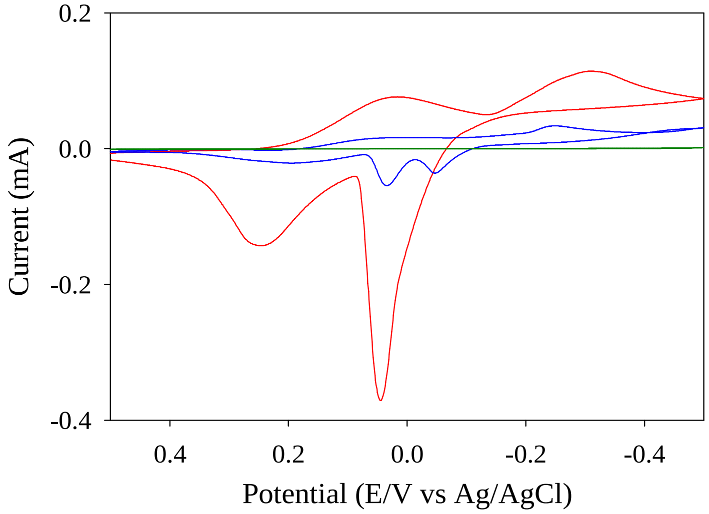

Fig. 2.23: CV's of free Cu(II) (red), Cu(II) in presence of a. ile (blue) and a. ile (green)

The voltammogram of Cu(II)-z. ile and Cu(II)-a. ile system compared with the CV of free $CuCl_2$ in Fig. 2.24. From the voltammogram of Cu(II) we see that both the peak potential and peak current has changed after mixing with ligand. So, Cu(II) interacts with both z. ile and a. ile. But since the peak current is minimum, the Cu(II)-a. ile interaction may be more pronounce over Cu(II)-z. ile interaction.

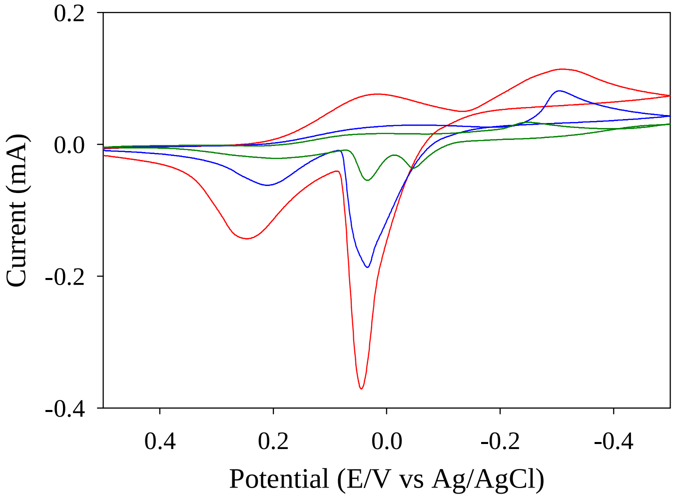

Fig. 2.24: CV's of free Cu(II) (red), Cu(II) in presence of z. ile (blue) and Cu(II) in presence of a. ile (green)

The interactions of Cu(II) with both zwitterionic isoleucine and anionic isoleucine are studied at different mole ratio. The voltammogram are compared in Fig. 2.25 and Fig. 2.26. Since the voltammogram are alike, the variation of mole ratio does not have any effect on the interaction of Cu(II) with z. ile. But there is a significant difference in the voltammogram of Cu(II)-a. ile system. The peak potential has drastically changed and minimum peak current is found during 1:2 interactions. Therefore it can be said that maximum interaction of Cu(II) occurs with anionic isoleucine in 1:2 mole ratio.

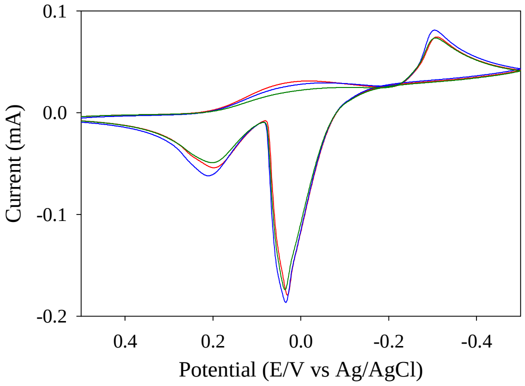

Fig. 2.25: **CV's of Cu(II) in presence of z. ile at 1:0.5 (red), 1:1 (blue) and 1:2 (green) mole ratio**

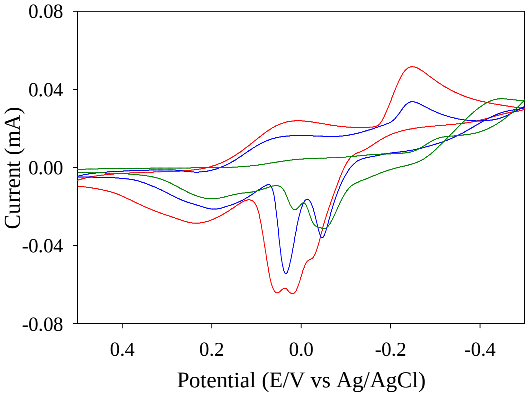

Fig. 2.26: **CV's of Cu(II) in presence of a. ile at 1:0.5 (red), 1:1 (blue) and 1:2 (green) mole ratio**

The redox behavior of Cu(II) in presence of anionic isoleucine was studied at different scan rate. The voltammogram are compared in Fig. 2.27 and the corresponding current-potential data are tabulated in Table 2.5 and Table 2.6. Some graphical analysis was done on the basis of the current-potential data and is displayed in Fig. 2.28 to Fig. 2.30. The analysis shows with the increase of scan rate peak current for both cathodic and anodic peaks increases almost linearly. Therefore the system is diffusion controlled. The peak potential separation is much larger. With the increase of scan rate the cathodic peak shifts towards negative potential and the anodic peak shifts towards positive potential. Therefore the peak potential separation increases with scan rate. The current function changes with scan rate. The peak current ratio is greater than unity. These facts indicate that the electrode process is quasi-reversible and chemical reaction may be occurring at the electrode surface [91-98].

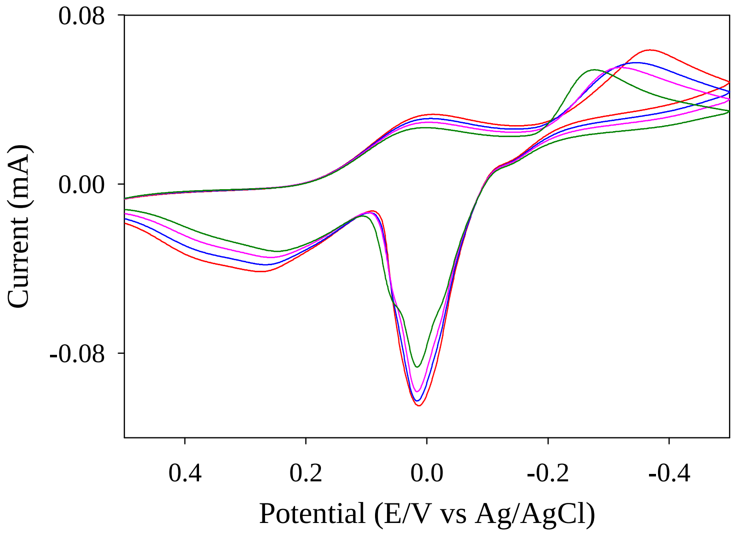

Fig. 2.27: CV's of Cu(II) in presence of anionic isoleucine at different scan rate

Table 2.5: Current-potential data for 1st peak pair of the voltammogram of Cu(II) in presence of anionic isoleucine at different scan rate

v Vs^{-1}	$v^{1/2}$ Vs^{-1}	$-E_{pc}$ Volt	$+E_{pa}$ Volt	$+i_{pc}$ mA	$-i_{pa}$ mA	ΔE_p Volt	i_{pa}/i_{pc}
0.04	0.2000	0.0042	0.2500	0.0264	0.0325	0.2458	1.23
0.05	0.2236	0.0040	0.2626	0.0276	0.0343	0.2586	1.24
0.06	0.2449	0.0040	0.2668	0.0300	0.0378	0.2628	1.26
0.07	0.2646	0.0082	0.2750	0.0312	0.0426	0.2668	1.36

v = scan rate, $v^{1/2}$ = SQRT of scan rate, E_{pc} = cathodic peak potential, E_{pa} = anodic peak potential, i_{pc} = cathodic peak current, i_{pa} = anodic peak current, ΔE_p = peak potential separation, i_{pa}/i_{pc} = peak current ratio

Table 2.6: **Current-potential data for 2nd peak pair of the voltammogram of Cu(II) in presence of anionic isoleucine at different scan rate.**

v Vs^{-1}	$v^{1/2}$ Vs^{-1}	$-E_{pc}$ Volt	$+E_{pa}$ Volt	$+i_{pc}$ mA	$-i_{pa}$ mA	ΔE_p Volt	i_{pa}/i_{pc}
0.04	0.2000	0.2790	0.0168	0.0311	0.0846	0.2622	2.72
0.05	0.2236	0.3208	0.0168	0.0286	0.0953	0.3040	3.33
0.06	0.2449	0.3458	0.0168	0.0310	0.0998	0.3290	3.22
0.07	0.2646	0.3708	0.0126	0.0357	0.1060	0.3582	2.97

v = scan rate, $v^{1/2}$ = SQRT of scan rate, E_{pc} = cathodic peak potential, E_{pa} = anodic peak potential, i_{pc} = cathodic peak current, i_{pa} = anodic peak current, ΔE_p = peak potential separation, i_{pa}/i_{pc} = peak current ratio

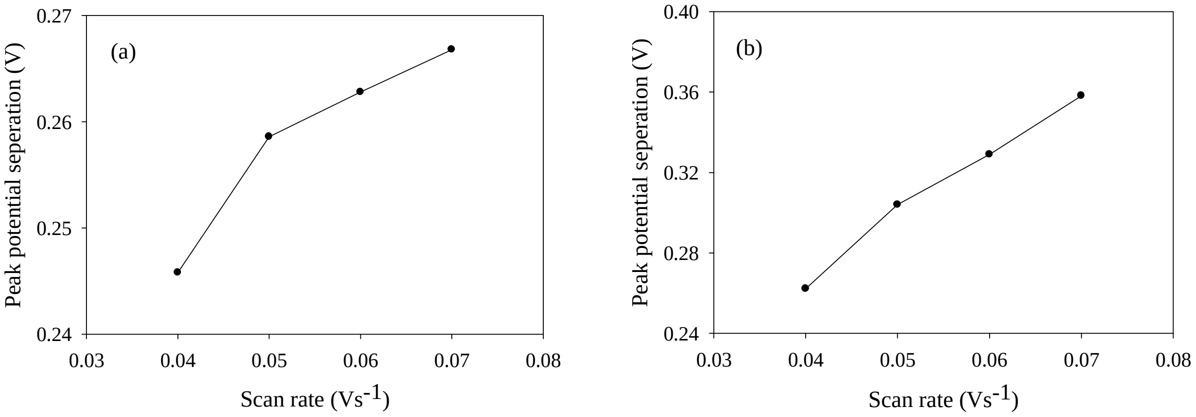

Fig. 2.28: Variation of peak potential separation with scan rate for (a) 1st and (b) 2nd peak pair

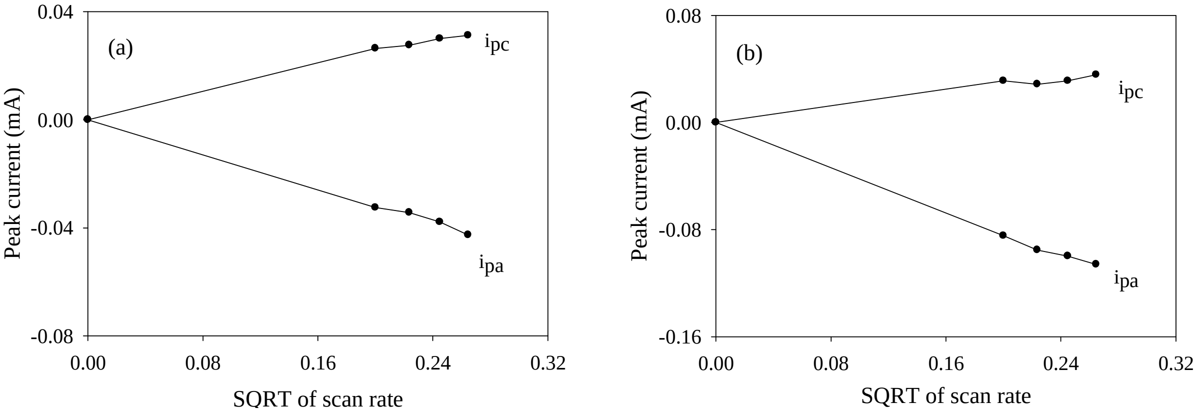

Fig. 2.29: Variation of peak current with SQRT of scan rate for (a) 1st and (b) 2nd peak pair

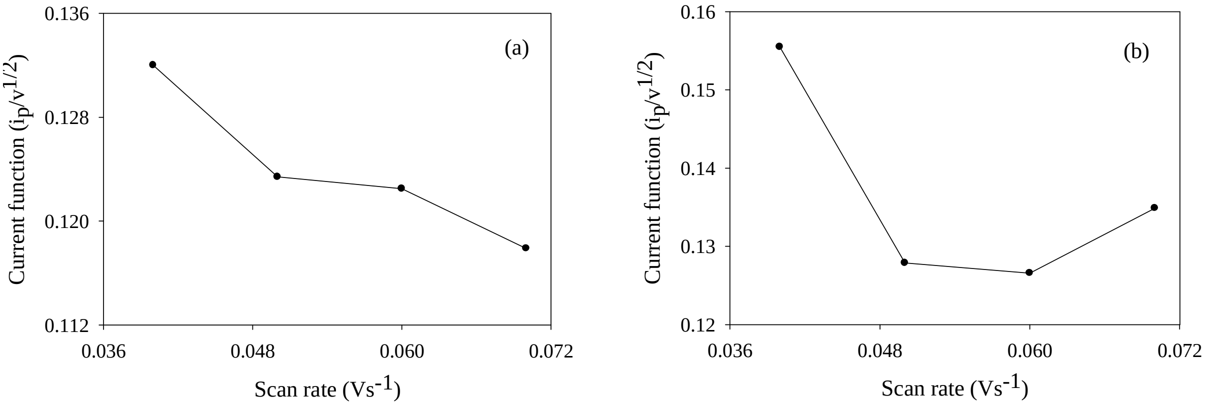

Fig. 2.30: Variation of current function with scan rate for (a) 1st and (b) 2nd peak pair

2.3.1.4 Comparison of interaction of Cu(II) with leucine and isoleucine

The interaction of Cu(II) with leucine and isoleucine is compared in Fig. 2.31 and Fig. 2.32. The voltammogram are almost alike with respect to peak position and peak current. Therefore, the metal ion interacts in a similar way with isoleucine and leucine. This is reasonable, because leucine and isoleucine are isomer to each other. There is no significant difference in their structure. Their structure only differs in the position of the methyl group of the hydrocarbon tail which is not the interaction site. The probable interaction site is the –NH_2 and the –COOH group which are identical in the two ligand. That's why both the ligand gives similar interaction.

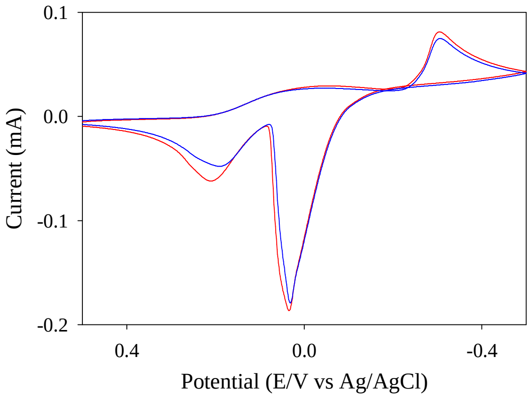

Fig. 2.31: CV's of Cu(II) in presence of z. ile (red) and Cu(II) in presence of z. leu (blue)

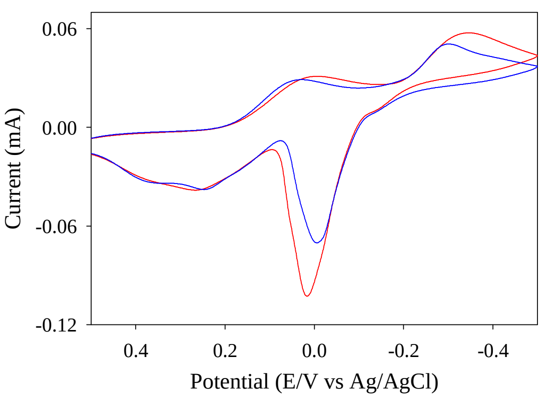

Fig. 2.32: CV's of Cu(II) in presence of a. ile (red) and Cu(II) in presence of a. leu (blue)

2.3.2 Cyclic voltammertic study of Zn(II) and Zn(II)-ligand interaction in aqueous medium at room temperature.

2.3.2.1 Redox behavior of Zn(II)

The redox behavior of $ZnCl_2$ in 0.1 M KCl was studied using cyclic voltammertic technique at glassy carbon electrode within the potential window from -0.6 V to -1.5 V. The pH of $ZnCl_2$ solution was found 5.55. A CV of the system is shown in Fig. 2.33. The voltammogram shows one cathodic peak at -1.185 V due to reduction of Zn(II) to Zn(0) and one anodic peak at -0.889 V due to oxidation of Zn(0) to Zn(II). The electrode reaction may be presented by the following equations:

Cathodic reaction: Zn(II) + 2e → Zn(0)

Anodic reaction: Zn(0) – 2e → Zn(II)

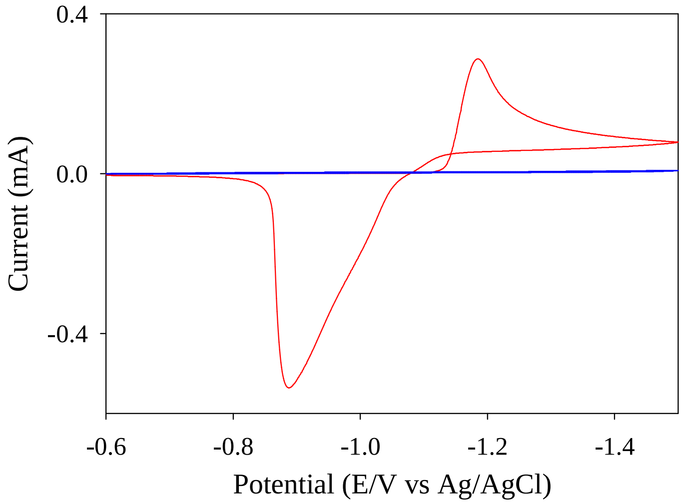

Fig. 2.33: CV of 0.01 M $ZnCl_2$ (red) and 0.1 M KCl (blue) at 0.03 Vs^{-1}

The system was also studied at different scan rates. The variation of the CV's of $ZnCl_2$ at different scan rate is shown in Fig. 2.34. The current-potential data obtained for the system is tabulated in Table 2.7. Some graphical analysis was done on the basis of the current-potential data and is displayed in Fig. 2.35 to Fig. 2.37. Faster scan rates lead to a decrease in the size of the diffusion layer; as a consequence, higher currents are observed. The peak current increases almost linearly with square root of scan rate. Therefore diffusion of the electroactive species occurs to the electrode surface. The peak potential separation is much larger and increases with scan rate. This is may be due to ohmic drop. The current function changes with scan rate. The peak current ratio is greater than unity. These facts indicate that the electrode process is quasi-reversible and coupled with some chemical reaction [91-98].

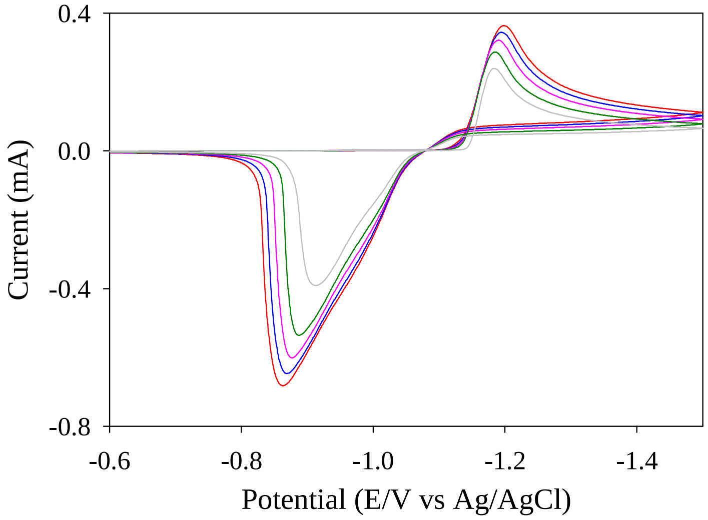

Fig. 2.34: CV's of 0.01 M $ZnCl_2$ at different scan rate

Table 2.7: Current-potential data of the voltammogram of Zn(II) at different scan rate.

v Vs^{-1}	$v^{1/2}$ Vs^{-1}	- E_{pc} Volt	- E_{pa} Volt	+ i_{pc} mA	- i_{pa} mA	ΔE_p Volt	i_{pa}/i_{pc}
0.02	0.1414	1.185	0.911	0.233	0.395	0.274	1.69
0.03	0.1732	1.185	0.889	0.287	0.540	0.296	1.88
0.04	0.2000	1.189	0.874	0.314	0.607	0.315	1.93
0.05	0.2236	1.196	0.870	0.343	0.650	0.326	1.89
0.06	0.2449	1.199	0.862	0.367	0.683	0.337	1.86

v = scan rate, $v^{1/2}$ = SQRT of scan rate, E_{pc} = cathodic peak potential, E_{pa} = anodic peak potential, i_{pc} = cathodic peak current, i_{pa} = anodic peak current, ΔE_p = peak potential separation, i_{pa}/i_{pc} = peak current ratio

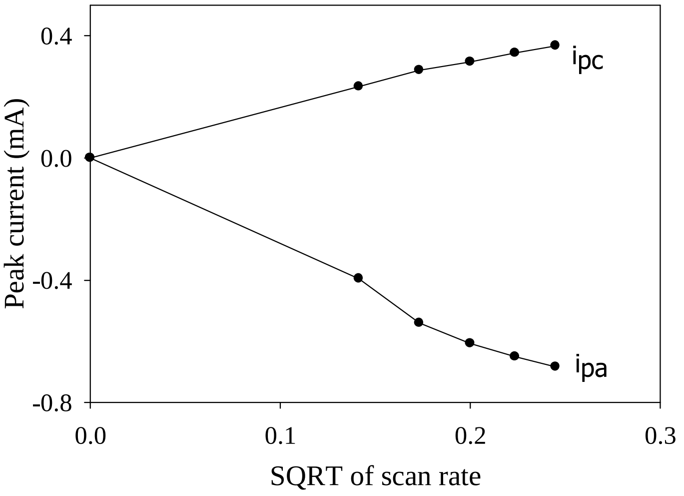

Fig. 2.35: Variation of peak current with SQRT of scan rate

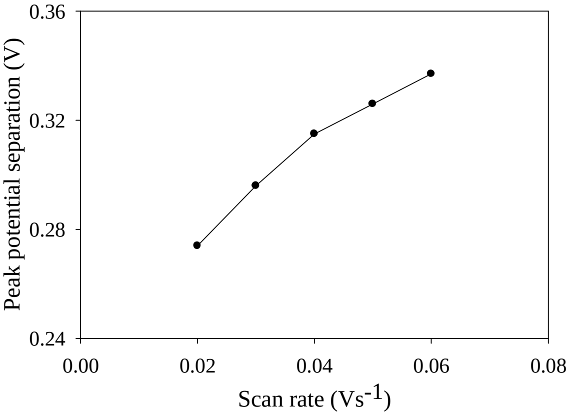

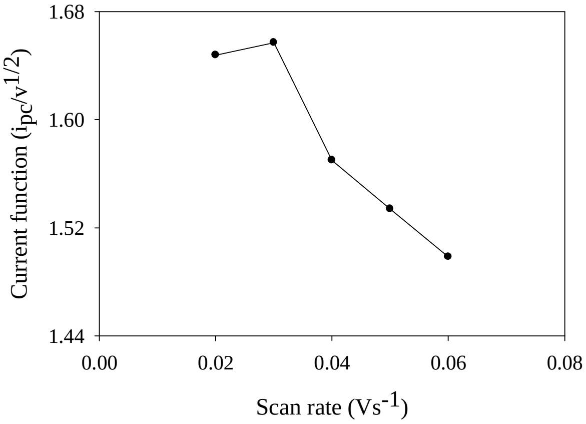

Fig. 2.36: Variation of peak potential separation with scan rate

Fig. 2.37: Variation of current function with scan rate

2.3.2.2 Redox behavior of Zn(II) in presence of leucine

The redox behavior of Zn(II) in presence of zwitterionic leucine (z. leu) in 1:1 mol ratio was studied within the potential window from -0.6 V to -1.5 V. The pH of the mixture was 5.57 while the pH of z. leu and $ZnCl_2$ was 6.45.and 5.55 respectively. Therefore the pH of $ZnCl_2$ does not changed significantly after mixing with z. leu. The voltammogram of Zn(II) in absence and in presence of z. leu is displayed in Fig. 2.38. The voltammogram shows that after mixing ligand to the metal ion solution, the peak potential remains almost unchanged but peak current decreases. This may be due to interaction of Zn(II) with z. leu.

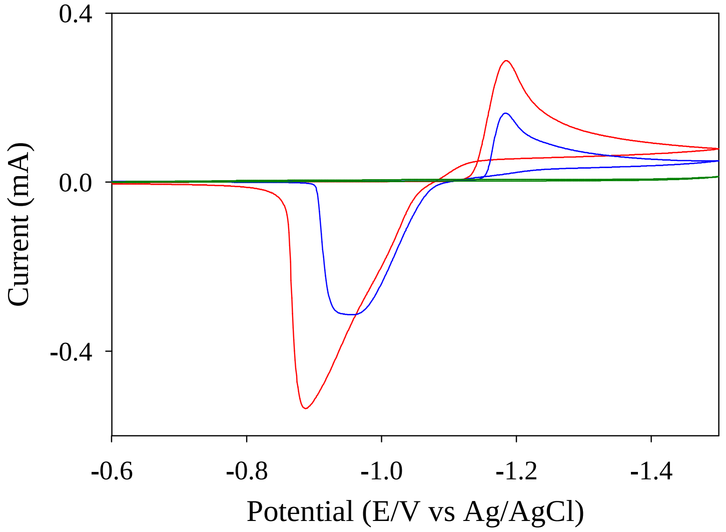

Fig. 2.38: CV's of free Zn(II) (red), Zn(II) in presence of z. leu (blue) and z. leu (green)

The redox behavior of Zn(II) in presence of anionic leucine (a. leu) in 1:1 mol ratio was also studied within the same potential window. The pH of the mixture was found 6.70 while the pH of a. leu and $ZnCl_2$ was 9.28 and 5.55 respectively. Here, the pH of the metal ion solution is changed significantly after mixing with anionic ligand. The voltammogram of $ZnCl_2$ in absence and in presence of a. leu is compared in Fig. 2.39. The voltammogram shows that although the peak potential remains almost unchanged but peak current decreases after mixing ligand to the metal ion solution,. Therefore Zn(II) also interacts with anionic leucine.

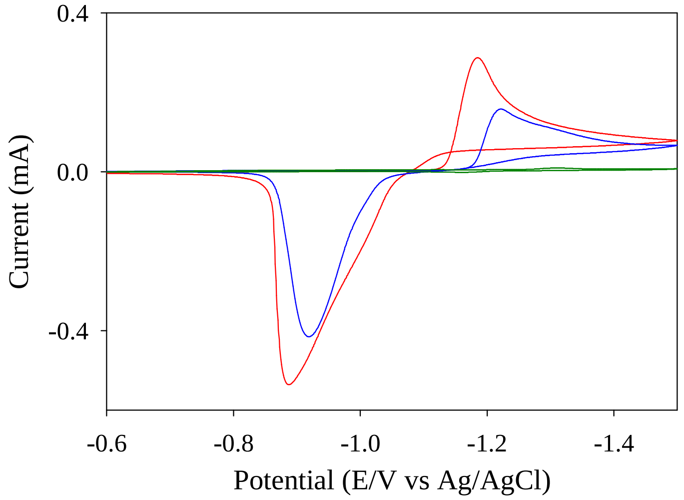

Fig. 2.39: CV's of free Zn(II) (red), Zn(II) in presence of a. leu (blue) and a. leu (green)

The voltammogram of Zn(II)-z. leu and Zn(II)-a. leu system is compared with the CV of free $ZnCl_2$ in Fig. 2.40. From the voltammogram of Zn(II) we see that peak current decreased after mixing with ligand. So, Zn(II) interacts with both z. leu and a. leu. But since the peak shape is slightly different, the Zn(II)-a. leu interaction may be more pronounce over Zn(II)-z. leu interaction.

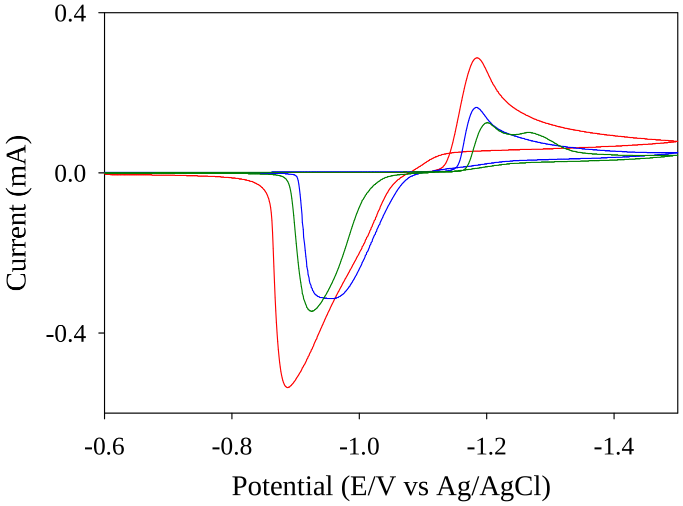

Fig. 2.40: CV’s of free Zn(II) (red), Zn(II) in presence of z. leu (blue) and Zn(II) in presence of a. leu (green)

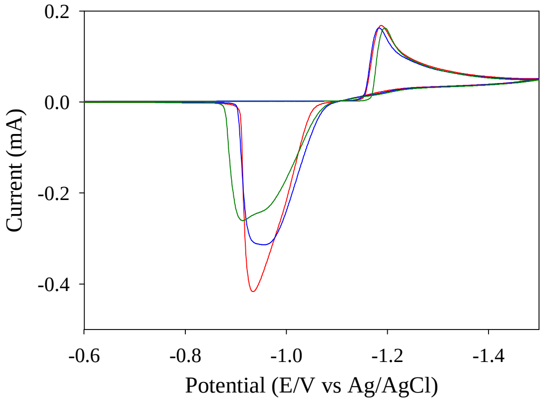

Fig. 2.41: CV’s of Zn(II) in presence of z. leu at 1:0.5 (red), 1:1 (blue) and 1:2 (green) mole ratio

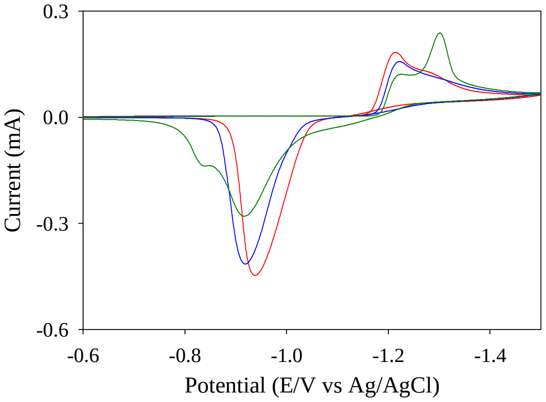

Fig. 2.42: CV’s of Zn(II) in presence of a. leu at 1:0.5 (red), 1:1 (blue) and 1:2 (green) mole ratio

The interactions of Zn(II) with both z. leu and a. leu are studied at different mole ratio. The voltammogram are compared in Fig. 2.41 and Fig. 2.42. Since the voltammogram are alike, the variation of mole ratio does not have any effect on the interaction of Zn(II) with

z. leucine. But there is a significant difference in the voltammogram of Zn(II)-a. leu system. The peak shape has significantly changed during 1:2 interactions. Therefore it can be said that maximum interaction of Zn(II) occurs with a. leu in 1:2 mole ratio.

The interaction of Zn(II) with a. leu was studied at different scan rate. The voltammogram are compared in Fig. 2.43 and the corresponding current-potential data are tabulated in Table 2.8. The current-potential data obtained from the voltammogram are analyzed graphically and are displayed in Fig. 2.44 to Fig. 2.46. From the analysis it is seen that both cathodic and anodic peak currents increases with the increase of scan rate. The peak current depends on the diffusion layer and the time taken to record the scan. In a slow voltage scan the diffusion layer grows much farther from the electrode in comparison to a fast scan. Consequently, the flux to the electrode surface is considerably smaller at slow scan rate than it is at faster rate. As the current is proportional to the flux towards the electrode, the magnitude of current becomes lower at slow scan rate and higher at higher scan rates. Again the increase of peak current is almost linear with square root of scan rate. Therefore the system is diffusion controlled.

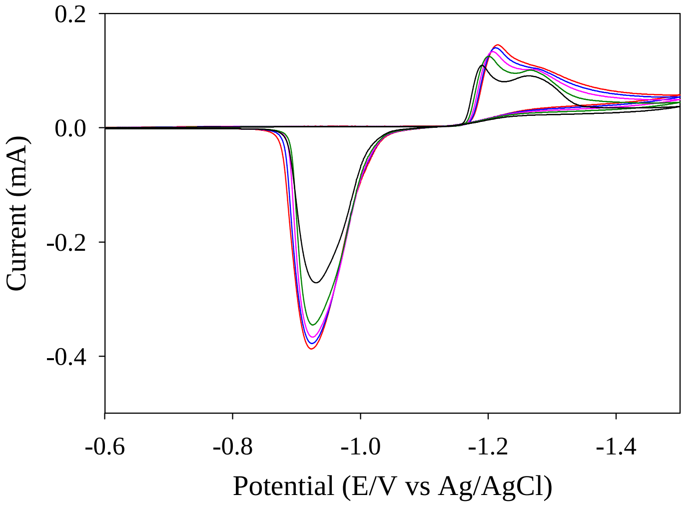

Fig. 2.43: CV's of Zn(II) in presence of anionic leucine at different scan rate

With the increase of scan rate the cathodic peak shifts towards more negative while the anodic peak shifts towards more positive value. Therefore the peak potential separation is much larger and increases with scan rate. This is may be due to ohmic drop. The current function decreases with scan rate. The peak current ratio is greater than unity and changes with scan rate. These facts indicate that the electrode process is quasi-reversible and chemical reactions may be following electron transfer [91-98].

Table 2.8: Current-potential data of the voltammogram of Zn(II) in presence of anionic leucine at different scan rate

v Vs^{-1}	$v^{1/2}$ Vs^{-1}	- E_{pc} Volt	- E_{pa} Volt	+ i_{pc} mA	- i_{pa} mA	ΔE_p Volt	i_{pa}/i_{pc}
0.02	0.1414	1.189	0.930	0.107	0.270	0.259	2.52
0.03	0.1732	1.200	0.922	0.125	0.350	0.278	2.80
0.04	0.2000	1.207	0.926	0.132	0.371	0.281	2.81
0.05	0.2236	1.211	0.922	0.138	0.379	0.289	2.75
0.06	0.2449	1.215	0.922	0.142	0.387	0.293	2.72

v = scan rate, $v^{1/2}$ = SQRT of scan rate, E_{pc} = cathodic peak potential, E_{pa} = anodic peak potential, i_{pc} = cathodic peak current, i_{pa} = anodic peak current, ΔE_p = peak potential separation, i_{pa}/i_{pc} = peak current ratio

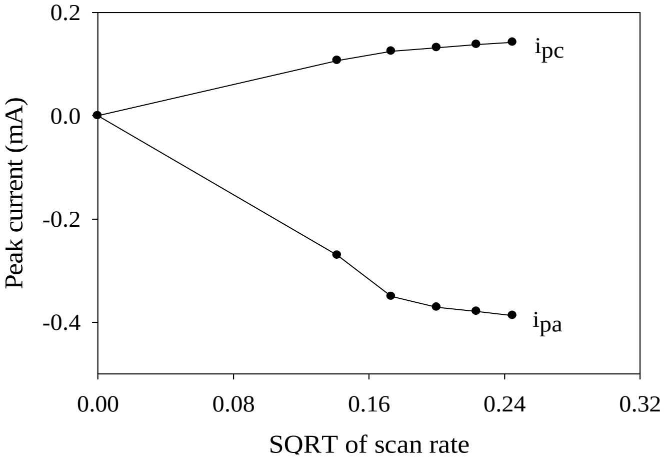

Fig. 2.44: Variation of peak current with SQRT of scan rate

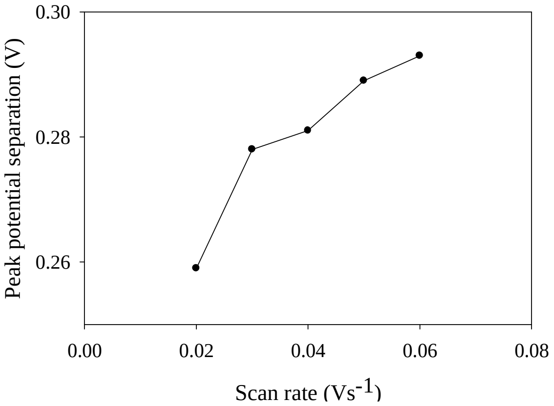

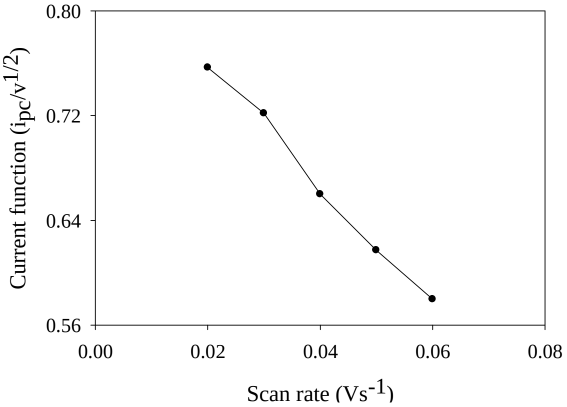

Fig. 2.45: **Variation of peak potential separation with scan rate**

Fig. 2.46: **Variation of current function with scan rate**

2.3.2.3 Redox behavior of Zn(II) in presence of isoleucine

The redox behavior of Zn(II) was studied in presence of zwitterionic isoleucine (z. ile) in 1:1 mol ratio. The potential window was set from -0.6 V to -1.5 V. The pH of $ZnCl_2$ and z. ile was found 5.55 and 6.20 respectively. But when z. ile was mixed with the metal salt, the pH of the mixture becomes 5.60. Therefore the pH of $ZnCl_2$ does not changed significantly after mixing with z. ile. The voltammogram of $ZnCl_2$ in absence and in presence of z. ile is compared in Fig. 2.47. The mixing of z. ile to the metal ion solution didn't change the peak position significantly but lowers the peak current. This lowering of peak current may be due to interaction of Zn(II) with z. ile.

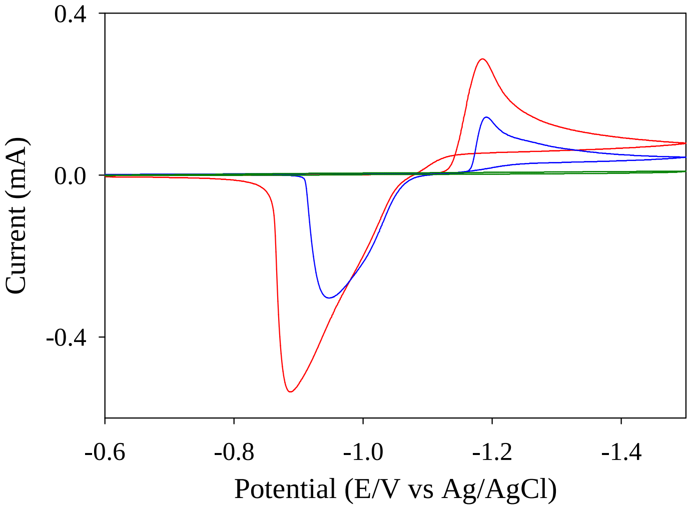

Fig. 2.47: CV's of free Zn(II) (red), Zn(II) in presence of z. ile (blue) and z. ile (green)

The voltammogram compared in Fig. 2.48 shows that the redox process of Zn(II) needs lower current to occur in presence of anionic isoleucine. The pH of the mixture was found 6.80 while recording the voltammogram. Before mixing the pH of anionic isoleucine (a. ile) was found 9.14 and that of $ZnCl_2$ was 5.55. Therefore the metal ion also interacts with anionic form of the ligand isoleucine.

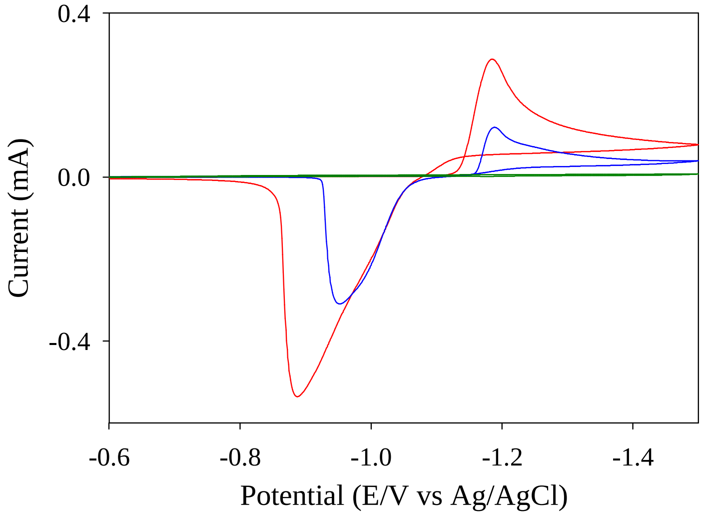

Fig. 2.48: CV's of free Zn(II) (red), Zn(II) in presence of a. ile (blue) and a. ile (green)

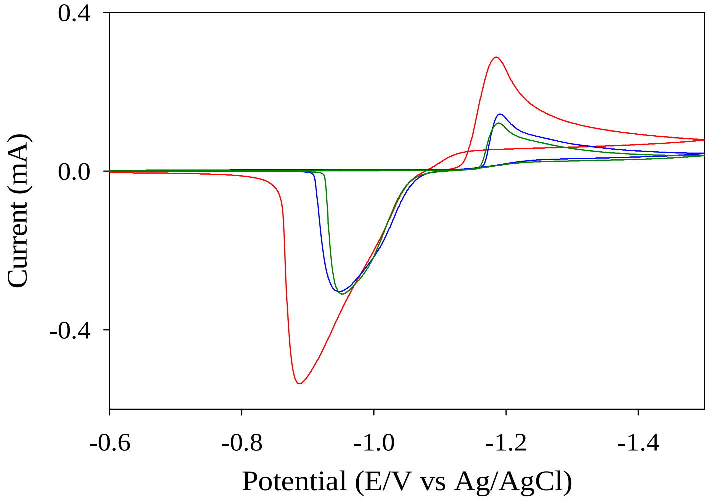

Fig. 2.49: CV's of free Zn(II) (red), Zn(II) in presence of z. ile (blue) and Zn(II) in presence of a. ile (green)

The voltammogram of Zn(II)-z. ile and Zn(II)-a. ile system is compared with the CV of free $ZnCl_2$ in Fig. 2.49. From the voltammogram of Zn(II) we see that peak current decreased after mixing with ligand. So, Zn(II) interacts with both z. ile and a. ile. But since the peak current and peak position is same, deprotonation of isoleucine does not affect the interaction with Zn(II). Therefore, both the zwitterionic and anionic isoleucine interacts with Zn(II) in a similar way.

The interactions of Zn(II) with both z. ile and a. ile are studied at different mole ratio. The voltammogram are compared in Fig. 2.50 and Fig. 2.51. Since there is no significant change in the voltammogram, the variation of mole ratio does not have any effect on the interaction of Zn(II) with z. ile. But the mole ratio variation affects the interaction of Zn(II)-a. ile system. The peak potential has significantly changed during 1:2 interactions. Therefore it can be said that maximum interaction of Zn(II) occurs with anionic isoleucine in 1:2 mole ratio.

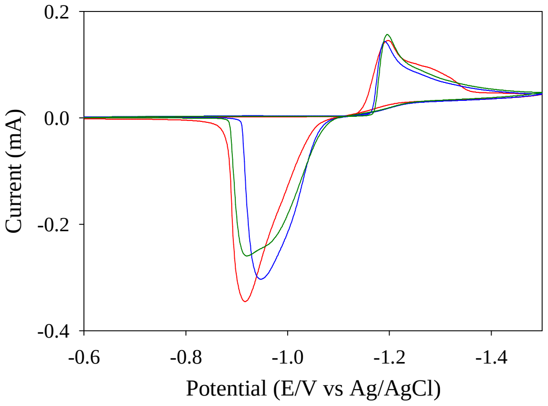

Fig. 2.50: CV's of Zn(II) in presence of z. ile at 1:0.5 (red), 1:1 (blue) and 1:2 (green) mole ratio

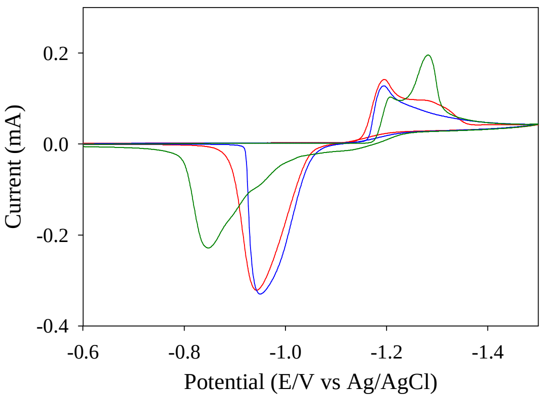

Fig. 2.51: CV's of Zn(II) in presence of a. ile at 1:0.5 (red), 1:1 (blue) and 1:2 (green) mole ratio

The scan rate was varied while recording the CV of Zn(II) in presence of a. ile. Fig. 2.52 compares the voltammogram and the corresponding current-potential data are tabulated in Table 2.9. The analysis of the current-potential data shows that with the increase of scan rate both cathodic and anodic peak currents increases. This is reasonable because in a slow voltage scan the diffusion layer grows much further from the electrode in comparison to a fast scan. Therefore the flux to the electrode surface is considerably smaller at slow scan rate than it is at faster rate. As the current is proportional to the flux towards the electrode, the magnitude of current becomes lower at slow scan rate and higher at higher scan rates. But the increase of peak current follows almost a linear relationship with square root of scan rate. This fact support the redox process to be diffusion controlled. The larger and variable peak potential separation value claims ohmic drop due to uncompensated solution resistance. The deviation of peak current ratio from unity, the change of current function with scan rate indicates a quasi-reversible electrode process followed by chemical reaction [91-98].

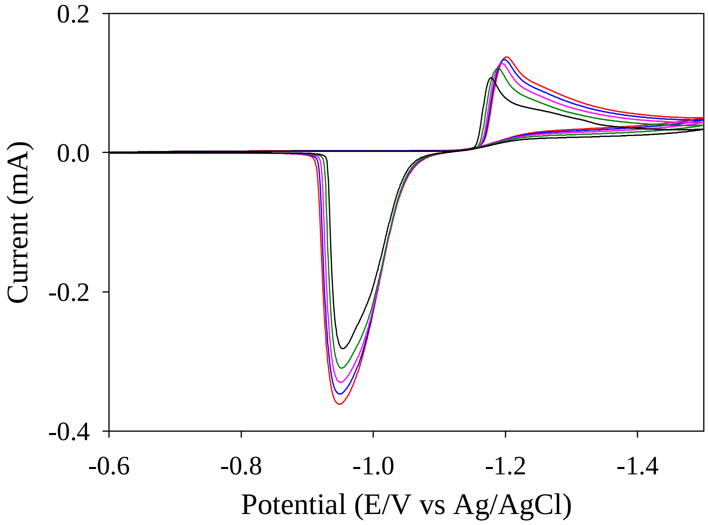

Fig. 2.52: CV's of Zn(II) in presence of anionic isoleucine at different scan rate

Table 2.9: Current-potential data of the voltammogram of Zn(II) in presence of anionic isoleucine at different scan rate.

v Vs^{-1}	$v^{1/2}$ Vs^{-1}	- E_{pc} Volt	- E_{pa} Volt	+ i_{pc} mA	- i_{pa} mA	ΔE_p Volt	i_{pa}/i_{pc}
0.02	0.1414	1.177	0.952	0.104	0.278	0.165	2.67
0.03	0.1732	1.189	0.952	0.118	0.311	0.237	2.64
0.04	0.2000	1.192	0.945	0.129	0.328	0.247	2.54
0.05	0.2236	1.196	0.945	0.132	0.346	0.251	2.62
0.06	0.2449	1.200	0.949	0.136	0.360	0.251	2.65

v = scan rate, $v^{1/2}$ = SQRT of scan rate, E_{pc} = cathodic peak potential, E_{pa} = anodic peak potential, i_{pc} = cathodic peak current, i_{pa} = anodic peak current, ΔE_p = peak potential separation, i_{pa}/i_{pc} = peak current ratio

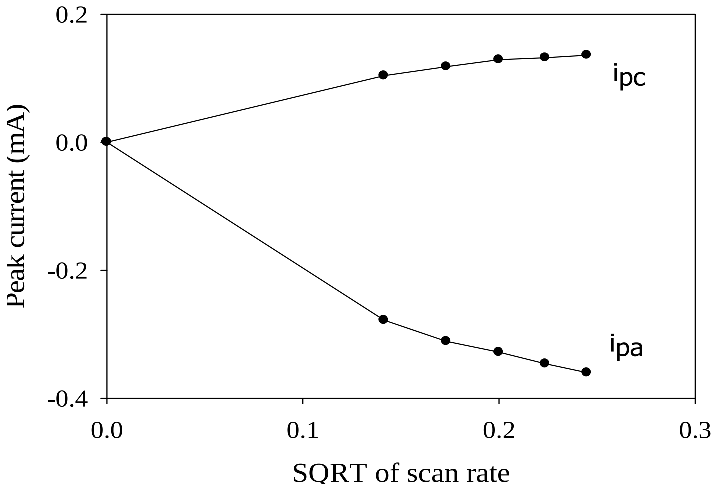

Fig. 2.53: Variation of peak current with SQRT of scan rate

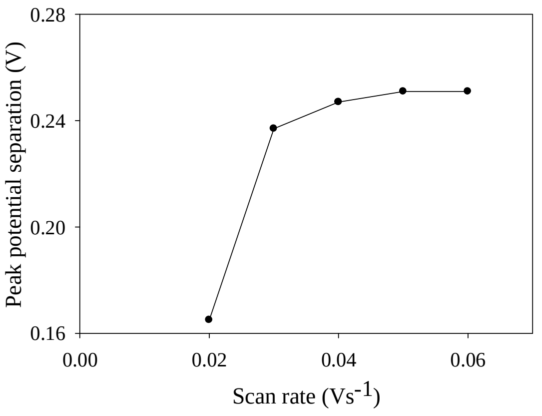

Fig. 2.54: Variation of peak potential separation with scan rate

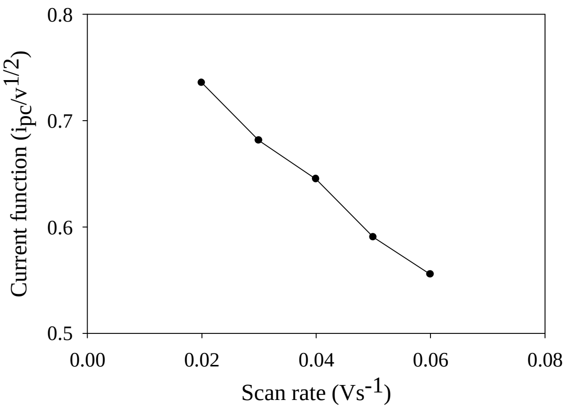

Fig. 2.55: Variation of current function with scan rate

2.3.2.4 Comparison of interaction of Zn(II) with leucine and isoleucine

The interaction of Zn(II) with leucine and isoleucine is compared in Fig. 2.56 and Fig. 2.57. The voltammogram are alike with respect to peak position and peak current. Therefore, the metal ion interacts with isoleucine and leucine in a similar way. This can be explained by the fact that the interaction site of both leucine and isoleucine are similar and therefore providing similar interaction with metal.

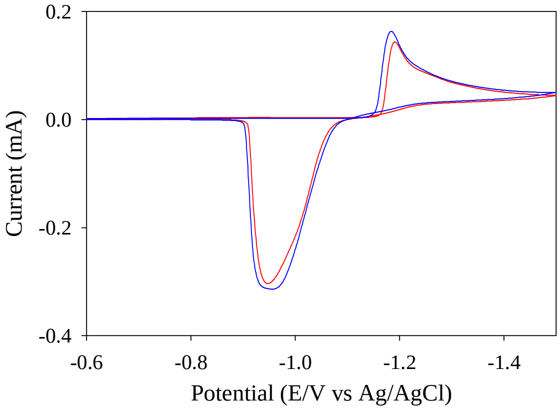

Fig. 2.56: **CV's of Zn(II) in presence of z. ile (red) and Zn(II) in presence of z. leu (blue)**

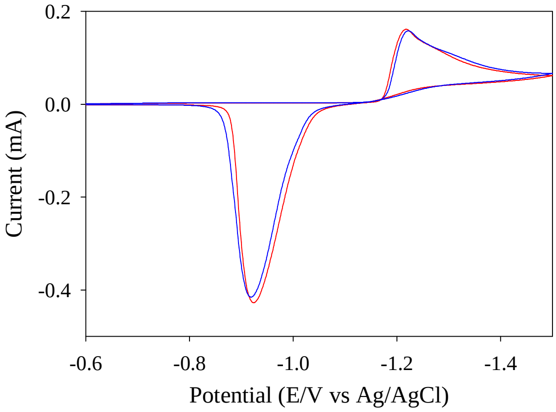

Fig. 2.57: **CV's of Zn(II) in presence of a. ile (red) and Zn(II) in presence of a. leu (blue)**

2.3.3 Cyclic voltammertic study of Cd(II) and Cd(II)-ligand interaction in aqueous medium at room temperature.

2.3.3.1 Redox behavior of Cd(II)

The redox behavior of $CdCl_2$ in 0.1 M KCl was studied using cyclic voltammertic technique at glassy carbon electrode. The potential window was set from -0.2 V to -1.2 V. The pH of the solution was 5.45. A CV of the system is shown in Fig. 2.58.

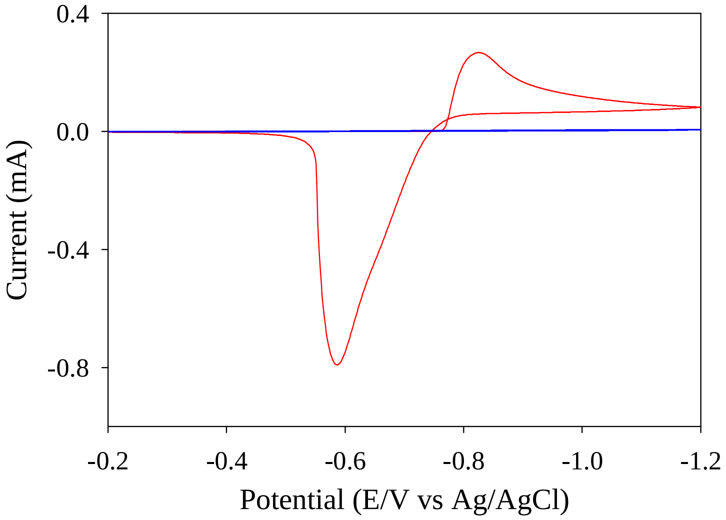

Fig. 2.58: CV of 0.1 M $CdCl_2$ (red) and 0.1 M KCl (blue) at 0.03 Vs^{-1}

The voltammogram shows one cathodic peak at -0.825 V due to reduction of Cd(II) to Cd(0) and one anodic peak at -0.5874 V due to oxidation of Cd(0) to Cd(II). The electrode reaction may be presented by the following equations:

Cathodic reaction: $Cd(II) + 2e \rightarrow Cd(0)$

Anodic reaction: $Cd(0) - 2e \rightarrow Cd(II)$

The variation of the CV's of $CdCl_2$ at different scan rate is shown in Fig. 2.59. The current-potential data for the system is tabulated in Table 2.10. The current-potential data provides some graphical analysis and is displayed in Fig. 2.60 to Fig. 2.62. The analysis shows with the increase of scan rate peak current for both cathodic and anodic peaks increases. This can be explained by the fact that at faster scan rate the diffusion layer grows much closer to theelectrode in comparison to a slow scan rate. Consequently, the flux to the electrode surface is considerably larger at higher scan rate. As the current is proportional to the flux towards the electrode, the magnitude of current becomes higher at faster scan rate. The linear increase of peak current with square root of scan rate supports a diffusion controlled electron transfer process.

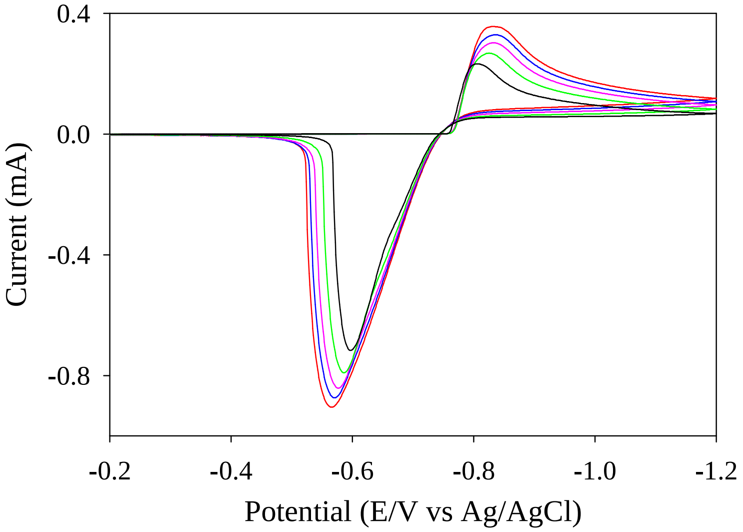

Fig. 2.59: CV of 0.01 M $CdCl_2$ at different scan rate

Table 2.10: Current-potential data of the voltammogram of Cd(II) at different scan rate.

v Vs^{-1}	$v^{1/2}$ Vs^{-1}	$-E_{pc}$ Volt	$-E_{pa}$ Volt	$+i_{pc}$ mA	$-i_{pa}$ mA	ΔE_p Volt	i_{pa}/i_{pc}
0.02	0.1414	0.8082	0.6000	0.2214	0.7140	0.2082	3.22
0.03	0.1732	0.8250	0.5874	0.2584	0.7916	0.2376	3.06
0.04	0.2000	0.8332	0.5790	0.2916	0.8496	0.2542	2.91
0.05	0.2236	0.8332	0.5708	0.3168	0.8748	0.2624	2.76
0.06	0.2449	0.8332	0.5666	0.3527	0.9044	0.2666	2.56

v = scan rate, $v^{1/2}$ = SQRT of scan rate, E_{pc} = cathodic peak potential, E_{pa} = anodic peak potential, i_{pc} = cathodic peak current, i_{pa} = anodic peak current, ΔE_p = peak potential separation, i_{pa}/i_{pc} = peak current ratio

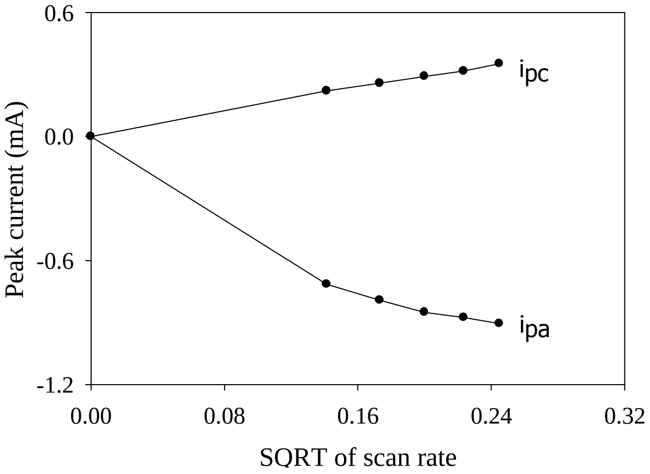

Fig. 2.60: Variation of peak current with SQRT of scan rate

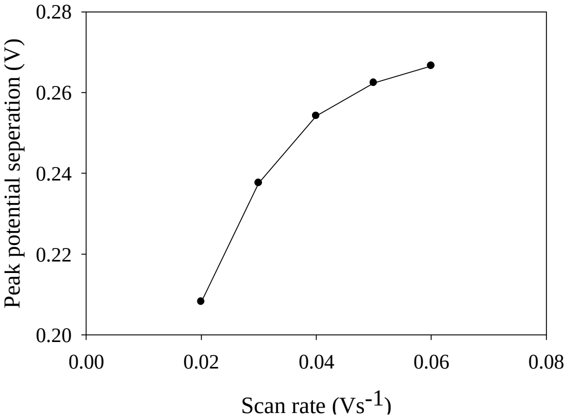

Fig. 2.61: Variation of peak potential separation with scan rate

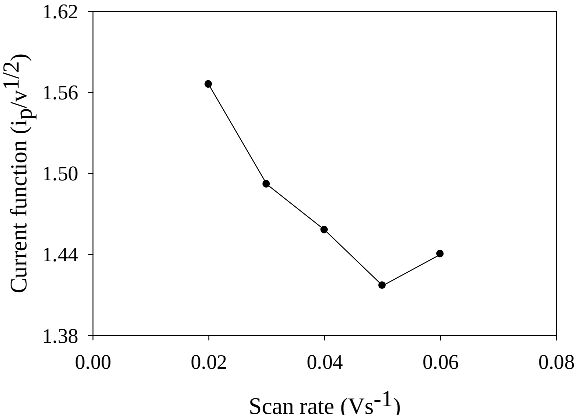

Fig. 2.62: Variation of current function with scan rate

Ohmic drop arises due to the uncompensated solution resistance. Therefore the peak potential separation value increases with scan rate. The current function changes when the voltammogram records at a faster rate. The peak current ratio is much larger than unity and varies with scan rate. These findings indicate that the electron transfer at the electrode surface is slow compared to the mass transport and that’s why chemical reactions are occurring at the electrode surface [91-98].

2.3.3.2 Redox behavior of Cd(II) in presence of leucine

The redox behavior of Cd(II) in presence of zwitterionic leucine (z. leu) in 1:1 mol ratio was studied from -0.2 V to -1.2 V. The pH of the mixture was 4.80 while the pH of z. leu and $CdCl_2$ was 6.45.and 5.45 respectively. Therefore the pH of $CdCl_2$ does changed significantly after mixing with z. leu. The voltammogram of Cd(II) before and after interaction is displayed in Fig. 2.63. The voltammogram shows that after mixing ligand to the metal ion solution, the peak potential didn't changed but peak current decreases. This may be due to interaction of Cd(II) with z. leu.

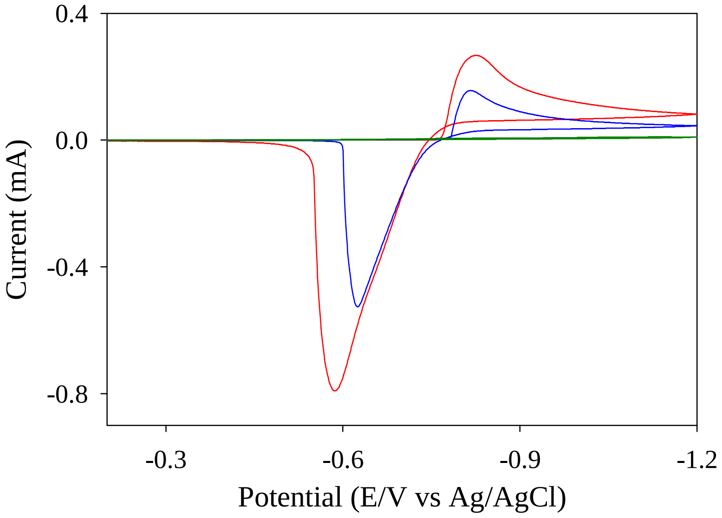

Fig. 2.63: CV's of free Cd(II) (red), Cd(II) in presence of z. leu (blue) and z. leu (green)

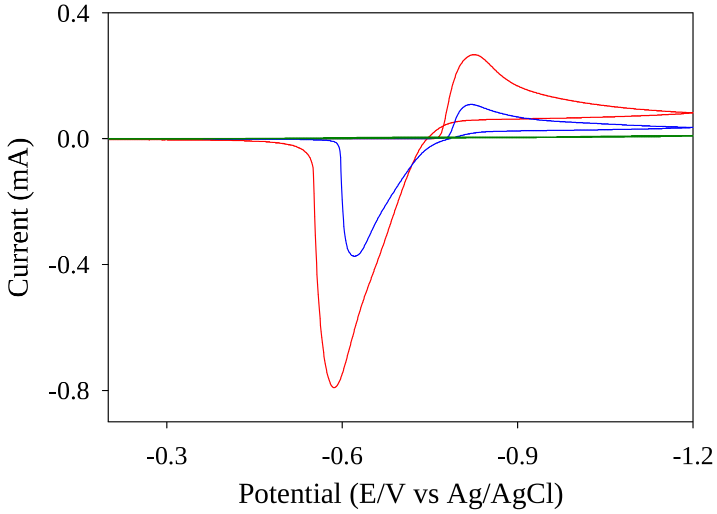

Fig. 2.64: CV's of free Cd(II) (red), Cd(II) in presence of a. leu (blue) and a. leu (green)

The redox behavior of Cd(II) in presence of anionic leucine (a. leu) was also studied. Equal moles of metal ion and anionic ligand were mixed together and voltammogram of the resultant mixture was taken. The pH of the mixture was found 7.80 while the pH of a. leu and $CdCl_2$ was 9.28 and 5.45 respectively. Therefore the pH of $CdCl_2$ changed significantly after mixing with a. leu. The voltammogram of $CdCl_2$ in absence and in presence of a. leu is compared in Fig. 2.64. A sharp lowering in peak current confirms the interaction of Cd(II) with anionic leucine.

The interaction of Cd(II) with both zwitterionic and anionic form of leucine is compared in the Fig. 2.65. Since the peak current is minimum, the Cd(II)-a. leu interaction may be more pronounce over Cd(II)-z. leu interaction.

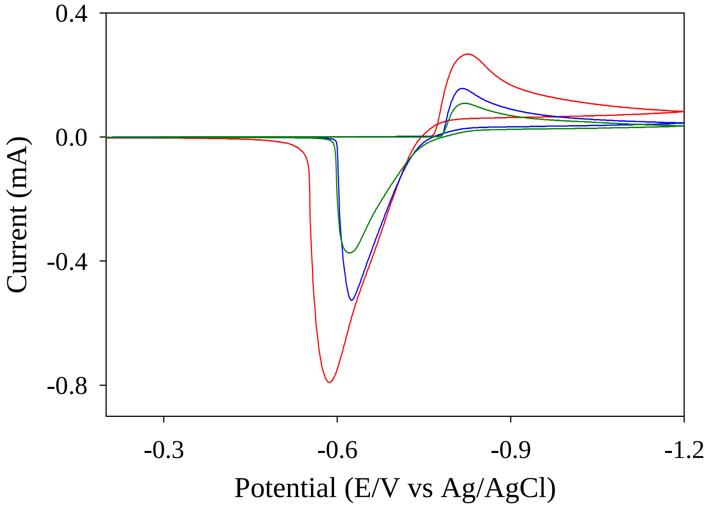

Fig. 2.65: CV's of free Cd(II) (red), Cd(II) in presence of z. leu (blue) and Cd(II) in presence of a. leu (green)

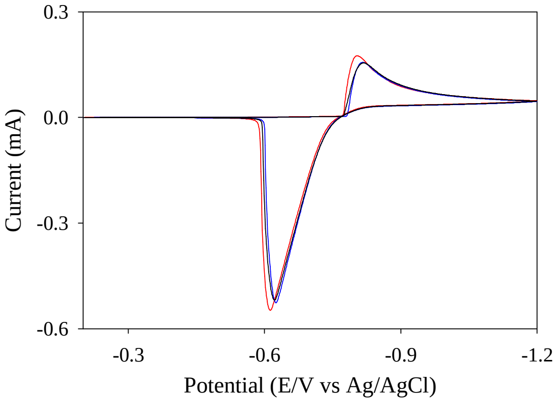

Fig. 2.66: CV's of Cd(II) in presence of z. leu at 1:0.5 (red), 1:1 (blue) and 1:2 (black) mole ratio

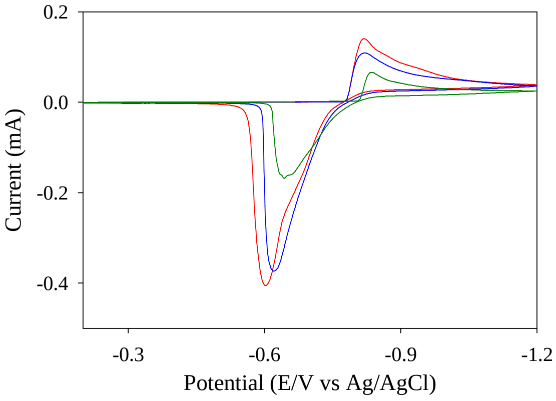

Fig. 2.67: CV's of Cd(II) in presence of a. leu at 1:0.5 (red), 1:1 (blue) and 1:2 (green) mole ratio

The interactions of Cd(II) with both z. leu and a. leu are studied at different mole ratio. The voltammogram are compared in Fig. 2.66 and Fig. 2.67. Since the voltammogram are alike, the variation of mole ratio does not have any effect on the interaction of Cd(II) with z. leu. But there is a significant difference in the voltammogram of Cd(II)-a. leu system. The peak current is minimum during 1:2 interactions. Therefore it can be said that maximum interaction of Cd(II) occurs with anionic leucine in 1:2 mole ratio.

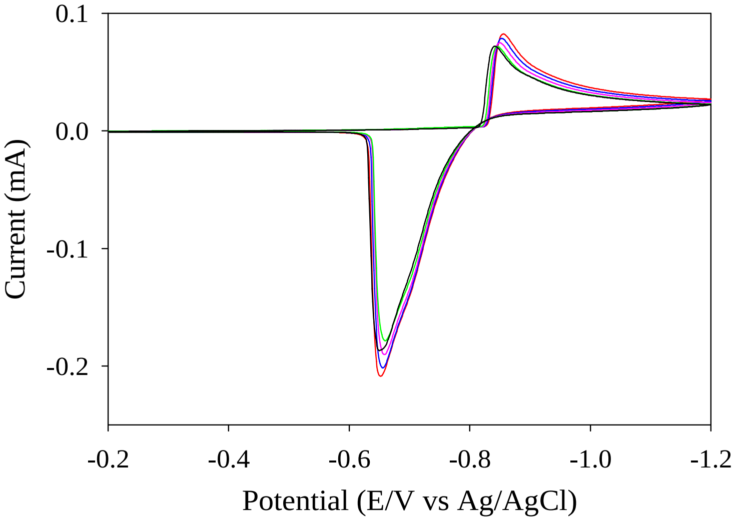

Fig. 2.68: CV's of Cd(II) in presence of anionic leucine at different scan rate

Table 2.11: Current-potential data of the voltammogram of Cd(II) in presence of anionic leucine at different scan rate

v Vs^{-1}	$v^{1/2}$ Vs^{-1}	$-E_{pc}$ Volt	$-E_{pa}$ Volt	$+i_{pc}$ mA	$-i_{pa}$ mA	ΔE_p Volt	i_{pa}/i_{pc}
0.02	0.1414	0.829	0.6208	0.057	0.1428	0.2082	2.50
0.03	0.1732	0.8374	0.6458	0.066	0.1642	0.1916	2.49
0.04	0.2000	0.8416	0.6500	0.071	0.1857	0.1916	2.61
0.05	0.2236	0.8458	0.6582	0.070	0.1786	0.1876	2.55
0.06	0.2449	0.8500	0.6582	0.075	0.1896	0.1918	2.53

v = scan rate, $v^{1/2}$ = SQRT of scan rate, E_{pc} = cathodic peak potential, E_{pa} = anodic peak potential, i_{pc} = cathodic peak current, i_{pa} = anodic peak current, ΔE_p = peak potential separation, i_{pa}/i_{pc} = peak current ratio

The interaction of Cd(II)-a. leu system was studied at different scan rate. The voltammogram are compared in Fig. 2.68 and the corresponding current- potential data are tabulated in Table 2.11. Some graphical analysis was done on the basis of the current-potential data and is displayed in Fig. 2.69 to Fig. 2.71. The analysis shows that the peak current changes almost linearly with square root of scan rate, the peak potential separation is larger and increases with scan rate, the current function changes with scan rate, the peak current ratio is greater than unity. All these facts indicate a diffusion controlled quasi-reversible electron transfer process where some sort of chemical reaction also occurring at the electrode surface [91-98].

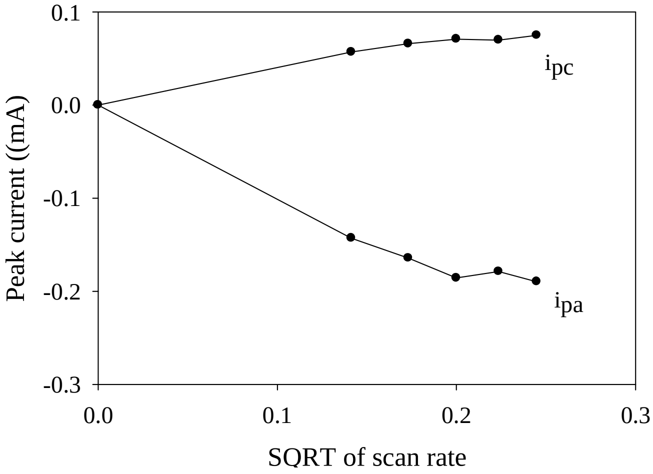

Fig. 2.69: Variation of peak current with SQRT of scan rate

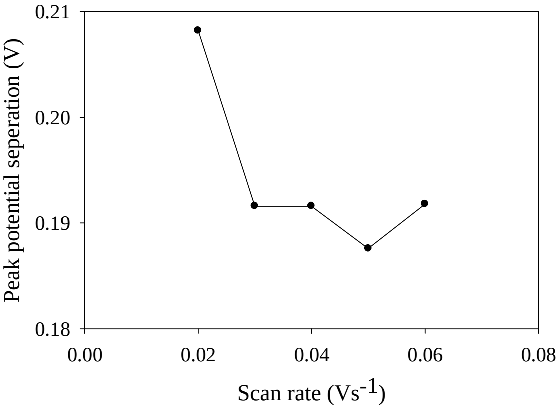

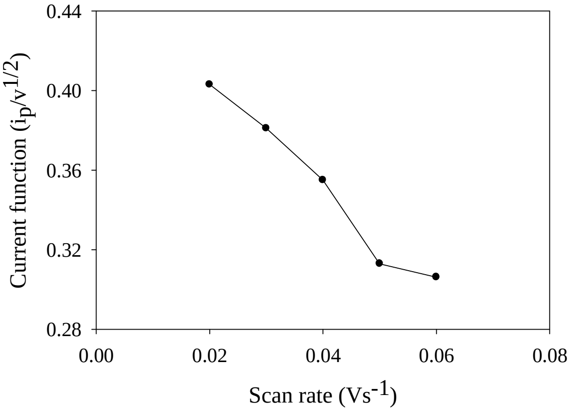

Fig. 2.70: Variation of peak potential separation with scan rate

Fig. 2.71: Variation of current function with scan rate

2.3.3.3 Redox behavior of Cd(II) in presence of isoleucine

The redox behavior of Cd(II) in presence of zwitterionic isoleucine (z. ile) in 1:1 mol ratio was studied within the potential window from -0.2 V to -1.2 V. The pH of the mixture was 5.40 while the pH of z. ile and $CdCl_2$ was 6.20.and 5.45 respectively. Therefore the pH of $CdCl_2$ does not changed significantly after mixing with z. ile. The voltammogram of $CdCl_2$ before and after interaction is compared with the CV of z. ile in Fig. 2.72. The voltammogram shows that after mixing ligand to the metal ion solution, the peak potential remains almost unchanged but peak current decreases. This may be due to interaction of Cd(II) with z. ile.

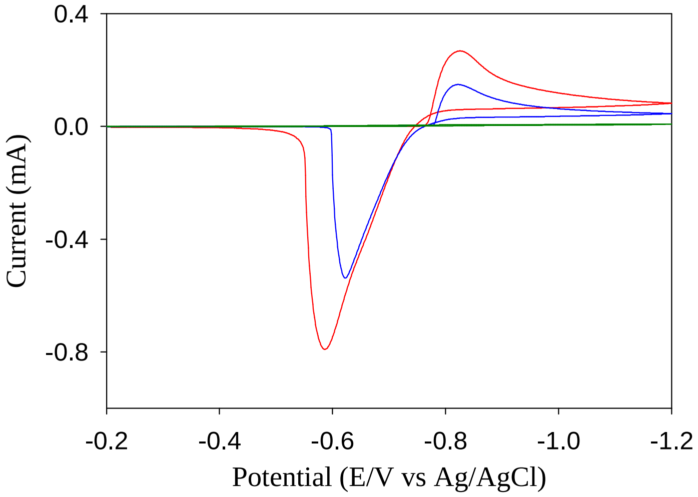

Fig. 2.72: CV's of free Cd(II) (red), Cd(II) in presence of z. ile (blue) and z. ile (green)

The redox behavior of Cd(II) in presence of anionic isoleucine (a. ile) in 1:1 mol ratio was also studied within the same potential window. The pH of the mixture was found 7.30 while the pH of a. ile and $CdCl_2$ was 9.14 and 5.45 respectively. Here, the pH of the metal ion solution is changed significantly after mixing with anionic ligand. The voltammogram of $CdCl_2$ in absence and in presence of a. ile is compared in Fig. 2.73. The voltammogram shows that after mixing ligand to the metal ion solution, the peak potential remains almost unchanged but peak current decreases. This may be due to interaction of Cd(II) with anionic isoleucine.

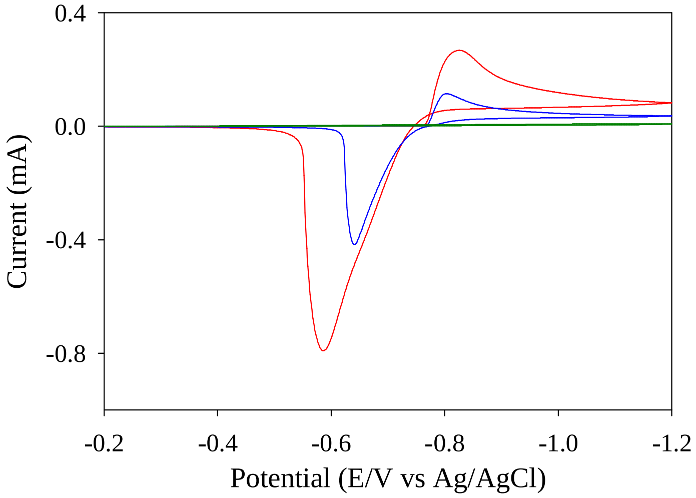

Fig. 2.73: CV's of free Cd(II) (red), Cd(II) in presence of a. ile (blue) and a. ile (green)

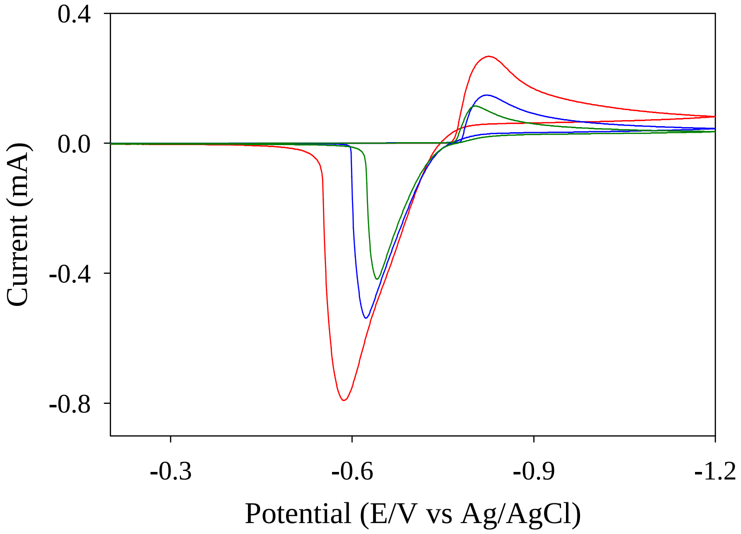

Fig. 2.74: CV's of free Cd(II) (red), Cd(II) in presence of z. ile (blue) and Cd(II) in presence of a. ile (green)

The voltammogram of Cd(II)-z. ile and Cd(II)-a. ile system compared with the CV of free $CdCl_2$ in the Fig. 2.74. From the voltammogram of Cd(II) we see that peak current has changed after mixing with ligand. So, Cd(II) interacts with both z. ile and a. ile. But since the peak current is minimum, the Cd(II)-a. ile interaction may be more pronounce over Cd(II)-z. ile interaction.

The interactions of Cd(II) with both z. ile and a. ile are studied at different mole ratio. The voltammogram are compared in Fig. 2.75 and Fig. 2.76. Since the voltammogram are alike, the variation of mole ratio does not have any effect on the interaction of Cd(II) with z. ile. But there is a significant difference in the voltammogram of Cd(II)-a. ile system. The peak potential has significantly changed and peak current is minimum during 1:2 interactions. Therefore it can be said that maximum interaction of Cd(II) occurs with anionic isoleucine in 1:2 mole ratio.

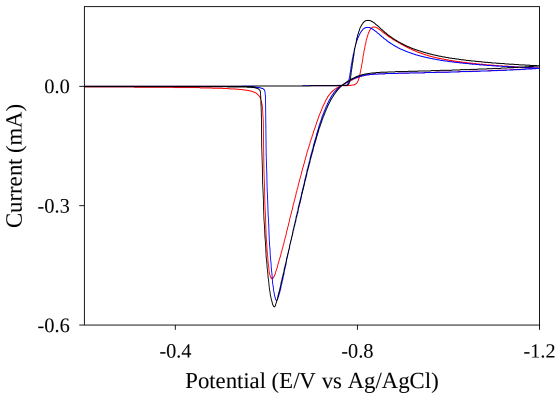

Fig. 2.75: **CV's of Cd(II) in presence of z. ile at 1:0.5 (red), 1:1 (blue) and 1:2 (black) mole ratio**

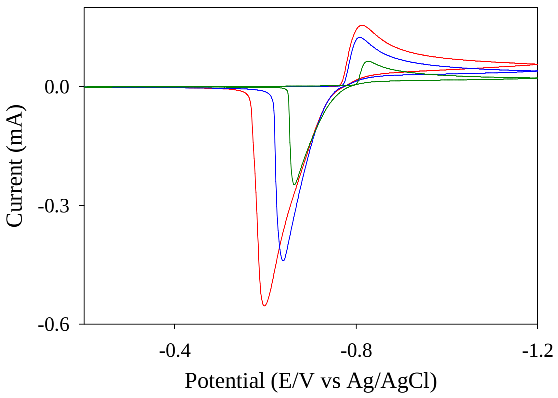

Fig. 2.76: **CV's of Cd(II) in presence of a. ile at 1:0.5 (red), 1:1 (blue) and 1:2 (green) mole ratio**

The interaction of Cd(II) in presence of anionic isoleucine was studied at different scan rate. The voltammogram are compared in Fig. 2.77 and the corresponding current- potential data are tabulated in Table 2.12. Some graphical analysis was done on the basis of the current-potential data and is displayed in Fig. 2.78 to Fig. 2.80. The analysis shows that the peak current changes almost linearly with square root of scan rate. Therefore the system is diffusion controlled. The peak potential separation is much larger. With the increase of scan rate the cathodic peak shifts towards negative potential and the anodic peak shifts towards positive potential. Therefore the peak potential separation increases with scan rate. The current function changes with scan rate. The peak current ratio is greater than unity. Therefore chemical reaction competes with electron transfer. The electrode process is termed quasi-reversible [91-98].

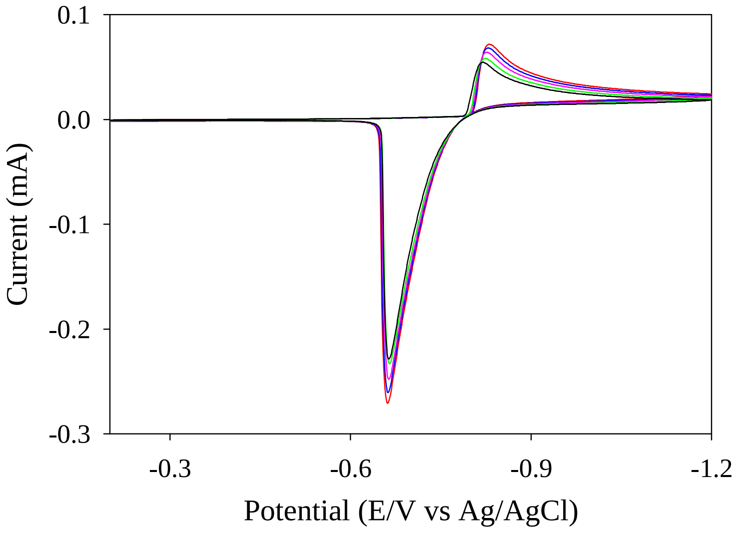

Fig. 2.77: CV's of Cd(II) in presence of anionic isoleucine at different scan rate

Table 2.12: Current-potential data of the voltammogram of Cd(II) in presence of anionic isoleucine at different scan rate

v Vs^{-1}	$v^{1/2}$ Vs^{-1}	- E_{pc} Volt	- E_{pa} Volt	+ i_{pc} mA	- i_{pa} mA	ΔE_p Volt	i_{pa}/i_{pc}
0.02	0.1414	0.8208	0.6624	0.0542	0.229	0.1584	4.22
0.03	0.1732	0.8250	0.6624	0.0563	0.233	0.1626	4.14
0.04	0.2000	0.8250	0.6624	0.0619	0.247	0.1626	3.99
0.05	0.2236	0.8290	0.6624	0.0667	0.262	0.1666	3.93
0.06	0.2449	0.8208	0.6040	0.1785	0.564	0.2168	3.16

v = scan rate, $v^{1/2}$ = SQRT of scan rate, E_{pc} = cathodic peak potential, E_{pa} = anodic peak potential, i_{pc} = cathodic peak current, i_{pa} = anodic peak current, ΔE_p = peak potential separation, i_{pa}/i_{pc} = peak current ratio

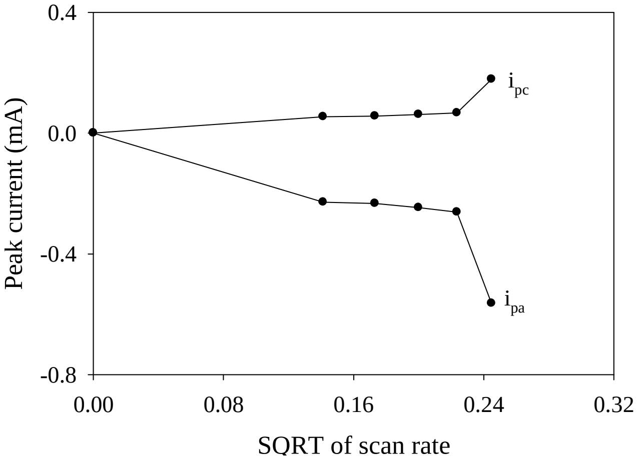

Fig. 2.78: Variation of peak current with SQRT of scan rate

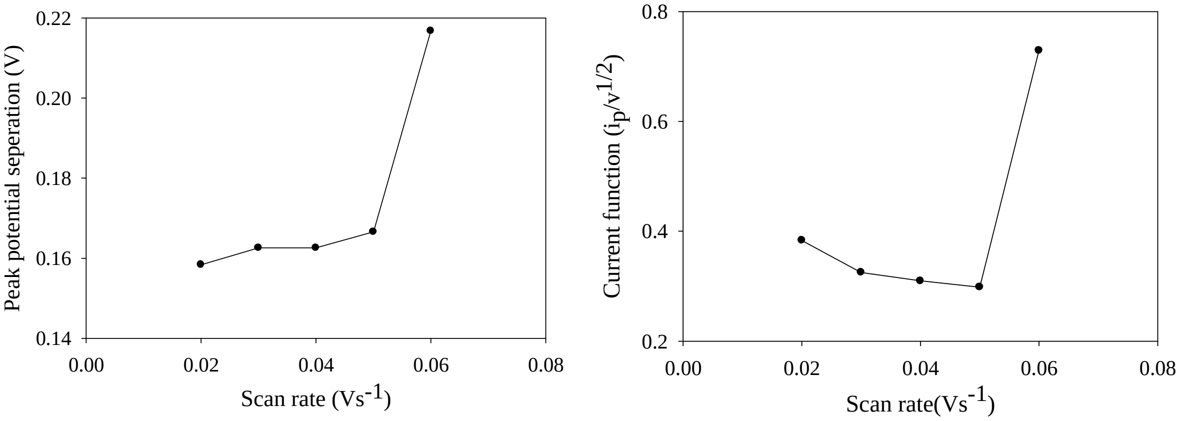

Fig. 2.79: Variation of peak potential separation with scan rate

Fig. 2.80: Variation of current function with scan rate

2.3.3.4 Comparison of interaction of Cd(II) with leucine and isoleucine

The interaction of Cd(II) with leucine and isoleucine is compared in Fig. 2.81 and Fig. 2.82. The voltammogram are alike with respect to peak position and peak current. Therefore, the metal ion interacts in a similar way with isoleucine and leucine. Similar interaction occurs due to the presence of identical interaction site in both the ligand.

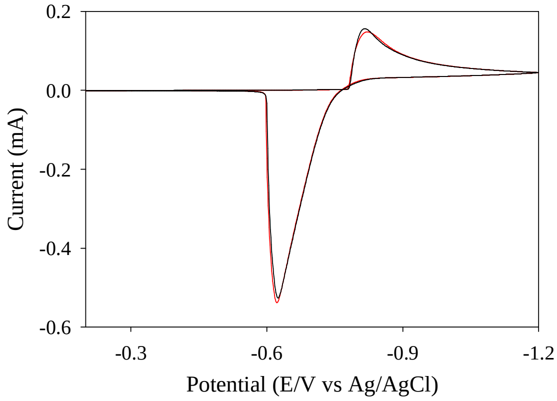

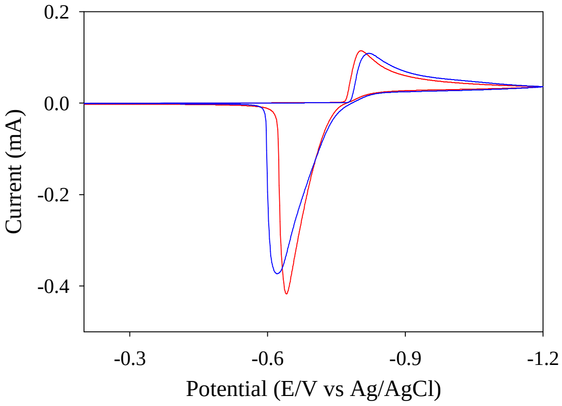

Fig. 2.81: **CV's of Cd(II) in presence of z. ile (red) and Cd(II) in presence of z. leu (black)**

Fig. 2.82: **CV's of Cd(II) in presence of a. ile (red) and Cd(II) in presence of a. leu (blue)**

2.3.4 Chronoamperometric and chronocoulometric study of Cu(II) and Cu(II)-ligand interaction in aqueous medium at room temperature.

2.3.4.1 CA and CC study of Cu(II)

The Cu(II) system was studied with chronoamperometric and chronocoulometric techniques. The CA experiment gives a current versus time curve which is known as current response or chronoamperogram. Such a current response for Cu(II) is shown in Fig. 2.83. The response shows a current spike followed by a gradual decay in current. The spike is due to initial electrolysis of species at the electrode surface and the decay is due to diffusion of molecules to the electrode surface.

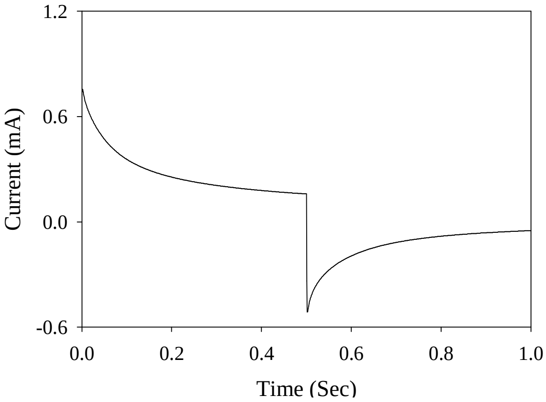

Fig. 2.83: **Current vs time plot of 1st peak for free Cu(II)**

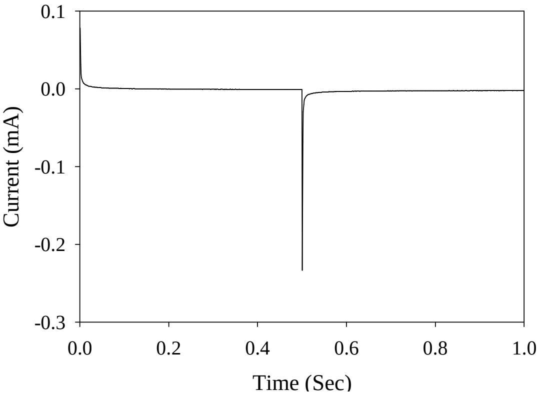

Fig. 2.84: **Current vs time plot for KCl**

Chronocoulometry (CC) is the integrated form of the chronoamperometry. So, in CC the monitored response is charge. It is also known as chronocoulogram. Such a charge response for Cu(II) is shown in Fig. 2.85. The response shows that the charge at τ is about 130.25 μC. Now if Q value obtained from time less than τ is plotted against $t^{1/2}$ and on the same graph $-Q_r$ is plotted against $\theta = [\tau^{1/2} + (t-\tau)^{1/2} - t^{1/2}]$, there will be two straight lines which intersects with each other at Q = 0 axis with equal slope, if there is no adsorption of reactant or product. Any deviation from such behavior means adsorption. Such plot is shown in Fig. 2.86. This shows that the two straight lines do not intersect each other at Q = 0 axis. Moreover they do not have equal slopes. Therefore, adsorption of reactant or products occurs at the electrode [91-99].

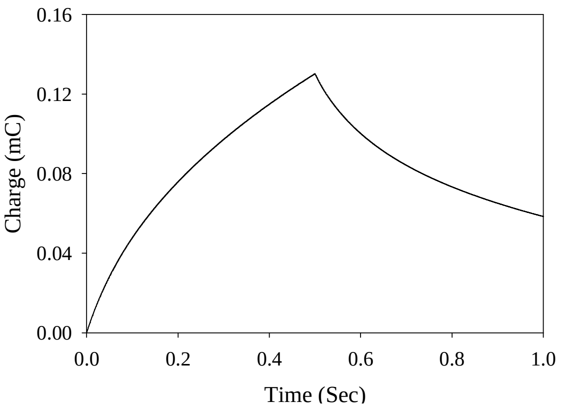

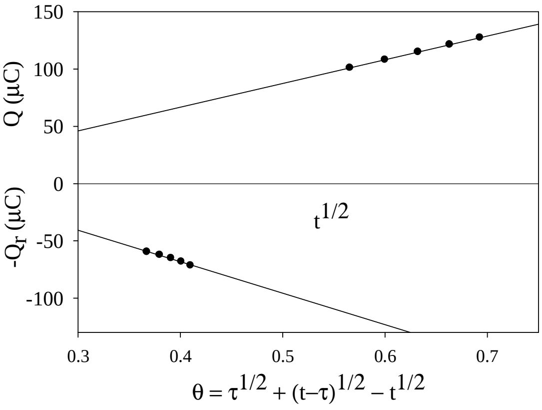

Fig. 2.85: **Charge vs time plot of 1st peak for free Cu(II)**

Fig. 2.86: **Plots of Q vs $t^{1/2}$ and $-Q_r$ vs θ of 1st peak for free Cu(II)**

2.3.4.2 CA and CC study of Cu(II) in presence of leucine

Chronoamperometric study of Cu(II) in presence of zwitterionic leucine and Cu(II) in presence of anionic leucine in 1:2 mol ratio was done. The amperogram are shown in Fig. 2.87 and Fig. 2.88 respectively. The response shows a current spike followed by a gradual decay in current. The spike is due to initial electrolysis of species at the electrode surface and the decay is due to diffusion of molecules to the electrode surface.

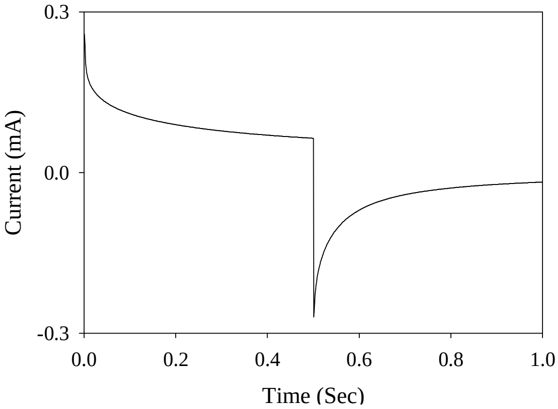

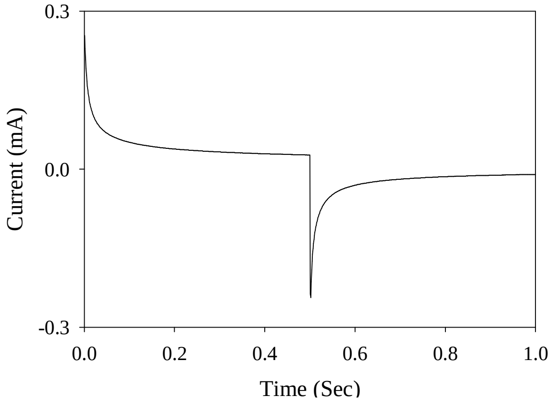

Fig. 2.87: **Current vs time plot of 1st peak for Cu(II) in presence of z. leu**

Fig. 2.88: **Current vs time plot of 1st peak for Cu(II) in presence of a. leu**

The corresponding charge responses are shown in Fig. 2.89 and Fig. 2.90. The response shows that the charges at τ is about 44.75 μC and 19.71 μC for Cu(II)-z. leu and Cu(II)-a. leu system respectively. The value is 130.25 μC for free Cu(II). The charge may be declined due to interaction. Again the charge is minimum for Cu(II)-anionic leucine system. Therefore, Cu(II)-a. leu interaction may be pronounced over Cu(II)-z. leu interaction.

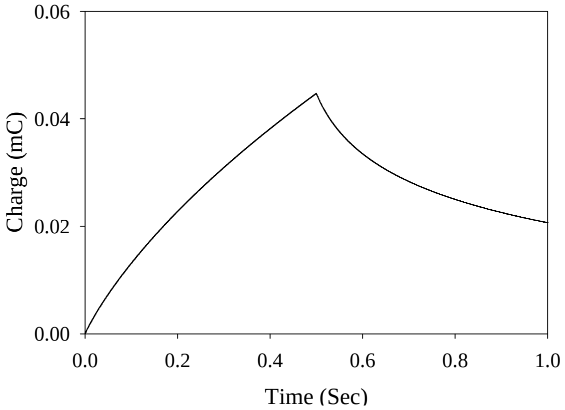

Fig. 2.89: **Charge vs time plot of 1st peak for Cu(II) in presence of z. leu**

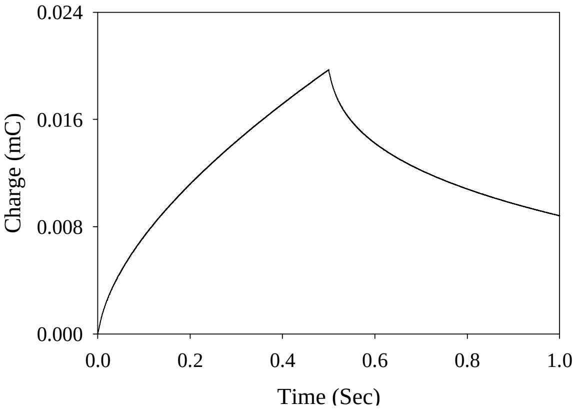

Fig. 2.90: **Charge vs time plot of 1st peak for Cu(II) in presence of a. leu**

Now if Q value obtained from time less than τ is plotted against $t^{1/2}$ and on the same graph $-Q_r$ is plotted against $\theta = [\tau^{1/2} + (t-\tau)^{1/2} - t^{1/2}]$, there will be two straight lines which intersects with each other at Q = 0 axis with equal slope, if there is no adsorption of reactant or product. Any deviation from such behavior means adsorption. Such plots are shown in Fig. 2.91 and Fig. 2.92. This shows that the two straight lines do not intersect each other at Q = 0 axis. Moreover they do not have equal slopes. Therefore, adsorption of reactant or products occurs on the electrode [91-99].

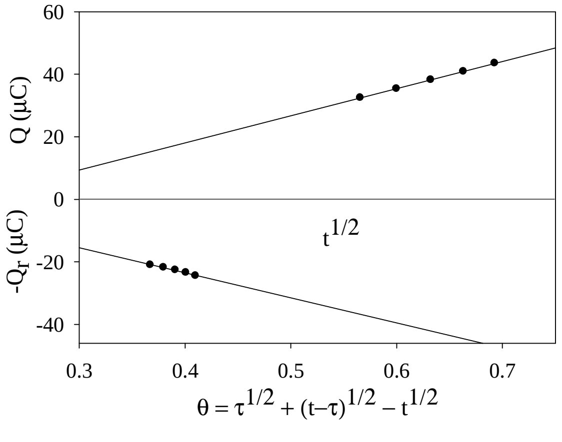

Fig. 2.91: **Plots of Q vs $t^{1/2}$ and $-Q_r$ vs θ of 1st peak for Cu(II) in presence of z. leu**

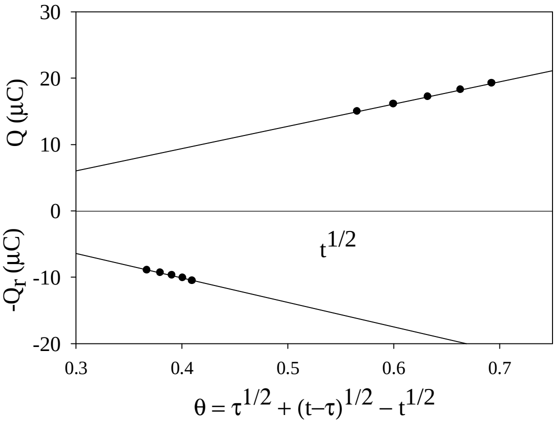

Fig. 2.92: **Plots of Q vs $t^{1/2}$ and $-Q_r$ vs θ of 1st peak for Cu(II) in presence of a. leu**

2.3.4.3 CA and CC study of Cu(II) in presence of isoleucine

Chronoamperometric study of Cu(II) in presence of zwitterionic isoleucine and Cu(II) in presence of anionic isoleucine in 1:2 mol ratio was done. The amperogram are shown in Fig. 2.93 and Fig. 2.94 respectively.

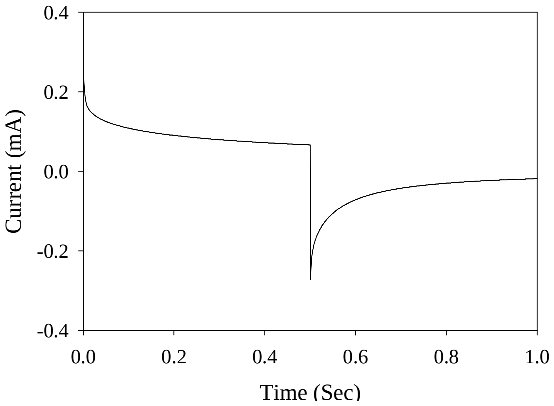

Fig. 2.93: **Current vs time plot of 1st peak for Cu(II) in presence of z. ile**

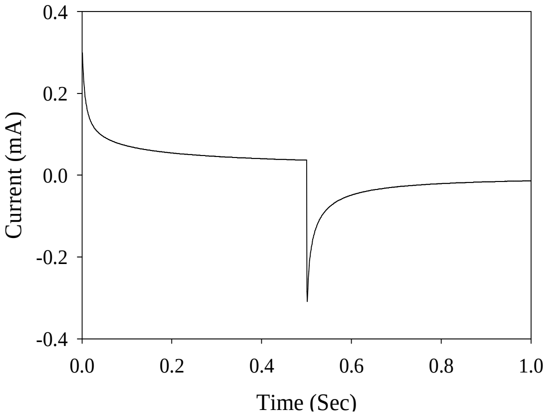

Fig. 2.94: **Current vs time plot of 1st peak for Cu(II) in presence of a. ile**

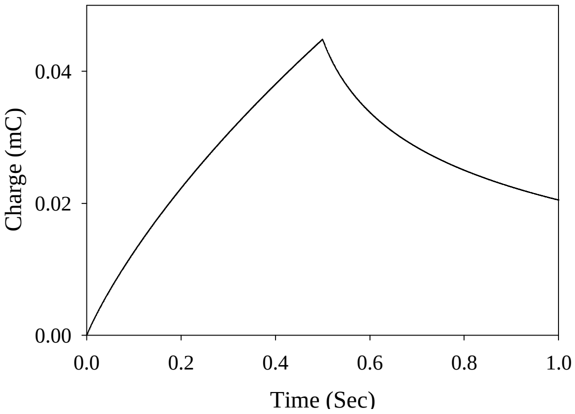

Fig. 2.95: **Charge vs time plot of 1st peak for Cu(II) in presence of z. ile**

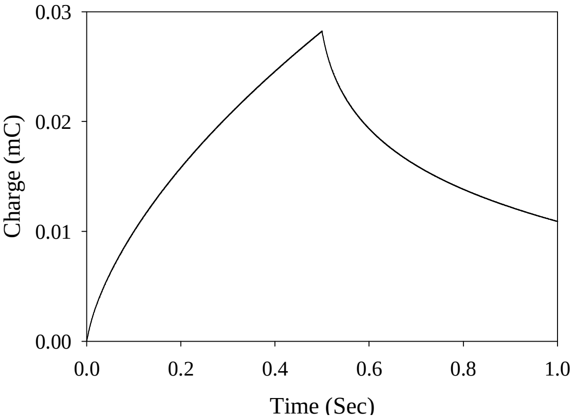

Fig. 2.96: **Charge vs time plot of 1st peak for Cu(II) in presence of a. ile**

The corresponding charge responses are shown in Fig. 2.95 and Fig. 2.96. The response shows that the charges at τ is about 44.85 μC and 28.24 μC for Cu(II)-z. ile and Cu(II)-a. ile system respectively. The value is 130.25 μC for free Cu(II). The charge may be declined due to interaction. Again the charge is minimum for Cu(II)-anionic isoleucine system. Therefore, Cu(II)-a. ile interaction may be pronounced over Cu(II)-z. ile interaction.

Now if Q value obtained from time less than τ is plotted against $t^{1/2}$ and on the same graph $-Q_r$ is plotted against $\theta = [\tau^{1/2} + (t-\tau)^{1/2} - t^{1/2}]$, there will be two straight lines which intersects with each other at Q = 0 axis with equal slope, if there is no adsorption of reactant or product. Any deviation from such behavior means adsorption. Such plots are shown in Fig. 2.97 and Fig. 2.98. This shows that the two straight lines do not intersect each other at Q = 0 axis. Moreover they do not have equal slopes. Therefore, adsorption of reactant or products occurs on the electrode [91-99].

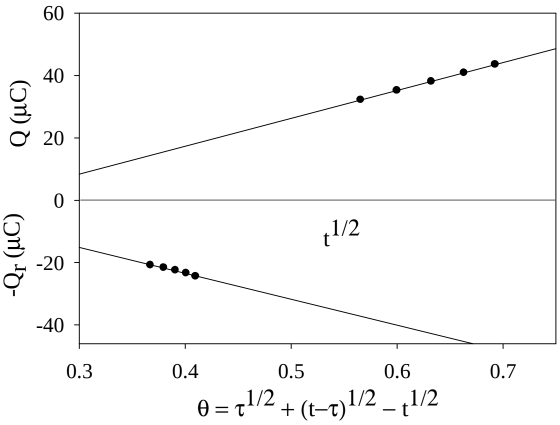

Fig. 2.97: **Plots of Q vs $t^{1/2}$ and $-Q_r$ vs θ of 1st peak for Cu(II) in presence of z. ile**

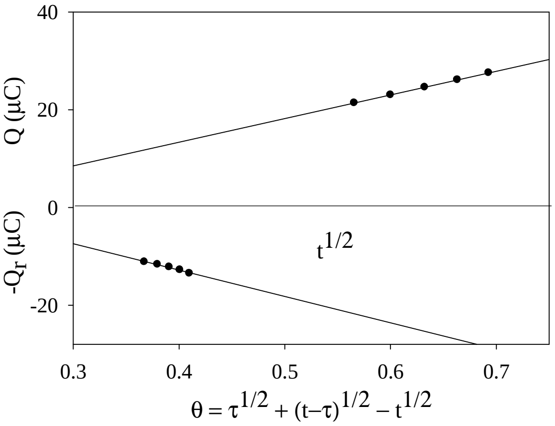

Fig. 2.98: **Plots of Q vs $t^{1/2}$ and $-Q_r$ vs θ of 1st peak for Cu(II) in presence of a. ile**

2.3.5 Chronoamperometric and chronocoulometric study of Zn(II) and Zn(II)-ligand interaction in aqueous medium at room temperature.

2.3.5.1 CA and CC study of Zn(II)

The Zn(II) system was studied with chronoamperometric and chronocoulometric techniques. The CA experiment gives a current versus time curve which is known as current response or chronoamperogram. Such a current response for Zn(II) is shown in Fig. 2.99. The response shows a current spike followed by a gradual decay in current. The spike is due to initial electrolysis of species at the electrode surface and the decay is due to diffusion of molecules to the electrode surface.

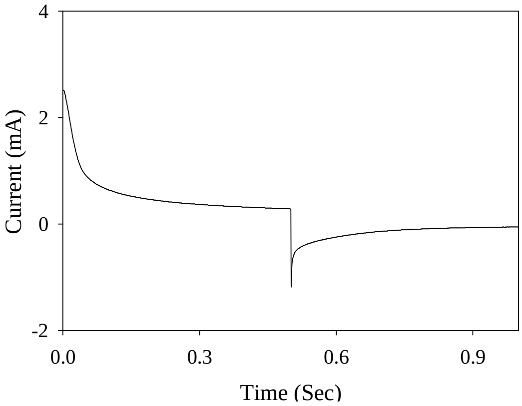

Fig. 2.99: Current vs time plot for free Zn(II)

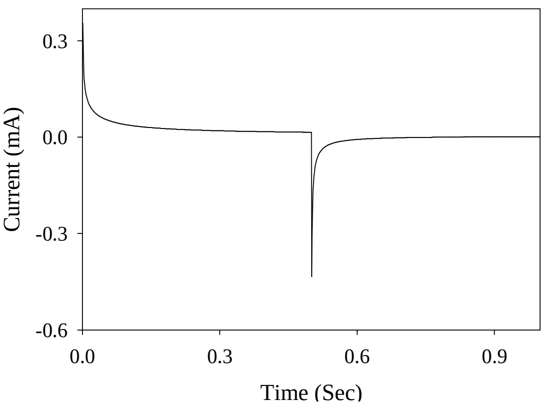

Fig. 2.100: Current vs time plot for KCl

Chronocoulometry (CC) is the integrated form of the chronoamperometry. So, in CC the monitored response is charge. It is also known as chronocoulogram. Such a charge response for Cd(II) is shown in Fig. 2.101. The response shows that the charge at τ is about 238.49 μC. Now if Q value obtained from time less than τ is plotted against $t^{1/2}$ and on the same graph $-Q_r$ is plotted against $\theta = [\tau^{1/2} + (t-\tau)^{1/2} - t^{1/2}]$, there will be two straight lines which intersects with each other at Q = 0 axis with equal slope, if there is no adsorption of reactant or product. Any deviation from such behavior means adsorption. Such plot is shown in Fig. 2.102. This shows that the two straight lines do not intersect each other at Q = 0 axis. Moreover they do not have equal slopes. Therefore, adsorption of reactant or products occurs on the electrode [91-99].

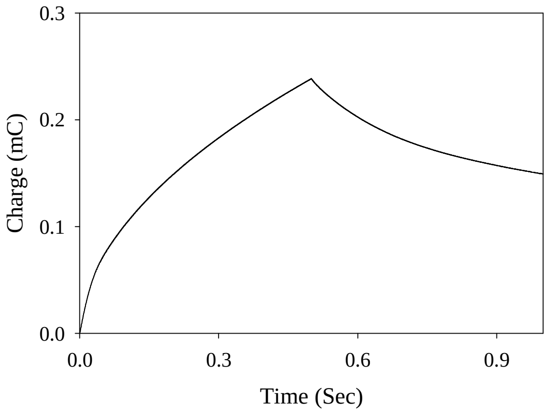

Fig. 2.101: **Charge vs time plot for free Zn(II)**

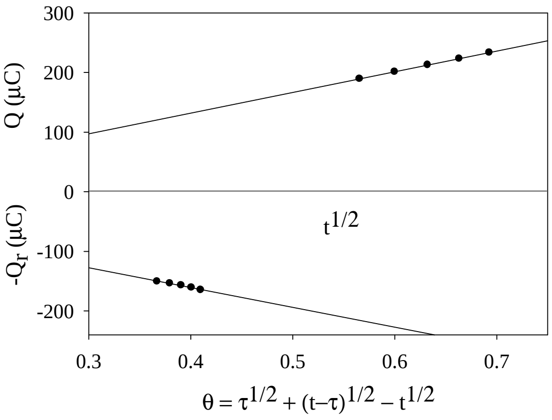

Fig. 2.102: **Plots of Q vs $t^{1/2}$ and $-Q_r$ vs θ for free Zn(II)**

2.3.5.2 CA and CC study of Zn(II) in presence of leucine

Chronoamperometric study of Zn(II) in presence of zwitterionic leucine (z. leu) and Zn(II) in presence of anionic leucine (a. leu) in 1:2 mol ratio was done. The amperogram are shown in Fig. 2.103 and Fig. 2.104 respectively. The response shows a current spike followed by a gradual decay in current. The spike is due to initial electrolysis of species at the electrode surface and the decay is due to diffusion of molecules to the electrode surface.

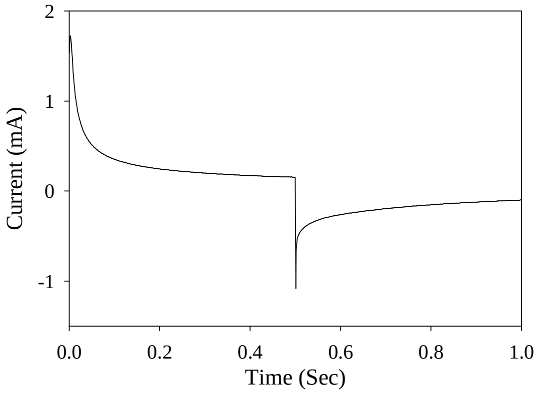

Fig. 2.103: **Current vs time plot for Zn(II) in presence of z. leu**

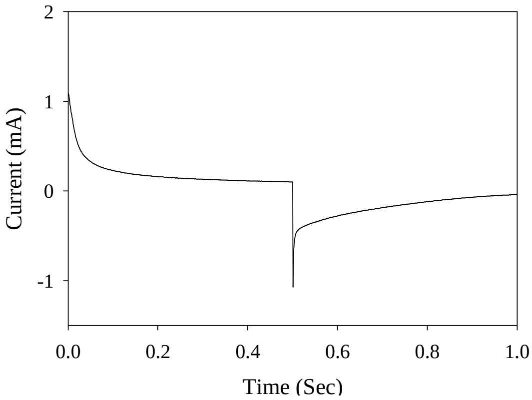

Fig. 2.104: **Current vs time plot for Zn(II) in presence of a. leu**

The corresponding charge responses are shown in Fig. 2.105 and Fig. 2.106. The response shows that the charges at τ is about 140.99 μC and 85.99 μC for Zn(II)-z. leu and Zn(II)-a.leu system respectively. The value is 238.49 μC for free Zn(II). The charge may be declined due to interaction. Again the charge is minimum for Zn(II)-anionic leucine system. Therefore, Zn(II)-anionic leucine interaction may be pronounced over Zn(II)-z. leu interaction.

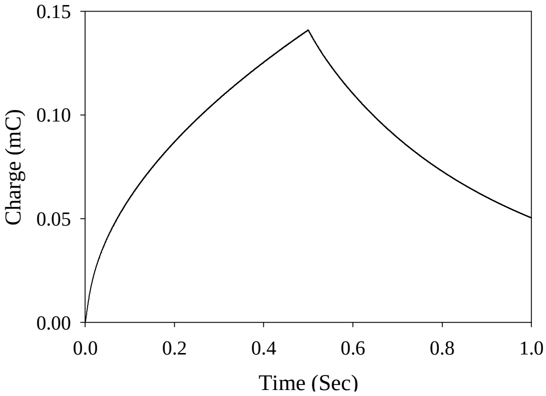

Fig. 2.105: **Charge vs time plot for Zn(II) in presence of z. leu**

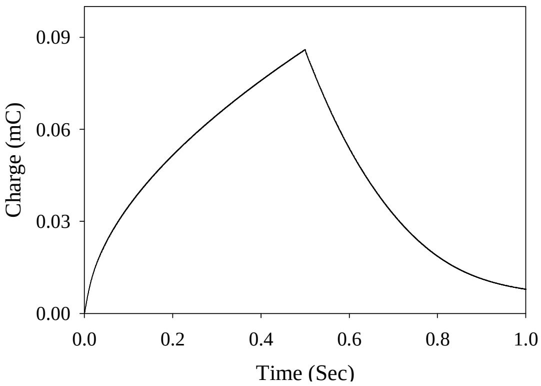

Fig. 2.106: **Charge vs time plot for Zn(II) in presence of a. leu**

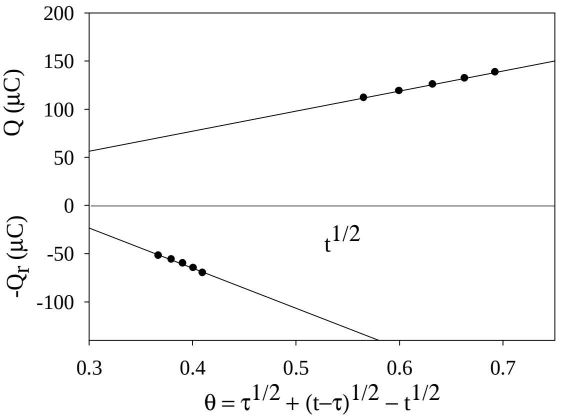

Fig. 2.107: **Plots of Q vs $t^{1/2}$ and $-Q_r$ vs θ for Zn(II) in presence of z. leu**

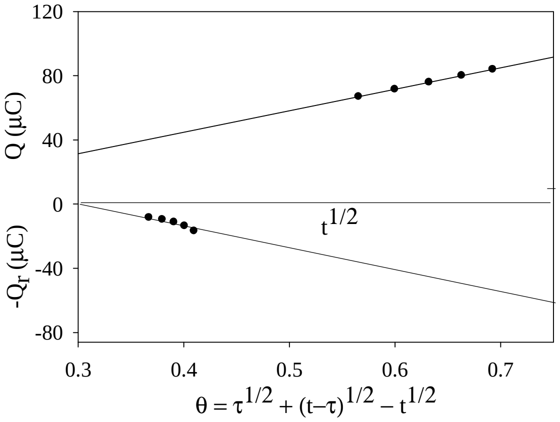

Fig. 2.108: **Plots of Q vs $t^{1/2}$ and $-Q_r$ vs θ for Zn(II) in presence of a. leu**

Now if Q value obtained from time less than τ is plotted against $t^{1/2}$ and on the same graph $-Q_r$ is plotted against $\theta = [\tau^{1/2} + (t-\tau)^{1/2} - t^{1/2}]$, there will be two straight lines which intersects with each other at Q = 0 axis with equal slope, if there is no adsorption of reactant or product. Any deviation from such behavior means adsorption. Such plots are shown in Fig. 2.107 and Fig. 2.108. This shows that the two straight lines do not intersect each other at Q=0 axis. Moreover they do not have equal slopes. Therefore, adsorption of reactant or products occurs on the electrode [91-99].

2.3.5.3 CA and CC study of Zn(II) in presence of isoleucine

Chronoamperometric study of Zn(II) in presence of zwitterionic isoleucine (z. ile) and Zn(II) in presence of anionic isoleucine (a. ile) in 1:2 mol ratio was done. The amperogram are shown in Fig. 2.109 and Fig. 2.110 respectively. The response shows a current spike followed by a gradual decay in current. The spike is due to initial electrolysis of species at the electrode surface and the decay is due to diffusion of molecules to the electrode surface.

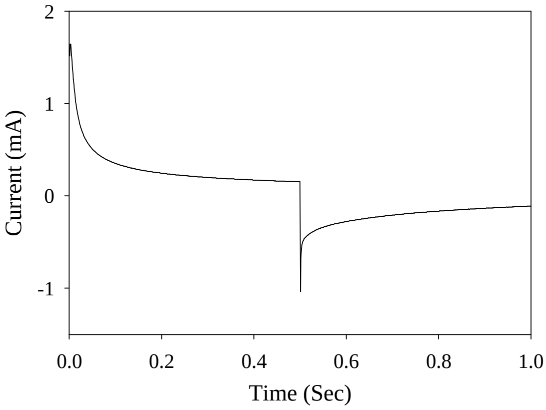

Fig. 2.109: Current vs time plot for Zn(II) in presence of z. ile

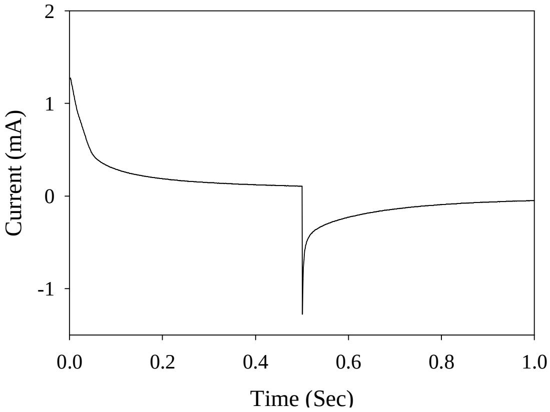

Fig. 2.110: Current vs time plot for Zn(II) in presence of a. ile

The corresponding charge responses are shown in Fig. 2.111 and Fig. 2.112. The response shows that the charges at τ is about 134.79 μC and 80.11 μC for Zn(II)-z. ile and Zn(II)-a.ile system respectively. The value is 238.49 μC for free Zn(II). The charge may be declined due to interaction. Again the charge is minimum for Zn(II)-anionic isoleucine system. Therefore, Zn(II)-a. ile interaction may be pronounced over Zn(II)-z. ile interaction.

Now if Q value obtained from time less than τ is plotted against $t^{1/2}$ and on the same graph $-Q_r$ is plotted against $\theta = [\tau^{1/2} + (t-\tau)^{1/2} - t^{1/2}]$, there will be two straight lines which intersects with each other at Q = 0 axis with equal slope, if there is no adsorption. Any deviation from such behavior means adsorption. Such plots are shown in Fig. 2.113 and Fig. 2.114. This shows that the two straight lines do not intersect each other at Q = 0 axis. Moreover they do not have equal slopes. Therefore, adsorption of reactant or products occurs on the electrode [91-99].

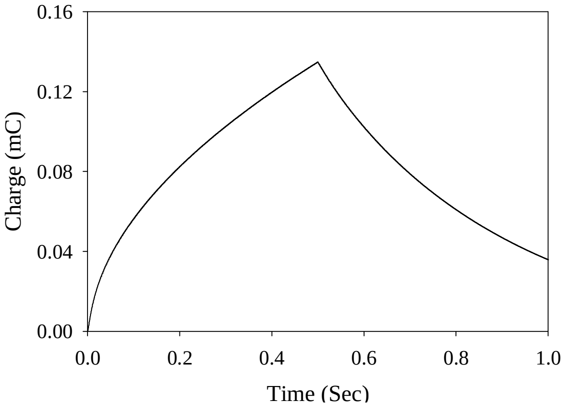

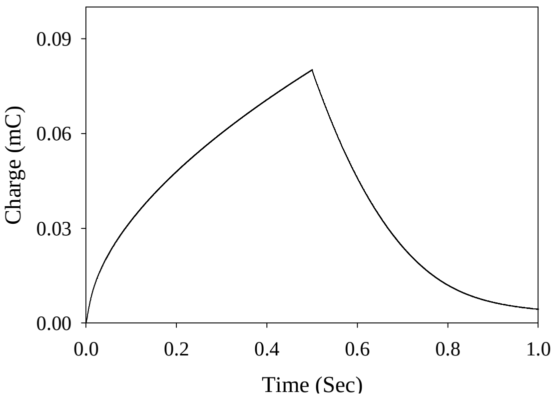

Fig. 2.111: **Charge vs time plot for Zn(II) in presence of z. ile**

Fig. 2.112: **Charge vs time plot for Zn(II) in presence of a. ile**

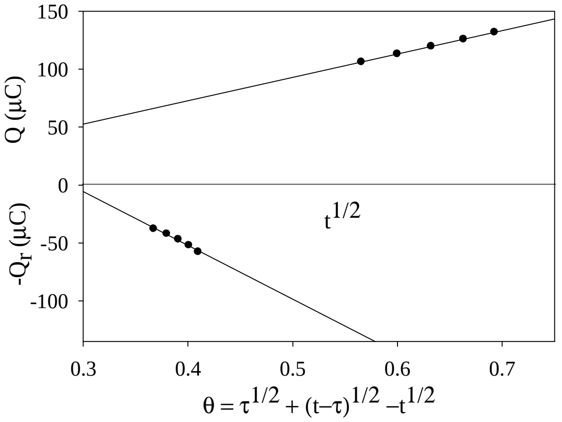

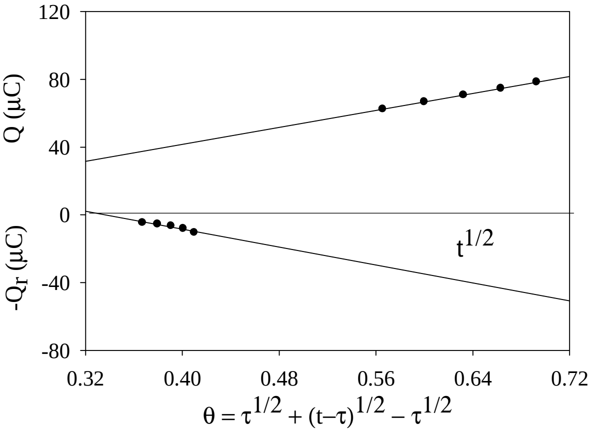

Fig. 2.113: **Plots of Q vs $t^{1/2}$ and $-Q_r$ vs θ for Zn(II) in presence of z. ile**

Fig. 2.114: **Plots of Q vs $t^{1/2}$ and $-Q_r$ vs θ for Zn(II) in presence of a. ile**

2.3.6 Chronoamperometric and chronocoulometric study of Cd(II) and Cd(II)-ligand interaction in aqueous medium at room temperature.

2.3.6.1 CA and CC study of Cd(II)

The Cd(II) system was studied with chronoamperometric and chronocoulometric techniques. The CA experiment gives a current versus time curve which is known as current response or chronoamperogram. Such a current response for Cd(II) is shown in Fig. 2.115. The response shows a current spike followed by a gradual decay in current. The spike is due to initial electrolysis of species at the electrode surface and the decay is due to diffusion of molecules to the electrode surface. The charge response for Cd(II) is shown in Fig. 2.117. The response shows that the charge at τ is about 163.11 μC.

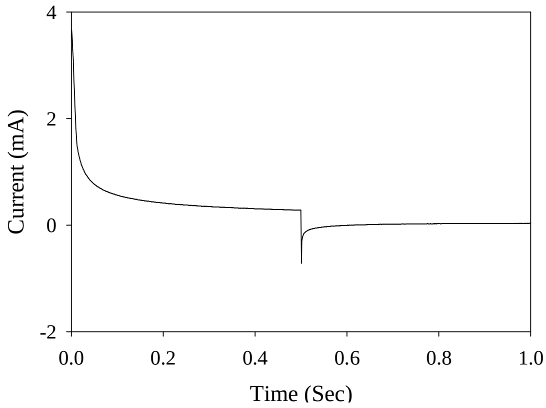

Fig. 2.115: Current vs time plot for free Cd(II)

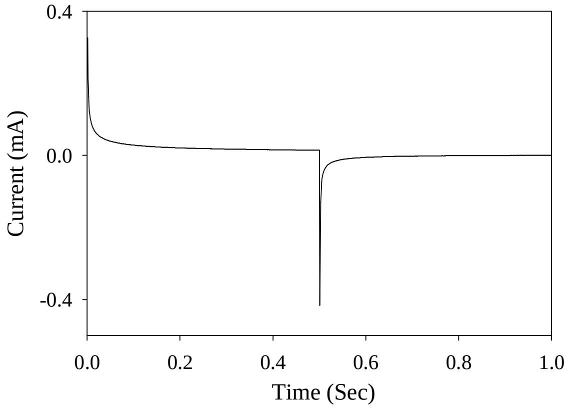

Fig. 2.116: Current vs time plot for KCl

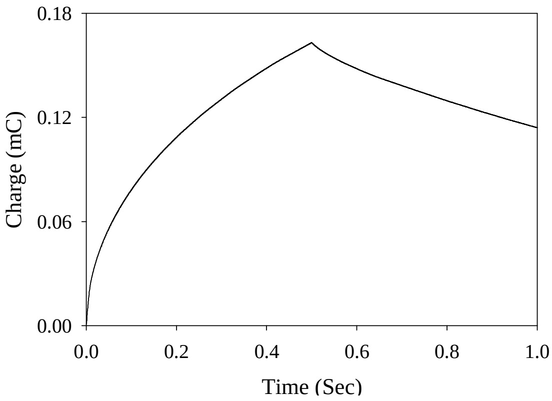

Fig. 2.117: Charge vs time plot for free Cd(II)

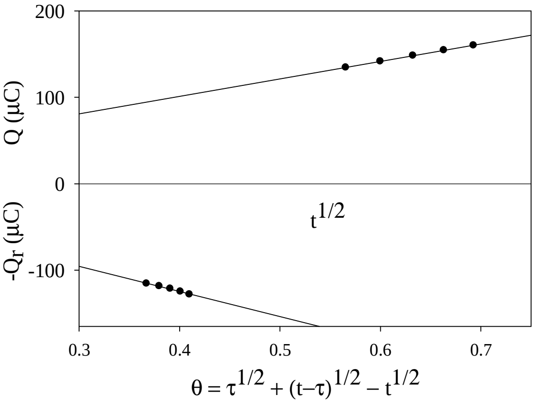

Fig. 2.118: Plots of Q vs $t^{1/2}$ and $-Q_r$ vs θ for free Cd(II)

Now if Q value obtained from time less than τ is plotted against $t^{1/2}$ and on the same graph $-Q_r$ is plotted against $\theta = [\tau^{1/2} + (t-\tau)^{1/2} - t^{1/2}]$, there will be two straight lines which intersects with each other at Q = 0 axis with equal slope, if there is no adsorption of reactant or product. Any deviation from such behavior means adsorption. Such plot is shown in Fig. 2.118. This shows that the two straight lines do not intersect each other at Q = 0 axis. Moreover they do not have equal slopes. Therefore, adsorption of reactant or products occurs on the electrode [91-99].

2.3.6.2 CA and CC study of Cd(II) in presence of leucine

Chronoamperometric study of Cd(II) in presence of zwitterionic leucine and Cd(II) in presence of anionic leucine in 1:2 mol ratio was done. The amperogram are shown in Fig. 2.119 and Fig. 2.120 respectively. The corresponding charge responses are shown in Fig. 2.121 and Fig. 2.122. The response shows that the charges at τ is about 150.78 μC and 41.09 μC for Cd(II)-z. leu and Cd(II)-a. leu system respectively. The value is 163.11 μC for free Cd(II). The charge may be declined due to interaction. Again the charge is minimum for Cd(II)-anionic leucine system. Therefore, Cd(II)-a. leu interaction may be pronounced over Cd(II)-z. leu interaction.

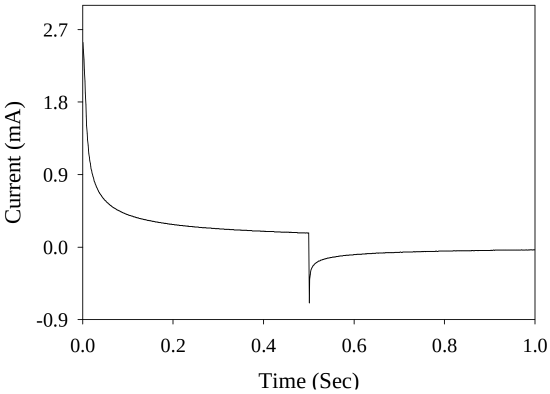

Fig. 2.119: **Current vs time plot for Cd(II) in presence of z. leu**

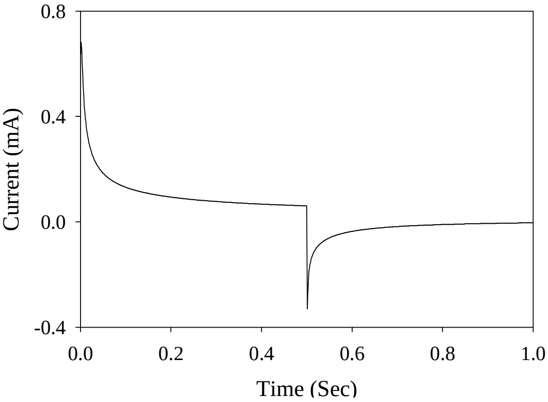

Fig. 2.120: **Current vs time plot for Cd(II) in presence of a. leu**

Now if Q value obtained from time less than τ is plotted against $t^{1/2}$ and on the same graph $-Q_r$ is plotted against $\theta = [\tau^{1/2} + (t-\tau)^{1/2} - t^{1/2}]$, there will be two straight lines which intersects with each other at Q = 0 axis with equal slope, if there is no adsorption of reactant or product. Any deviation from such behavior means adsorption. Such plots are shown in Fig. 2.123 and Fig. 2.124. This shows that the two straight lines do not intersect each other at Q = 0 axis.

Moreover they do not have equal slopes. Therefore, adsorption of reactant or products occurs on the electrode [91-99].

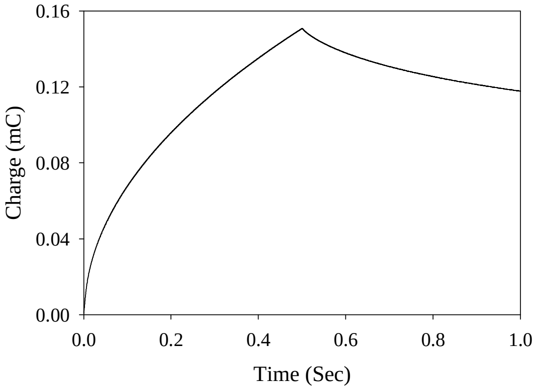

Fig. 2.121: **Charge vs time plot for Cd(II) in presence of z. leu**

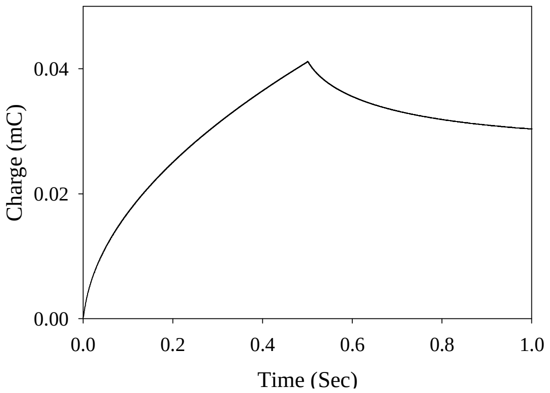

Fig. 2.122: **Charge vs time plot for Cd(II) in presence of a. leu**

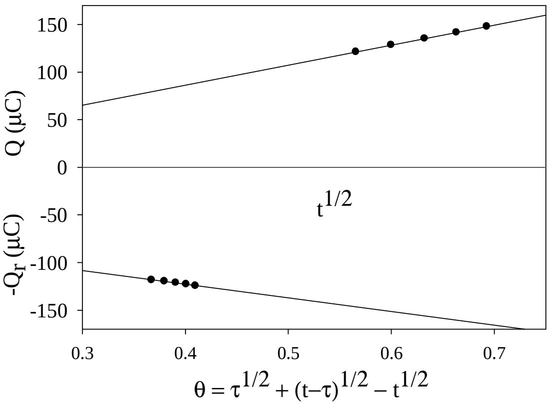

Fig. 2.123: **Plots of Q vs $t^{1/2}$ and $-Q_r$ vs θ for Cd(II) in presence of z. leu**

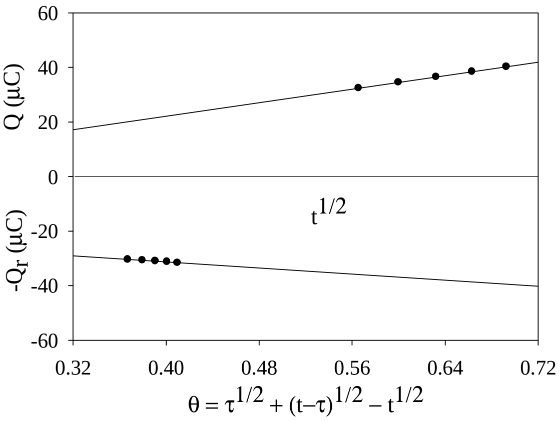

Fig. 2.124: **Plots of Q vs $t^{1/2}$ and $-Q_r$ vs θ for Cd(II) in presence of a. leu**

2.3.6.3 CA and CC study of Cd(II) in presence of isoleucine

Chronoamperometric study of Cd(II) in presence of zwitterionic isoleucine and Cd(II) in presence of anionic isoleucine in 1:2 mol ratio was done. The amperogram are shown in Fig. 2.125 and Fig. 2.126 respectively. The corresponding charge responses are shown in Fig. 2.127 and Fig. 2.128. The response shows that the charges at τ is about 146.08 μC and 36.78 μC for Cd(II)-z. ile and Cd(II)-a. ile system respectively. The value is 163.11 μC for free Cd(II). The charge may be declined due to interaction. Again the charge is drastically declined for Cd(II)-anionic isoleucine system. Therefore, Cd(II)-a. ile interaction may be pronounced over Cd(II)-z. ile interaction.

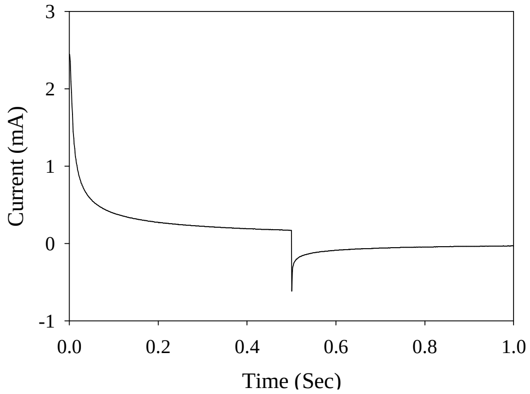

Fig. 2.125: **Current vs time plot for Cd(II) in presence of z. ile**

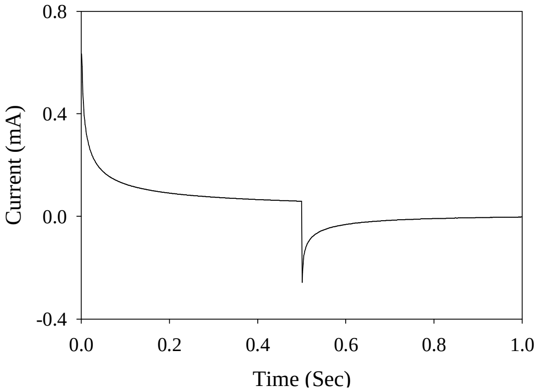

Fig. 2.126: **Current vs time plot for Cd(II) in presence of a. ile**

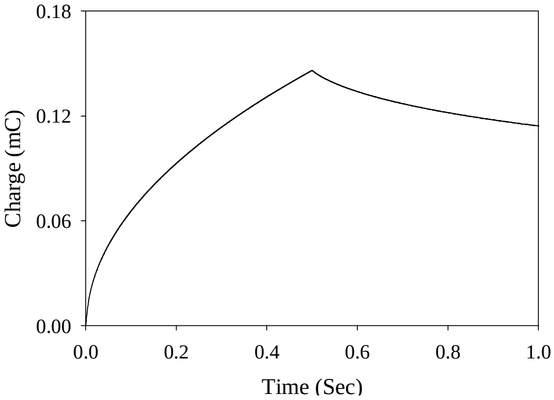

Fig. 2.127: **Charge vs time plot for Cd(II) in presence of z. ile**

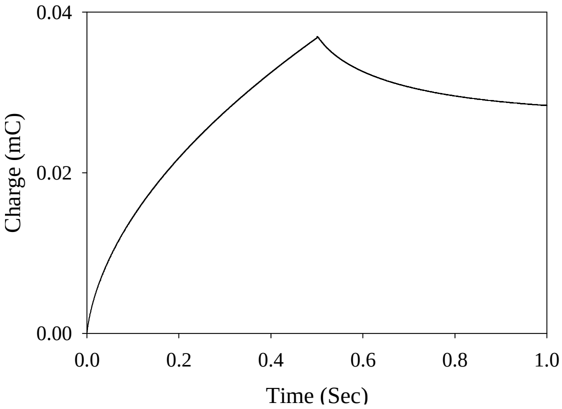

Fig. 2.128: **Charge vs time plot for Cd(II) in presence of a. ile**

Now if Q value obtained from time less than τ is plotted against $t^{1/2}$ and on the same graph $-Q_r$ is plotted against θ, there will be two straight lines which intersects with each other at Q = 0 axis with equal slope, if there is no adsorption of reactant or product. Any deviation from such behavior means adsorption. Such plots are shown in Fig. 2.129 and Fig. 2.130. This shows that the two straight lines do not intersect each other at Q = 0 axis. Moreover they do not have equal slopes. Therefore, adsorption of reactant or products occurs on the electrode [91-99].

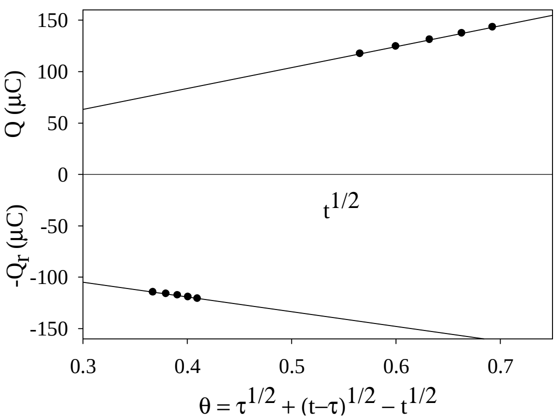

Fig. 2.129: **Plots of Q vs $t^{1/2}$ and $-Q_r$ vs θ for Cd(II) in presence of z. ile**

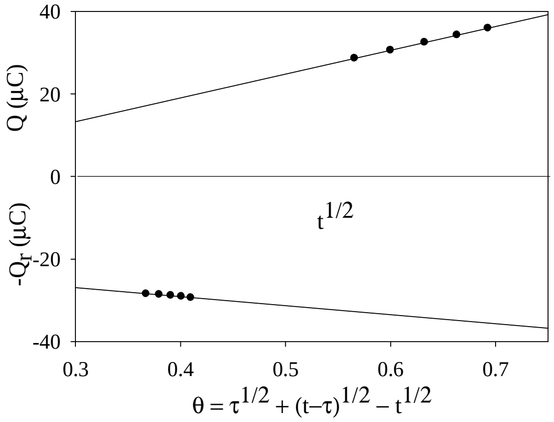

Fig. 2.130: **Plots of Q vs $t^{1/2}$ and $-Q_r$ vs θ for Cd(II) in presence of a. ile**

STUDY OF METAL-LIGAND INTERACTION IN SOLID STATE

3.1 Introduction

The interaction of transition metals with leucine and isoleucine in solution were studied in the earlier chapter. But to understand the interaction more deeply it should be needed to isolate solid products and then characterize the products by different analytical techniques. The metal complexes can be prepared by the reaction between metal ion and the ligand. But sometimes it is not so easy to isolate solid products. To isolate solid product, sometimes the ligand need to be deprotonated or sometimes a secondary ligand need to be added to the reaction mixture. The polarity and pH of the reaction medium often need to change in this purpose.

Various techniques are available to characterize metal complexes. Any new synthesized product should be formulated for further analysis. Elemental (CHN) analysis is the prime tool for the formulation of any new chemical species. The metal analysis is also necessary for the formulation of metal complexes. Mass spectroscopy can be applied to identify the molecular ion in order to determine the molecular weight. The different fragments of the molecule can be studied separately using mass spectroscopy. The purity, thermal stability, melting temperature, crystallization temperature, heat capacity, amount of coordinated water or moisture content in the complexes can better determined by thermal analysis especially thermogravimetry (TG), differential scanning calorimetry (DSC), differential thermal analysis (DTA). The structural elucidation, presence of different functional groups in the complexes can be done by Infra red (IR) and UV-Visible absorption spectroscopy. Infrared spectrum of a compound is actually known as its fingerprint. The nuclear magnetic resonance (NMR) spectroscopy gives idea about the number and nature of protons. If the solid product comes out as crystal, then X-ray diffraction technique can be used to determine the molecular structure.

3.2 Experimental

Materials, methods and equipments

Pure and analytical graded chemicals were used in synthesis work to isolate pure solid product. The glassware used in the preparative process was clean. The instruments used to characterize the product were calibrated before use. The sources of different chemicals, the instruments and brief description of the methods used to prepare and characterize the solid product are described below.

3.2.1 Chemicals: All chemicals, solvents and ligand used in the synthetic and analytical work were analytical grade obtained from E. Merck of Germany, British Drug House (BDH) of England and Sigma-Aldrich Chemical Co. of USA. Water used in all of the experimental processes was de-ionized.

3.2.2 Methods and equipments: Different analytical techniques were used in this work. The theories, experimental setup of the techniques are described on the basis of some standard books.

3.2.2.1 Elemental analysis: Micro analytical data for carbon, hydrogen and nitrogen of the complexes were obtained from laboratory of Organic Structural Chemistry (Prof. Shinmyozu laboratory), Department of Molecular Chemistry, Graduate School of Sciences and IMCE, Kyushu University, Japan.

Fig. 3.1: Elemental (C, H, N) analyzer

3.2.2.2 Metal analysis: Metal content of the complexes were quantitatively determined by complexometric titration using Na_2EDTA solution [100,101]. Direct titration method was followed in all cases.

Table 3.1: Summary of determination of metal content by complexometric titration

Metal ion	Buffer	pH	Indicator	Color Change
Co(II)	Hexamine	6	Xylenol orange	Red to Yellow
Ni(II)	Aq. NH_3/NH_4Cl	7-10	Murexide	Yellow to Violet
Cu(II)	-	-	Fast sulphon black	Purple to green
Zn(II)	Aq. NH_3/NH_4Cl	10	Eriocrome black T	Red to Blue
Cd(II)	Hexamine	5	Xylenol orange	Red to Yellow
Hg(II)	Hexamine	6	Xylenol orange	Red to Yellow

A stock solution was prepared by dissolving complex compound in de-ionized water with the addition of few drops of 0.1 M Nitric acid and was marked to a desired volume with the addition of de-ionized water. A known volume of the prepared solution was taken, adjusted to desired pH with a suitable buffer and then titrated with standard Na_2EDTA solution in presence of a suitable indicator. The end point was determined by detecting the color change of the solution. Calculation of the metal content has done from equivalence relationship. The procedure of determination of metal content in the complexes is summarized in Table 3.1.

3.2.2.3 Preparation of indicators: The preparation of the indicators [100] used to determine the metal content in the complexes were,

Murexide: This indicator solution was prepared by suspending 0.5 g of the powdered dyestuff in water, shaking thoroughly, and allowing the undissolved portion to settle. The saturated supernatant liquid was used for titrations.

Eriochrome black T: This indicator solution is prepared by dissolving 0.2 g of the dyestuff in 15 mL of triethanolamine with the addition of 5 mL of absolute ethanol to reduce the viscosity.

Fast sulphon black F: This indicator solution consists of 0.5 % aqueous solution of sodium salt of 1-hydroxy-8-(2-hydroxynaphthylazo)-2-(sulphonaphthylazo)-3, 6-disulphonic acid.

3.2.2.4 Chloride (Cl^-) ion test: Chloride content of all the complexes were qualitatively tested by $AgNO_3$ solution. A stock solution was prepared by dissolving complex compounds in de-ionized water with the addition of few drops of dilute nitric acid and the solution was warmed. About 2-3 mL of the solution was taken in a test tube and few drops of $AgNO_3$ solution was added to the solution.

3.2.2.5 Solubility test: The solubility of all compounds was examined (qualitatively) in water and some common organic solvents such as methanol, ethanol, acetone and dimethylformamide (DMF).

3.2.2.6 Melting point determination: The melting point of all the complexes were measured in a heating device, MEL-TEMP II, Laboratory Devices made in USA with a thermometer.

3.2.2.7 Infrared spectral analysis: Infrared spectrum is used to characterize structural information about a molecule. Each type of bond has its own different natural frequency of vibration and two of the same type of bond in two different compounds is in two slightly different environments. So, no two molecules of different structure have exactly the same infrared absorption pattern. Thus, infrared spectrum can be used for molecules much as a fingerprint can be used for humans [102-104].

Only those bonds that have a dipole moment that changes as a function of time are capable of absorbing infrared radiation. The changing electrical dipole of the bond can then couple with the sinusoidally changing electromagnetic field of the incoming radiation.

A diatomic molecule can be considered as two vibrating masses connecting by a spring. Whenever the spring is stretched or compressed beyond the equilibrium distance, the potential energy of the system increases. As for any harmonic oscillator, whrn a bond vibrates, its energy of vibration is continually and periodically changing from kinetic to potential energy and back again. The total amount of energy is proportional to the frequency of the vibration, $E_{osc} \propto h\upsilon_{osc}$

which for a harmonic oscillator is determined by the force constant (K) of the spring or its stiffness and the masses (m_1 and m_2) of the two bonded atoms. The natural frequency of vibration of a bond derived from Hook's law for vibrating springs is given by the equation,

$$\overline{\nu} = \frac{1}{2\pi c}\left(\frac{K}{\mu}\right)^{1/2}$$

where, K is force constant, c is velocity of light and υ is the reduced mass of the system.

$$\mu = \frac{m_1 m_2}{m_1 + m_2}$$

This equation can be used to calculate the approximate position of a band in the infrared spectrum.

3.2.2.7.1 Instrumentation of infrared spectral analysis: Infrared spectrum of the complexes were recorded on a calibrated Fourier Transformation Infrared Spectrophotometer (Shimadzu FTIR IR prestige-21 S/N) in the range 500-4500 cm^{-1} as KBr pellets at Department of Chemistry, University of Dhaka, Bangladesh. The KBr disk was prepared by mixing and grinding uniformly a small amount of sample (0.1% - 0.2%) with dry and pure KBr, then compressing the powder in a special metal under pressure.

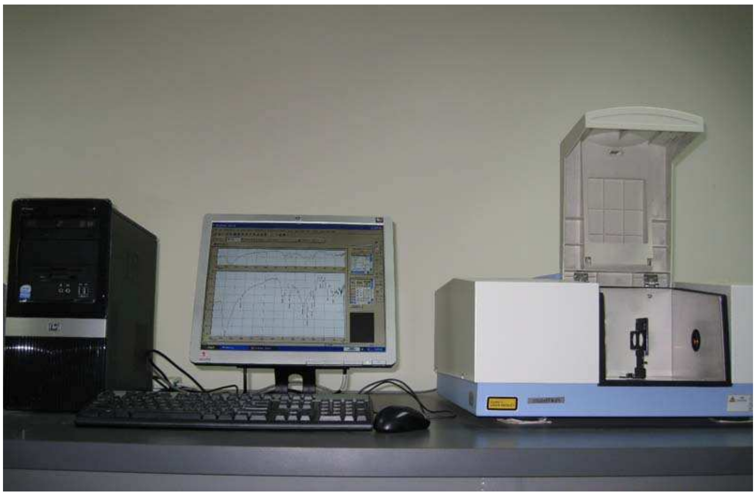

Fig. 3.2: Fourier Transformation Infrared Spectrophotometer

3.2.2.8 Electronic spectral analysis: Most organic molecules and functional groups are transparent in the portions of the electromagnetic spectrum which we call the ultraviolet (UV) and visible (Vis) regions that is the regions where wavelengths range from 190 nm to 800 nm. When continuous radiation passes through a transparent material, then two different phenomenons arises depending on absorption or reflection of radiation. The phenomenon are described below on the basis of some standard books [102-106].

3.2.2.8.1 UV-Visible absorption spectral analysis: When continuous radiation passes through a transparent material, a portion of the radiation may be absorbed. If that occurs, the residual radiation, when it is passed through a prism, yields a spectrum with gaps in it, called an absorption spectrum. As a result of energy absorption, atoms or molecules pass from a state of low energy to a state of high energy. Fig. 3.3 depicts the excitation process, which is quantized.

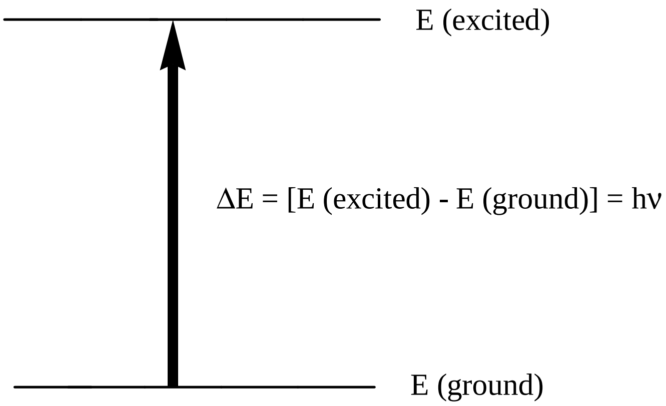

Fig. 3.3: The excitation of electron from lower to higher energy state

The electromagnetic radiation that is absorbed has energy exactly equal to the energy difference between the excited and ground states. In the case of ultraviolet and visible spectroscopy, the transitions that results from the absorption of electromagnetic radiation in this region of the spectrum are transitions between electronic energy levels. As a molecule absorbs energy, an electron is promoted from an occupied orbital to an unoccupied orbital of greater potential energy. Generally the most probable transition is from highest occupied molecular orbital (HOMO) to lowest unoccupied molecular orbital (LUMO). The absorption of UV or visible radiation corresponds to the excitation of outer electrons. There are three types of electronic transition which can be considered;

(i) Transitions involving p, s, and n electrons
(ii) Transitions involving charge-transfer electrons
(iii)Transitions involving *d* and *f* electrons

Possible electronic transitions of p, s and n electrons are:

(a) *$\sigma \rightarrow \sigma^*$ transitions:* Molecules which contain nothing but single bonds and lack atoms with unshared electron pairs, the only transitions possible are of the $\sigma \rightarrow \sigma^*$ type. In alkanes this type of transition occurs. These transitions are of such a high energy that they absorb ultraviolet energy at very short wavelengths.

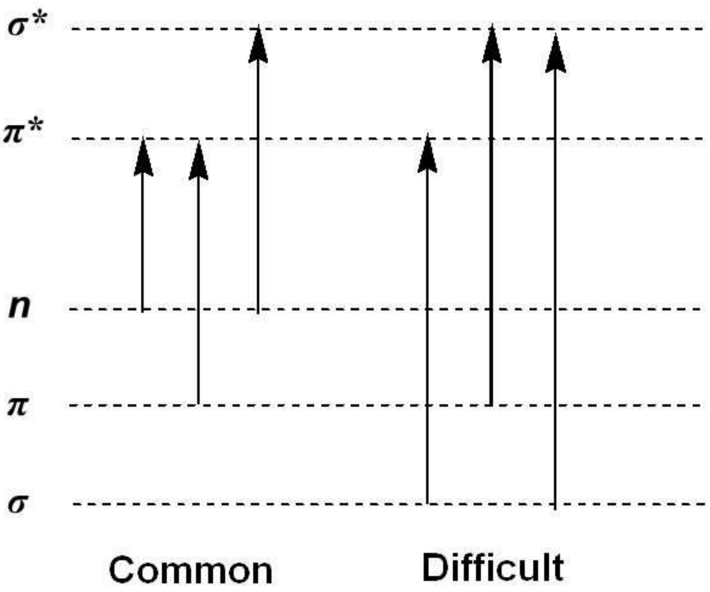

Fig. 3.4: Possible transition of electrons at different electronic energy levels

(b) *n → σ* transitions:* In saturated molecules that contain atoms bearing nonbonding pairs of electrons, transitions of the *n → σ** type become important. This transition is found in molecules such as water, alcohols, ethers, amines and sulfur compounds.

(c) *π → π* transitions:* Molecules possessing double or triple bonds involve with π → π* transition. Such transitions occur in olefins, dienes, and aromatic systems.

(d) *n → π* transitions:* Unsaturated molecules that contain atoms such as oxygen or nitrogen may also undergo n → π* transitions. These are perhaps the most interesting and most studied transitions, particularly among carbonyl compounds.

Charge-transfer transitions usually appear in light absorption of inorganic molecules. For a molecule to allow a charge transfer transition must have a component (atom or group) able to donate an electron and another component must be able to accept an electron. The absorption of radiation involves an electron transfer from a donor orbital to an acceptor orbital. Charge transfer transitions are common in metal-ligand complexes. Typical charge transfer transitions are, transfer of an electron from a metal orbital to a ligand orbital (MLCT) and transfer of an electron from a ligand orbital to a metal orbital (LMCT).

The d-d transitions arise from transitions between the d orbitals of the metal that have been split in a ligand field; they are also known as d-d spectra.

3.2.2.8.2 UV-Visible diffuse reflectance spectral analysis: UV-Visible diffuse reflectance spectroscopy is an optical technique which describes the electronic behavior present in the structure of the solid. This technique concerns with the relative change in the amount of reflected light off of a surface. Diffuse reflectance spectra are taken for measuring the band gap energy. The separation between the energy of the lowest conduction band and that of the highest valence band is called the band gap, energy gap or forbidden energy gap (E_g). The semiconductor properties of a solid are strongly affected by the E_g parameter. Eg can be determined by applying the Kubelka-Munk (K-M or F(R)) method [107]. The K-M method is based on the following equation:

$$F(R) = (1-R)^2/2R \qquad \text{(i)}$$

Where R is the reflectance, F(R) is proportional to the extinction coefficient (α).

The modified K-M function is, $(F(R) * h\nu)^n$ (ii)

The band gap energy is determined by plotting this equation as a function of energy in eV and then extrapolating the slope to $\alpha = 0$. Where $n=2$.

3.2.2.8.3 Instrumentation of electronic spectral analysis: The electronic spectrum of the complexes were recorded on a Shimadzu UV-Visible recording spectrophotometer (UV-1800A), in the wavelength 190 nm - 1100 nm at Department of Chemistry, University of Dhaka, Bangladesh.

Fig. 3.5: Shimadzu UV-Visible spectrophotometer (UV-1800)

3.2.2.9 Nuclear magnetic resonance (NMR) spectroscopy: Nuclear magnetic resonance has been playing an important role in the fields of physical techniques available to the chemist for years. It is becoming a more and more useful method to probe the structure of molecules. Nuclear magnetic resonance, NMR, is a physical phenomenon of resonance transition between magnetic energy levels, happening when atomic nuclei are immersed in an external magnetic field and applied an electromagnetic radiation with specific frequency. By detecting the absorption signals, one can acquire NMR spectrum. According to the positions, intensities and fine structure of resonance peaks, people can study the structures of molecules quantitatively [102, 103].

Many atomic nuclei have a property called spin. The more common nucleus that possesses spin is proton. In the absence of applied magnetic field, all the spin states of the nucleus are of equivalent energy, i.e degenerate. But in an applied magnetic field the spin states are not degenerate. A hydrogen nucleus may have a clockwise (+ ½) or anticlockwise (- ½) spin, and the nuclear magnetic moments (μ) in the two cases are pointed in opposite directions. In an applied magnetic field all protons have their magnetic moments either aligned with the field or opposed to it which is illustrated in Fig. 3.6.

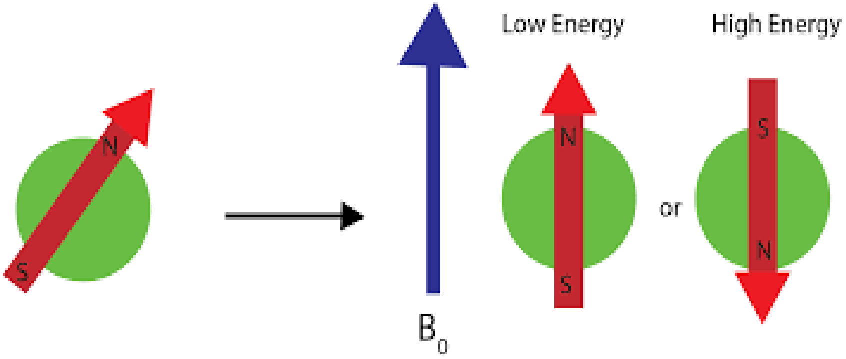

Fig. 3.6: The two allowed spin states of a proton

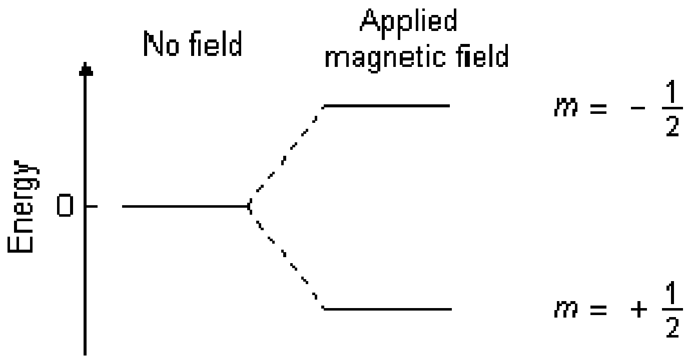

Fig. 3.7: The spin states of a proton in absence and in presence of applied magnetic field

The spin state + ½ is of lower energy since it is aligned with the field, while the spin state – ½ is of higher energy since it is opposed to the applied field. The nuclear magnetic resonance phenomenon occurs when nuclei aligned with an applied field are induced to absorb energy and change their spin orientation with respect to the applied field.

When the magnetic field is applied, the nucleus begins too precess about its own spin axis with angular frequency ω, called Larmor frequency. The frequency of precession is directly proportional to the applied magnetic field. The precession generates an oscillating electric field of the same frequency. If radiofrequency waves of this frequency are supplied to the precissing proton, the energy can be absorbed causing a spin change, called resonance.

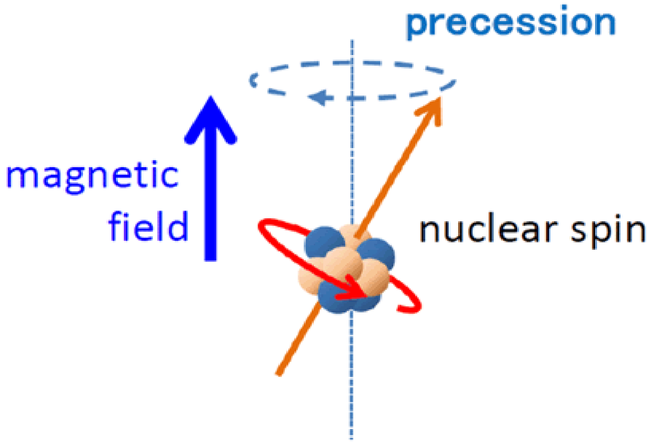

Fig. 3.8: The precession of a spinning nucleus in presence of an applied magnetic field

3.2.2.9.1 Instrumentation of nuclear magnetic resonance (NMR) spectral analysis: The NMR spectrum of the complexes were recorded on a Bruker NMR spectrometer in methanol solution at Wazed Miah Science Research Center, Jahangirnagar University, Bangladesh.

Fig. 3.9: Bruker NMR spectrometer

3.2.2.10 Thermal analysis (TA): Thermal methods of analysis are those techniques in which changes in physical and/or chemical properties of a substance are measured as a function of temperature [100]. Thermo gravimetry (TG) and Differential Scanning Calorimetry (DSC) are important among the thermal techniques. The thermo-gravimetric analysis is a dynamic technique based on the change in the weight of a substance recorded as the function of temperature or time. DSC is a technique in which the difference in energy inputs into a substance and a reference material is measured as a function of temperature whilst the substance and reference material are subjected to a controlled temperature programme.

The thermal analysis is applied for the determination of the purity, thermal stability, and mode of decomposition and composition of complex mixtures. It gives an idea about the bond strength of various constituent parts of the complex.

3.2.2.10.1 Instrumentation of thermal analysis: The thermo gravimetric (TG) and differential scanning calorimetry (DSC) analysis of the complexes was carried out with a simultaneous thermal analyzer (NETZSCH STA 449F3 STA449F3A-1311-M) at Bangladesh Council of Scientific and Industrial Research (BCSIR), Dhaka, Bangladesh.

Fig. 3.10: Thermo gravimetric analyzer

About 10 mg of the sample to be examined was taken in an alumina cell and was kept in the furnace of the analyzer by means of a pan. The thermal decomposition of the complexes was recorded in nitrogen atmosphere from room temperature to 900 ^{o}C with a temperature rate 10 ^{0}C/minute.

3.2.2.11 Magnetic properties: The magnetic susceptibility of a complex provides different significant information's about the transition metal complexes e.g. assignment of the oxidation state of the transition metal, steriochemical information's, information concerning ligand field strength, antiferromagnetic interactions in dimmers and polymers, effect of ligands on magnetic behavior and the criterion of purity or contamination of the complex to be examined [108-112].

The magnetic and electrical properties of molecules are analogues. For instance, some molecules possess permanent magnetic dipole moments, and an applied magnetic field can induce a magnetic moment. The analogue of the electric polarization P is the magnetization M, the magnetic dipole moment per unit volume. The magnetization in the presence of a field strength H is proportional to H and we may write

$$M = \chi H \qquad (1)$$

where χ is the dimensionless volume magnetic susceptibility.

A closely related quantity is the molar magnetic susceptibility, χ_m

$$\chi_m = \chi V_m \qquad (2)$$

where V_m is the molar volume of the substance. Materials for which χ is positive are called paramagnetic; those for which χ is negative are called diamagnetic. The following general expression for mass susceptibility, χ_g in cgs units can be derived as for the Gouy method.

$$\chi_g = (1/m) [C (R - R_0) + \chi_{vair} * A] \qquad (3)$$

where, C = a constant of proportionality, R = the reading obtained for tube and sample , R_0 = the empty tube reading (normally a negative value), l = the sample length (in cm), m = the sample mass (in gm), A = the cross sectional area of the tube (in cm^2), χ_{vair} = the volume susceptibility of the displaced air.

For powdered sample the air correction term, χ_{vair} x A, may be ignored. The constant of proportionality, C is related to the balance calibration constant (C_{Bal}) of a given balance by the formula

$$C = C_{Bal}/ 10^9 \qquad (4)$$

Therefore the eqn. (3) can be expressed as

$$\chi_g = [C_{Bal} * l * (R - R_0)]/10^9 * m \qquad (5)$$

The molar susceptibility

$$\chi_m = \chi_g * MW \qquad (6)$$

where, MW = Molecular weight of the substance.

For compounds containing a paramagnetic ion, χ_m will be less than the susceptibility per gram atom of paramagnetic ion, χ_A, because of the diamagnetic contribution of the other groups or ligand present. When the diamagnetic contribution is negligible

$$\chi_A = [\{C_{Bal} * l * (R - R_0)\}/10^9 * m] * MW \qquad (7)$$

For paramagnetic metal ion, the effective magnetic moment, μ_{eff} in Bohr magnetrons (BM) is

$$(\mu_{eff})^2 = (3kT\,\chi_A) / N\beta^2 \qquad (8)$$

where, N = Avogadro number, β = The Bohr magnetron, k = Boltzmann's constant, T = Absolute temperature. Hence,

$$\mu_{eff} = 2.828 \sqrt{}(T * \chi_A) \qquad (9)$$

For compounds containing unpaired electrons, both the spin angular momentum and the orbital angular momentum of the electrons can contribute to the observed paramagnetism. However, for a complex of transition metal ions, the orbital contribution is largely quenched by the field due to the surrounding ligands. In this case we have the simple spin-only formula,

$$\mu_{eff} = \sqrt{}[n(n+2)]\ BM \qquad (10)$$

where n = number of unpaired electrons.

3.2.2.11.1 Instrumentation of magnetic property analysis: The magnetic properties of the complexes were studied at ambient temperature on a magnetic susceptibility balance, Magway MSB Mk1 Sherwood Scientific Ltd, Cambridge, England at Department of Chemistry, University of Dhaka, Bangladesh.

Fig. 3.11: Magway MSB Mk1 magnetic susceptibility balance

The magnetic susceptibility balance was calibrated first using standard sample tube and the balance calibration constant, C_{Bal} was measured. Then the sample (blended uniform powder) to be examined was packed introducing into the cleaned, dried and previously weighed sample tube, and the bottom of the tube was taped gently on a wooden bench a number of times to settle the solid particulates. This procedure was repeated until a sufficient amount of sample was added corresponding to a sample length, *l*, in the range 1.5 to 2.0 cm was recommended. The sample mass, m in grams and the sample length, *l* in cm were noted simultaneously. The packed sample tube was placed into sample guide and was taken the reading; R. Using these readings molar susceptibility and magnetic moment were calculated.

3.2.3 Preparation of the complexes

The complexes were prepared in aqueous medium by mixing the chloride salt of metal with the anionic ligand in 1:1 mol ratio. To do so, about 10 mmol ligand was boiled with 10 mmol $NaHCO_3$. The mixture was then filtered. The resultant solution then added to 10 mmol metal salt solution with stirring. Immediately a precipitate was formed. The precipitate was then filtered, washed and dried over silica gel. The products were stable in light and air. It was not possible to isolate Mn and Fe complex because of hydrolysis of the respective metal salt in the anionic ligand solution.

$HgCl_2$ dissolves in hot water but precipitated when cooled. Therefore there is a probability to remain unreacted $HgCl_2$ in the Hg complex. That's why $HgCl_2$ was mixed with the anionic ligand in 1:2 mol ratios. The product formed was washed with boiled water several times so that no unreacted $HgCl_2$ remains in the complex.

The reaction scheme is presented as the following equation.

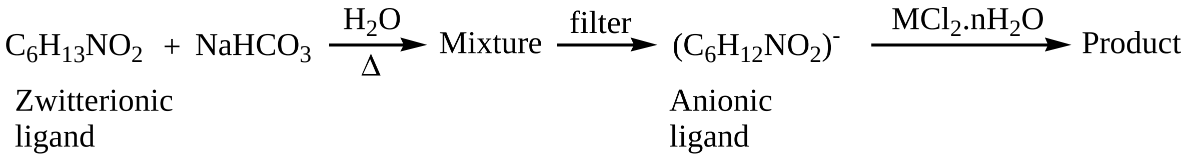

$$\underset{\text{Zwitterionic ligand}}{C_6H_{13}NO_2} + NaHCO_3 \xrightarrow[\Delta]{H_2O} \text{Mixture} \xrightarrow{\text{filter}} \underset{\text{Anionic ligand}}{(C_6H_{12}NO_2)^-} \xrightarrow{MCl_2.nH_2O} \text{Product}$$

where M(II) = Co(II), Ni(II), Cu(II), Zn(II), Cd(II), Hg(II) and Pb(II).

3.3 Results and discussions

In the present study the metal complexes are characterized by different analytical techniques. Among the techniques, spectroscopy plays the important role. Several spectroscopic techniques like IR, UV-Visible, NMR were applied to study the structural features of the complexes. Elemental and metal analysis was done to formulate the complexes. Thermal analysis was done to determine the thermal stability and the composition of the complexes.

3.3.1 Characterization of the metal-leucine complexes

The complexes were prepared by direct reaction between aqueous solution of the metal salt and anionic leucine (section 3.2.3). The precipitate formed was filtered, washed and dried over silica gel.

3.3.1.1 Formulation

Elemental analysis is the prime tool for the formulation of any new chemical species. The formulation of the prepared complexes were done by comparing the elemental (C, H and N) and metal analysis data and the calculated values.

3.3.1.1.1 Elemental analysis: Microanalysis for carbon, hydrogen, nitrogen in the complexes of leucine was performed in an elemental micro analyzer. Metals were estimated by complexometric titration method using ordinary laboratory glassware. Chloride content of all the complexes was qualitatively tested by using $AgNO_3$ solution. The complexes didn't respond to this test. Thus chloride is absent in the complexes.

Comparing all the experimental data and theoretical values the proposed empirical formula of the complexes are,

Co- Leucine complex	$Co(C_6H_{12}NO_2)_2.2H_2O$
Ni- Leucine complex	$Ni(C_6H_{12}NO_2)_2.2H_2O$
Cu- Leucine complex	$Cu(C_6H_{12}NO_2)_2$
Zn- Leucine complex	$Zn(C_6H_{12}NO_2)_2$
Cd- Leucine complex	$Cd(C_6H_{12}NO_2)_2$
Hg- Leucine complex	$Hg(C_6H_{12}NO_2)_2$

The C, H, N data does not confirm the formation of Pb complex. The percent composition of carbon, hydrogen, nitrogen and metal of the complexes are tabulated in Table 3.2.

Table 3.2: Percent composition of C, H, N and metal in the metal-leucine complexes

Compound	% C		% H		% N		% Metal		% Yield based on metal
	Fnd.	Cal.	Fnd.	Cal.	Fnd.	Cal.	Fnd.	Cal.	
$Co(C_6H_{12}NO_2)_2.2H_2O$	40.45	40.57	8.07	7.89	7.90	7.89	16.50	16.60	54
$Ni(C_6H_{12}NO_2)_2.2H_2O$	40.34	40.60	7.98	7.89	7.80	7.89	15.65	16.55	50
$Cu(C_6H_{12}NO_2)_2$	43.35	44.51	7.16	7.42	8.45	8.65	17.92	19.63	67
$Zn(C_6H_{12}NO_2)_2$	43.88	44.25	7.56	7.37	8.56	8.60	19.11	20.10	81
$Cd(C_6H_{12}NO_2)_2$	37.52	38.67	5.95	6.44	7.10	7.52	28.23	30.18	65
$Hg(C_6H_{12}NO_2)_2$	30.96	31.26	5.10	5.21	5.90	6.08	42.60	43.55	55
$Pb(C_6H_{12}NO_2)_2$	1.58	30.82	0.77	5.14	3.10	5.99	-	44.35	-

Cal. = Calculated, Fnd. = Found

3.3.1.2 Physicochemical properties

The solubility, melting temperature of the complexes were conducted which are described below.

3.3.1.2.1 Solubility: Solubility of a compound actually depends on the mode of interaction between solute and solvent molecule, lattice energy, solvation energy and temperature. Solubility of the complexes was investigated qualitatively at room temperature in some common solvents such as water, methanol, ethanol, acetone, DMSO and is shown in Table 3.3. The solubility analysis of the complexes indicates that they are insoluble in most of the common solvents. The lattice enthalpy of the complexes may be higher than the solvation energy of the solvents or it may be due to the formation of strong M-O and M-N coordination bond in the complexes or may be due to the presence of a hydrocarbon tail in the ligand part which is the main obstacle for the solvation of the complexes in the mentioned solvents.

Table 3.3: Solubility of the prepared metal-leucine complexes

Compound	Appearance	Soluble in	Insoluble in
$Co(C_6H_{12}NO_2)_2.2H_2O$	Pink	-	H_2O, CH_3OH, C_2H_5OH, CH_3COCH_3, DMSO
$Ni(C_6H_{12}NO_2)_2.2H_2O$	Sky blue	CH_3OH	H_2O, C_2H_5OH, CH_3COCH_3, DMSO
$Cu(C_6H_{12}NO_2)_2$	Blue	-	H_2O, CH_3OH, C_2H_5OH, CH_3COCH_3, DMSO
$Zn(C_6H_{12}NO_2)_2$	Colorless	-	H_2O, CH_3OH, C_2H_5OH, CH_3COCH_3, DMSO
$Cd(C_6H_{12}NO_2)_2$	Colorless	-	H_2O, CH_3OH, C_2H_5OH, CH_3COCH_3, DMSO
$Hg(C_6H_{12}NO_2)_2$	Colorless	-	H_2O, CH_3OH, C_2H_5OH, CH_3COCH_3, DMSO

3.3.1.2.2 Melting temperature: The temperature at which the solid and the liquid phases of a compound are in equilibrium under a pressure of one atmosphere is referred to as the melting point of the solid compound. Ionic compound has higher melting point than covalent one. The melting temperatures of the complexes are given in Table 3.4. Melting point of the complexes are more than 250 ^{0}C. The high melting point may be due to the ionic character of the complexes or may be due to the presence of strong M-L bond.

Table 3.4: Melting temperature of prepared metal-leucine complexes

Compound	Melting temperature (^{0}C)
$Co(C_6H_{12}NO_2)_2.2H_2O$	>250 ^{0}C
$Ni(C_6H_{12}NO_2)_2.2H_2O$	>250 ^{0}C
$Cu(C_6H_{12}NO_2)_2$	>250 ^{0}C
$Zn(C_6H_{12}NO_2)_2$	>250 ^{0}C
$Cd(C_6H_{12}NO_2)_2$	>250 ^{0}C
$Hg(C_6H_{12}NO_2)_2$	>250 ^{0}C

3.3.1.3 Infrared spectral analysis

The compounds having covalent bonds will be found to absorb various frequencies of electromagnetic radiation in the infrared (IR) region of the spectrum. The IR spectrum originates from the different modes of vibration of a molecule due to the absorption of radiation energy in the IR region. However, it is essential that a change in dipole moment occurs during the vibration. In the absorption process, those frequencies of IR radiation will be absorbed which match the natural vibrational frequencies of the molecule. Since every different type of bond has a different frequency of vibration, and since the same type of bond in two different compounds is in a different environment, no two molecules of different structure will have exactly the same infrared absorption pattern. This is why IR spectrum is a very authentic identity of the compounds which are IR active. Another more important use of the IR spectrum is that it gives structural information about a molecule.

In the present study, a calibrated Fourier Transform Infrared (FTIR) spectrophotometer has been used to record the IR spectrum of the complexes. The design of the optical pathway produces a pattern called an interferogram. An interferogram is essentially a plot of intensity vs time (a time domain spectrum). A mathematical operation known as a Fourier Transform (FT) can separate the individual absorption frequencies from the interferogram, producing a spectrum virtually identical to that obtained with a dispersive spectrometer. There are, however, great advantages in the use of FTIR because all the frequencies are recorded simultaneously; there is an improvement in signal-to-noise (S/N) ratios, and it is easier to study small samples or materials with weak absorptions. In addition to this, the time taken for a full spectral scan is less than 1 second and this makes it possible to obtain improved spectra by carrying out repetitive scans and averaging the collected signals. This is because the S/N ratio is directly related to $\sqrt{n}$, where n is the number of scans. The tentative band assignments have been made empirically on the basis of some standard books [102-104].

3.3.1.3.1 IR spectrum of leucine: The FTIR spectrum of leucine is shown in Fig. 3.12. All the vibrational frequencies and their tentative band assignments are listed in Table 3.5. A weak broad peak at 3070 cm^{-1} is due to N-H stretching vibration of NH_3^+ group. The C-H stretching vibration appears at 2960 cm^{-1}. Asymmetric and symmetric stretching vibrations for carboxyl group (COO^-) occur at 1575 and 1400 cm^{-1}. Asymmetric and symmetric N-H bending vibration appears at 1610 cm^{-1} and 1510 cm^{-1}. A sharp peak at 1080 cm^{-1} appears due to C-N stretching.

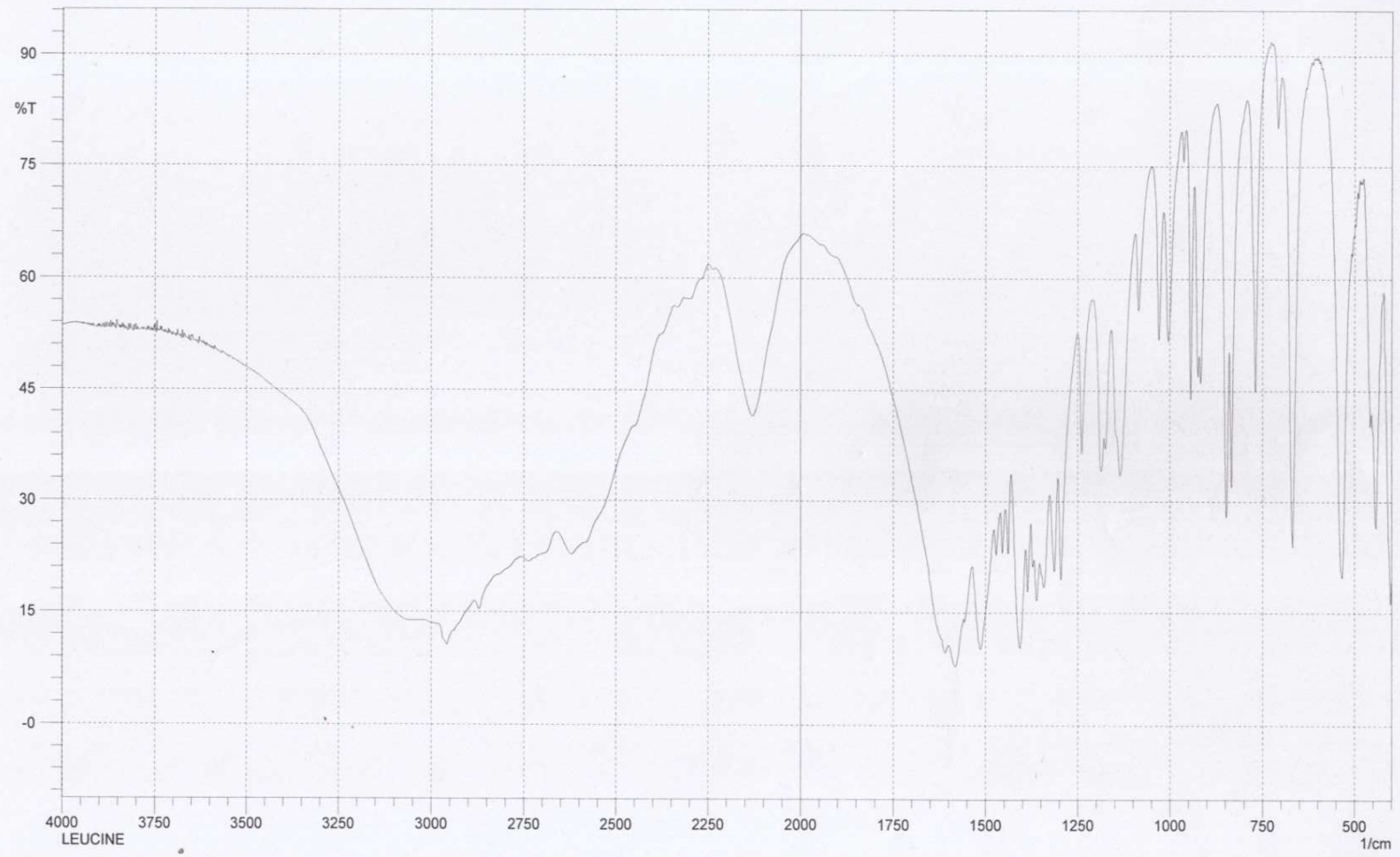

Fig. 3.12: FTIR spectrum of leucine ($C_6H_{13}NO_2$)

Table 3.5: Tentative assignment of IR bands of leucine ($C_6H_{13}NO_2$)

Wave no. (cm^{-1})	Relative intensity	Tentative band assignment
3070	w, b	$^+NH_3$ stretching
2960	w, sh	-C-H stretching
2125	ms, sp	
1610	w, sh	Asymmetric N-H bending
1575	w, sp	Asymmetric COO^- stretching
1510	ms, sp	Symmetric N-H bending
1400	ms, sp	symmetric COO^- stretching
1350	m, sp	
1300	m, sp	
1240	m, sp	
1175	m, sp	
1125	ms, sp	
1080	m, sp	C-N stretching
1025	m, sp	
1000	m, sp	
940	ms, sp	
850	S, sp	
760	ms, sp	
660	s, sp	
550	s, sp	
450	ms, sp	
400	s, sp	

vs = very strong, s = strong, ms = medium strong, m = medium, w = weak, sp = sharp, b = broad, sh = shoulder

3.3.1.3.2 IR spectrum of leucine complexes: The FTIR spectrum of metal-leucine complexes are shown in Fig. 3.13 to Fig. 3.19. All the vibrational frequencies and their tentative band assignments are listed in Table 3.6 to Table 3.11. In all the complexes two sharp bands between 3100-3360 cm^{-1} appears due to N-H stretching vibration for the free –NH_2 group.. The C-H stretching vibration appears at 2950 to 2975 cm^{-1}. Two sharp peak ataround 1575 and 1400 cm^{-1} appears due to asymmetric and symmetric stretching vibrations for carboxyl group (COO^-). Asymmetric and symmetric N-H bending vibration appears at around 1600 cm^{-1} and 1500 cm^{-1}. At around 1100 cm^{-1} C-N stretching vibration appears as a sharp band. In few cases the N-H bending and $–COO^-$ group stretching vibrations overlap with each other and appears as a single band. The pattern of the IR spectrum of the complexes is almost similar with each other with few exceptions. Most of the important bands in all the complexes were shifted significantly compare to that of leucine which indicate the formation of new compound. The intensity of bands in the complexes has been changed in most of the cases comparing the intensity of bands found in the free ligand. The IR spectrum does not confirm the formation of Pb complex.

Table 3.6: Tentative assignment of IR bands of $[Co(C_6H_{12}NO_2)_2.2H_2O]$

Wave no. (cm^{-1})	Relative intensity	Tentative band assignment
3360	s, sp	Asymmetric N-H stretching
3300	m, sp	Symmetric N-H stretching
2950	s, sp	-C-H stretching
2875	m, sp	
1625	s, b	Asymmetric N-H bending and
		Asymmetric COO^- stretching
1475	ms, sp	Symmetric N-H bending
1400	s, sp	symmetric COO^- stretching
1300	ms, sp	
1125	m, sp	
1100	ms, sp	C-N stretching
1050	ms, sp	
980	m, sp	
760	m, sp	
600	m, sp	

vs = very strong, s = strong, ms = medium strong, m = medium, w = weak, sp = sharp, b = broad, sh = shoulder

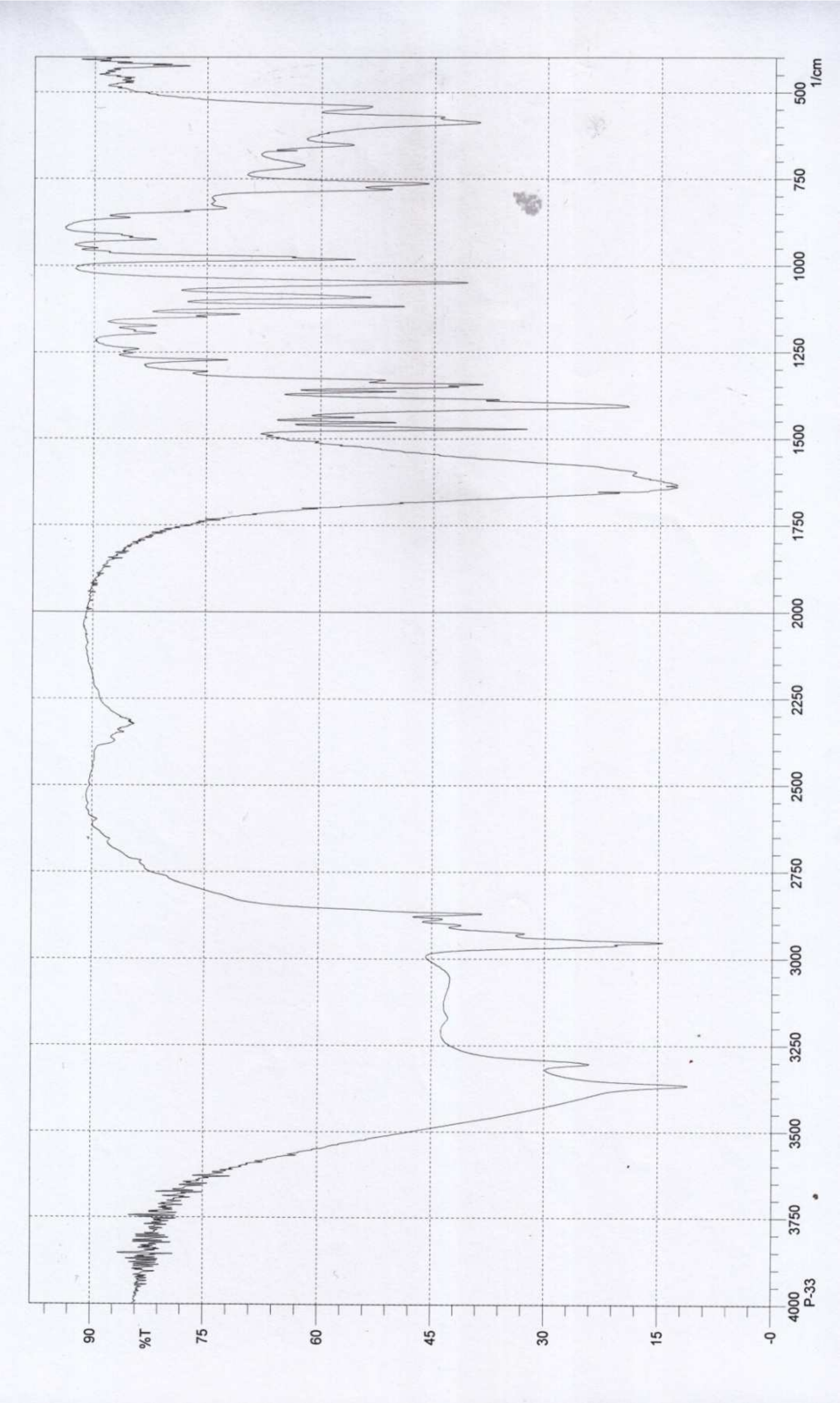

Fig. 3.13: FTIR spectrum of $Co(C_6H_{12}NO_2)_2.2H_2O$

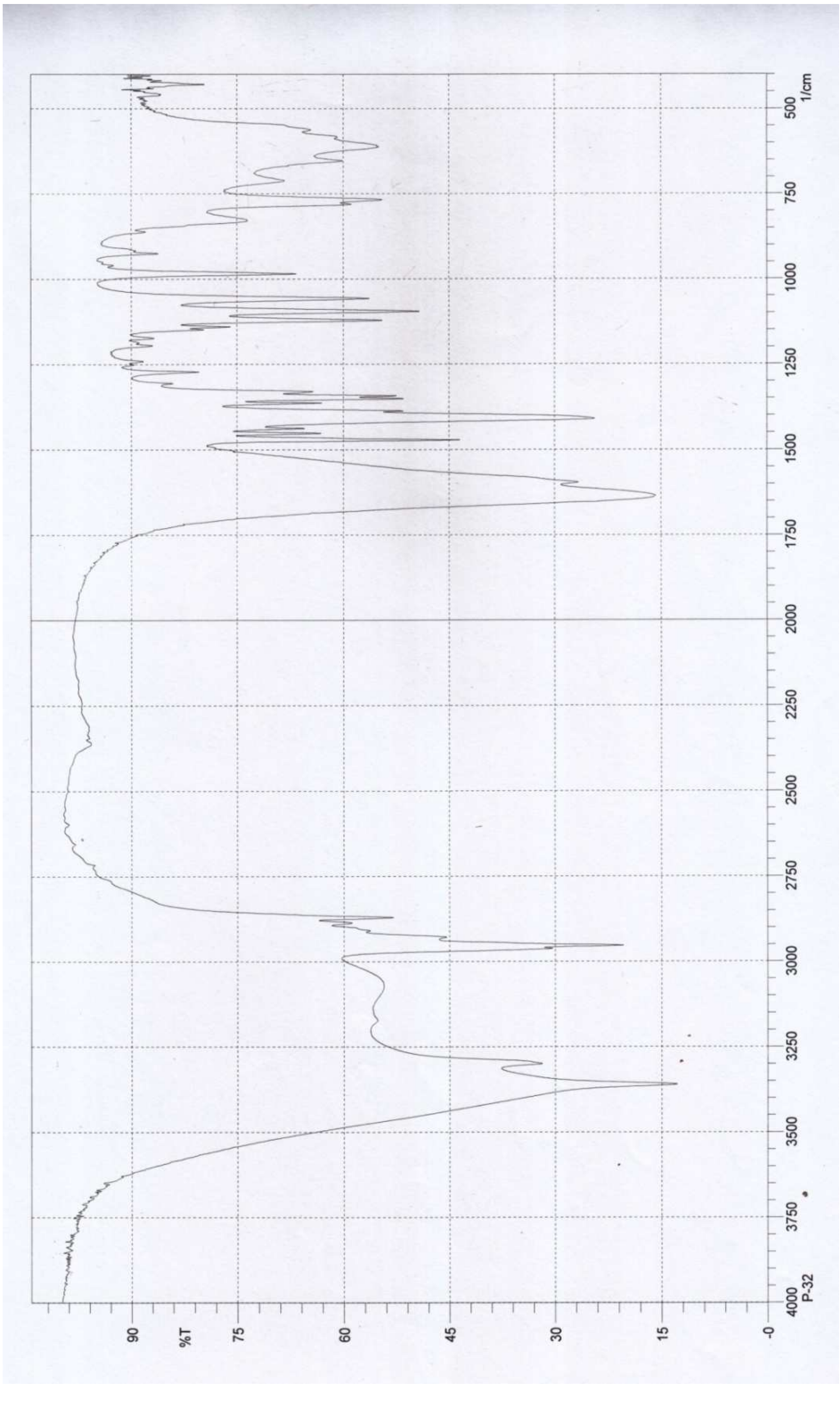

Fig. 3.14: FTIR spectrum of $Ni(C_6H_{12}NO_2)_2.2H_2O$

Table 3.7: Tentative assignment of IR bands of $Ni(C_6H_{12}NO_2)_2.2H_2O$

Wave no. (cm^{-1})	Relative intensity	Tentative band assignment
3360	s, sp	Asymmetric N-H stretching
3300	w, sp	Symmetric N-H stretching
2950	s, sp	-C-H stretching
2875	m, sp	
1640	s, sp	Asymmetric N-H bending
1580	w, sh	Asymmetric COO^- stretching
1475	ms, sp	Symmetric N-H bending
1410	s, sp	symmetric COO^- stretching
1346	m, sp	
1125	ms, sp	
1100	ms, sp	C-N stretching
1060	ms, sp	
985	ms, sp	
760	ms, sp	
625	m, sp	
710	w, sh	
650	w, sh	
610	w, sh	

vs = very strong, s = strong, ms = medium strong, m = medium, w = weak, sp = sharp, b = broad, sh = shoulder

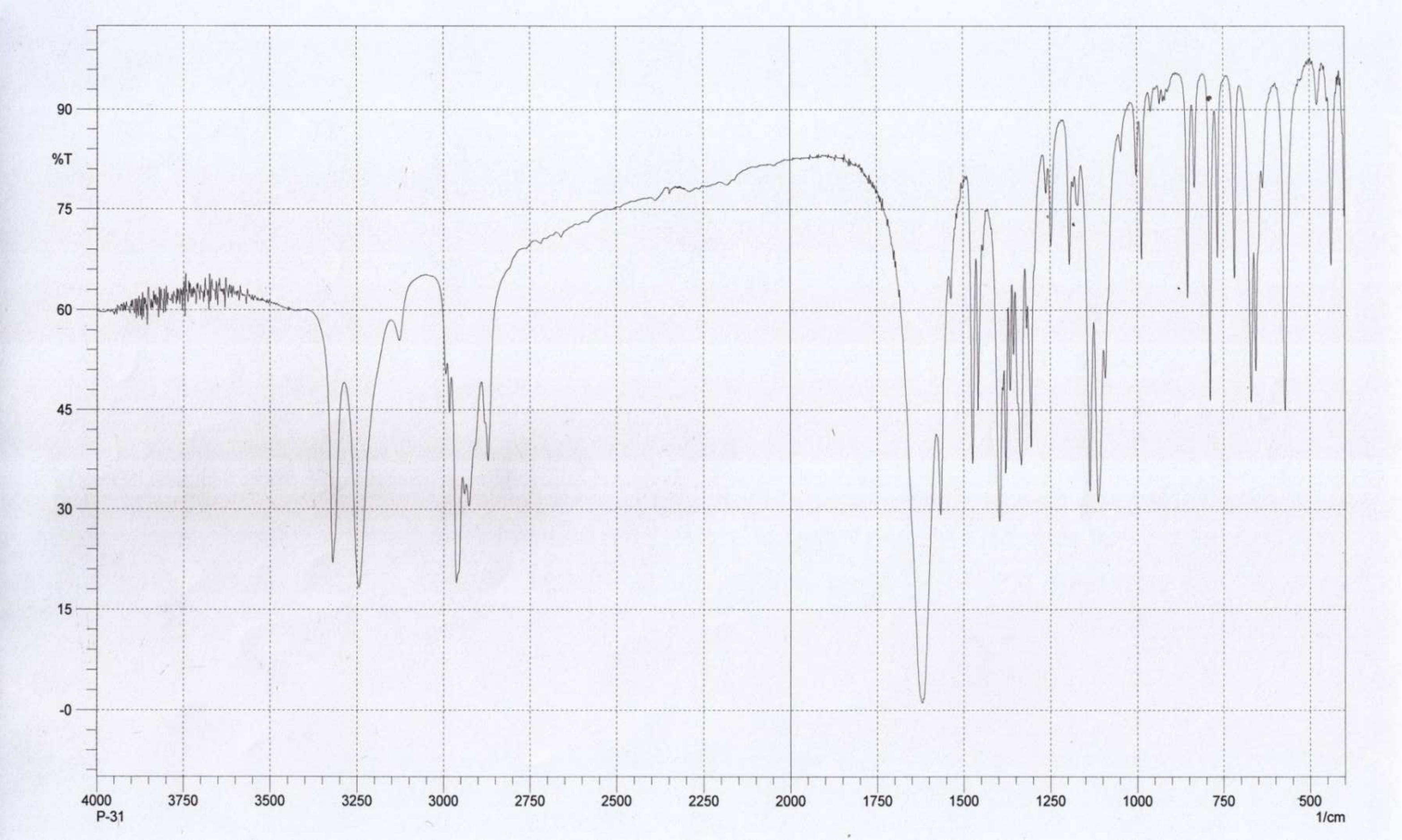

Fig. 3.15: FTIR spectrum of $Cu(C_6H_{12}NO_2)_2$

Table 3.8: Tentative assignment of IR bands of $Cu(C_6H_{12}NO_2)_2$

Wave no. (cm^{-1})	Relative intensity	Tentative band assignment
3325	s, sp	Asymmetric N-H stretching
3250	s, sp	Symmetric N-H stretching
2975	s, sp	-C-H stretching
2925	w, sp	
2875	m, sp	
1625	s, sp	Asymmetric N-H bending
1575	m, sp	Asymmetric COO^- stretching
1480	ms, sp	Symmetric N-H bending
1400	m, sp	symmetric COO^- stretching
1375	ms, sp	
1325	ms, sp	
1150	ms, sp	
1120	ms, sp	C-N stretching
990	m, sp	
860	m, sp	
800	ms, sp	
775	m, sp	
725	m, sp	
675	ms, sp	
575	ms, sp	

vs = very strong, s = strong, ms = medium strong, m = medium, w = weak, sp = sharp, b = broad, sh = shoulder

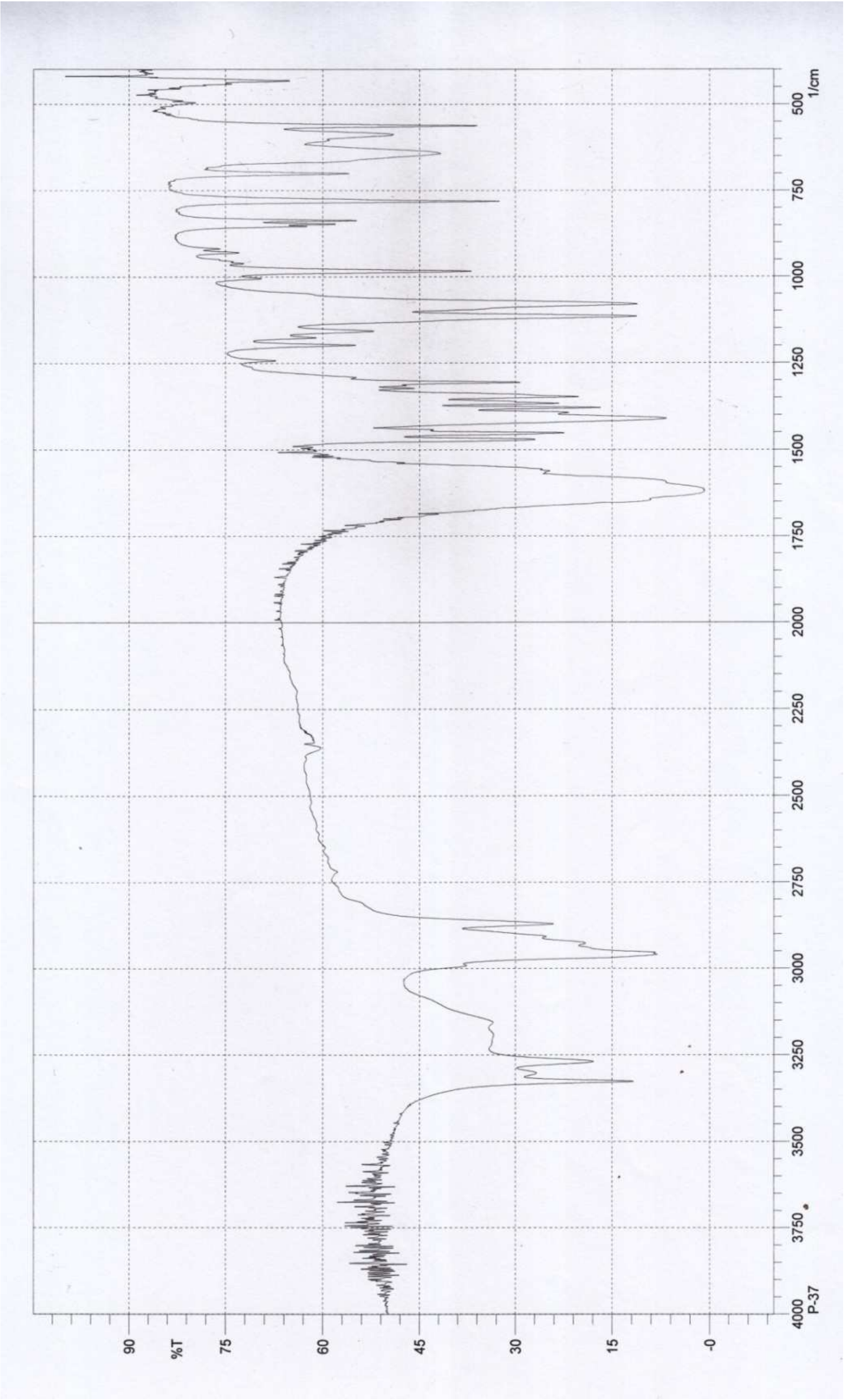

Fig. 3.16: FTIR spectrum of $Zn(C_6H_{12}NO_2)_2$

Table 3.9: Tentative assignment of IR bands of $Zn(C_6H_{12}NO_2)_2$

Wave no. (cm^{-1})	Relative intensity	Tentative band assignment
3325	ms, sp	Asymmetric N-H stretching
3260	ms, sp	Symmetric N-H stretching
2960	ms, sp	-C-H stretching
2875	m, sp	
1625	s, b	Asymmetric N-H bending Asymmetric COO^- stretching
1570	w, sh	
1475	m, sp	Symmetric N-H bending
1410	ms, sp	symmetric COO^- stretching
1110	s, sp	C-N stretching
1075	s, sp	
980	ms, sp	
775	ms, sp	

vs = very strong, s = strong, ms = medium strong, m = medium, w = weak, sp = sharp, b = broad, sh = shoulder

Table 3.10: Tentative assignment of IR bands of $Cd(C_6H_{12}NO_2)_2$

Wave no. (cm^{-1})	Relative intensity	Tentative band assignment
3350	m, sp	Asymmetric N-H stretching
3250	ms, sp	Symmetric N-H stretching
2960	ms, sp	-C-H stretching
1600	ms, sp	Asymmetric N-H bending
1560	ms, sp	Asymmetric COO^- stretching
1400	s, b	Symmetric N-H bending symmetric COO^- stretching
1080	m, sp	C-N stretching
860	s, sp	
775	ms, sp	
725	ms, sp	

vs = very strong, s = strong, ms = medium strong, m = medium, w = weak, sp = sharp, b = broad, sh = shoulder

Fig. 3.17: FTIR spectrum of Cd($C_6H_{12}NO_2$)$_2$

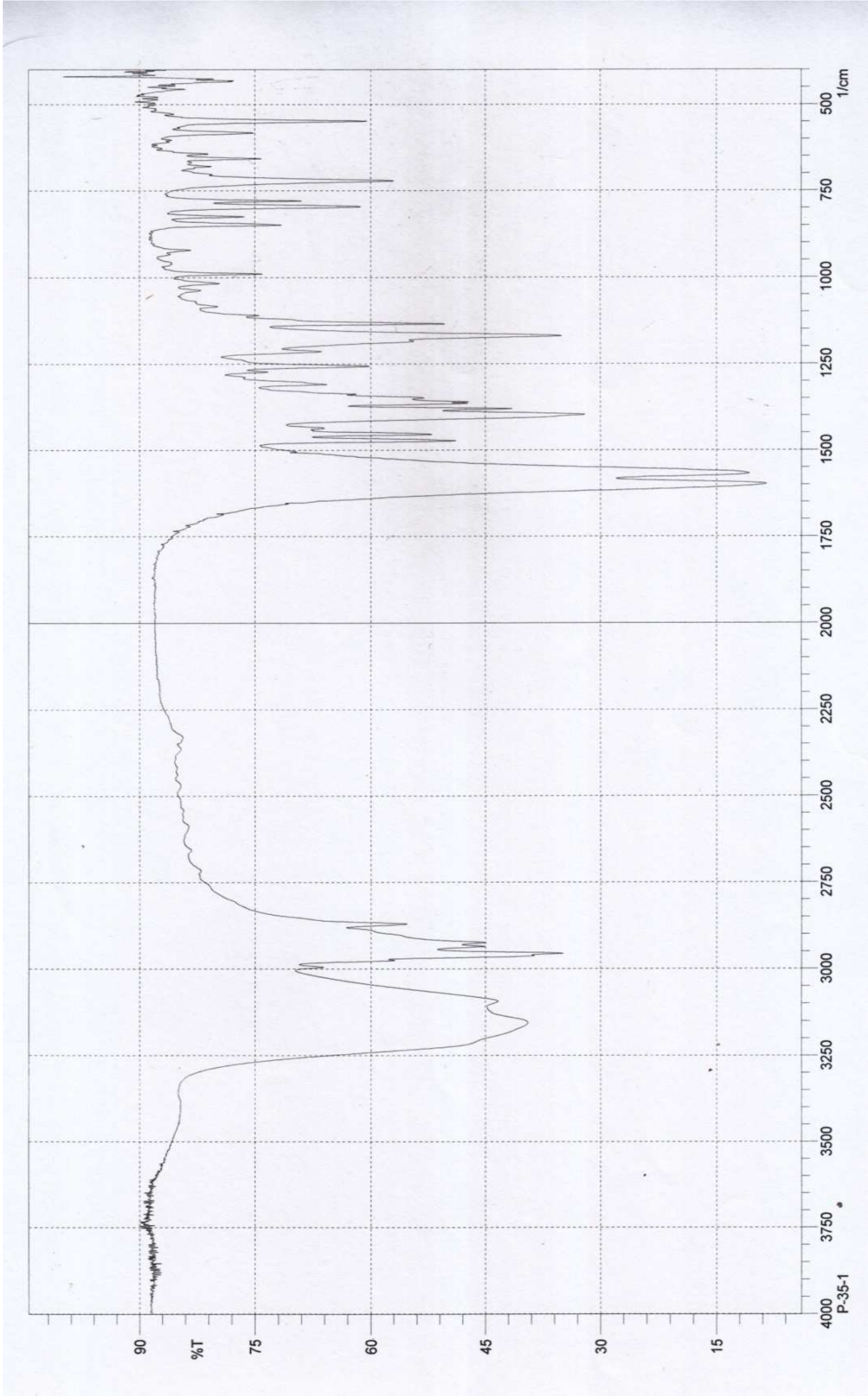

Fig. 3.18: FTIR spectrum of $Hg(C_6H_{12}NO_2)_2$

Table 3.11: Tentative assignment of IR bands of $Hg(C_6H_{12}NO_2)_2$

Wave no. (cm^{-1})	Relative intensity	Tentative band assignment
3150	m, b	Asymmetric N-H stretching
3100	w, sh	Symmetric N-H stretching
2960	ms, sp	-C-H stretching
2925	m, sp	
2875	m, sp	
1600	s, sp	Asymmetric N-H bending
1575	s, sp	Asymmetric COO^- stretching
1475	m, sp	Symmetric N-H bending
1400	ms, sp	symmetric COO^- stretching
1150	m, sp	C-N stretching
800	m, sp	
740	m, sp	
550	m, sp	

vs = very strong, s = strong, ms = medium strong, m = medium, w = weak, sp = sharp, b = broad, sh = shoulder

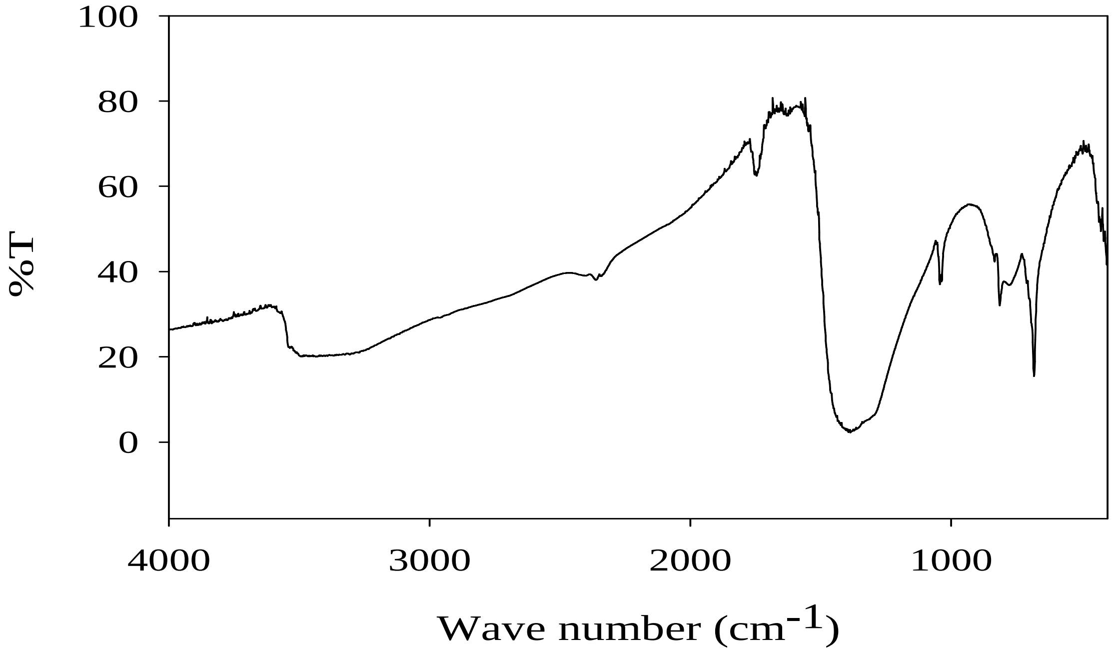

Fig. 3.19: FTIR spectrum of Pb-leucine complex

3.3.1.4 Electronic spectral analysis:

In the present study the electronic spectrum of leucine and its metal complexes were recorded on a Shimadzu UV-Vis recording spectrophotometer (UV- 1800A) in the wavelength range 190 to 1100 nm.

3.3.1.4.1 UV-Visible absorption spectral analysis: UV-Visible absorption spectrum was carried out to understand the electronic transitions occur within the molecule. The absorption spectrum of the complex was recorded on a Shimadzu UV-Visible recording spectrophotometer (UV- 1800A) in the range of 190 nm to 1100 nm. The complexes were insoluble in the most common solvents and only Ni complex is soluble in methanol. So, the absorption spectrum of leucine and Ni-leucine complex were studied in methanol solution and shown in Fig. 3.20 – Fig. 3.22. The tentative band assignments have been made empirically on the basis of some standard books [102-106] and tabulated in Table 3.12.

The absorption band at ~ 200 nm was observed for the organic part of the complex. The absorption band at around 370 nm in the complex may be due to charge transfer between metal orbital and ligand orbital. The presence of $\pi \rightarrow \pi^*$, $n \rightarrow \pi^*$ and $n \rightarrow \sigma^*$ bands as a single band in the ligand and the complex indicate low energy difference for these transitions (e.g. -C=O, $-NH_2$). Appearing of a new band at 620 nm for d-d transitions also indicate the presence of metal ion in the complex. Shifting of the absorption bands in the complexes and appearing of a new band for d-d transitions also indicate the probability of forming M←L coordination bonds in the complexes.

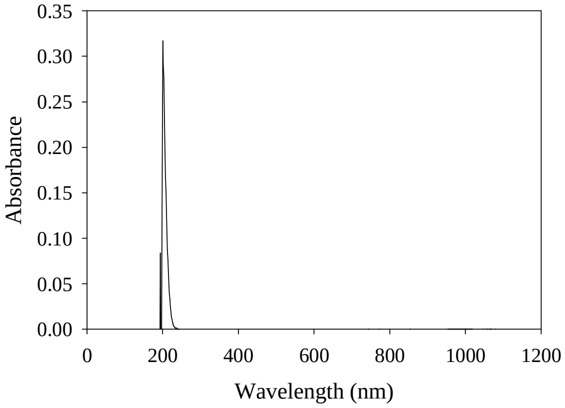

Fig. 3.20: **UV-Vis spectrum of leucine ($C_6H_{13}NO_2$)**

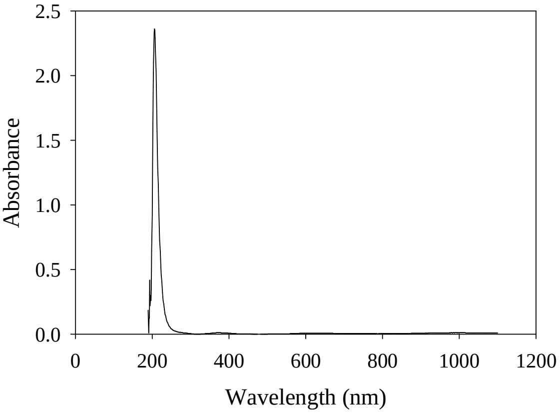

Fig. 3.21: **UV-Vis spectrum of $Ni(C_6H_{12}NO_2)_2.2H_2O$**

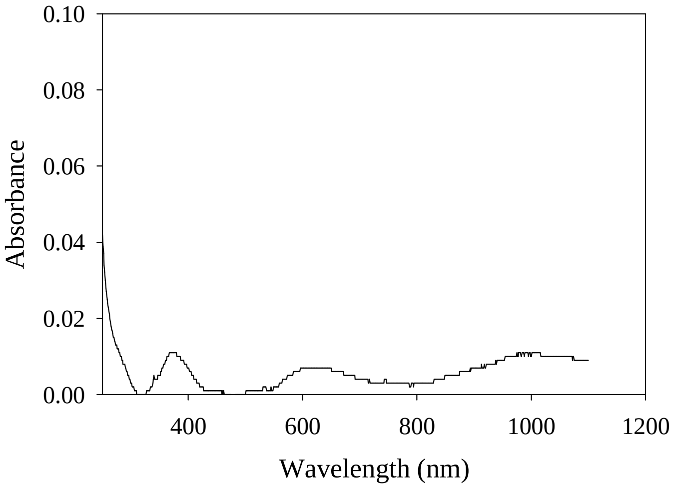

Fig. 3.22: UV-Vis spectrum of $Ni(C_6H_{12}NO_2)_2.2H_2O$

Table 3.12: Absorption bands of leucine and its complex

Compound	Absorption band		
	d-d	CT	IL
Leucine ($C_6H_{13}NO_2$)			201
$Ni(C_6H_{12}NO_2)_2.2H_2O$	620	370	206

d-d = d-d transition, CT = charge transfer transition, IL = Intraligand charge transfer

3.3.1.4.2 UV-Visible diffuse reflectance spectral analysis: UV-Visible diffuse reflectance spectroscopy is an optical technique which describes the electronic behavior present in the structure of the solid. This technique concerns with the relative change in the amount of reflected light off of a surface. Diffuse reflectance spectrum are taken for measuring the band gap energy. The separation between the energy of the lowest conduction band and that of the highest valence band is called the band gap, energy gap or forbidden energy gap (E_g). The semiconductor properties of a solid are strongly affected by the E_g parameter.

The reflectance spectrum and the corresponding energy function of the compounds are displayed in the Fig. 3.23 to Fig. 3.29. The determined band gap energy of the compounds is listed in Table 3.13. All the samples have lower band gap energy, indicating they may be good conductor [107].

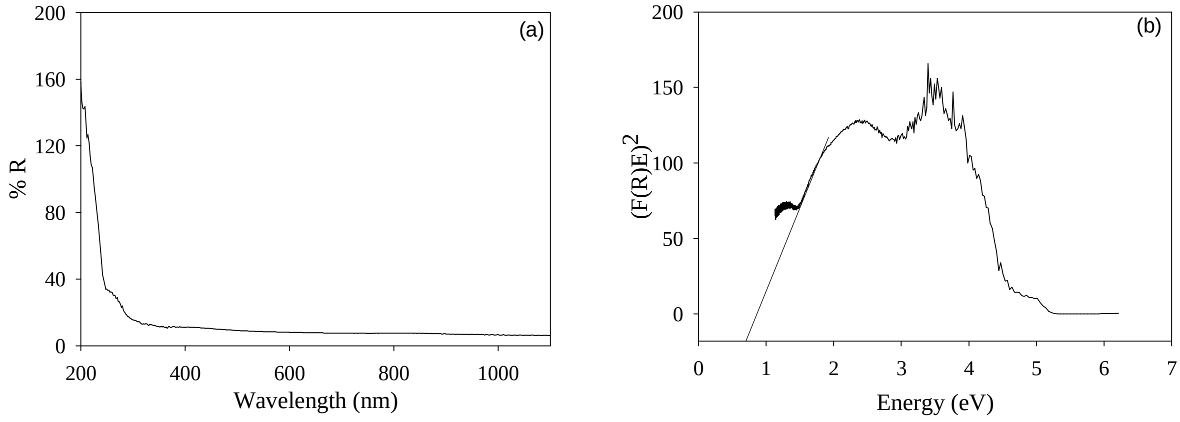

Fig. 3.23: (a) Reflectance spectrum and (b) $(F(R)E)^2$ vs E plot for leucine ($C_6H_{13}NO_2$)

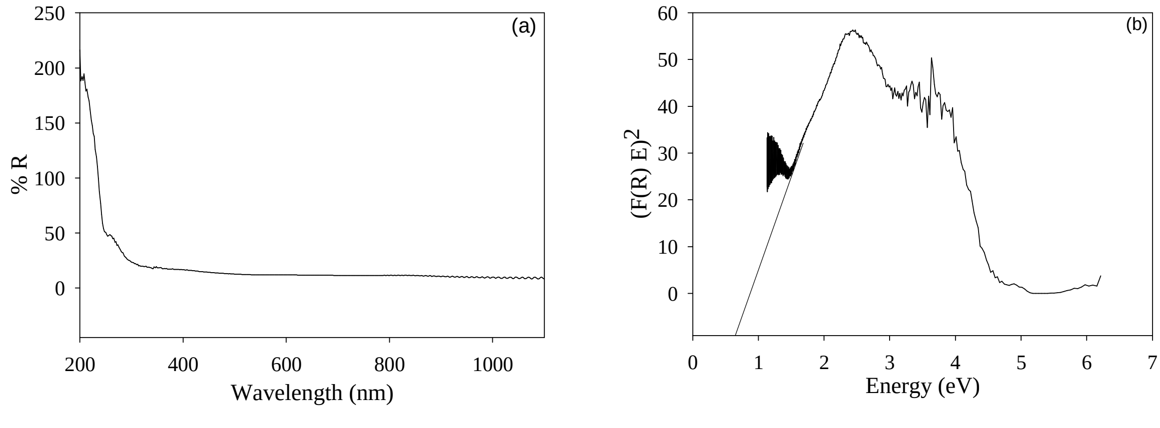

Fig. 3.24: (a) Reflectance spectrum and (b) $(F(R)E)^2$ vs E plot for $Co(C_6H_{12}NO_2)_2.2H_2O$

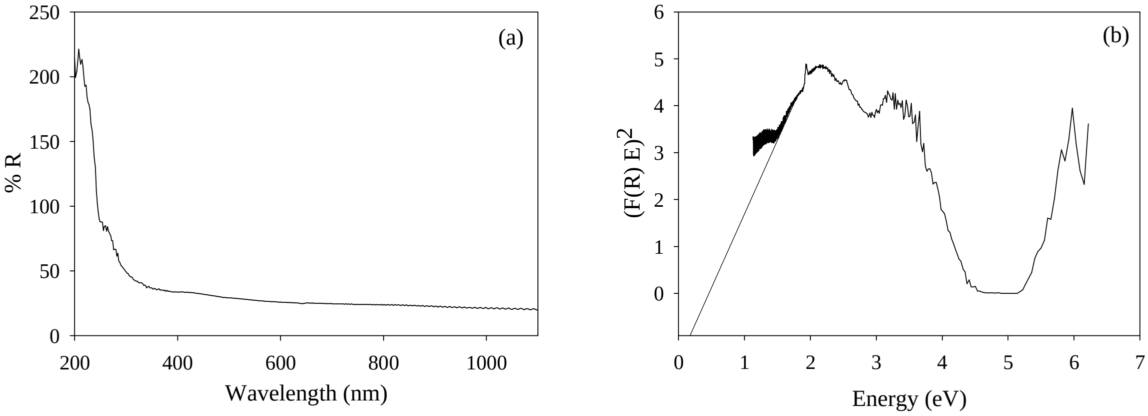

Fig. 3.25: (a) Reflectance spectrum and (b) $(F(R)E)^2$ vs E plot for $Ni(C_6H_{12}NO_2)_2.2H_2O$

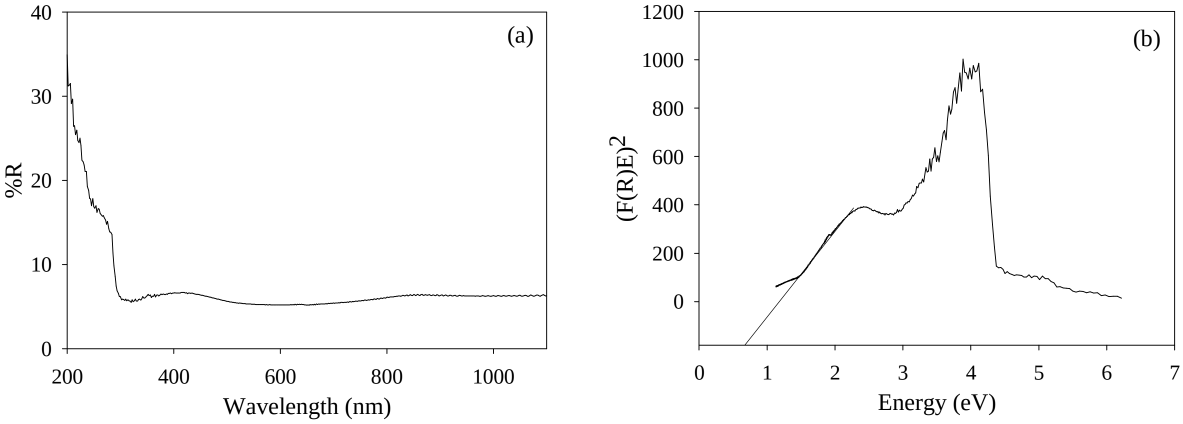

Fig. 3.26: (a) Reflectance spectrum and (b) $(F(R)E)^2$ vs E plot for $Cu(C_6H_{12}NO_2)_2$

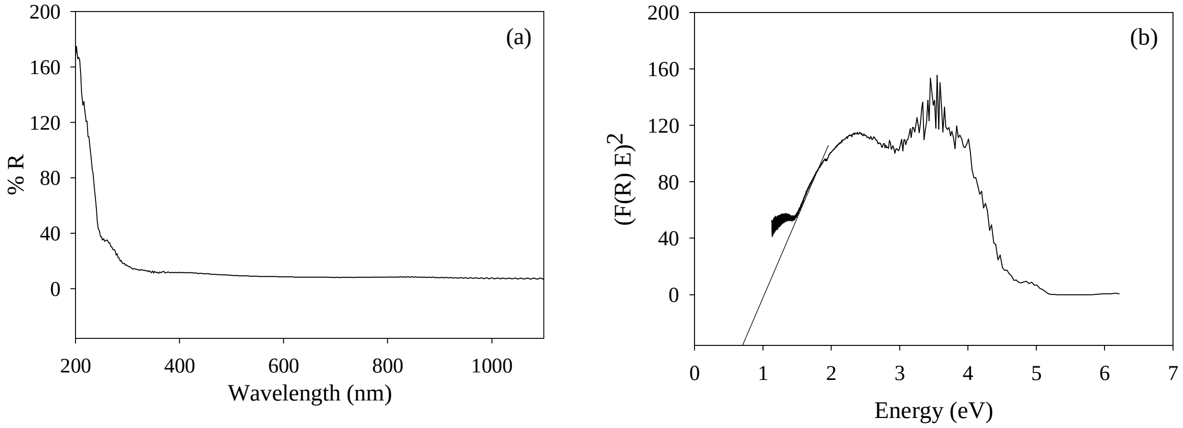

Fig. 3.27: (a) Reflectance spectrum and (b) $(F(R)E)^2$ vs E plot for $Zn(C_6H_{12}NO_2)_2$

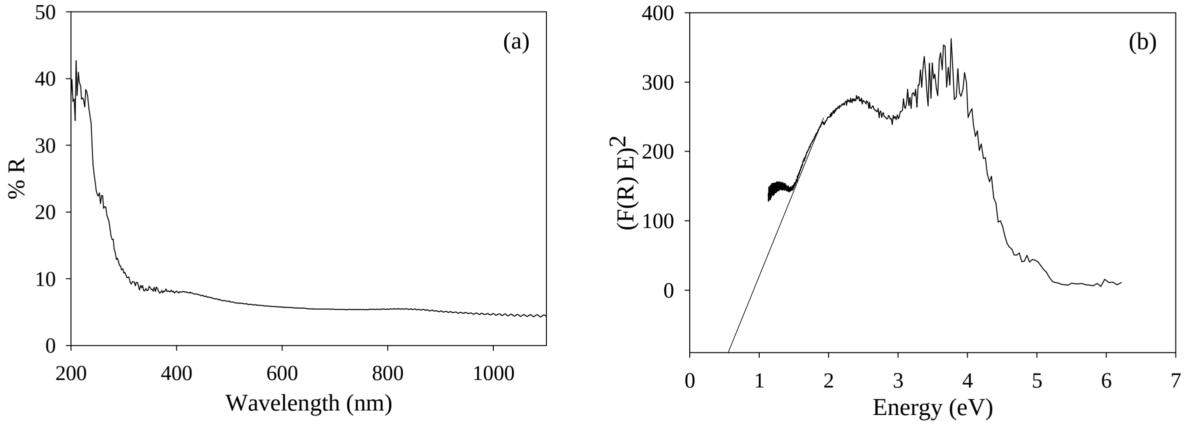

Fig. 3.28: (a) Reflectance spectrum and (b) $(F(R)E)^2$ vs E plot for $Cd(C_6H_{12}NO_2)_2$

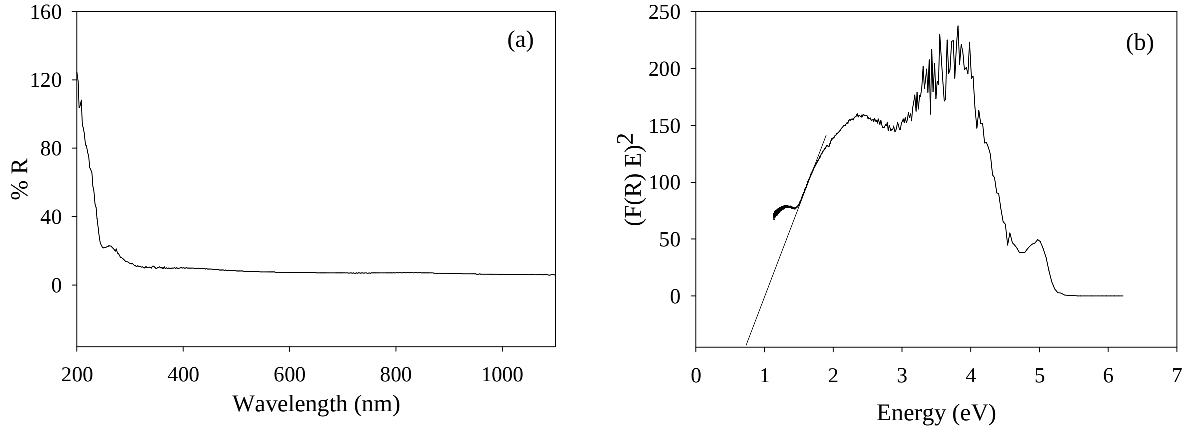

Fig. 3.29: (a) Reflectance spectrum and (b) $(F(R)E)^2$ vs E plot for $Hg(C_6H_{12}NO_2)_2$

Table 3.13: The determined band gap energy of leucine and its complexes

Sample	Band gap energy (eV)
Leucine ($C_6H_{13}NO_2$)	0.7
$Co(C_6H_{12}NO_2)_2.2H_2O$	0.8
$Ni(C_6H_{12}NO_2)_2.2H_2O$	0.2
$Cu(C_6H_{12}NO_2)_2$.	0.7
$Zn(C_6H_{12}NO_2)_2$	0.7
$Cd(C_6H_{12}NO_2)_2$	0.5
$Hg(C_6H_{12}NO_2)_2$	0.7

3.3.1.5 Nuclear magnetic resonance (NMR) spectral analysis

In the present study the NMR spectrum of leucine and its nickel complex were recorded on a Bruker NMR spectrometer in methanol solution and shown in Fig. 3.30 - Fig. 3.32. The tentative assignment of the position of the peaks is done on the basis of some standard books [102, 103]. The assignments are shown on the body of the graph.

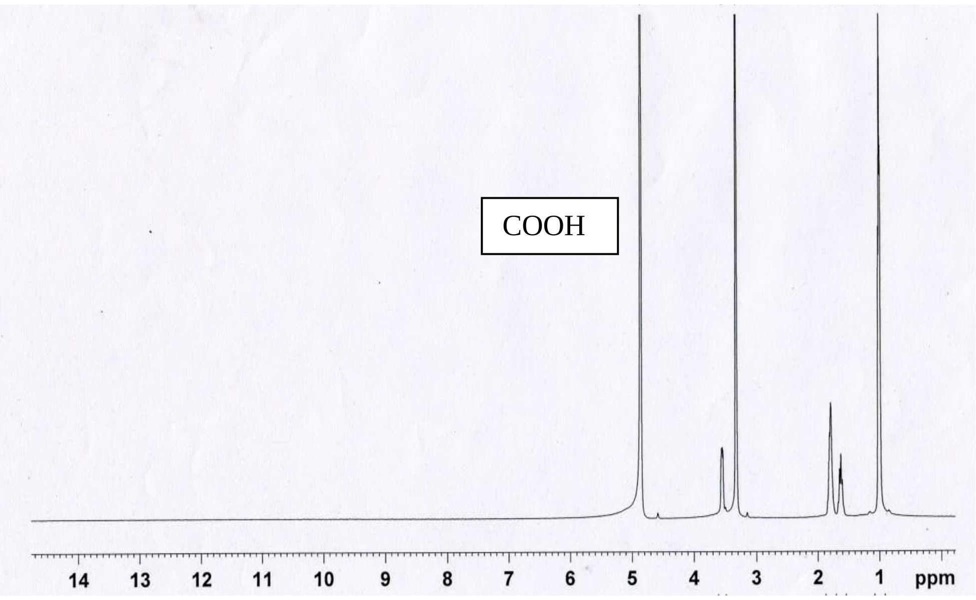

Fig. 3.30: NMR spectrum of leucine ($C_6H_{13}NO_2$)

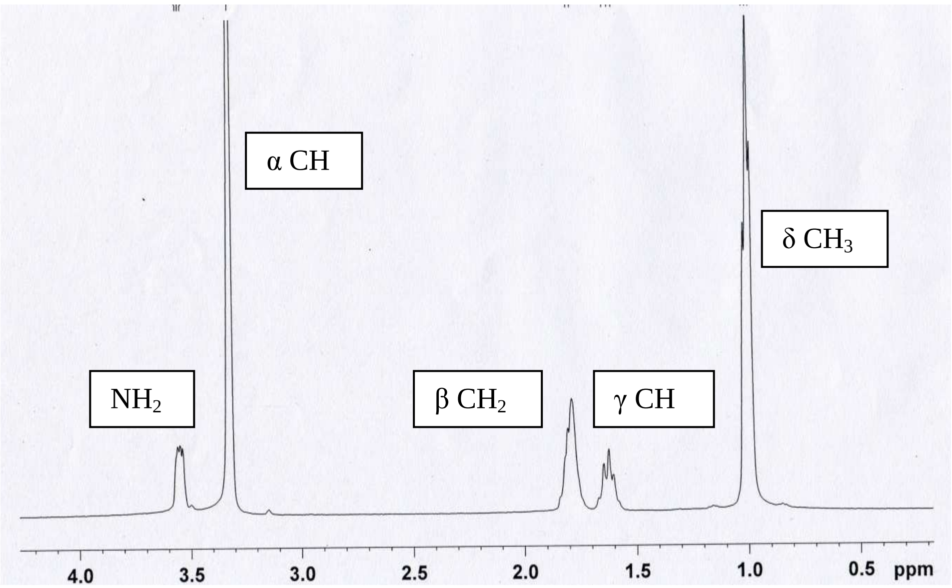

Fig. 3.31: NMR spectrum of leucine ($C_6H_{13}NO_2$)

Lucine shows a peak at chemical shift 5 ppm for –COOH proton. Since the –COOH protons are highly deshielded the peak appears most far from the TMS position. The $-CH_3$ protons are most shielded. So, the $-CH_3$ peak appears close to the TMS position at chemical shift 1.0. The splitting of the peaks indicates that the protons may be overlapping with each other.

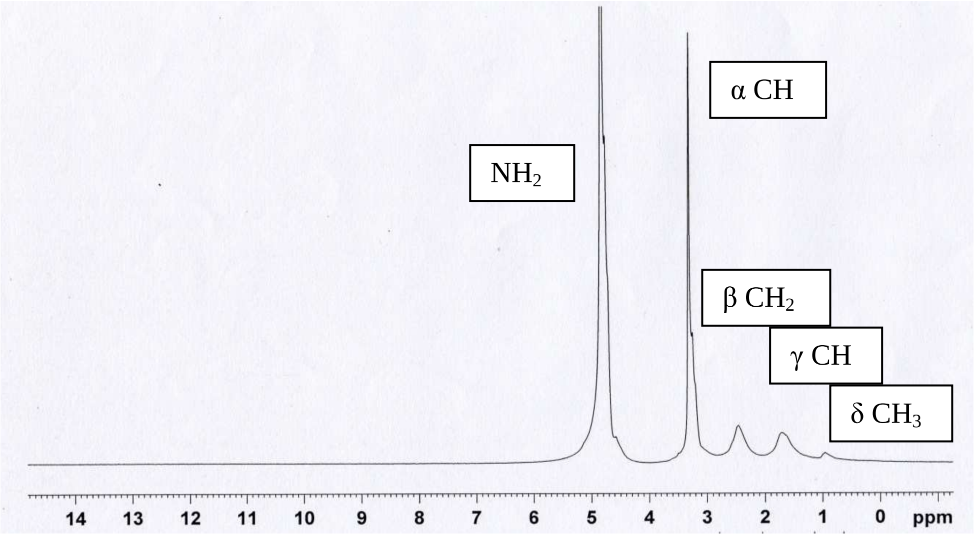

Fig. 3.32: NMR spectrum of $Ni(C_6H_{12}NO_2)_2.2H_2O$

A peak for –COOH proton appears in the ligand but in the complex it is not seen. This may be due to complexation of leucine with the metal. The position of the other peaks in the complex is consistent with that of leucine.

3.3.1.6 Thermal analysis (TA)

Thermal methods of analysis are those techniques in which changes in physical and/or chemical properties of a substance are measured as a function of temperature. Thermo-gravimetry (TG) and Differential Scanning Calorimetry (DSC) are important among them.

The thermo-gravimetric analysis is a dynamic technique based on the change in the weight of a substance recorded as the function of temperature or time. On the other hand, DSC is a technique in which the difference in energy inputs into a substance and a reference material is measured as a function of temperature whilst the substance and reference material are subjected to a controlled temperature programme. Thermal analysis is applied for the determination of the purity and thermal stability of primary and secondary standards, phase transition, enthalpy change, degree of crystallinity, and for the determination of the composition of complex mixtures. It gives an idea about the bond strength of various constituent parts of the complex. Weight loss at lower temperature is generally due to removal of purely lattice component or other components simply hydrogen bonded to some parts of ligand weakly coordinated to central metal atom.

3.3.1.6.1 Thermal analysis of leucine: The TG and DSC curves of leucine are shown in Fig. 3.33. The ligand decomposes continuously in one step. There is no sharp transition up to 200 ^{0}C. So it can be said that the ligand do not contain any water of crystallization. It is logical since the molecular formula of the ligand do not contain any water of crystallization. At about 950 ^{0}C only 2.3% of the ligand sample remains as residue. So it can be said that the ligand almost completely decomposed.

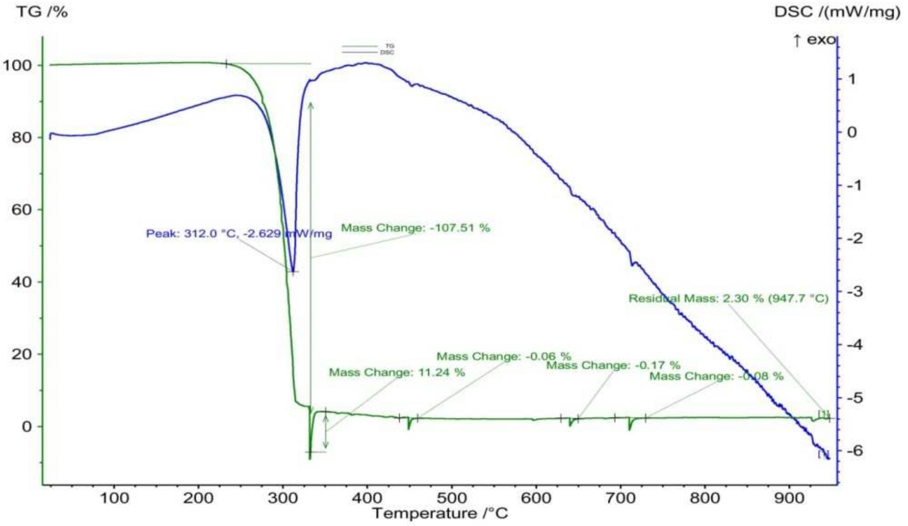

Fig. 3.33: TG and DSC curves of leucine ($C_6H_{13}NO_2$)

3.3.1.6.2 Thermal analysis of leucine complexes: The TG and DSC curves of leucine complexes are shown in Fig. 3.34 to Fig. 3.39. The weight loss at different stages of the TG curves is explained in Table 3.14. The Co and Ni complex contains two molecules of water of crystallization. The Cu, Zn, Cd and Hg complex does not contain any water of crystallization or coordinated water. The Co, Zn and Cd complex decomposed in a wide temperature range. On the other hand sharp decomposition occurs of Ni, Cu and Hg complex. Co, Zn and Cd complex may be more stable compared to Ni, Cu and Hg complex. The residue remained after 900 ^{0}C confirms that after decomposition the Co, Ni, Cu, Zn and Cd complex almost converted to the respective metal oxide. The Hg complex undergone about 97% decomposition at around 250 ^{0}C. The mercury oxide formed may be further decomposed. This is reasonable since HgO decomposes on exposure to light or on heating producing mercury fumes and oxygen. The Differential Scanning Calorimetry (DSC) curve of the complexes is sharp endothermic. Therefore, the weight changes monitored by thermogravimetry involved absorption of energy [100].

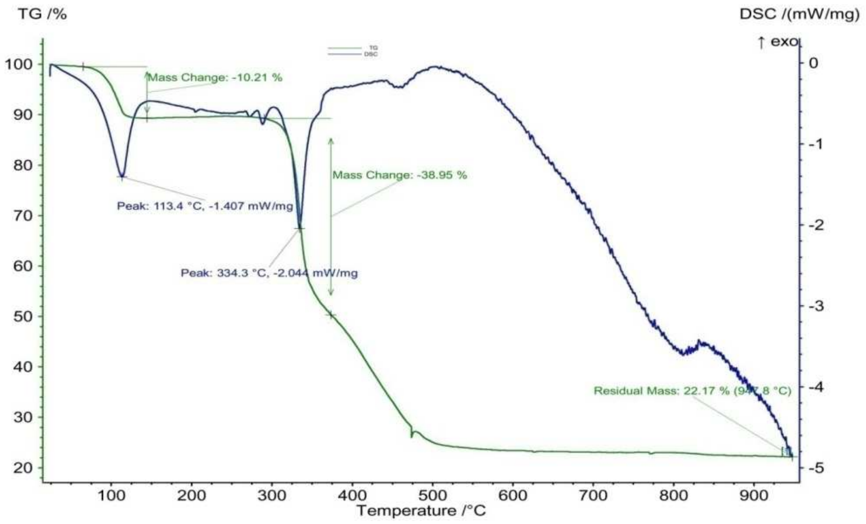

Fig. 3.34: TG and DSC curves of $Co(C_6H_{12}NO_2)_2.2H_2O$

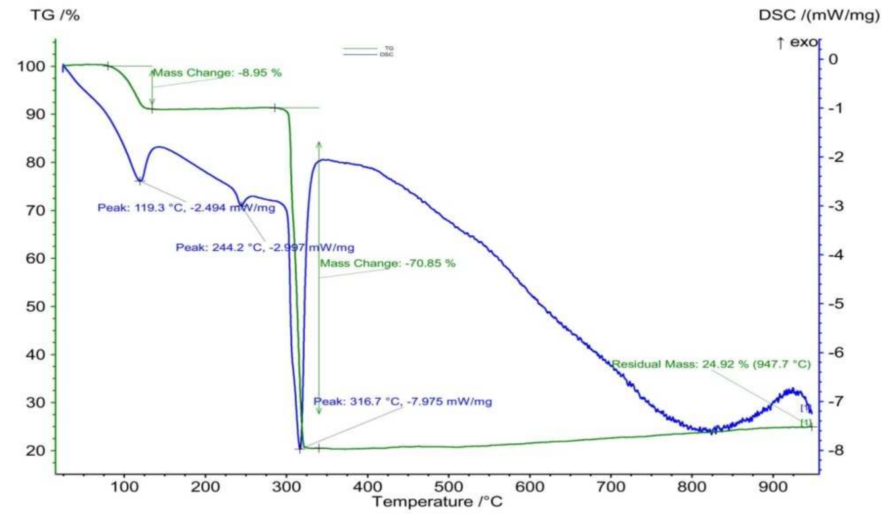

Fig. 3.35: TG and DSC curves of $Ni(C_6H_{12}NO_2)_2.2H_2O$

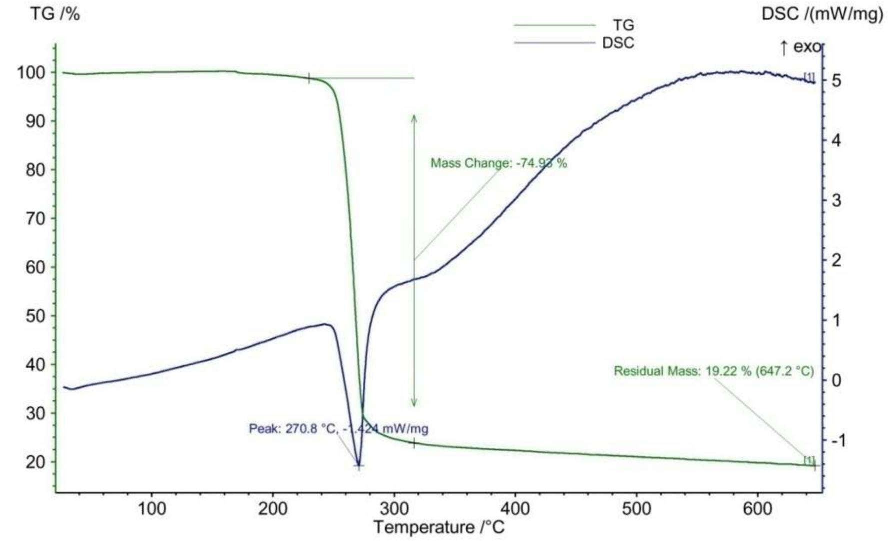

Fig. 3.36: TG and DSC curves of $Cu(C_6H_{12}NO_2)_2$

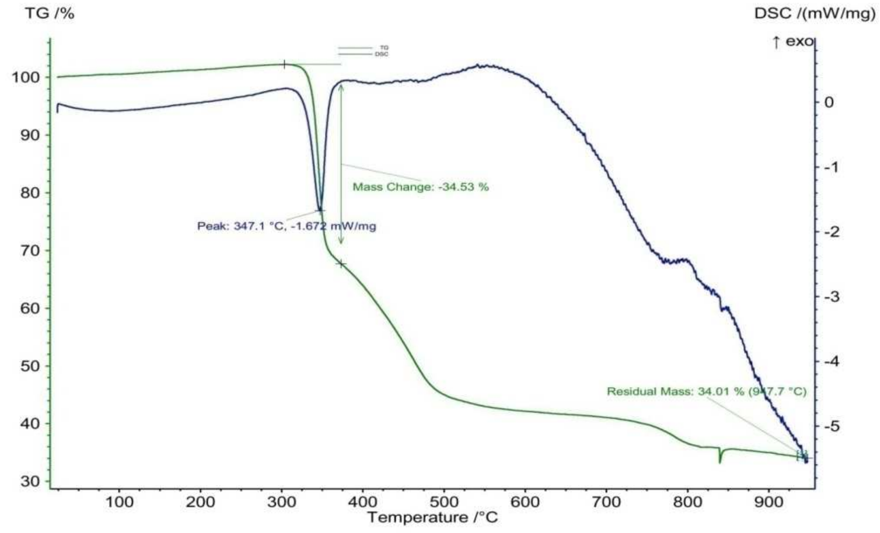

Fig. 3.37: TG and DSC curves of Zn($C_6H_{12}NO_2$)$_2$

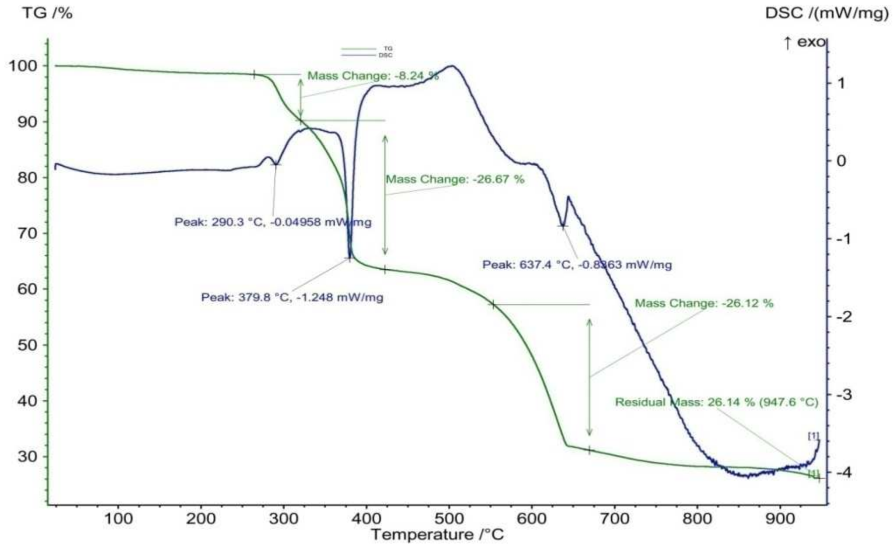

Fig. 3.38: TG and DSC curves of Cd($C_6H_{12}NO_2$)$_2$

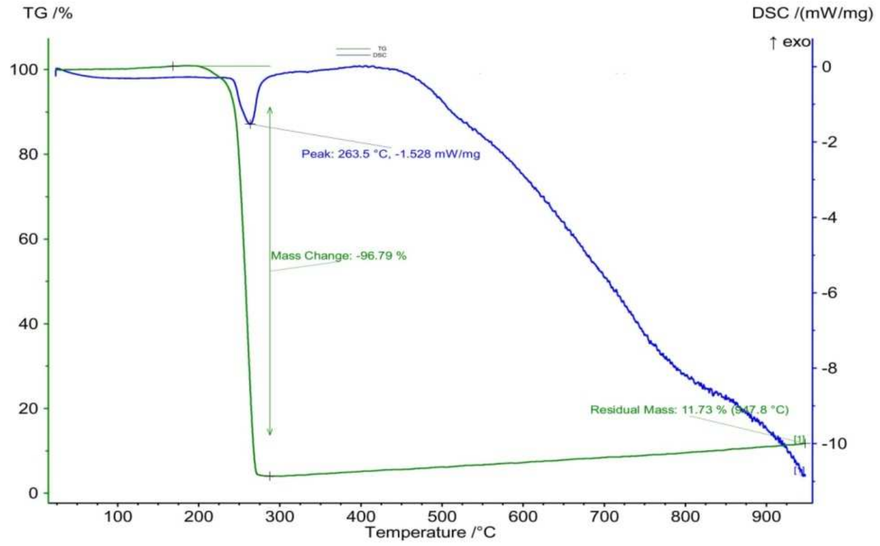

Fig. 3.39: TG and DSC curves of Hg($C_6H_{12}NO_2$)$_2$

Table 3.14: Weight loss at different stages of TG analysis of leucine and its complexes

Compound	Temperature range	Mass change	Inference
Leucine($C_6H_{13}NO_2$)	0 ^{0}C- 225 ^{0}C	0%	No moisture
	225 ^{0}C – 325 ^{0}C	97 %	Total decomposition
	947 ^{0}C	2.3 %	Residue
Co($C_6H_{12}NO_2$)$_2$.2H_2O	0 ^{0}C – 75 ^{0}C	0 %	No moisture
	75 ^{0}C – 120 ^{0}C	10 %	Two water molecule may be lost
	300 ^{0}C – 500 ^{0}C	67 %	The weight loss may be due to loss of NH_3, CO_2, CH_4
	947 ^{0}C	22 %	May be cobalt oxide
Ni($C_6H_{12}NO_2$)$_2$.2H_2O	0 ^{0}C - 80 ^{0}C	0 %	No moisture
	80 ^{0}C – 120 ^{0}C	9 %	Two water molecule may be lost
	300 ^{0}C – 320 ^{0}C	71 %	The weight loss may be due to loss of NH_3, CO_2, CH_4
	947 ^{0}C	25 %	May be nickel oxide
Cu($C_6H_{12}NO_2$)$_2$	0 ^{0}C- 225 ^{0}C	0%	No moisture or chemically bound water
	225 ^{0}C – 325 ^{0}C	97 %	The weight loss may be due to loss of NH_3, CO_2, CH_4
	647 ^{0}C	19 %	May be copper oxide

Compound	Temperature range	Mass change	Inference
$Zn(C_6H_{12}NO_2)_2$	0 ^{0}C- 275 ^{0}C	0%	No moisture or chemically bound water
	225 ^{0}C – 900 ^{0}C	65 %	The weight loss may be due to loss of NH_3, CO_2, CH_4
	947 ^{0}C	34 %	May be zinc oxide
$Cd(C_6H_{12}NO_2)_2$	0 ^{0}C – 250 ^{0}C	0 %	No moisture or chemically bound water
	250 ^{0}C – 400 ^{0}C	35 %	The weight loss may be due to loss of NH_3, CO_2, CH_4
	400 ^{0}C – 900 ^{0}C	35 %	The rest of the organic part may be lost
	947 ^{0}C	26 %	May be cadmium oxide
$Hg(C_6H_{12}NO_2)_2$	0 ^{0}C – 200 ^{0}C	0 %	No moisture or chemically bound water
	200 ^{0}C – 275 ^{0}C	97 %	The weight loss may be due to loss of NH_3, CO_2, CH_4
	947 ^{0}C	11 %	May be liquid metal

3.3.1.7 Magnetic properties

An interesting characteristic of transition metals is their ability to form magnets. Metal complexes that have unpaired electrons are magnetic. Since the last electrons reside in the d orbitals, this magnetism must be due to having unpaired d electrons. Considering only monometallic complexes, unpaired electrons arise because the complex has an odd number of electrons or because electron pairing is destabilized. When an electron in an atom or ion is unpaired, the magnetic moment due to its spin makes the entire atom or ion paramagnetic**.** The size of the magnetic moment of a system containing unpaired electrons is related directly to the number of such electrons: the greater the number of unpaired electrons, the larger the magnetic moment. Magnetic susceptibility measures the force experienced by a substance in a magnetic field.

Specimen calculation:

Sample ID: $Ni(C_6H_{12}NO_2)_2.2H_2O$

The balance calibration constant,

$C_{Bal} = C_{tube} / (R_s - R_0) = 1090 / (1060 + 33) = 0.9972$

Where R_s = reading for standard sample tube.

The molar susceptibility,

$$\chi_A = \frac{C_{Bal} * l * (R - R_0)}{10^9 * m} * MW$$

$$= \frac{0.9972 * 2 * (699 + 32)}{10^9 * 0.11} \times 354.69$$

$$= 4.7 * 10^{-3} \text{ cgs}$$

Here,
$R = 699$
$R_0 = -32$
$l = 2\text{cm}$
$m = 0.11$ g
$C_{Bal} = 0.9972$

The magnetic moment,

$\mu_{eff} = 2.828 \sqrt{(T * \chi_A)} = 2.828 \sqrt{(300 * 4.7 * 10^{-3})} = 3.3$ BM

From the result found we may decided the number of unpaired electron n = 1

The magnetic properties of the complexes of leucine were examined by magnetic susceptibility balance and are tabulated in Table 3.15.

Table 3.15: Magnetic properties of the metal-leucine complexes

Compound	χ_A (cgs) x 10^{-3}	μ_{eff} BM (at 300K)		No. of unpaired electron (n)	Config.	Inference
		Found	Theo.			
$Co(C_6H_{12}NO_2)_2.2H_2O$	7.4	4.2	4.3-5.2	3	d^7	Paramagnetic
$Ni(C_6H_{12}NO_2)_2.2H_2O$	4.7	3.3	3.0-3.3	2	d^8	Paramagnetic
$Cu(C_6H_{12}NO_2)_2$	1.5	1.9	1.8-2.1	1	d^9	Paramagnetic
$Zn(C_6H_{12}NO_2)_2$	negative	0*		0	d^{10}	Diamagnetic
$Cd(C_6H_{12}NO_2)_2$	negative	0*		0	d^{10}	Diamagnetic
$Hg(C_6H_{12}NO_2)_2$	negative	0*		0	d^{10}	Diamagnetic

Theo. = Theoretical values [112]. *The negative value of χ_A indicates that the tube and sample have a net diamagnetism. In that case μ_{eff} can be considered as zero.

From the experimental results, we get the following information’s about the magnetic properties of the complexes.

$Co(C_6H_{12}NO_2)_2.2H_2O$: Experimentally observed magnetic moment of Co(II)-complex is 4.2, which implies in the complex Co exists as Co^{2+} ion with three unpaired electrons, d^7 (t_{2g}^5 e_g^2). The experimental magnetic moment quite agrees with the theoretical value (4.3-5.2 BM).

$Ni(C_6H_{12}NO_2)_2.2H_2O$: Experimentally observed magnetic moment of Ni(II)-complex is 3.3, which implies in the complex Ni exists as Ni^{2+} ion with two unpaired electrons, d^8 (t_{2g}^6 e_g^2). This magnetic moment quite agrees with the theoretical value (3.0-3.3 BM).

$Cu(C_6H_{12}NO_2)_2$: Experimentally observed magnetic moment of Cu(II)-complex is 1.9, which implies in the complex Cu exists as Cu^{2+} ion with one unpaired electrons, d^9 (t_{2g}^6 e_g^3). This magnetic moment quite agrees with the theoretical value (1.8-2.1 BM).

$Zn(C_6H_{12}NO_2)_2$, $Cd(C_6H_{12}NO_2)_2$ and $Hg(C_6H_{12}NO_2)_2$: The magnetic susceptibility of Zn(II), Cd(II) and Hg(II) complex shows that they has no unpaired electron i.e. they possess d^{10} configuration with diamagnetic character [112].

3.3.1.8 Theoretical studies

All calculations were performed with the Gaussian 09 software package. Gas phase equilibrium geometries of the complexes were fully optimized and then vibrational frequencies were calculated at density functional theory (B3LYP) using 6-31 G(d) and SDD basis set. After computing the optimized structure and vibrational frequencies molecular orbital calculations were conducted with all compounds using same level of theory for analyzing the transition metal effects on the HOMO-LUMO energies. For calculating the excited state properties of the complexes, time dependent density functional theory (TD-DFT) is employed with CAM-B3LYP/6-31 +G (d,p) and B3LYP/SDD [59, 113-117].

3.3.1.8.1 Optimized structure: The optimized structure of leucine and its complexes are shown in Fig. 3.40 to Fig. 3.46. The calculated bond distances and angles are listed in Table 3.16 and Table 3.17.

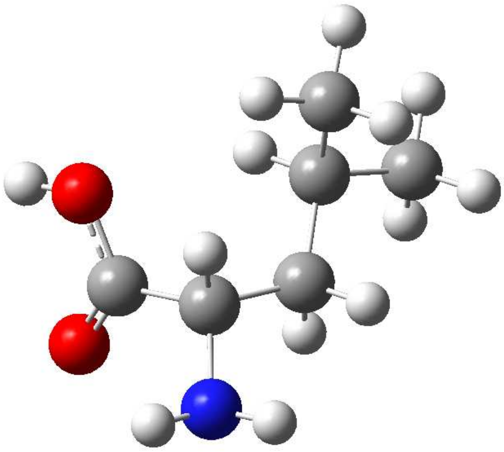

Fig. 3.40: Optimized structure of leucine calculated at B3LYP/SDD level of theory

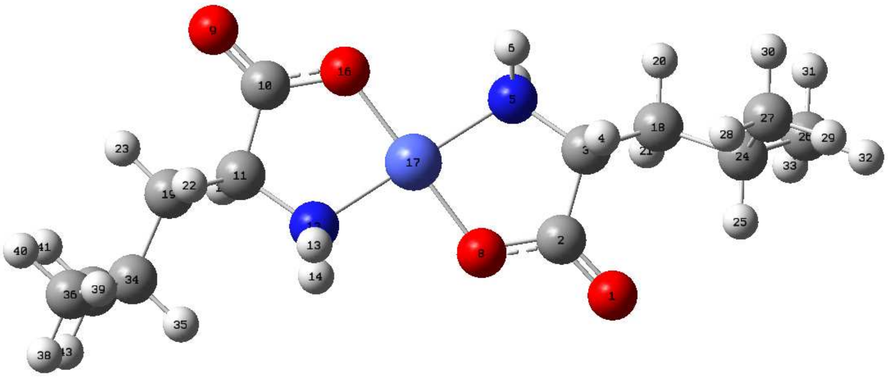

Fig. 3.41: Optimized structure of Co(leu)$_2$ calculated at B3LYP/SDD level of theory

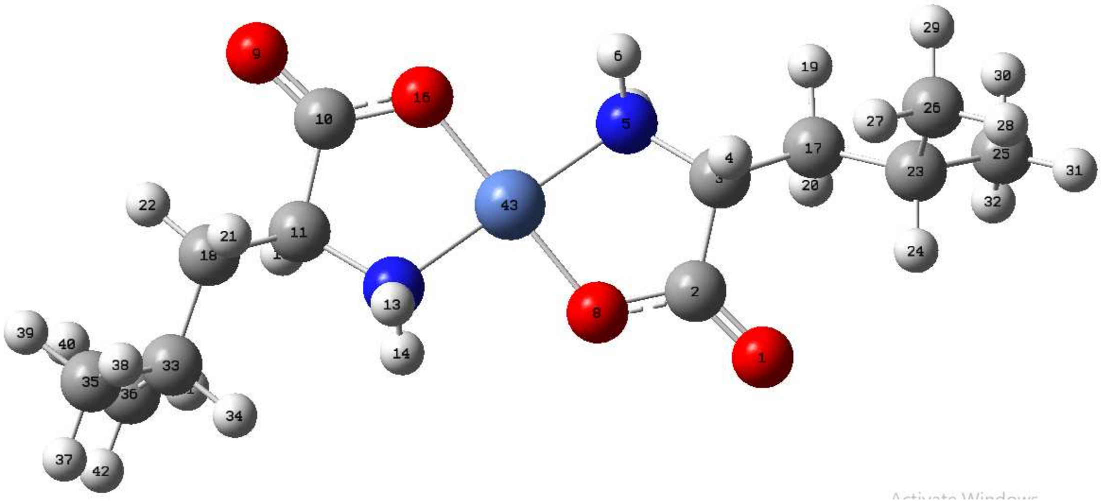

Fig. 3.42: Optimized structure of Ni(leu)$_2$ calculated at B3LYP/SDD level of theory

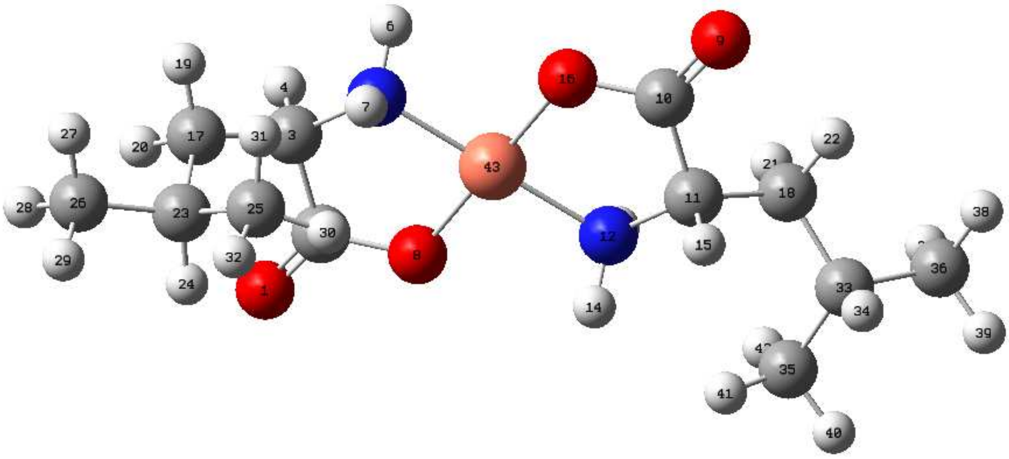

Fig. 3.43: Optimized structure of Cu(leu)$_2$ calculated at B3LYP/SDD level of theory

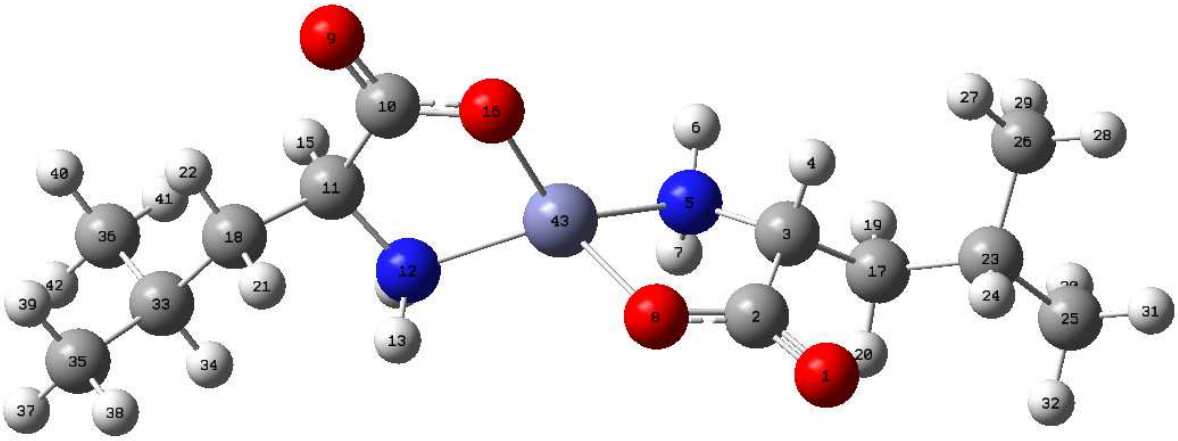

Fig. 3.44: Optimized structure of Zn(leu)$_2$ calculated at B3LYP/SDD level of theory

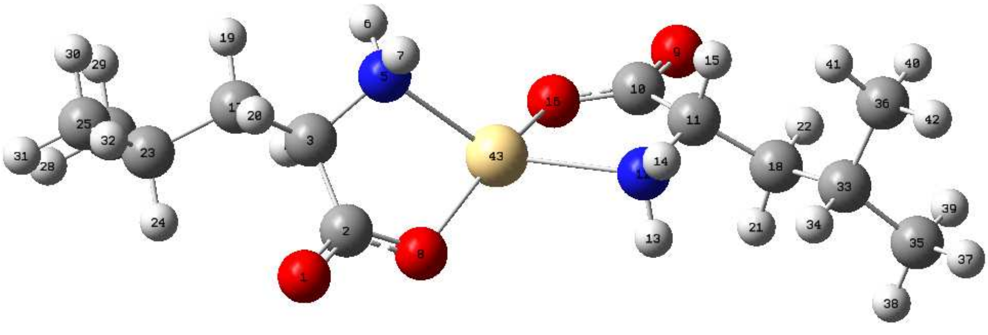

Fig. 3.45: Optimized structure of Cd(leu)$_2$ calculated at B3LYP/SDD level of theory

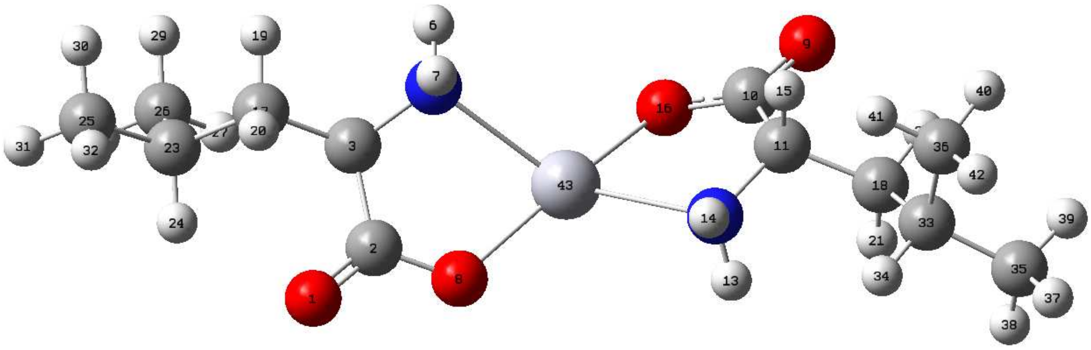

Fig. 3.46: Optimized structure of Hg(leu)$_2$ calculated at B3LYP/SDD level of theory

Table 3.16: Selected bond distances (Å) and angles of leucine

Assignment	Leucine
C=O	1.212
C–O	1.343
C–N	1.459
O–H	0.972
N–H	1.016
O–C–O	122.1
C–O–H	108.5
C–C–N	109.4

The C-O and C-N bond distances have deviated in the complexes compared to the ligand. This may be due to the complex formation with the metal ion. The N-M-O bond angles of the Co, Ni and Cu complexes are close to each other. Therefore they forms square planner structure. The difference in N-M-O bond angles indicates that the Zn, Cd and Hg complexes form distorted tetrahedral structure [59, 113-117].

Table 3.17: Selected bond distances (Å) and angles of the metal-leucine complexes

	$Co(leu)_2$	$Ni(leu)_2$	$Cu(leu)_2$	$Zn(leu)_2$	$Cd(leu)_2$	$Hg(leu)_2$
M–O	1.884	1.854	1.815	1.976	2.126	2.128
M–O	1.882	1.854	1.817	1.991	2.115	2.125
M–N	1.969	1.921	1.929	2.068	2.339	2.488
M–N	1.973	1.925	1.928	2.068	2.334	2.521
O–C	1.340	1.338	1.379	1.325	1.336	1.342
O–C	1.338	1.336	1.381	1.324	1.332	1.348
N–C	1.513	1.511	1.516	1.510	1.512	1.502
N–C	1.510	1.512	1.517	1.511	1.518	1.497
C–C	1.547	1.545	1.545	1.559	1.571	1.563
C–C	1.548	1.547	1.549	1.559	1.572	1.565
C=O	1.258	1.258	1.228	1.265	1.251	1.250
C=O	1.258	1.258	1.228	1.265	1.252	1.248
N–M–O	85.6	86.9	87.6	85.0	78.1	75.2
N–M–O	85.9	86.4	87.8	83.6	77.6	74.5
N–M–O	94.5	93.6	92.3	127.5	115.9	112.3
N–M–O	94.1	93.1	92.3	118.5	111.9	113.9
M–N–C	110.3	110.4	110.8	108.7	108.4	107.3
M–N–C	110.5	110.1	111.4	107.9	103.7	101.0
M–O–C	117.1	116.8	117.0	115.6	118.2	120.4
M–O–C	117.4	116.7	117.1	115.9	119.9	121.8

The binding energy of the complexes is calculated in terms of gas phase electronic energy, enthalpy and Gibbs free energy. These are summarized in Table 3.18. The positive ΔH and ΔG values indicate that the process of formation of the complexes is endothermic i.e not spontaneous [59, 113-117].

Table 3.18: Cation-binding energy, enthalpy, Gibbs free energy (Kcal/mol) of metal-leucine complexes calculated at B3LYP/SDD level of theory

	$Co(leu)_2$	$Ni(leu)_2$	$Cu(leu)_2$	$Zn(leu)_2$	$Cd(leu)_2$	$Hg(leu)_2$
ΔE	-31865	426.7	709.1	-3250.5	577.3	621.2
ΔH	219.6	426.7	709.1	514.5	577.3	621.2
ΔG	244.7	451.8	734.2	539.6	533.4	646.3

3.3.1.8.2 Vibrational frequencies: The computed IR frequencies of the complexes have been visualized and confirmed by Gauss view program. The spectrums are shown in Fig. 3.47 to Fig. 3.53. The IR frequencies and their intensities of the complexes are compared with the ligand in Table 3.19. The computed IR frequencies are compared with the experimental values in Table 3.20. The experimental IR vibrational frequencies are very consistent with the calculated values.

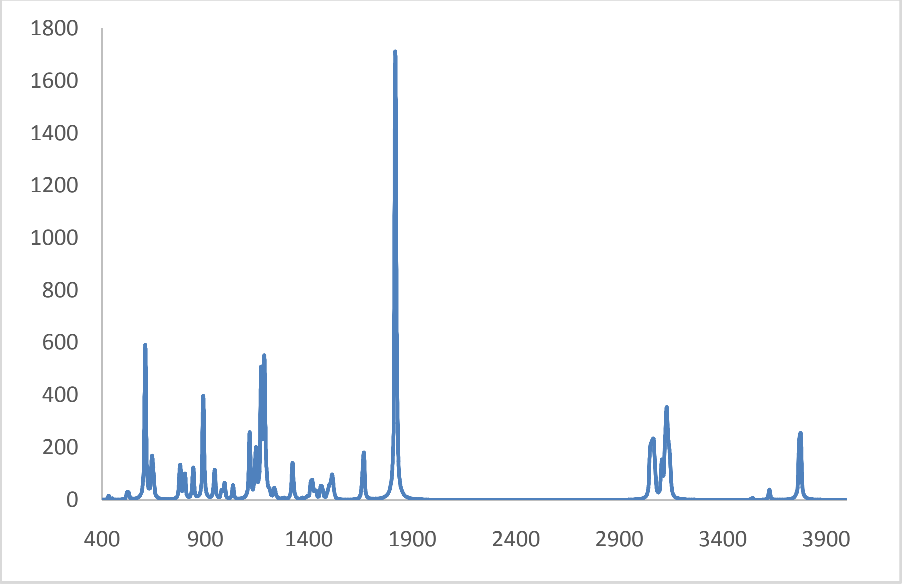

Fig. 3.47: Calculated IR spectrum of leucine

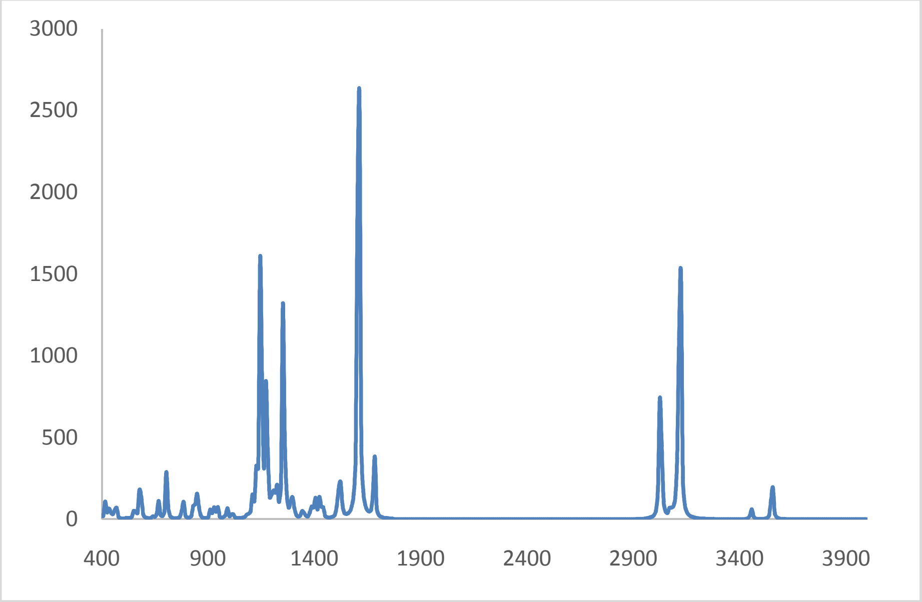

Fig. 3.48: Calculated IR spectrum of Co(leu)$_2$

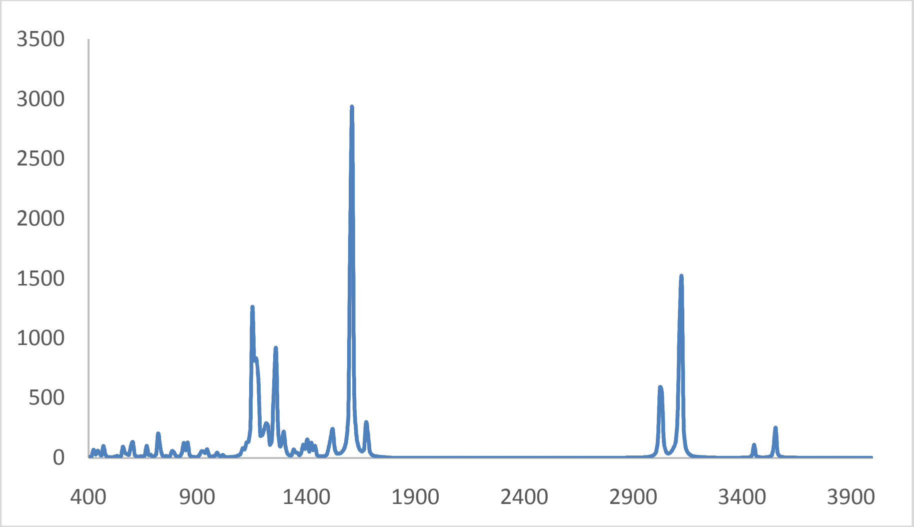

Fig. 3.49: Calculated IR spectrum of Ni(leu)$_2$

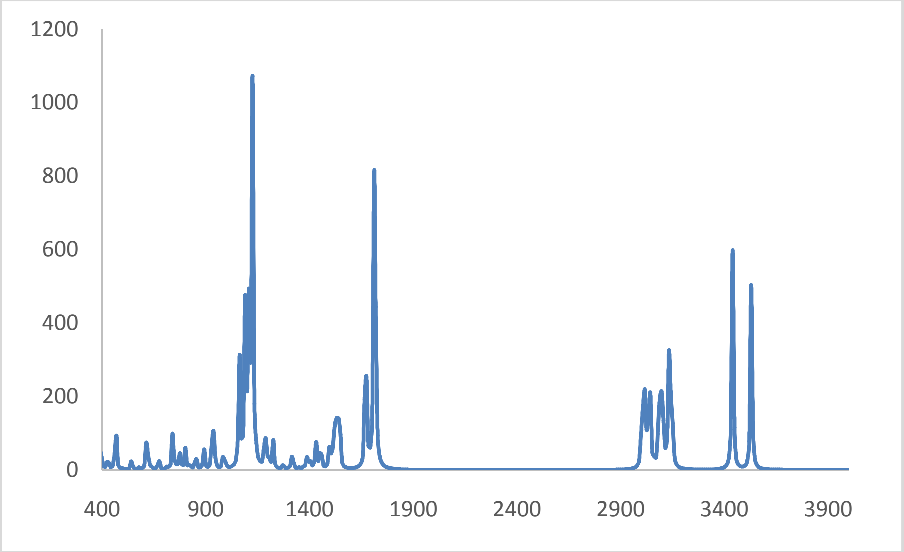

Fig. 3.50: Calculated IR spectrum of Cu(leu)$_2$

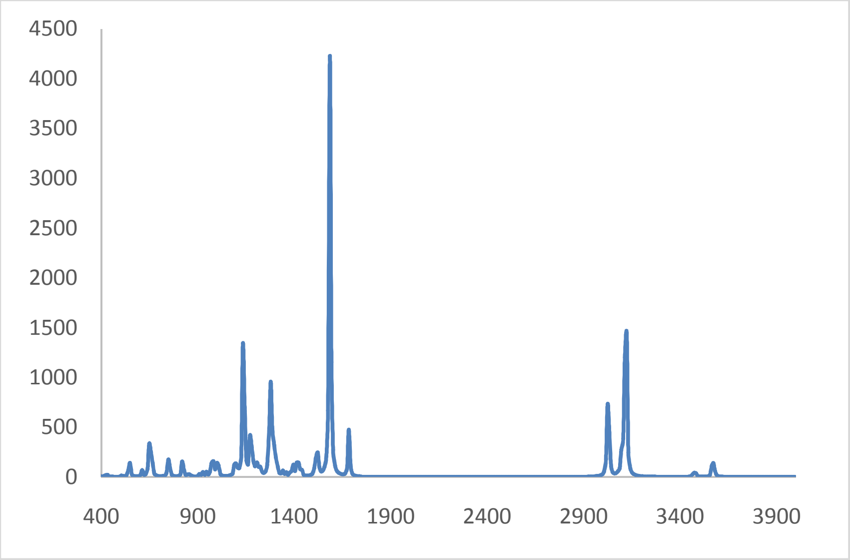

Fig. 3.51: Calculated IR spectrum of Zn(leu)$_2$

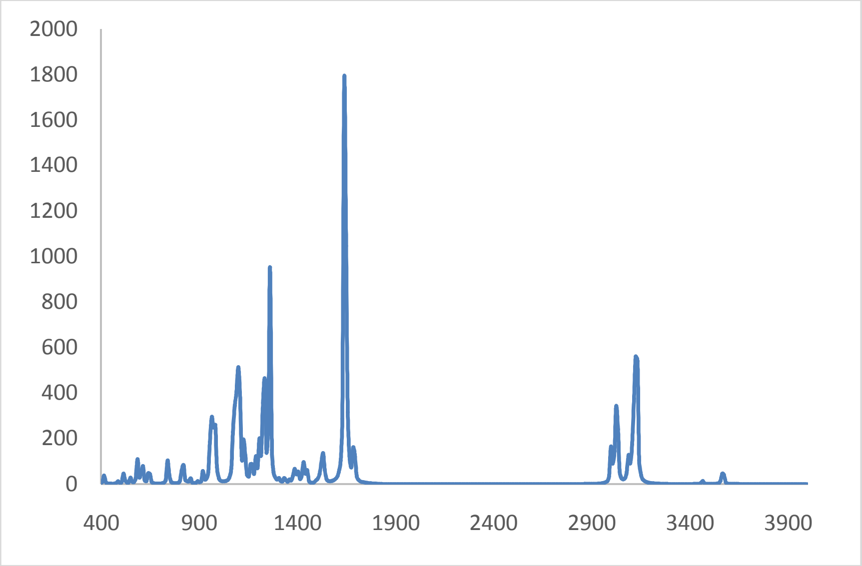

Fig. 3.52: Calculated IR spectrum of Cd(leu)$_2$

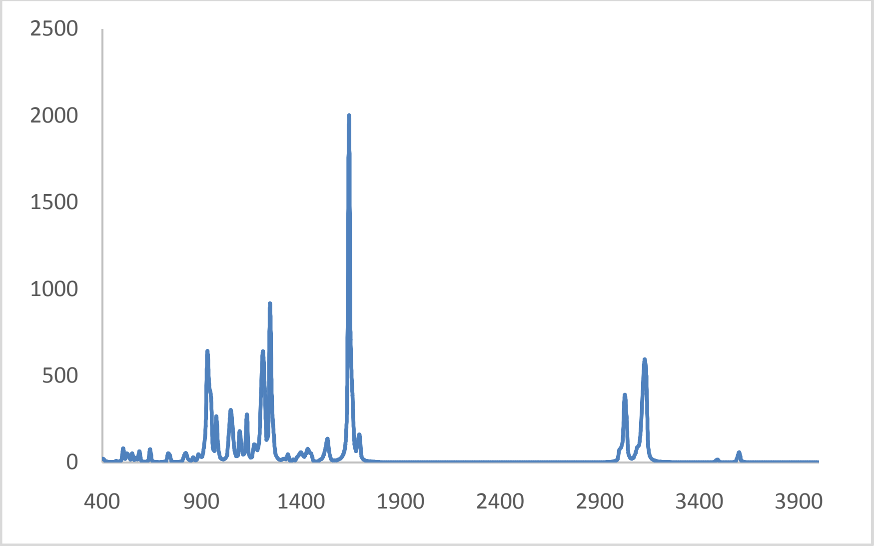

Fig. 3.53: Calculated IR spectrum of Hg(leu)$_2$

Table 3.19: Comparison of calculated IR frequencies and their intensities of the metal-leucine complexes (intensities in parentheses)

Compound	N–Hstr. (asymm)	N–H str. (symm)	C–H str.	C=O str.	N–H bending
Leucine	3622(11)	3540(3)	3068(36)	1817(587)	1661(67)
Co(leu)$_2$	3555(44)	3457(13)	3121(175)	1607(1465)	1679(86)
Ni(leu)$_2$	3555(49)	3453(19)	3120(172)	1607(1545)	1676(80)
Cu(leu)$_2$	3529(94)	3437(159)	3002 (68)	1712 (249)	1668 (91)
Zn(leu)$_2$	3576(45)	3479(15)	3119(178)	1584(1171)	1681(80)
Cd(leu)$_2$	3570(14)	3467(3)	3127(83)	1650(100)	1686(27)
Hg(leu)$_2$	3600(14)	3491(4)	3127(77)	1650(215)	1688(46)

Table 3.20: Comparison of the scaled IR frequencies of the metal-leucine complexes with the experimental values (experimental values in parentheses)

Compound	N–H str. (asymm)	N–H str. (symm)	C–H str.
Leucine	3482 (3070)	3403 (3070)	2949 (2960)
Co(leu)$_2$	3424(3360)	3329(3300)	3006(2950)
Ni(leu)$_2$	3424(3360)	3325(3300)	3005(2950)
Cu(leu)$_2$	3399(3325)	3310(3250)	2891 (2975)
Zn(leu)$_2$	3444(3325)	3351(3260)	3004(2960)
Cd(leu)$_2$	3438(3350)	3339(3250)	3012(2960)
Hg(leu)$_2$	3467(3150)	3362(3100)	3012(2960)

Scaling factor 0.9613 is applied

3.3.1.8.3 UV-Visible spectral analysis: The UV-Visible absorption spectrum of the complexes were calculated at B3LYP/SDD and B3LYP/6-31+G(d,p) level of theory and are displayed from Fig. 3.54 to Fig. 3.60. The corresponding absorption properties are tabulated from Table 3.21 to Table 3.27. It was observed that the calculated results are very consistent with the experimental results.

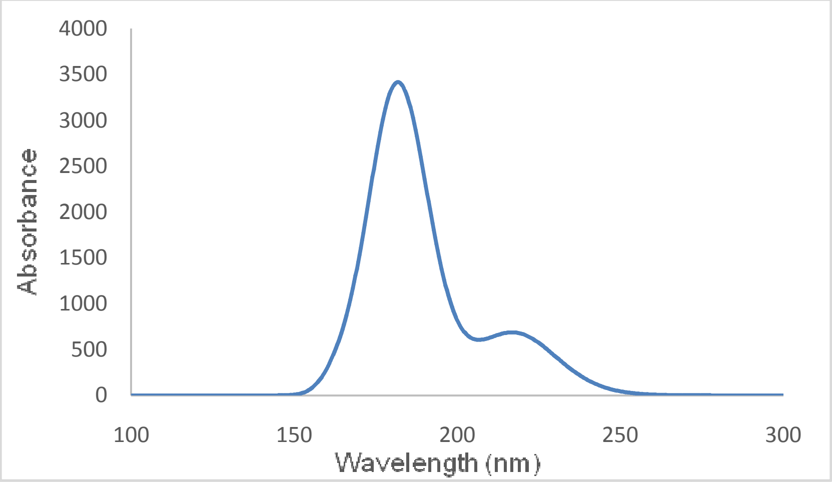

Fig. 3.54: Calculated UV-Vis spectrum of leucine

Table 3.21: The absorption properties of leucine calculated at CAM- B3LYP/6 31+G(d,p) level of theory

Wavelength	Excitation energies (eV)	Oscillator strengths	MO contribution	Assignments
224	5.51	0.0051	H-1 → L (13.3%)	
			H → L (83.2%)	IL
219	5.64	0.0035	H-1 → L (73.9%)	IL
			H → L (15.0%)	
214	5.78	0.0090	H → L+1 (72.2%)	IL
			H → L+2 (21.6%)	

d-d = d-d transition, CT = charge transfer transition, IL = Intraligand charge transfer

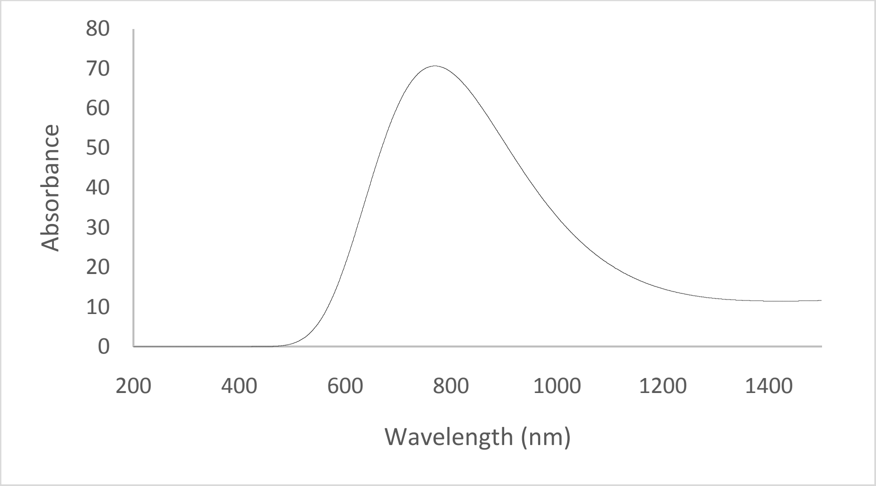

Fig. 3.55: Calculated UV-Vis spectrum of $Co(leu)_2$

Table 3.22: The absorption properties of $Co(leu)_2$ calculated at CAM- B3LYP/6 31+G(d,p) level of theory

Wavelength	Excitation energies (eV)	Oscillator strengths	MO contribution	Assignments
795	1.56	0.0009	H-5 → L (89.5%)	d-d
769	1.61	0.0001	H-6 → L (89.8%)	d-d

d-d = d-d transition, CT = charge transfer transition, IL = Intraligand charge transfer

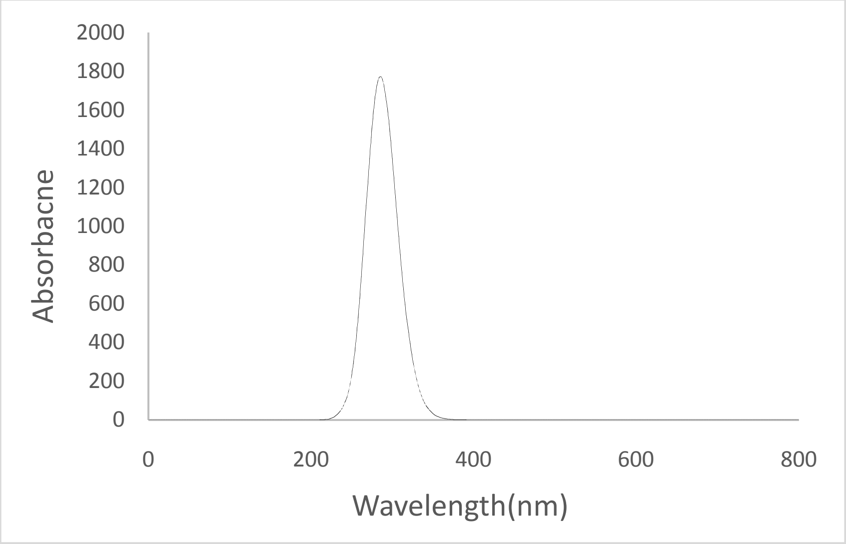

Fig. 3.56: Calculated UV-Vis spectrum of $Ni(leu)_2$

Table 3.23: The absorption properties of $Ni(leu)_2$ calculated at CAM- B3LYP/6 31+G(d,p) level of theory

Wavelength	Excitation energies (eV)	Oscillator strengths	MO contribution	Assignments
604	2.05	0	H → L (82.8%)	d-d
569	2.18	0	H-3 → L (69.9%)	d-d
482	2.57	0	H-5 → L (91.4%)	CT
470	2.64	0	H-7 → L (47.2%)	CT
285	4.34	0.0435	H-1 → L (90.1%)	IL
273	4.54	0	H-2 → L (55.9%)	IL
256	4.83	0.0012	H-4 → L (94.7%)	IL
249	4.96	0	H → L+1 (42.0%)	IL
248	4.99	0.0005	H → L+1 (46.6%)	IL
245	5.06	0.0002	H-1→L+2 (24.1%)	IL

d-d = d-d transition, CT = charge transfer transition, IL = Intraligand charge transfer

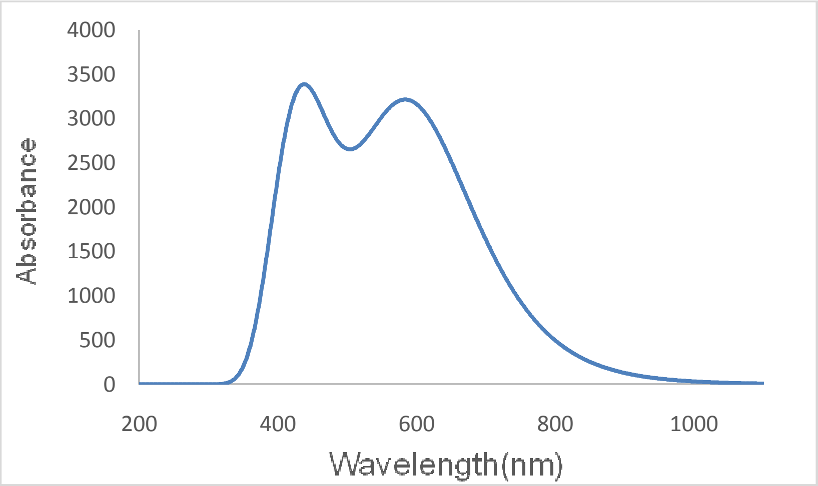

Fig. 3.57: Calculated UV-Vis spectrum of $Cu(leu)_2$

Table 3.24: The absorption properties of Cu(leu)$_2$ calculated at CAM- B3LYP/6 31+G(d,p) level of theory

Wavelength	Excitation energies (eV)	Oscillator strengths	MO contribution	Assignments
664	1.86	0.0002	H-2 → L (53.8%)	d-d
607	2.04	0.0073	H-1 → L (73.6%)	d-d
590	2.10	0.0689	H → L (67.4%)	d-d
493	2.51	0.0001	H-9 → L (65.4%)	CT
450	2.75	0.0268	H-4 → L (55.9%)	CT
447	2.77	0.0009	H-3 → L (93.8%)	CT
435	2.85	0.0026	H-7 → L (57.3%)	CT
427	2.90	0.0257	H-5 → L (68.4%)	CT
425	2.92	0.0274	H-6 → L (59.1%)	CT
420	2.95	0.0008	H-8 → L (84.4%)	CT

d-d = d-d transition, CT = charge transfer transition, IL = Intraligand charge transfer

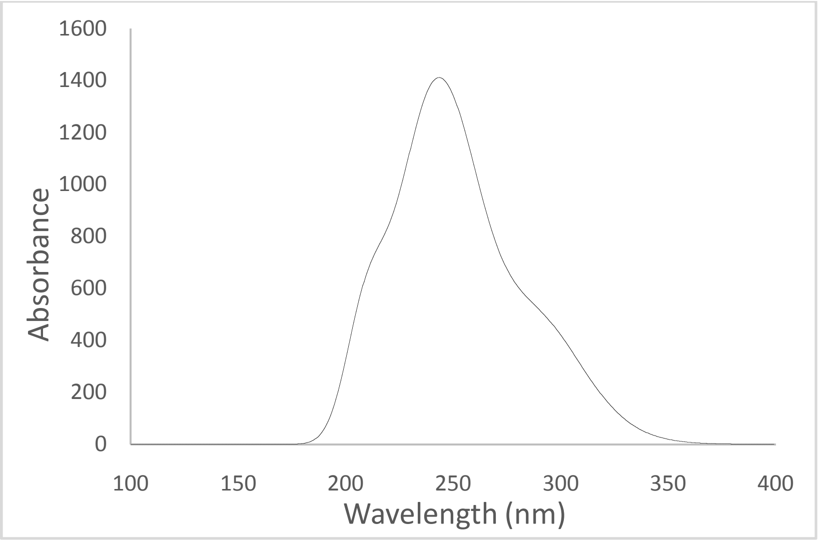

Fig. 3.58: Calculated UV-Vis spectrum of Zn(leu)$_2$

Table 3.25 **The absorption properties of Zn(leu)$_2$ calculated at CAM- B3LYP/6 31+G(d,p) level of theory**

Wavelength	Excitation energies (eV)	Oscillator strengths	MO contribution	Assignments
293	4.23	0.0069	H → L (95.1%)	IL
289	4.28	0.0036	H-1 → L (95.1%)	IL
256	4.83	0.0092	H-2 → L (95.2%)	IL
254	4.87	0.0082	H-3 → L (97.9%)	IL
249	4.98	0.0006	H-1 → L+1 (42.8%)	IL
241	5.13	0.0019	H → L+3 (43.0%)	IL
240	5.15	0.0109	H-4 → L (90.5%)	IL
233	5.32	0.0126	H-5 → L (97.3%)	IL
212	5.84	0.0134	H → L+1 (60.8%)	IL
202	6.13	0.0021	H-4 → L+1 (41.3%)	IL

d-d = d-d transition, CT = charge transfer transition, IL = Intraligand charge transfer

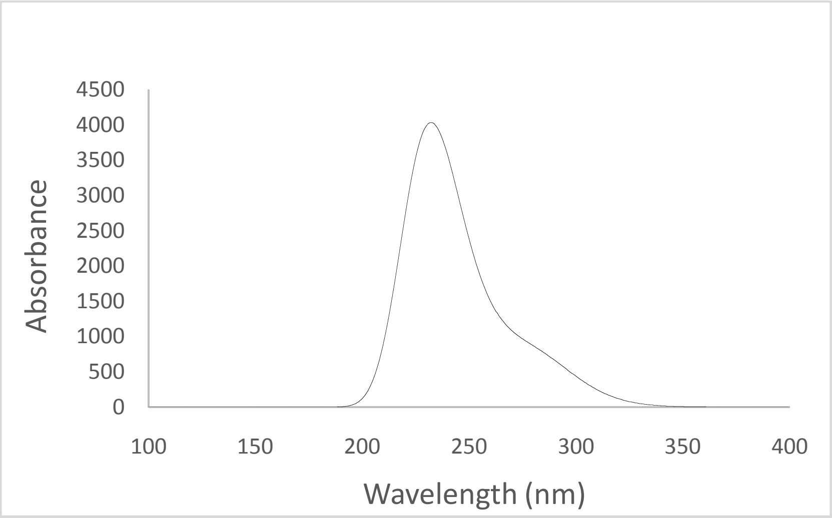

Fig. 3.59: Calculated UV-Vis spectrum of Cd(leu)$_2$

Table 3.26: The absorption properties of $Cd(leu)_2$ calculated at CAM- B3LYP/6 31+G(d,p) level of theory

Wavelength	Excitation energies (eV)	Oscillator strengths	MO contribution	Assignments
285	4.34	0.0069	H → L (97.2%)	IL
277	4.46	0.0103	H-1 → L (94.8%)	IL
252	4.91	0.0041	H-2 → L (50.8%)	IL
251	4.93	0.0094	H-2 → L (50.8%) H-1 → L+1 (21.9%)	IL
249	4.97	0.0079	H-3 → L (74.0%)	IL
241	5.14	0.0030	H → L+4 (43.0%)	IL
238	5.20	0.0014	H-4 → L (85.6%)	IL
232	5.34	0.0717	H-5 → L (91.1%)	IL
222	5.57	0.0103	H → L+1 (37.6%) H → L+2 (26.1%)	IL
221	5.60	0.0134	H → L+1 (38.2%) H → L+2 (57.5%)	IL

d-d = d-d transition, CT = charge transfer transition, IL = Intraligand charge transfer

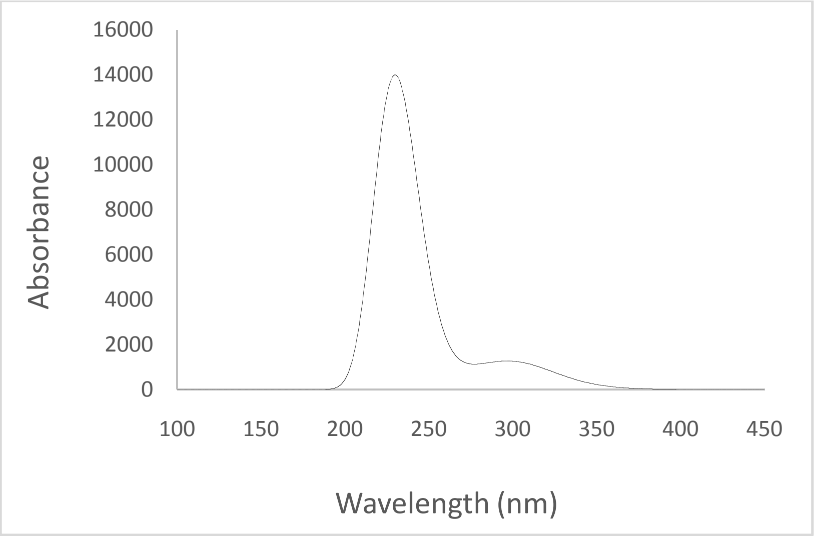

Fig. 3.60: Calculated UV-Vis spectrum of $Hg(leu)_2$

Table 3.27: The absorption properties of $Hg(leu)_2$ calculated at CAM- B3LYP/6 31+G(d,p) level of theory

Wavelength	Excitation energies (eV)	Oscillator strengths	MO contribution	Assignments
316	3.91	0.0062	H → L (97.1%)	IL
302	4.10	0.0201	H-1 → L (94.7%)	IL
276	4.48	0.0106	H-3 → L (24.4%) H-2 → L (68.4%)	IL
275	4.50	0.0031	H-3 → L (70.4%)	IL
255	4.85	0.0010	H-4 → L (83.5%)	IL
253	4.90	0.0004	H-1 → L+2 (64.0%)	IL
245	5.05	0.0013	H → L+4 (42.1%) H → L+1 (32.2%)	IL
235	5.25	0.1751	H-5 → L (84.0%)	IL
225	5.50	0.0441	H → L+1 (46.0%)	IL
224	5.51	0.1614	H-6 → L (72.9%)	IL

d-d = d-d transition, CT = charge transfer transition, IL = Intraligand charge transfer

UV–Vis studies reveal that Co, Ni and Cu complex demonstrate characteristic metal to ligand charge transfer (MLCT) or ligand to metal charge transfer (LMCT) and d–d transitions bands. On the other hand Zn, Cd and Hg complex does not show any charge transfer or d-d transition bands. This is reasonable since the respective metal ions in the later case have d^{10} configuration [59, 113-117].

3.3.1.8.4 Frontier molecular orbital: Selected frontier molecular orbital of leucine and its complexes is displayed from Fig. 3.61 to Fig. 3.67 and the corresponding molecular orbital energy is listed in Table 3.28 and Table 3.29.

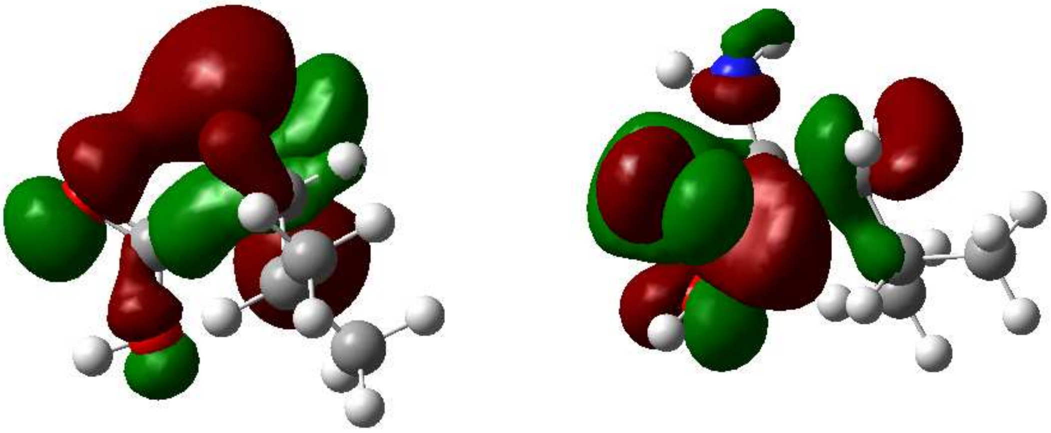

HOMO LUMO

Fig. 3.61: HOMO and LUMO of leucine

Table 3.28: Energies (Hartree) of HOMO and LUMO orbital's, HOMO-LUMO gaps are calculated at B3LYP/SDD level of theory for leucine

HOMO-5	-0.44	LUMO+5	0.03	
HOMO-4	-0.44	LUMO+4	0.02	
HOMO-3	-0.42	LUMO+3	0.01	
HOMO-2	-0.38	LUMO+2	0.00	
HOMO-1	-0.36	LUMO+1	-0.02	
HOMO	-0.34	LUMO	-0.11	0.23

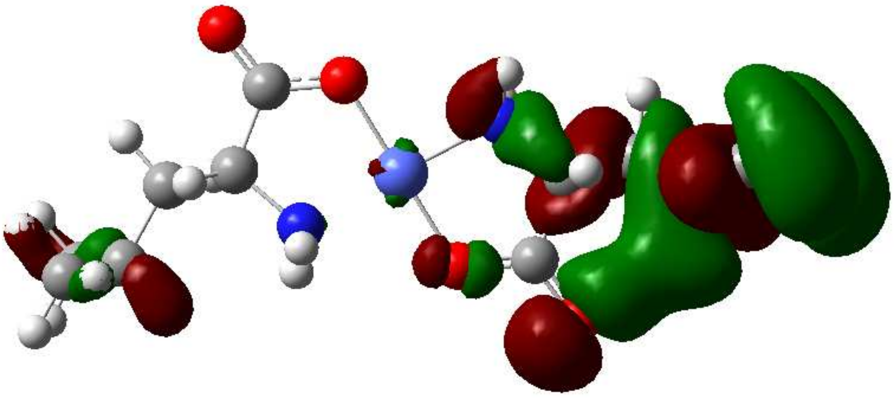

Co(leu)$_2$: HOMO-5

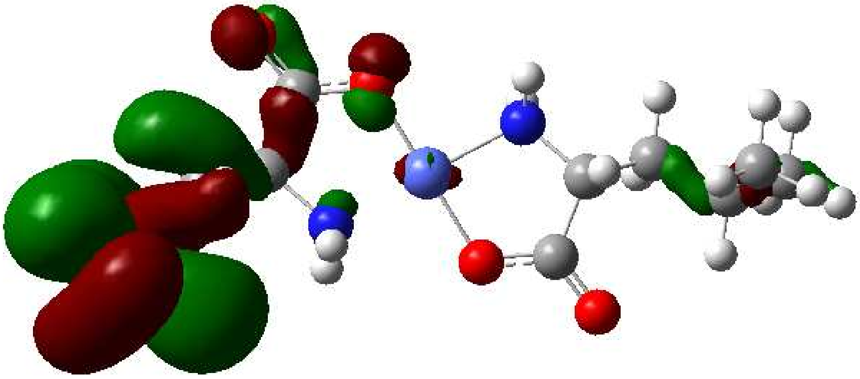

Co(leu)$_2$: HOMO-4

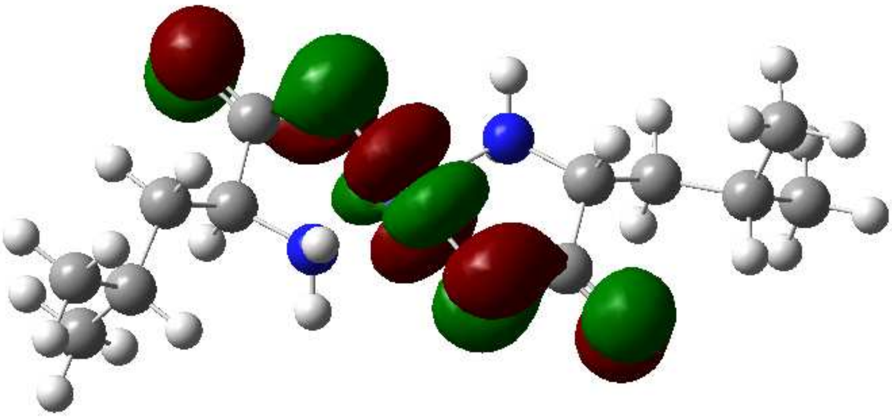

Co(leu)$_2$: LUMO

Fig. 3.62: HOMO and LUMO of Co(leu)$_2$

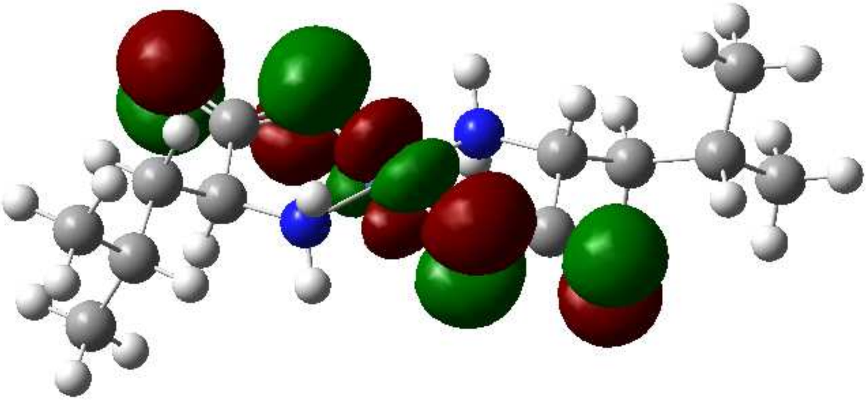

Ni(leu)$_2$: HOMO

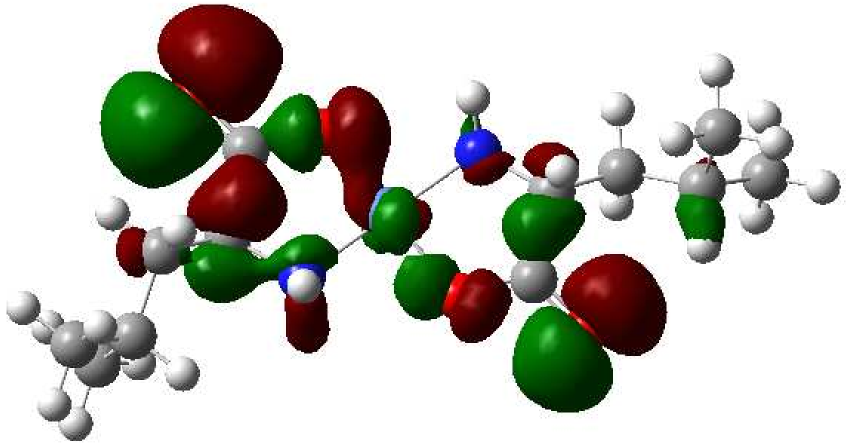

Ni(leu)$_2$: HOMO-1

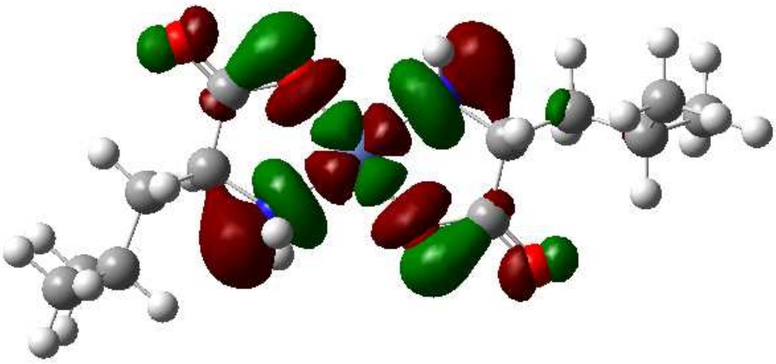

Ni(leu)$_2$: LUMO

Fig. 3.63: HOMO and LUMO of Ni(leu)$_2$

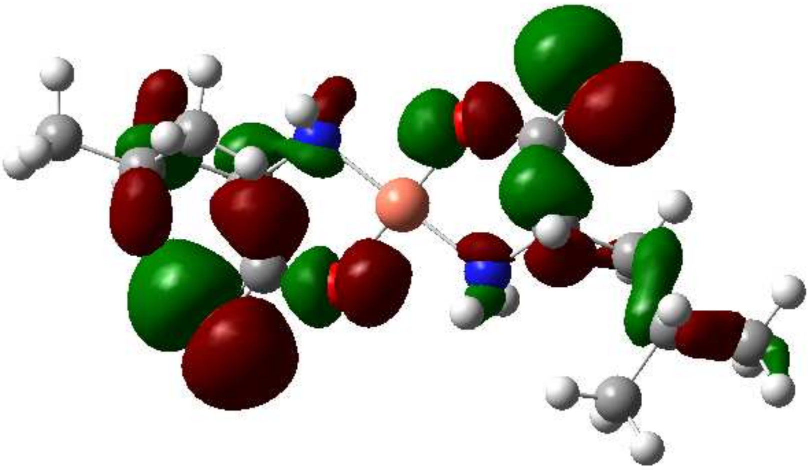

Cu(leu)$_2$: HOMO

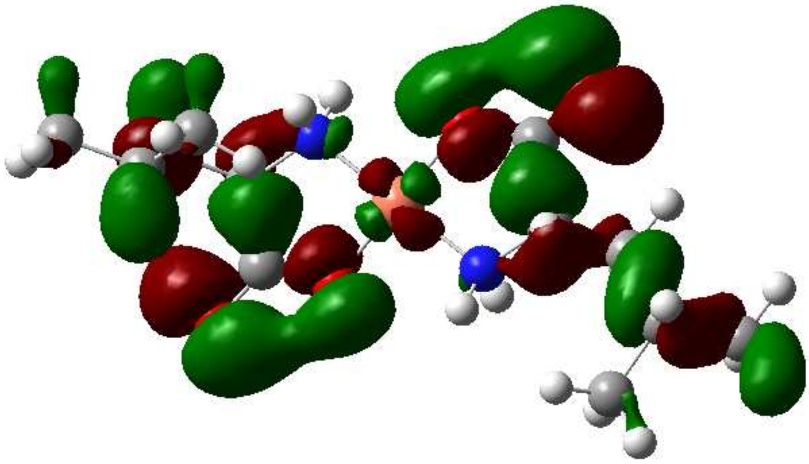

Cu(leu)$_2$: HOMO-1

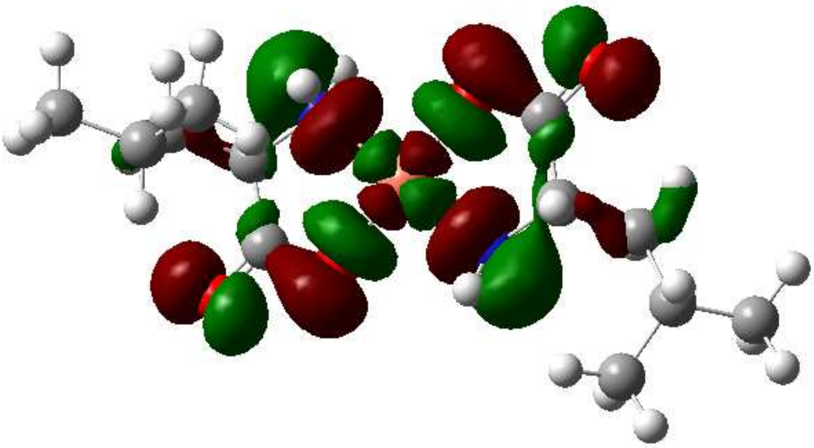

Cu(leu)$_2$: LUMO

Fig. 3.64: HOMO and LUMO of Cu(leu)$_2$

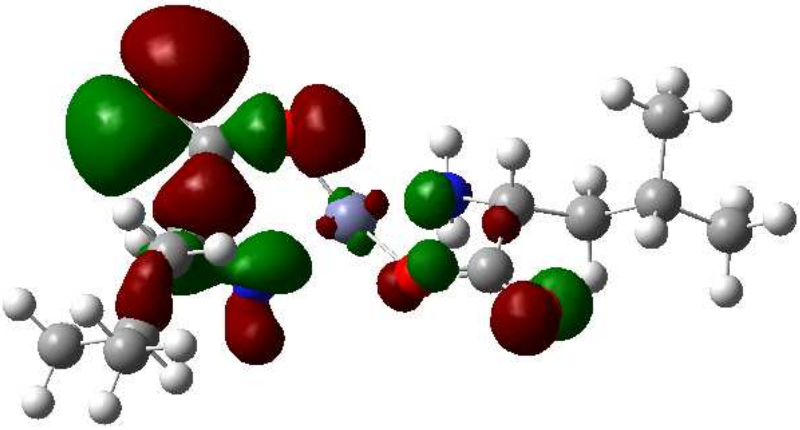

$Zn(leu)_2$: HOMO

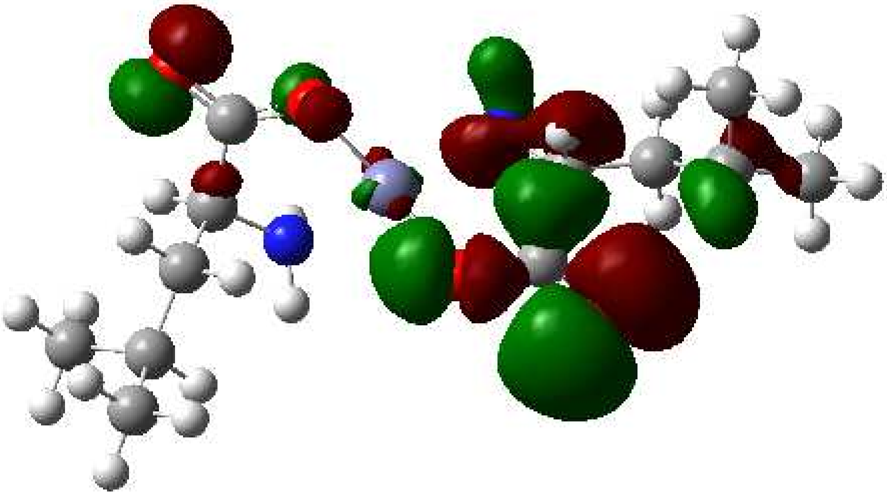

$Zn(leu)_2$: HOMO-1

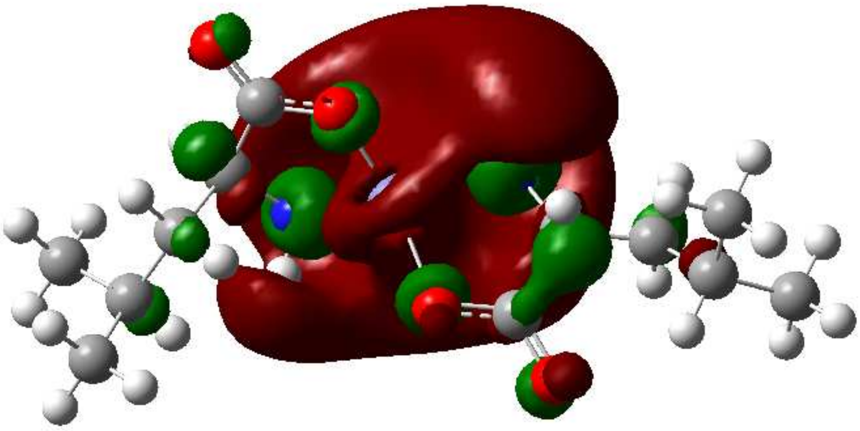

$Zn(leu)_2$: LUMO

Fig. 3.65: HOMO and LUMO of $Zn(leu)_2$

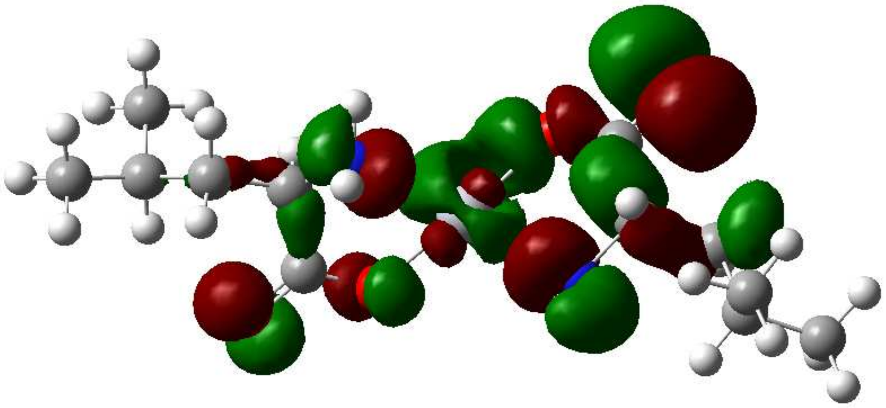

Hg(leu)$_2$: HOMO

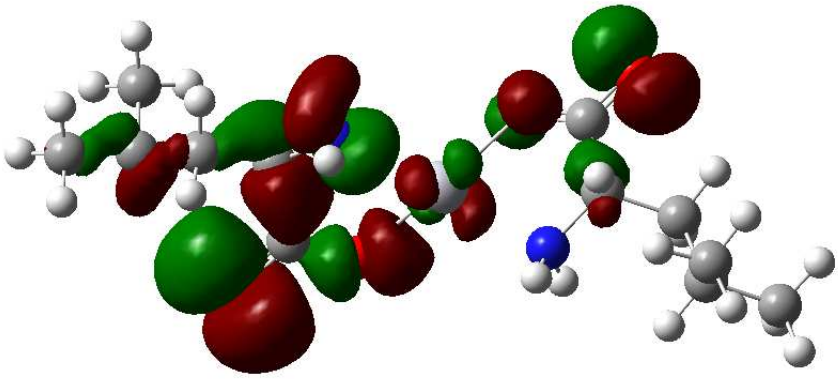

Hg(leu)$_2$: HOMO-1

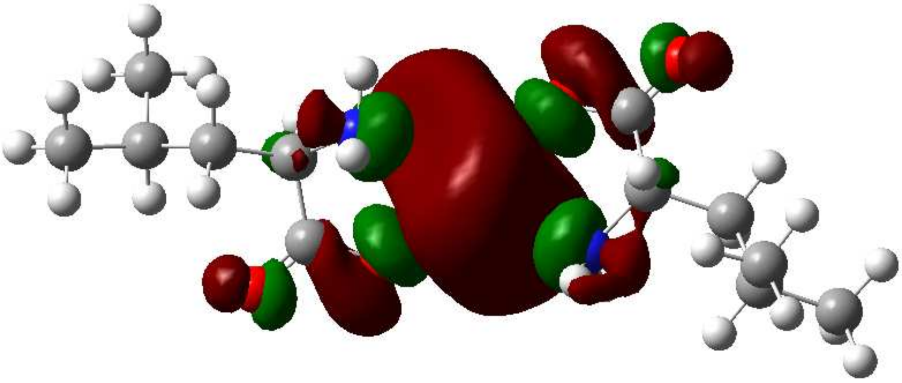

Hg(leu)$_2$: LUMO

Fig. 3.66: HOMO and LUMO of Hg(leu)$_2$

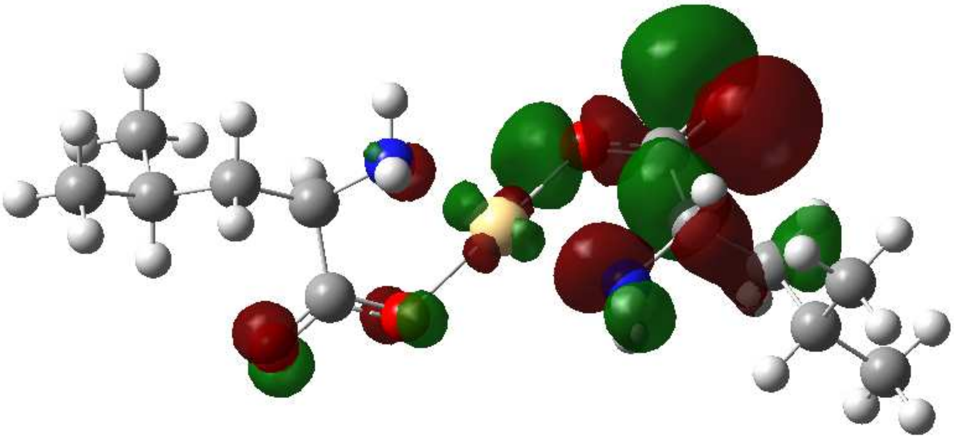

Cd(leu)$_2$: HOMO

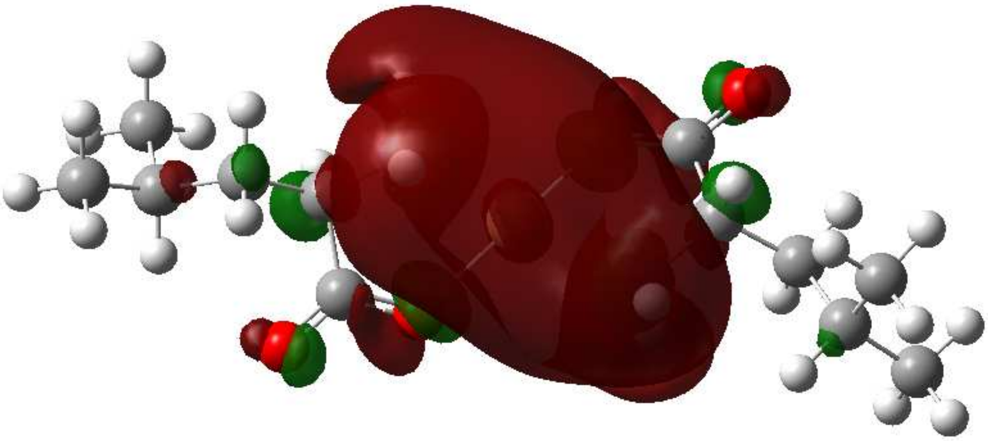

Cd(leu)$_2$: LUMO

Fig. 3.67: HOMO and LUMO of Cd(leu)$_2$

Table. 3.29: Energies (Hartree) of HOMO and LUMO orbital's, HOMO-LUMO gaps are calculated at B3LYP/SDD level of theory for all metal-leucine complexes

Molecular orbital	Co(leu)$_2$	Ni(leu)$_2$	Cu(leu)$_2$	Zn(leu)$_2$	Cd(leu)$_2$	Hg(leu)$_2$
HOMO-5	-0.36	-0.30	-0.45	-0.29	-0.28	-0.29
HOMO-4	-0.36	-0.27	-0.45	-0.29	-0.28	-0.29
HOMO-3	-0.25	-0.27	-0.44	-0.27	-0.27	-0.28
HOMO-2	-0.24	-0.26	-0.44	-0.27	-0.27	-0.27
HOMO-1	-0.23	-0.24	-0.43	-0.25	-0.25	-025
HOMO	-0.22	-0.24	-0.42	-0.24	-0.24	-0.24
LUMO	-0.16	-0.05	-0.32	-0.04	-0.06	-0.08
LUMO+1	-0.12	-0.02	-0.16	0.00	-0.02	-0.02
LUMO+2	-0.12	-0.01	-0.16	0.01	-0.01	-0.02
LUMO+3	-0.08	0.00	-0.15	0.02	0.01	0.00
LUMO+4	-0.07	0.02	-0.13	0.03	0.02	0.01
LUMO+5	-0.06	0.03	-0.12	0.04	0.03	0.02
GAP	0.06	0.19	0.10	0.20	0.18	0.16

The HOMO-LUMO gap of the complexes is decreased from the parent leucine. Therefore metal has a noticeable effect on the frontier molecular orbital energies [59, 113-117].

3.3.1.9 Antimicrobial activity: Attempt was taken to study the antimicrobial activity of the complexes. The samples are insoluble in water. Therefore it was not possible to get any information in this field.

3.3.2 Characterization of the metal-isoleucine complexes

The complexes were prepared by direct reaction between aqueous solution of the metal salt and anionic isoleucine (section 3.2.3). The precipitate formed was filtered, washed and dried over silica gel.

3.3.2.1 Formulation

Elemental analysis is the prime tool for the formulation of any new chemical species. The formulation of the prepared complexes were done by comparing the elemental (C, H and N) and metal analysis data and the calculated values.

3.3.2.1.1 Elemental analysis: Microanalysis for carbon, hydrogen, nitrogen in the complexes of isoleucine was performed in an elemental micro analyzer. Metals were estimated by complexometric titration method using ordinary laboratory glassware. Chloride content of all the complexes was qualitatively tested by using $AgNO_3$ solution. The complexes didn't respond to this test. Thus chloride is absent in the complexes.

The percent composition of carbon, hydrogen, nitrogen and metal of the complexes are tabulated in Table 3.30. The C, H, N data does not confirm the formation of Pb complex.

Table 3.30: Percent composition of C, H, N and metal in the metal-isoleucine complexes

Compound	% C		% H		% N		% Metal		% Yield based on metal
	Fnd.	Cal.	Fnd.	Cal.	Fnd.	Cal.	Fnd.	Cal.	
$Co(C_6H_{12}NO_2)_2.2H_2O$	41.21	40.56	7.94	7.89	7.91	7.89	15.50	16.62	55
$Ni(C_6H_{12}NO_2)_2.2H_2O$	40.42	40.60	8.08	7.89	7.89	7.89	15.55	16.55	52
$Cu(C_6H_{12}NO_2)_2. H_2O$	42.37	42.17	7.84	7.61	8.20	8.20	17.45	18.59	60
$Zn(C_6H_{12}NO_2)_2.½ H_2O$	36.42	43.11	6.72	7.49	7.06	8.38	18.34	19.46	46
$Cd(C_6H_{12}NO_2)_2$	36.89	38.67	6.12	6.44	7.16	7.52	28.90	30.18	48
$Hg(C_6H_{12}NO_2)_2$	30.10	31.26	4.98	5.21	5.82	6.08	42.89	43.55	50
$Pb(C_6H_{12}NO_2)_2$	4.10	30.82	0.69	5.14	0.79	5.99	-	44.35	-

Cal. = Calculated, Fnd. = Found

Comparing all the experimental data and theoretical values the proposed empirical formula of the complexes are:

Co- isoleucine complex	$Co(C_6H_{12}NO_2)_2.2H_2O$
Ni- isoleucine complex	$Ni(C_6H_{12}NO_2)_2.2H_2O$
Cu- isoleucine complex	$Cu(C_6H_{12}NO_2)_2. H_2O$
Zn- isoleucine complex	$Zn(C_6H_{12}NO_2)_2.½ H_2O$
Cd- isoleucine complex	$Cd(C_6H_{12}NO_2)_2$
Hg- isoleucine complex	$Hg(C_6H_{12}NO_2)_2$

3.3.2.2 Physicochemical properties

The physical appearance, solubility, melting temperature of the complexes were conducted which are described below.

3.3.2.2.1 Solubility: Solubility of a compound actually depends on the mode of interaction between solute and solvent molecule, lattice energy, solvation energy and temperature. Solubility of the complexes was investigated qualitatively at room temperature in some common solvents such as water, methanol, ethanol, acetone, DMSO and is shown in Table 3.31.

Table 3.31: Solubility of the prepared metal-isoleucine complexes

Compound	Appearance	Soluble in	Insoluble in
$Co(C_6H_{12}NO_2)_2.2H_2O$	Pink	CH_3OH	H_2O, C_2H_5OH, CH_3COCH_3, DMSO
$Ni(C_6H_{12}NO_2)_2.2H_2O$	Sky blue	CH_3OH	H_2O, C_2H_5OH, CH_3COCH_3, DMSO
$Cu(C_6H_{12}NO_2)_2. H_2O$	Blue	CH_3OH	H_2O, C_2H_5OH, CH_3COCH_3, DMSO
$Zn(C_6H_{12}NO_2)_2.½ H_2O$	Colorless	-	H_2O, CH_3OH, C_2H_5OH, CH_3COCH_3, DMSO
$Cd(C_6H_{12}NO_2)_2$	Colorless	-	H_2O, CH_3OH, C_2H_5OH, CH_3COCH_3, DMSO
$Hg(C_6H_{12}NO_2)_2$	Colorless	-	H_2O, CH_3OH, C_2H_5OH, CH_3COCH_3, DMSO

The solubility analysis of the complexes indicates that they are insoluble in most of the common solvents. The lattice enthalpy of the complexes may be higher than the salvation energy of the solvents or it may be due to the formation of strong M-O and M-N coordination bond in the complexes or may be due to the presence of a hydrocarbon tail in the ligand part which is the main obstacle for the salvation of the complexes in the mentioned solvents.

3.3.2.2.2 Melting temperature: The temperature at which the solid and the liquid phases of a compound are in equilibrium under a pressure of one atmosphere is referred to as the melting point of the solid compound. Ionic compound has higher melting point than covalent one. The melting temperatures of the complexes are given in the Table 3.32. Melting point of the complexes are more than 250 ^{0}C. The high melting point may be due to the ionic character of the complexes or may be due to the presence of strong M-L bond.

Table 3.32: Melting temperature of prepared metal-isoleucine complexes

Compound	Melting temperature (^{0}C)
$Co(C_6H_{12}NO_2)_2.2H_2O$	>250 ^{0}C
$Ni(C_6H_{12}NO_2)_2.2H_2O$	>250 ^{0}C
$Cu(C_6H_{12}NO_2)_2.\ H_2O$	>250 ^{0}C
$Zn(C_6H_{12}NO_2)_2.½\ H_2O$	>250 ^{0}C
$Cd(C_6H_{12}NO_2)_2$	>250 ^{0}C
$Hg(C_6H_{12}NO_2)_2$	>250 ^{0}C

3.3.2.3 Infrared spectral analysis

The compounds having covalent bonds will be found to absorb various frequencies of electromagnetic radiation in the infrared (IR) region of the spectrum. The IR spectrum originates from the different modes of vibration of a molecule due to the absorption of radiation energy in the IR region. However, it is essential that a change in dipole moment occurs during the vibration. In the absorption process, those frequencies of IR radiation will be absorbed which match the natural vibrational frequencies of the molecule. Since every different type of bond has a different frequency of vibration, and since the same type of bond in two different compounds is in a different environment, no two molecules of different structure will have exactly the same infrared absorption pattern. This is why IR spectrum is a very authentic identity of the compounds which are IR active. Another more important use of the IR spectrum is that it gives structural information about a molecule.

In the present study, a calibrated Fourier Transform Infrared (FTIR) spectrophotometer has been used to record the IR spectrum of the complexes. The design of the optical pathway produces a pattern called an interferogram. An interferogram is essentially a plot of intensity vs time (a time domain spectrum). A mathematical operation known as a Fourier Transform (FT) can separate the individual absorption frequencies from the interferogram, producing a spectrum virtually identical to that obtained with a dispersive spectrometer. There are, however, great advantages in the use of FTIR because all the frequencies are recorded simultaneously; there is an improvement in signal-to-noise (S/N) ratios, and it is easier to study small samples or materials with weak absorptions. In addition to this, the time taken for a full spectral scan is less than 1 second and this makes it possible to obtain improved spectra by carrying out repetitive scans and averaging the collected signals. This is because the S/N ratio is directly related to $\sqrt{n}$, where n is the number of scans. The tentative band assignments have been made empirically on the basis of some standard books [102-104].

3.3.2.3.1 IR spectrum of isoleucine: The FTIR spectrum of isoleucine is shown in Fig. 3.68. All the vibrational frequencies and their tentative band assignments are listed in Table 3.33. A weak broad peak at 3125 cm^{-1} is due to N-H stretching vibration of $^{+}NH_3$ group. The C-H stretching vibration appears at 2960 cm^{-1}. Asymmetric and symmetric stretching vibrations for carboxyl group (COO^-) occurs at around 1500 and 1410 cm^{-1}. Asymmetric and symmetric N-H bending vibration appears at 1590 cm^{-1} and 1450 cm^{-1}. A sharp peak at 1140 cm^{-1} appears due to C-N stretching.

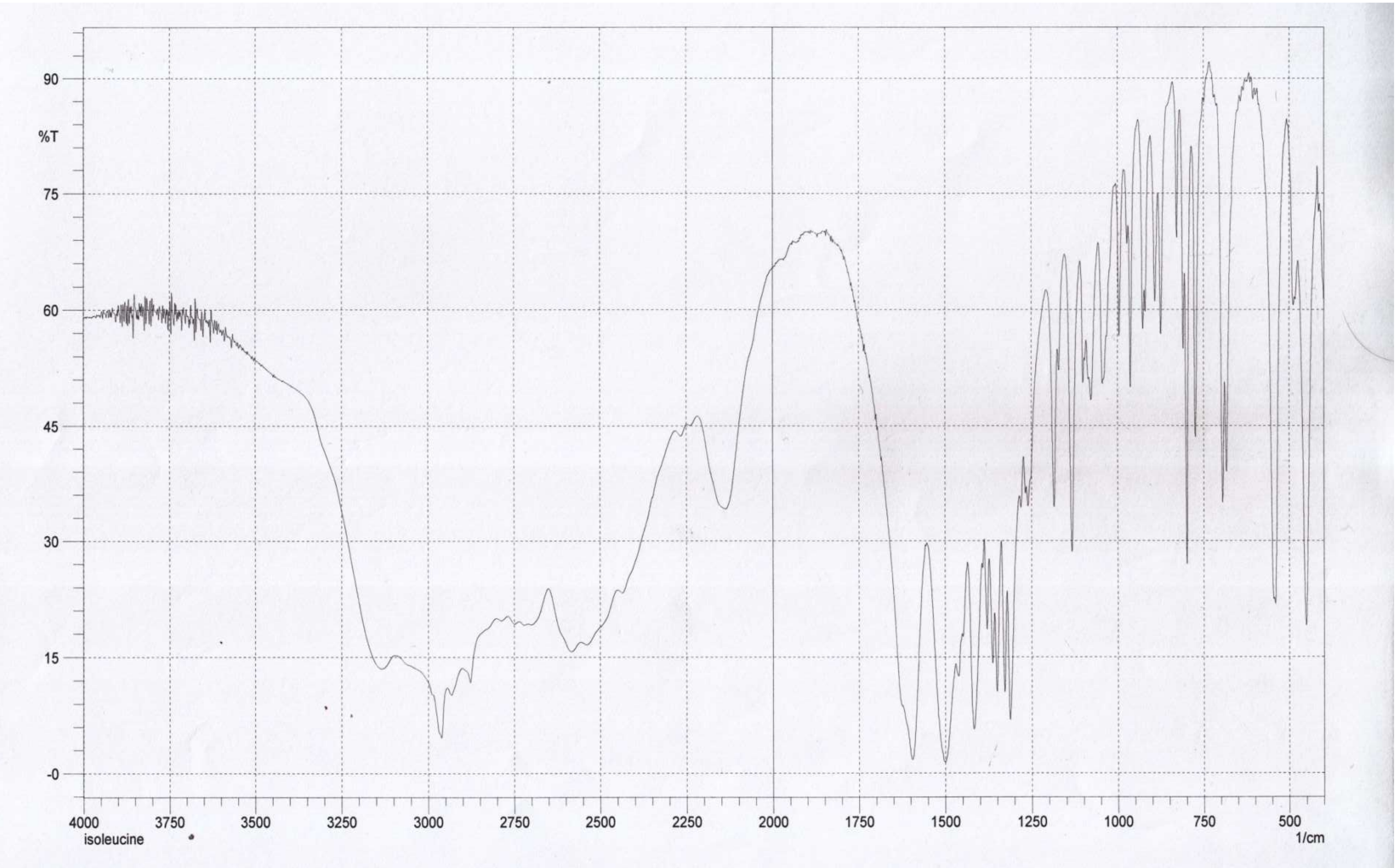

Fig. 3.68: FTIR spectrum of isoleucine ($C_6H_{13}NO_2$)

Table 3.33: Tentative assignment of IR bands of isoleucine ($C_6H_{13}NO_2$)

Wave no. (cm^{-1})	Relative intensity	Tentative band assignment
3125	w, b	$^+NH_3$ stretching
2960	w, sp	-C-H stretching
2550	w, b	
2125	m sp	
1590	s, sp	Asymmetric N-H bending
1500	s, sp	Asymmetric COO^- stretching
1450	w, sh	Symmetric N-H bending
1410	ms, sp	symmetric COO^- stretching
1300	m, sp	
1200	m, sp	
1140	m, sp	C-N stretching
800	s, sp	
700	s, sp	
550	s, sp	

vs = very strong, s = strong, ms = medium strong, m = medium, w = weak, sp = sharp, b = broad, sh = shoulder

3.3.2.3.2 IR spectrum of isoleucine complexes: The FTIR spectrum of metal-isoleucine complexes are shown in Fig. 3.69 to Fig. 3.75. All the vibrational frequencies and their tentative band assignments are listed in Table 3.34 to Table 3.39. In all the complexes two sharp bands between 3100-3350 cm^{-1} appears due to N-H stretching vibration for the free $–NH_2$ group. The C-H stretching vibration appears at around 2960 cm^{-1}. Two sharp peak at around 1575 and 1400 cm^{-1} appears due to asymmetric and symmetric stretching vibrations for carboxyl group (COO^-). Asymmetric and symmetric N-H bending vibration appears at around 1600 cm^{-1} and 1460 cm^{-1}. At around 1100 cm^{-1} C-N stretching vibration appears as a sharp band. In few cases the N-H bending and $–COO^-$ group stretching vibrations overlap with each other and appears as a single band. The pattern of the IR spectrum of the complexes is almost similar with each other with few exceptions. The position and intensity of most of the important bands in all the complexes were changed significantly compare to that of isoleucine which indicate the formation of new compound. The IR spectrum does not confirm the formation of Pb complex.

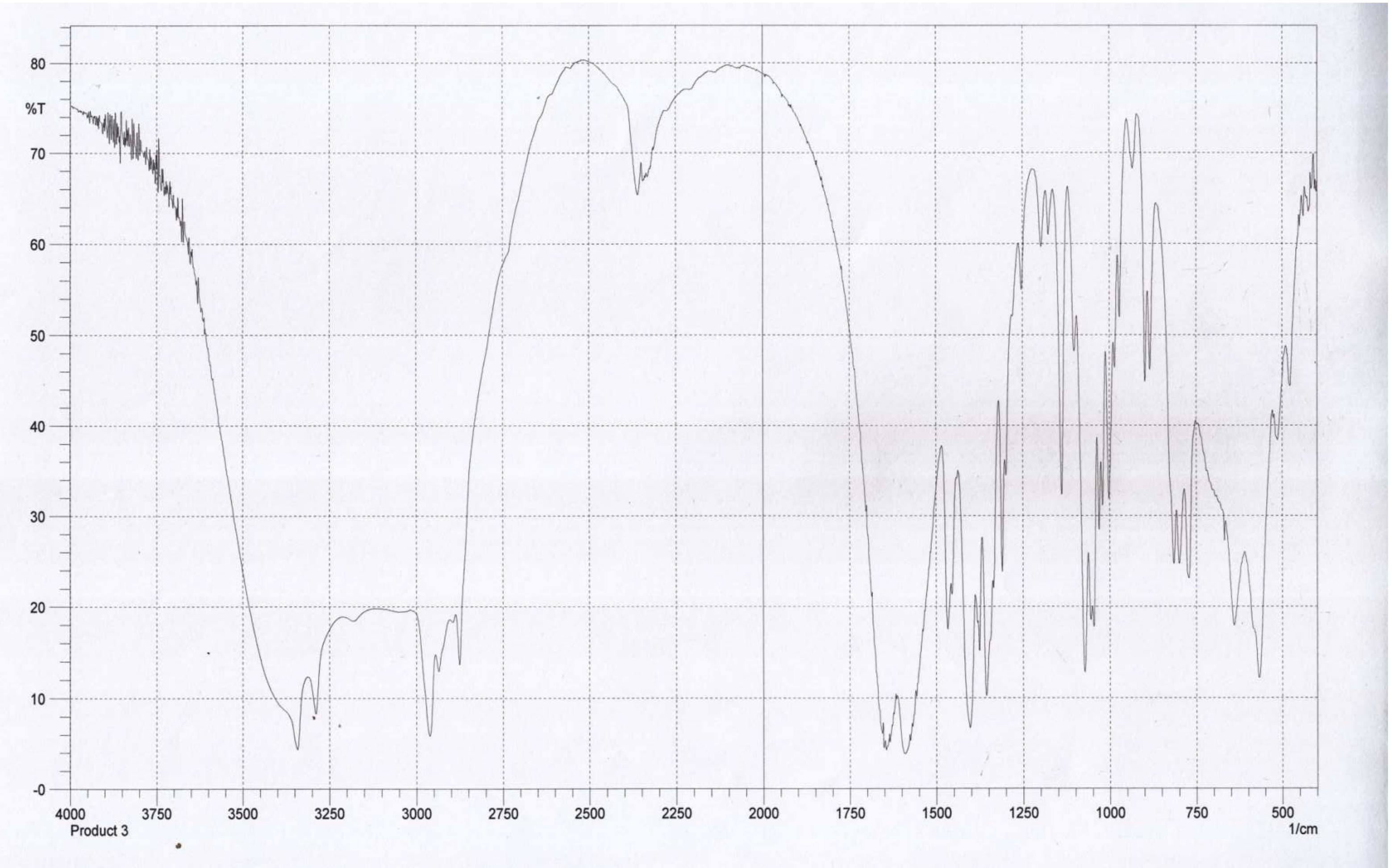

Fig. 3.69: FTIR spectrum of $Co(C_6H_{12}NO_2)_2.2H_2O$

Table 3.34: Tentative assignment of IR bands of $Co(C_6H_{12}NO_2)_2.2H_2O$

Wave no. (cm^{-1})	Relative intensity	Tentative band assignment
3340	w, sp	Asymmetric N-H stretching
3290	w, sp	Symmetric N-H stretching
2960	m, sp	-C-H stretching
2930	w, sh	
2875	m, sp	
1650	m, b	Asymmetric N-H bending and
1590	m, b	Asymmetric COO^- stretching
1460	mS, sp	Symmetric N-H bending
1400	ms, sp	symmetric COO^- stretching
1375	m, sp	
1355	m, sp	
1310	m, sp	
1140	ms, sp	
1100	w, sh	
1075	s, sp	C-N stretching
1045	ms, sp	
760	m, sp	

vs = very strong, s = strong, ms = medium strong, m = medium, w = weak, sp = sharp, b = broad, sh = shoulder

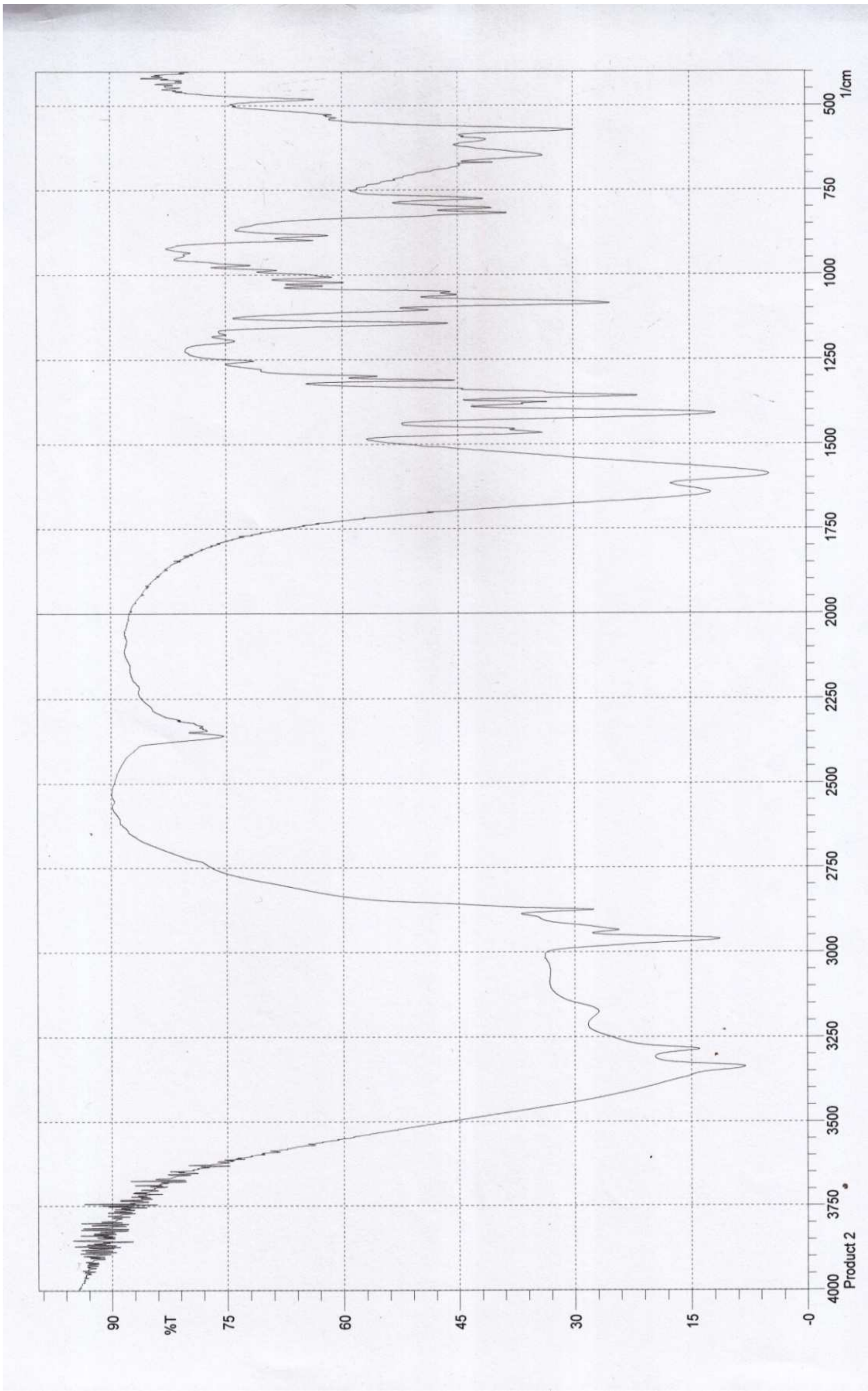

Fig. 3.70: FTIR spectrum of $Ni(C_6H_{12}NO_2)_2.2H_2O$

Table 3.35: Tentative assignment of IR bands of $Ni(C_6H_{12}NO_2)_2.2H_2O$

Wave no. (cm^{-1})	Relative intensity	Tentative band assignment
3340	ms, sp	Asymmetric N-H stretching
3285	m, sp	Symmetric N-H stretching
3165	w, sh	
2960	ms, sp	-C-H stretching
2925	w, sh	
2875	m, sp	
1650	m, sp	Asymmetric N-H bending
1580	ms, sp	Asymmetric COO^- stretching
1475	m, sp	Symmetric N-H bending
1410	s, sp	symmetric COO^- stretching
1375	m, sp	
1360	ms, sp	
1310	m, sp	
1150	ms, sp	
1100	w, sh	
1080	s, sp	C-N stretching
650	m, sp	
575	m, sp	

vs = very strong, s = strong, ms = medium strong, m = medium, w = weak, sp = sharp, b = broad, sh = shoulder

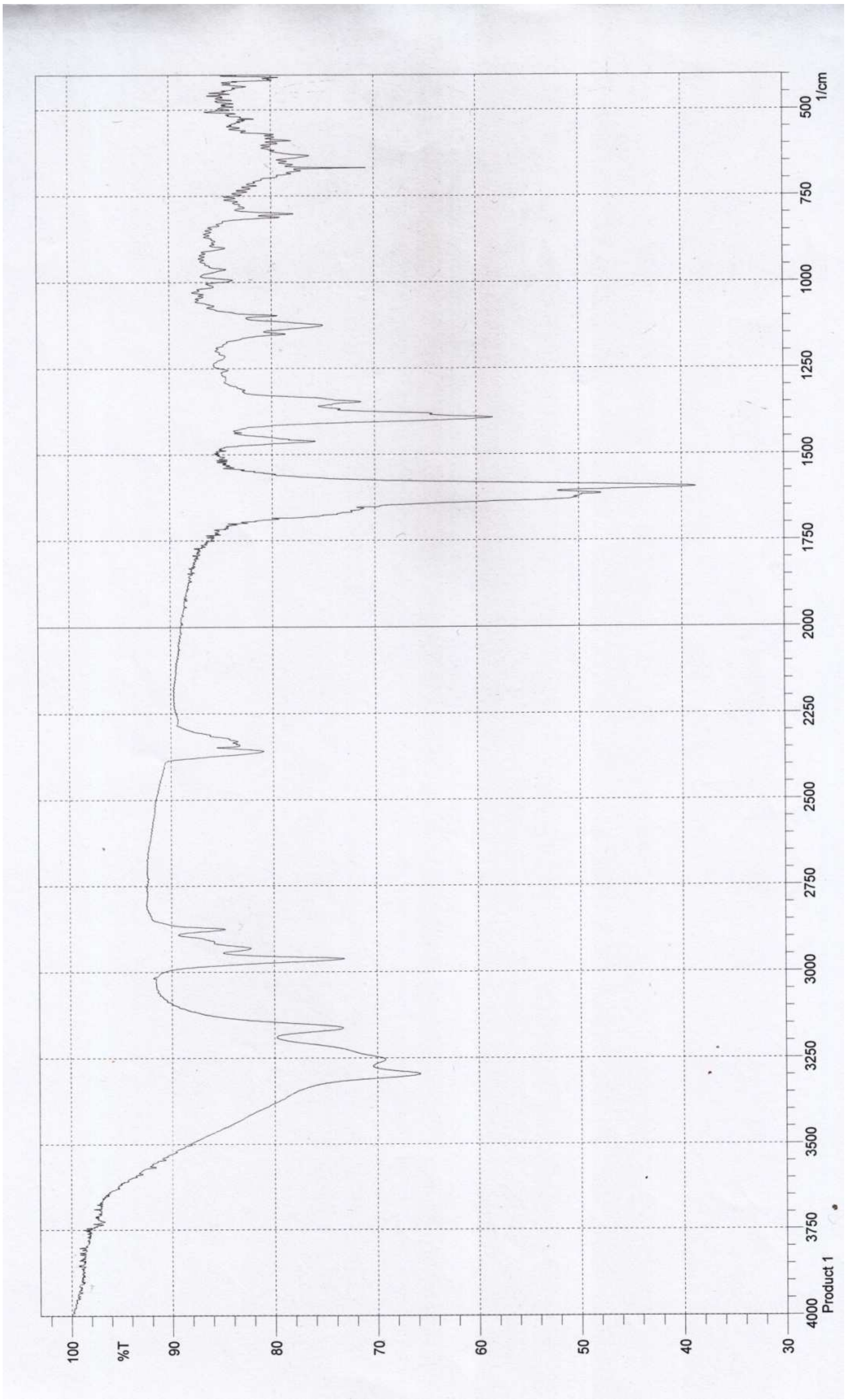

Fig. 3.71: FTIR spectrum of $Cu(C_6H_{12}NO_2)_2 . H_2O$

Table 3.36: Tentative assignment of IR bands of $Cu(C_6H_{12}NO_2)_2$. H_2O

Wave no. (cm^{-1})	Relative intensity	Tentative band assignment
3300	m, sp	Asymmetric N-H stretching
3250	w, sh	Symmetric N-H stretching
3160	m, sp	
2975	ms, sp	-C-H stretching
1610	w, sp	Asymmetric N-H bending
1600	ms, sp	Asymmetric COO^- stretching
1460	m, sp	Symmetric N-H bending
1400	ms, sp	symmetric COO^- stretching
1125	m, sp	C-N stretching

vs = very strong, s = strong, ms = medium strong, m = medium, w = weak, sp = sharp, b = broad, sh = shoulder

Table 3.37: Tentative assignment of IR bands of $Zn(C_6H_{12}NO_2)_2$.½ H_2O

Wave no. (cm^{-1})	Relative intensity	Tentative band assignment
3325	w, sp	Asymmetric N-H stretching
3260	w, sh	Symmetric N-H stretching
2960	s, sp	-C-H stretching
2940	w, sp	
2875	m, sp	
1600	s, b	Asymmetric N-H bending Asymmetric COO^- stretching
1475	m, sp	Symmetric N-H bending
1400	ms, sp	symmetric COO^- stretching
1100	s, sp	C-N stretching
800	s, sp	

vs = very strong, s = strong, ms = medium strong, m = medium, w = weak, sp = sharp, b = broad, sh = shoulder

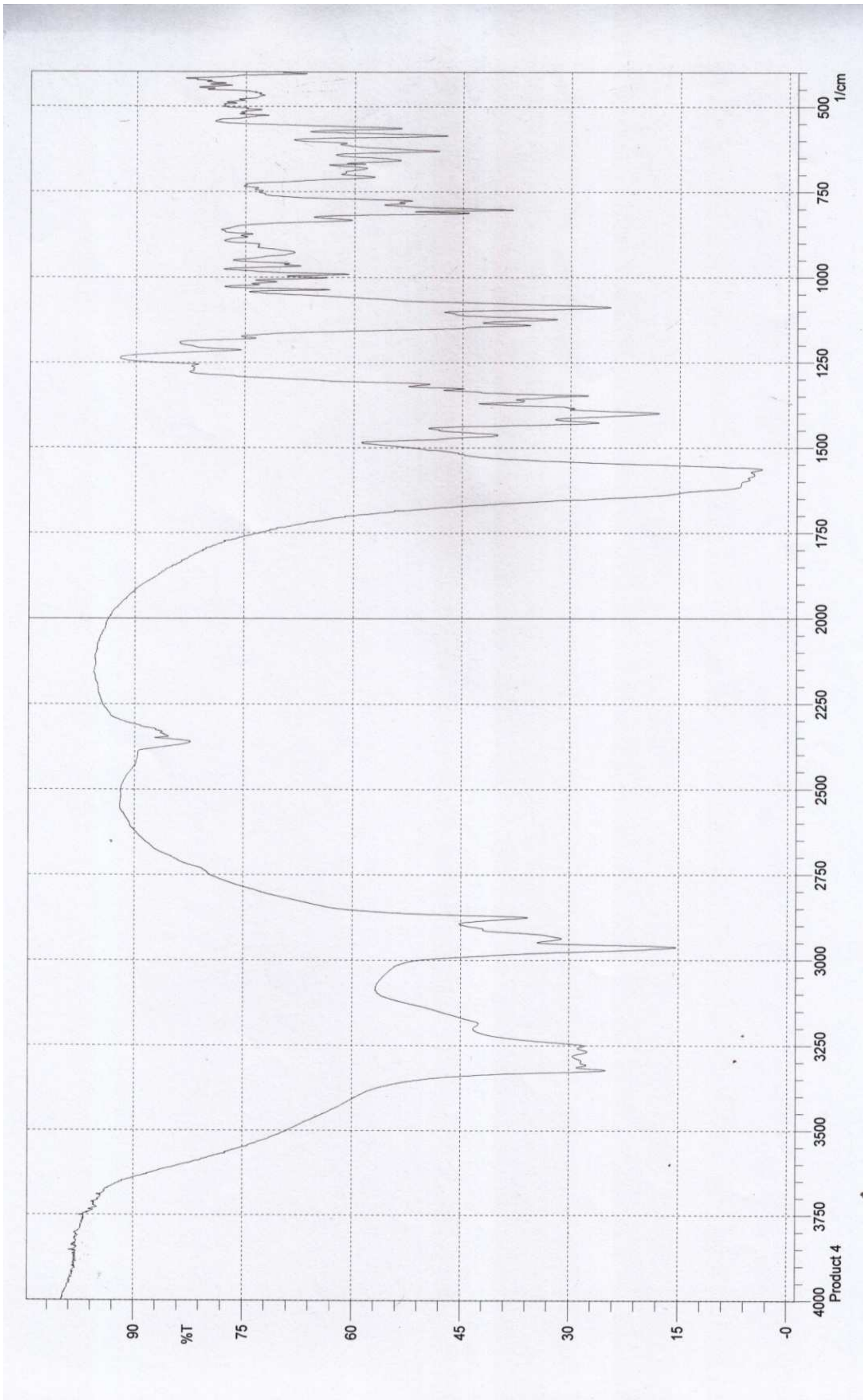

Fig. 3.72: FTIR spectrum of $Zn(C_6H_{12}NO_2)_2.½\ H_2O$

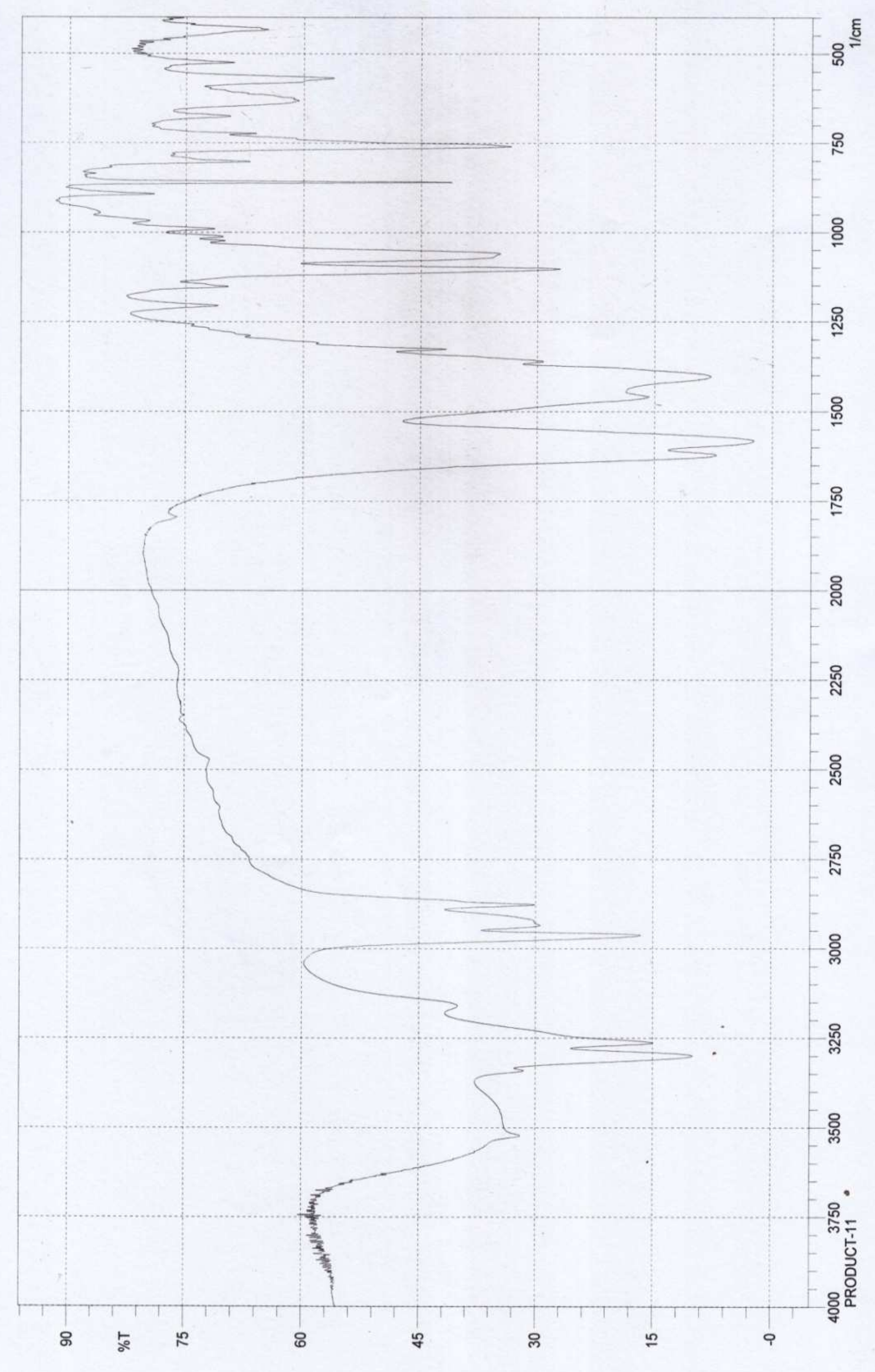

Fig. 3.73: FTIR spectrum of $Cd(C_6H_{12}NO_2)_2$

Table 3.38: Tentative assignment of IR bands of $Cd(C_6H_{12}NO_2)_2$

Wave no. (cm^{-1})	Relative intensity	Tentative band assignment
3300	m, sp	Asymmetric N-H stretching
3260	m, sp	Symmetric N-H stretching
3160	w, sh	
2960	ms, sp	-C-H stretching
2925	w, sp	
2875	m, sp	
1620	m, sp	Asymmetric N-H bending
1575	m, sp	Asymmetric COO^- stretching
1460	w, sh	Symmetric N-H bending
1400	m, sp	symmetric COO^- stretching
1120	s, sp	C-N stretching
1060	s, sp	
860	s, sp	
750	s, sp	
630	m, sp	
570	m, sp	
525	w, sp	
430	w, sp	

vs = very strong, s = strong, ms = medium strong, m = medium, w = weak, sp = sharp, b = broad, sh = shoulder

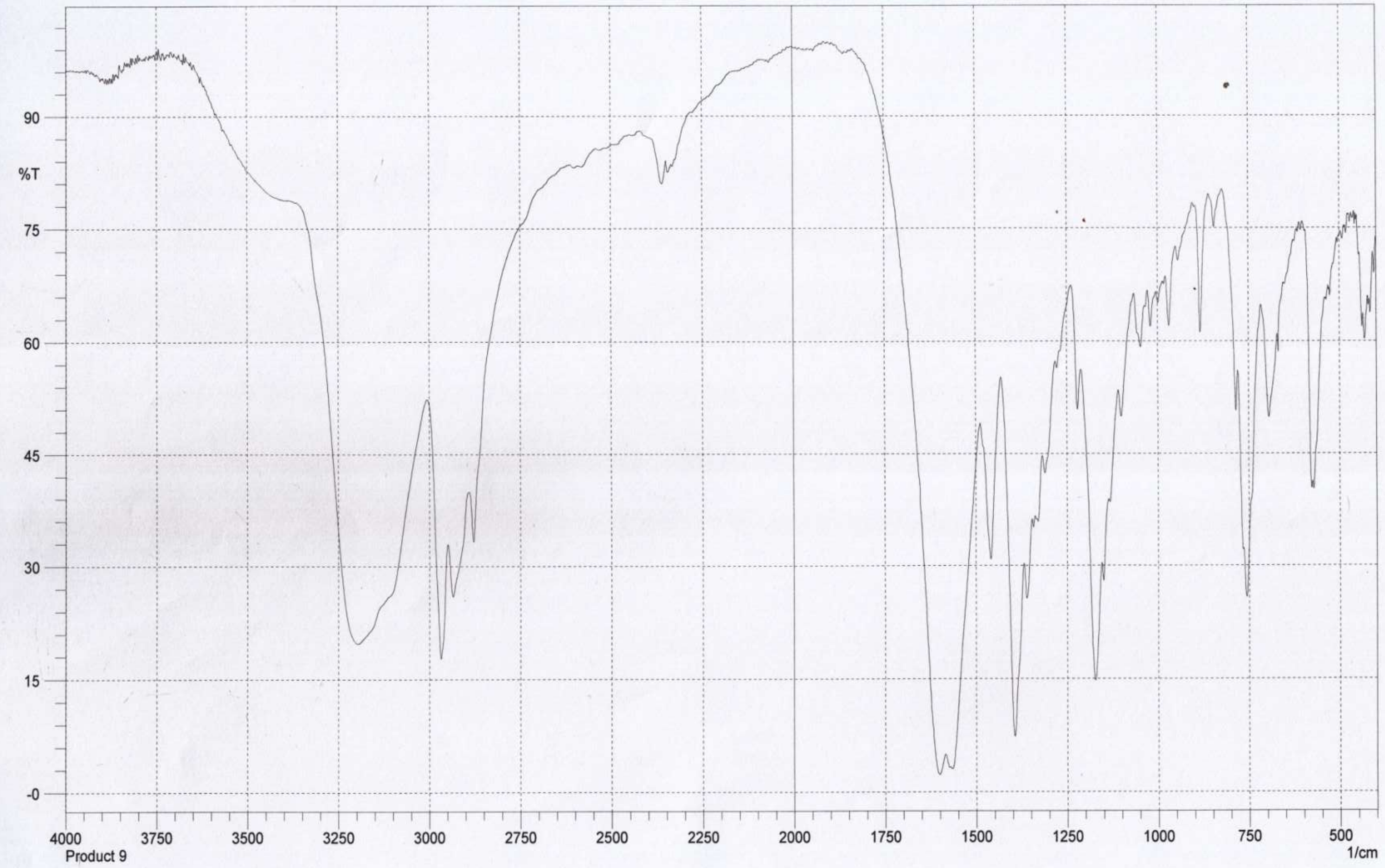

Fig. 3.74: FTIR spectrum of $Hg(C_6H_{12}NO_2)_2$

Table 3.39: Tentative assignment of IR bands of $Hg(C_6H_{12}NO_2)_2$

Wave no. (cm^{-1})	Relative intensity	Tentative band assignment
3200	m, b	Asymmetric N-H stretching
3100	w, sh	Symmetric N-H stretching
2975	ms, sp	-C-H stretching
2940	m, sp	
2875	m, sp	
1600	w, sh	Asymmetric N-H bending
1575	w, sh	Asymmetric COO^- stretching
1460	m, sp	Symmetric N-H bending
1400	s, sp	symmetric COO^- stretching
1175	s, sp	C-N stretching
750	s, sp	
700	m, sp	
575	ms, sp	

vs = very strong, s = strong, ms = medium strong, m = medium, w = weak, sp = sharp, b = broad, sh = shoulder

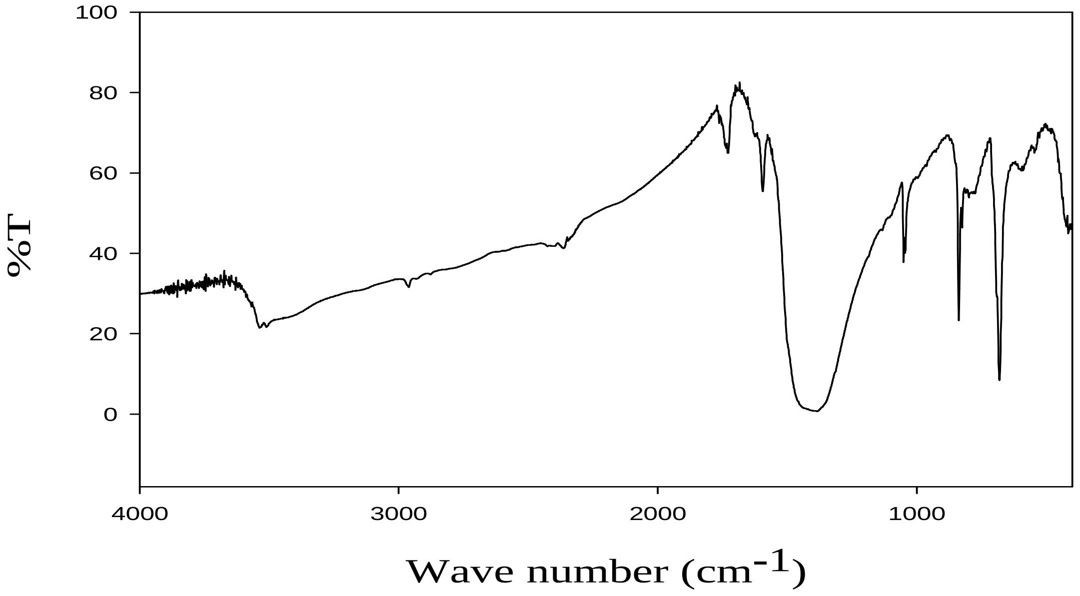

Fig. 3.75: FTIR spectrum of Pb-isoleucine complex

3.3.2.4 Electronic spectral analysis

In the present study the electronic spectrum of isoleucine and its metal complexes were recorded on a Shimadzu UV-Vis recording spectrophotometer (UV- 1800A) in the wavelength range 190 to 1100 nm.

3.3.2.4.1 UV-Visible absorption spectral analysis: UV-Visible absorption spectrum was carried out to understand the electronic transitions occur within the molecule. The complexes were insoluble in the most common solvents but only Co, Ni and Cu complexes are soluble in methanol. So, the absorption spectrum of these samples were studied in methanol solution and shown in Fig. 3.76 to Fig. 3.79. The absorption band assignments have been made empirically on the basis of some standard books [102-106] and explained in Table 3.40.

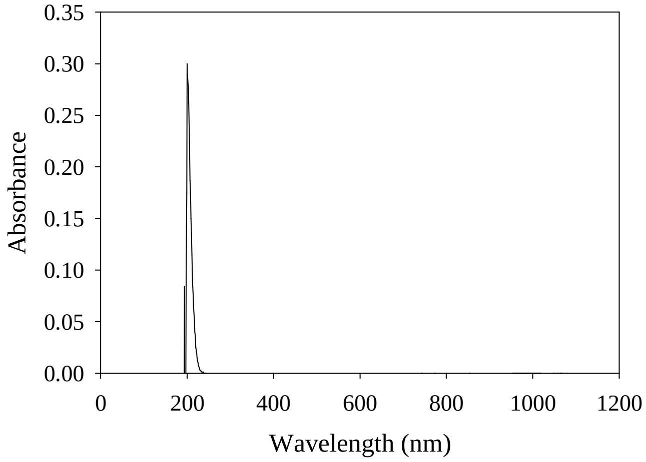

Fig. 3.76: UV-Vis spectrum of isoleucine ($C_6H_{13}NO_2$)

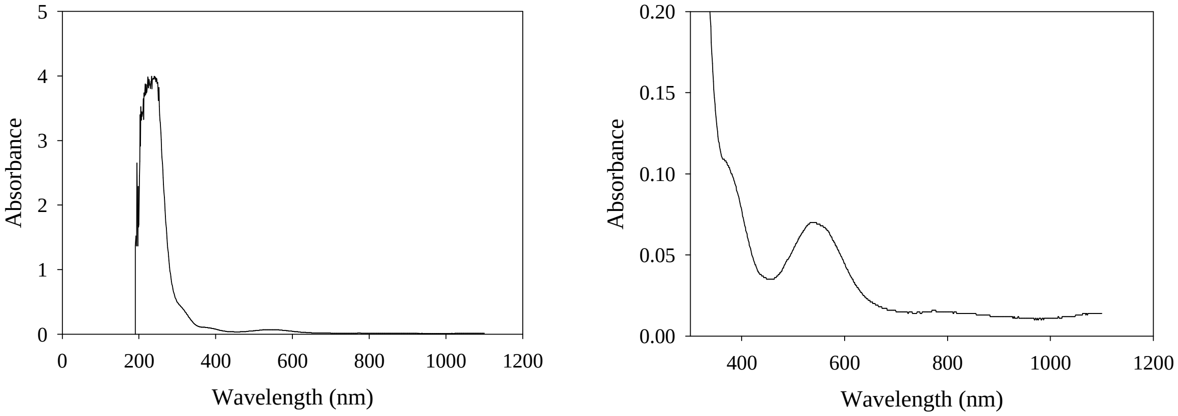

Fig. 3.77: UV-Vis spectrum of $Co(C_6H_{12}NO_2)_2.2H_2O$

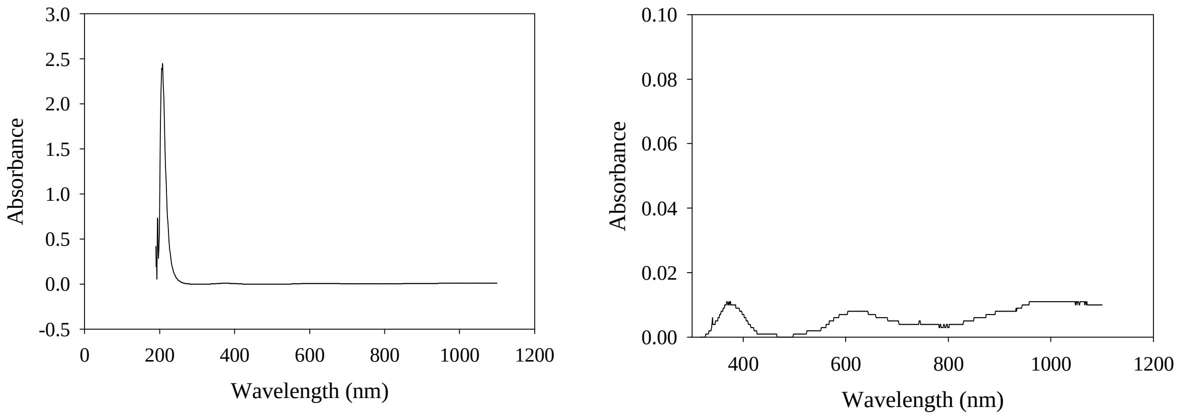

Fig. 3.78: UV-Vis spectrum of $Ni(C_6H_{12}NO_2)_2.2H_2O$

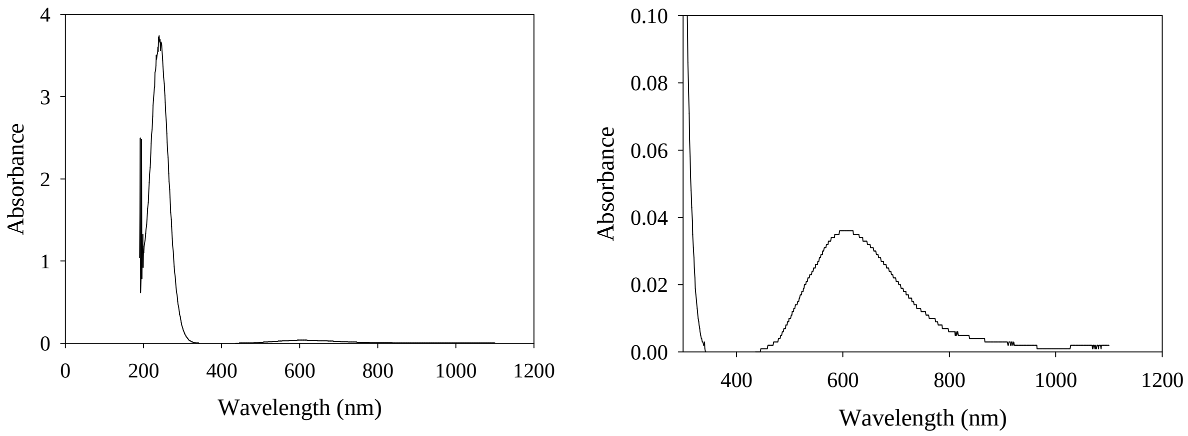

Fig. 3.79: UV-Vis spectrum of $Cu(C_6H_{12}NO_2)_2.H_2O$

Table 3.40: Absorption bands of isoleucine and its complex

Compound	Absorption band		
	d-d	CT	IL
Isoleucine ($C_6H_{13}NO_2$)	-	-	200
$Co(C_6H_{12}NO_2)_2.2H_2O$	535	-	240
$Ni(C_6H_{12}NO_2)_2.2H_2O$	625	380	208
$Cu(C_6H_{12}NO_2)_2.H_2O$	605	-	240

d-d = d-d transition, CT = charge transfer transition, IL = Intraligand charge transfer

The absorption band at ~ 200 nm was observed for the organic part of the complex. The absorption band at around 380 nm in the Ni-complex may be due to charge transfer between metal orbital and ligand orbital. The presence of $\pi \rightarrow \pi^*$, $n \rightarrow \pi^*$ and $n \rightarrow \sigma^*$ bands as a single band in the ligand and the complex indicate low energy difference for these transitions (e.g. -C=O, $-NH_2$). Appearing of a new band at 535 nm, 605 nm and 625 nm for d-d transitions also indicate the presence of metal ion in the complexes. Shifting of the absorption bands in the complexes and appearing of a new band for d-d transitions also indicate the probability of forming M←L coordination bonds in the complexes.

3.3.2.4.2 UV-Visible diffuse reflectance spectral analysis: UV-Visible diffuse reflectance spectroscopy is an optical technique which describes the electronic behavior present in the structure of the solid. This technique concerns with the relative change in the amount of reflected light off of a surface. Diffuse reflectance spectrum are taken for measuring the band gap energy. The separation between the energy of the lowest conduction band and that of the highest valence band is called the band gap, energy gap or forbidden energy gap (E_g). The semiconductor properties of a solid are strongly affected by the E_g parameter.

The reflectance spectrum and the corresponding energy function of the compounds are displayed in the Fig. 3.80 to Fig. 3.86. The determined band gap energy of the compounds is listed in Table 3.41. All the samples have lower band gap energy, indicating they may be good conductor [107].

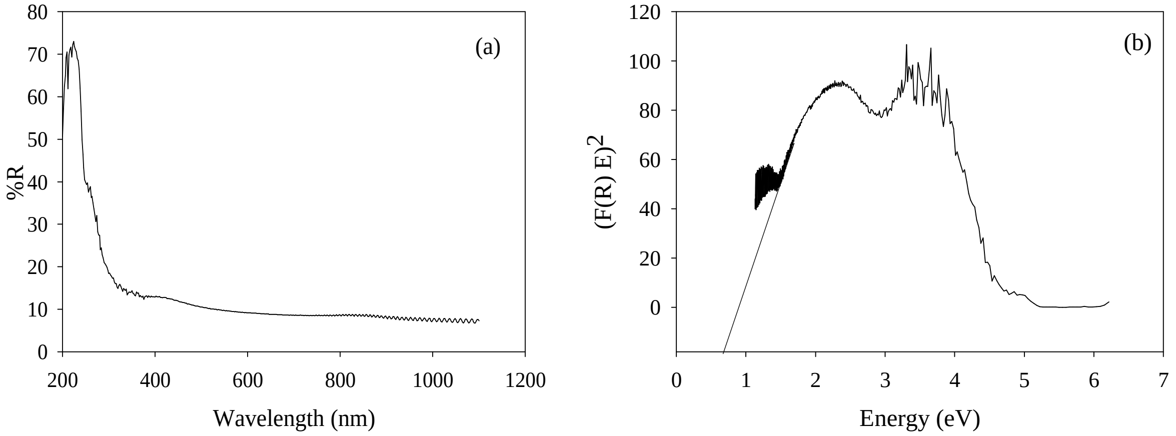

Fig. 3.80: (a) Reflectance spectrum and (b) $(F(R)E)^2$ vs E plot for isoleucine ($C_6H_{13}NO_2$)

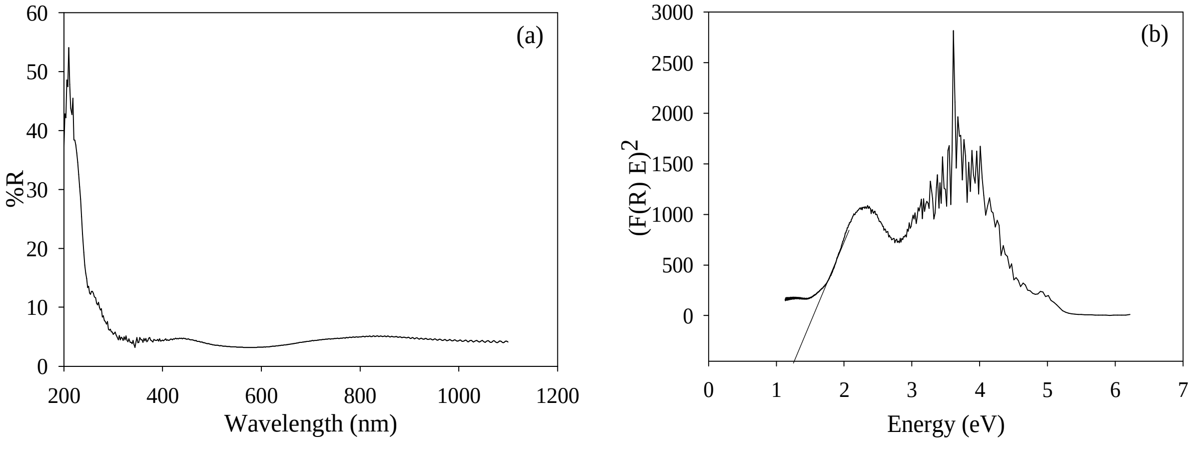

Fig. 3.81: (a) Reflectance spectrum and (b) $(F(R)E)^2$ vs E plot for $Co(C_6H_{12}NO_2)_2.2H_2O$

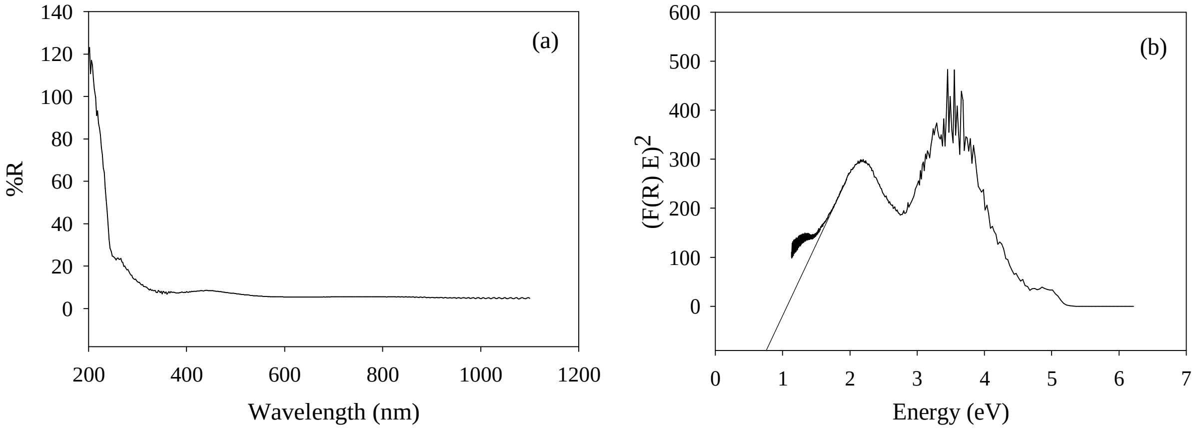

Fig. 3.82: (a) Reflectance spectrum and (b) $(F(R)E)^2$ vs E plot for $Ni(C_6H_{12}NO_2)_2.2H_2O$

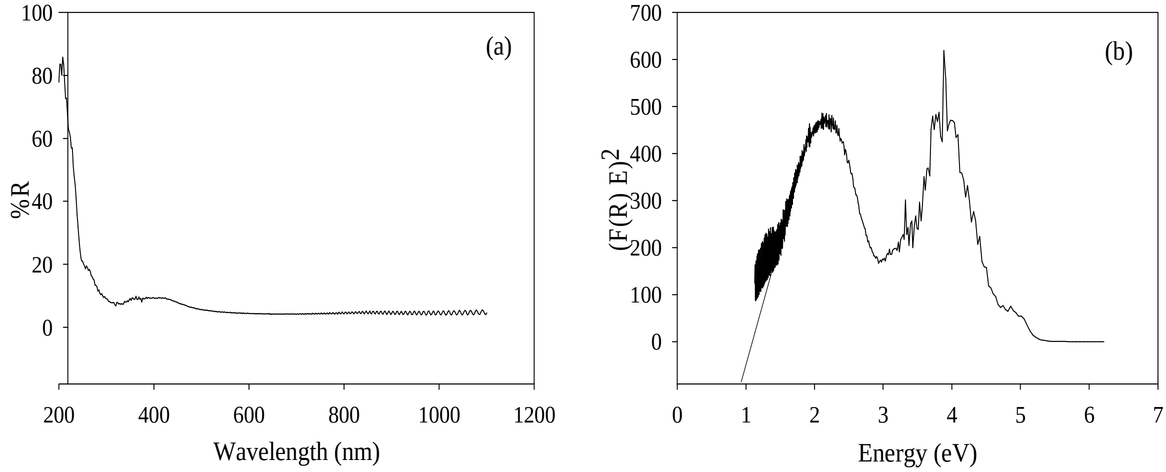

Fig. 3.83: (a) Reflectance spectrum and (b) $(F(R)E)^2$ vs E plot for $Cu(C_6H_{12}NO_2)_2.H_2O$

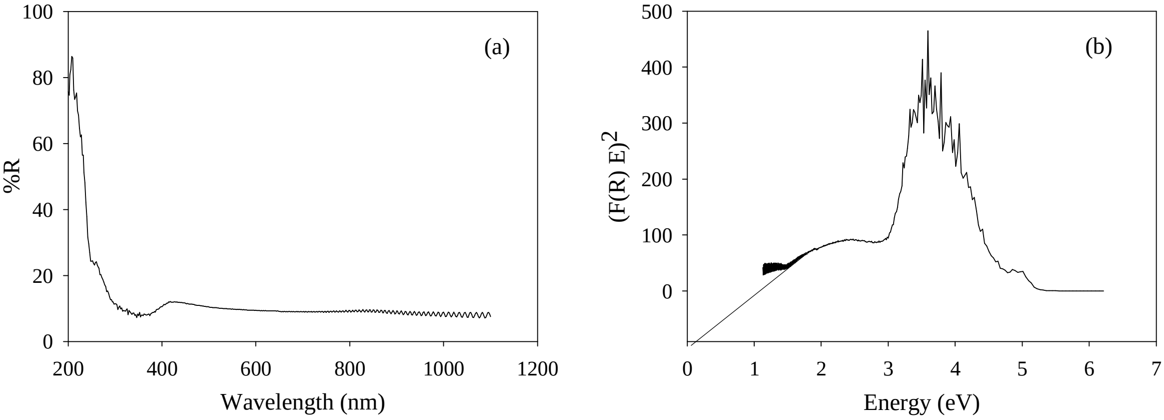

Fig. 3.84: (a) Reflectance spectrum and (b) $(F(R)E)^2$ vs E plot for $Zn(C_6H_{12}NO_2)_2.½ H_2O$

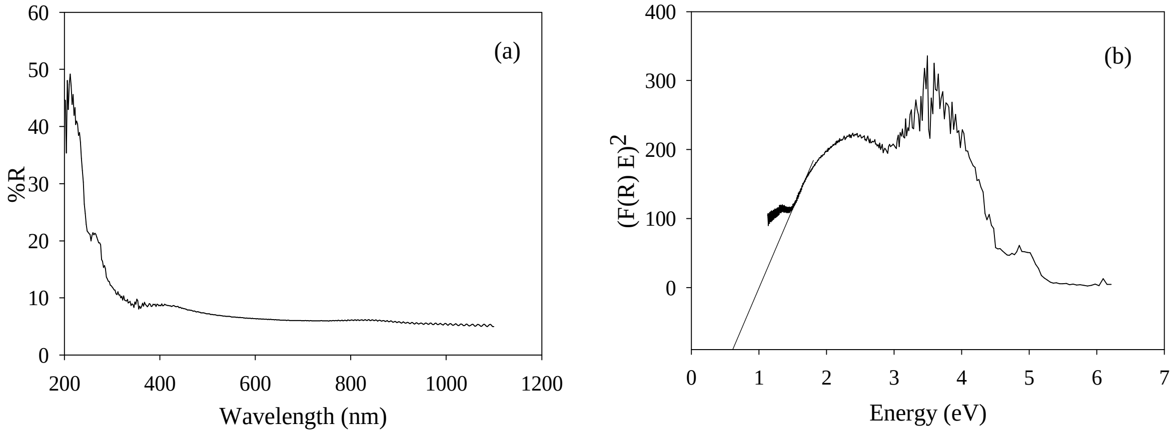

Fig. 3.85: (a) Reflectance spectrum and (b) $(F(R)E)^2$ vs E plot for $Cd(C_6H_{12}NO_2)_2$

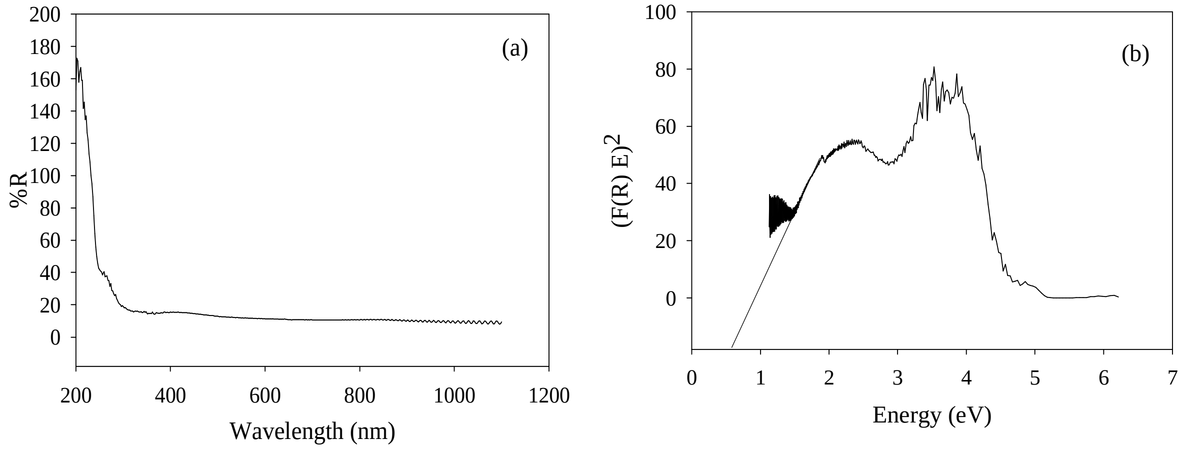

Fig. 3.86: (a) Reflectance spectrum and (b) $(F(R)E)^2$ vs E plot for $Hg(C_6H_{12}NO_2)_2$

Table 3.41: The determined band gap energy of isoleucine and its complexes

Sample	Band gap energy (eV)
isoleucine ($C_6H_{13}NO_2$)	0.7
$Co(C_6H_{12}NO_2)_2.2H_2O$	1.2
$Ni(C_6H_{12}NO_2)_2.2H_2O$	0.8
$Cu(C_6H_{12}NO_2)_2.\ H_2O$	0.9
$Zn(C_6H_{12}NO_2)_2.½\ H_2O$	0.1
$Cd(C_6H_{12}NO_2)_2$	0.6
$Hg(C_6H_{12}NO_2)_2$	0.6

3.3.2.5 Nuclear magnetic resonance (NMR) spectral analysis

In the present study the NMR spectrum of isoleucine and its complex were recorded on a Bruker NMR spectrometer in methanol solution and shown in Fig. 3.87 - Fig. 3.91. The tentative assignment of the position of the peaks is done on the basis of some standard books [102, 103]. The assignments are shown on the body of the graph.

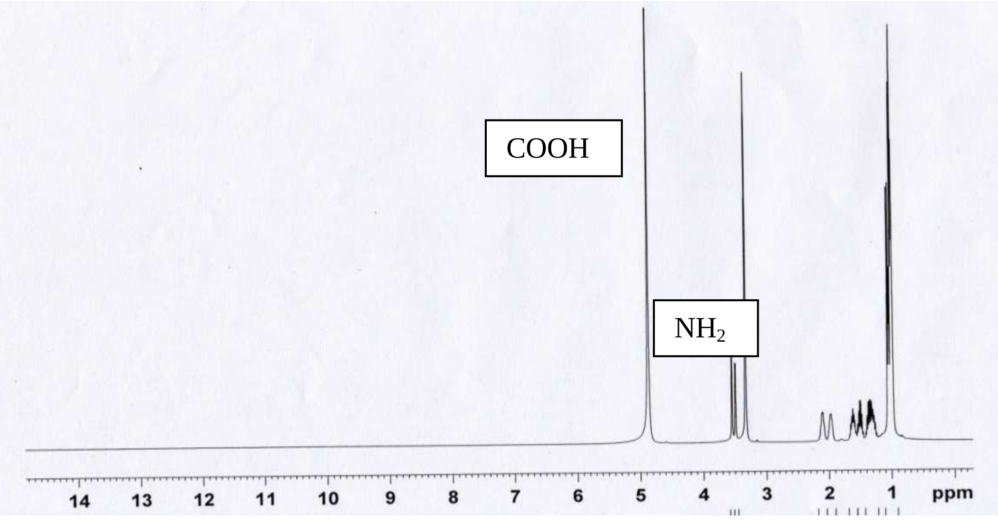

Fig. 3.87: NMR spectrum of isoleucine ($C_6H_{13}NO_2$)

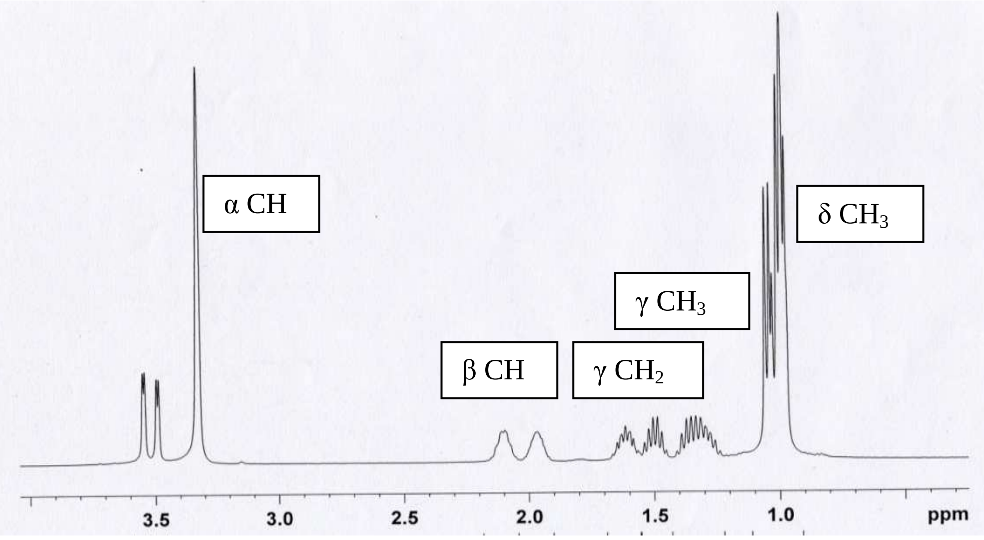

Fig. 3.88: NMR spectrum of isoleucine ($C_6H_{13}NO_2$)

Isolucine shows a peak at chemical shift 5 ppm for –COOH proton. Since the –COOH protons are highly deshielded the peak appears most far from the TMS position. The –CH_3 protons are most shielded. So, the –CH_3 peak appears close to the TMS position at chemical shift 1.0. The splitting of the peaks indicates that the protons overlap with each other.

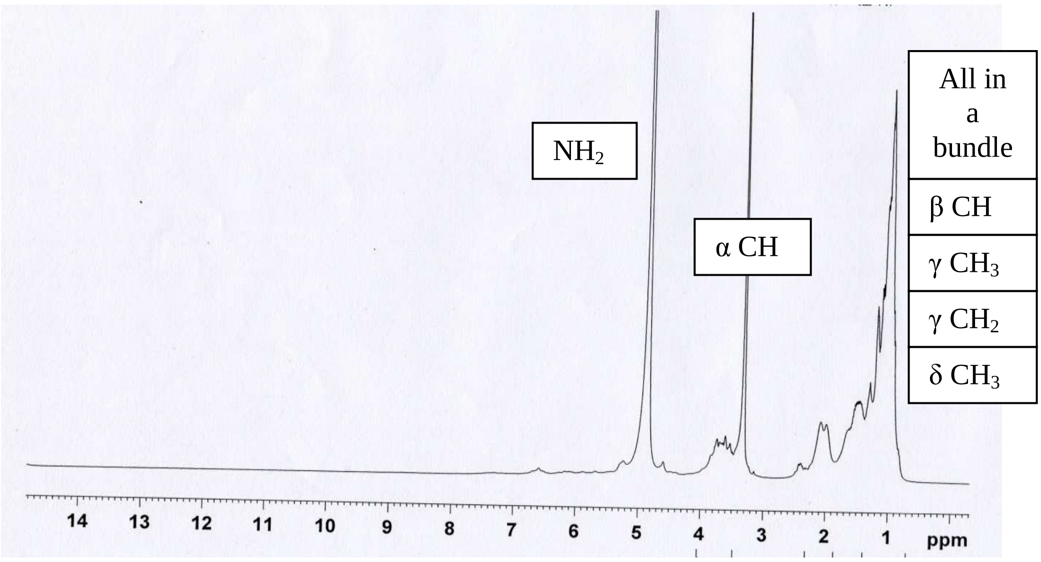

Fig. 3.89: NMR spectrum of Co($C_6H_{12}NO_2$)$_2$.2H_2O

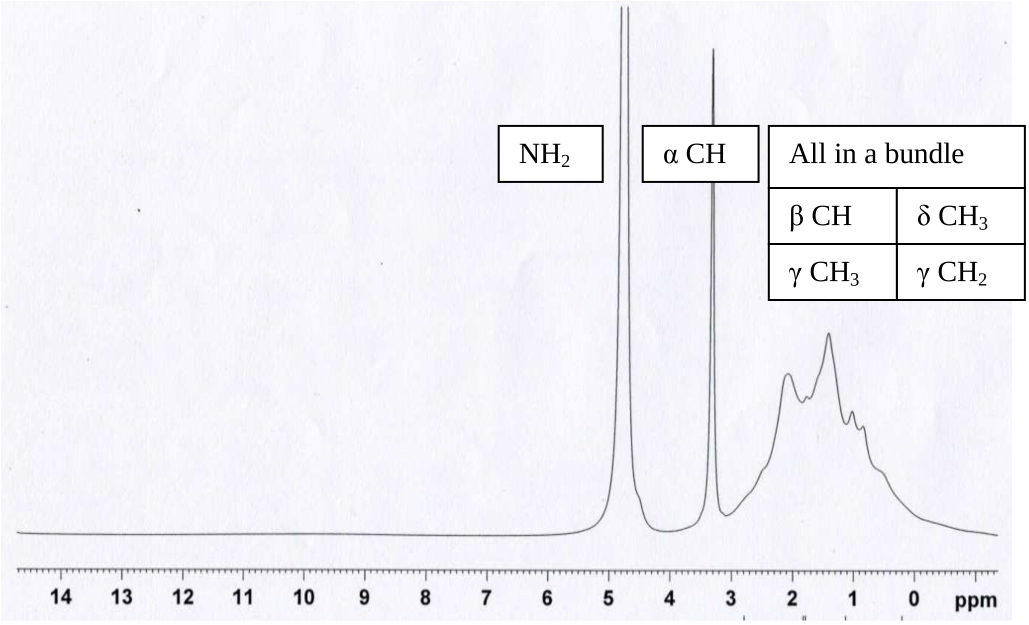

Fig. 3.90: NMR spectrum of Ni($C_6H_{12}NO_2$)$_2$.2H_2O

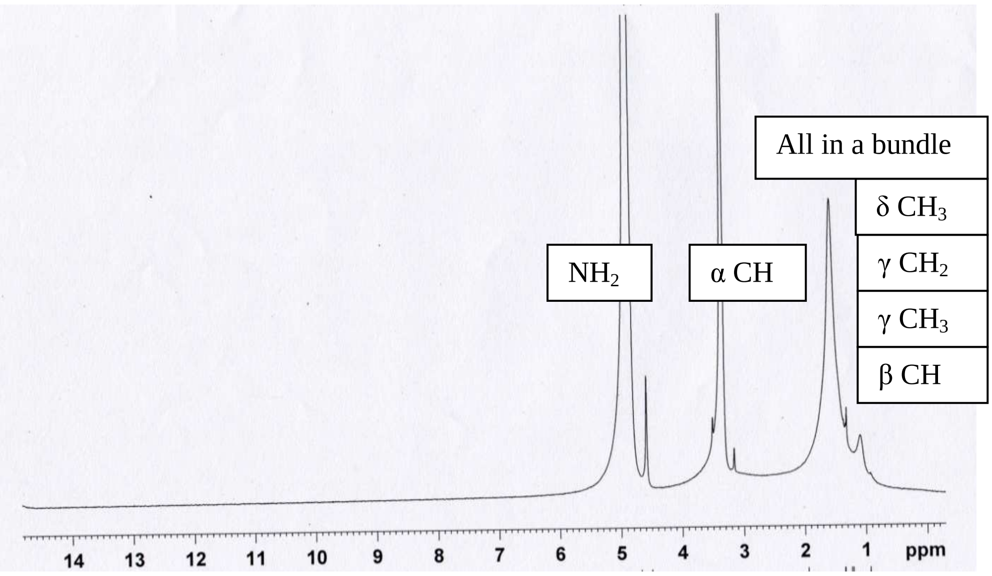

Fig. 3.91: NMR spectrum of $Cu(C_6H_{12}NO_2)_2.H_2O$

In the complexes the chemical shift position for the β, γ, δ protons appear as a bundle and cannot isolated while in isoleucine they are quite distinct and isolated. A peak for –COOH proton appears in the ligand but in the complex it is not seen. This may be due to complexation of isoleucine with the metal.

3.3.2.6 Thermal analysis (TA)

Thermal methods of analysis are those techniques in which changes in physical and/or chemical properties of a substance are measured as a function of temperature. Thermo-gravimetry (TG) and Differential Scanning Calorimetry (DSC) are important among the thermal techniques.

The thermo-gravimetric analysis is a dynamic technique based on the change in the weight of a substance recorded as the function of temperature or time. On the other hand, DSC is a technique in which the difference in energy inputs into a substance and a reference material is measured as a function of temperature whilst the substance and reference material are subjected to a controlled temperature programme. Thermal analysis is applied for the determination of the purity and thermal stability of primary and secondary standards, phase transition, enthalpy change, degree of crystallinity, the investigation of correct drying temperature and for the determination of the composition of complex mixtures. It gives an idea about the bond strength of various constituent parts of the complex.

3.3.2.6.1 Thermal analysis of isoleucine: The TG and DSC curve of isoleucine is shown in Fig. 3.92. The ligand decomposes continuously in one step. There is no sharp transition up to 200^0C. So it can be said that the ligand do not contain any water of crystallization. It is logical since the molecular formula of the ligand do not contain any water of crystallization. At about 950^0C only 0.08% of the ligand sample remains as residue. So it can be said that the ligand almost completely decomposed.

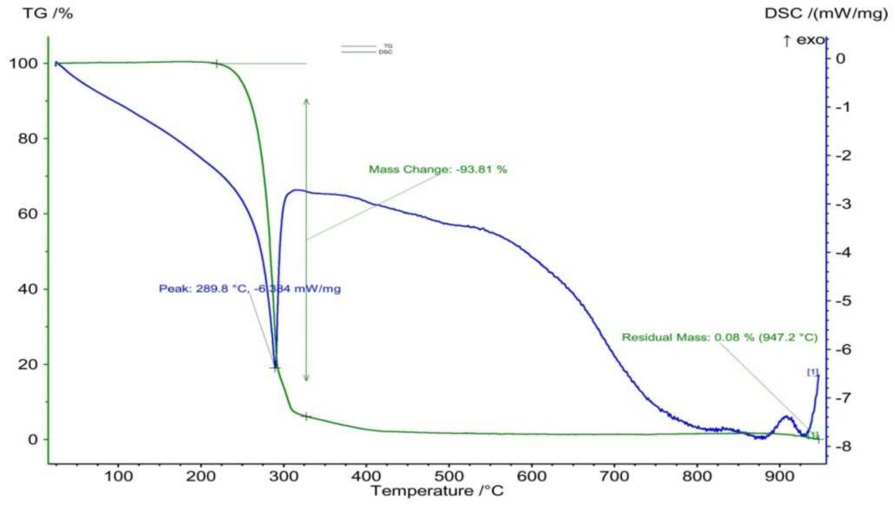

Fig. 3.92: TG and DSC curves of isoleucine ($C_6H_{13}NO_2$)

3.3.2.6.2 Thermal analysis of isoleucine complexes: The TG and DSC curve of isoleucine complexes are shown in Fig. 3.93 to Fig. 3.98. The weight loss at different stages is described in Table 3.42. The Co and Ni complex contains two molecules of crystalline water. The Cu complex contains one water molecule and Zn complex contain half molecule of water of crystallization. Cd and Hg complex does not contain any water of crystallization or coordinated water. The Co, Zn and Cd complex decomposed in a wide temperature range. On the other hand sharp decomposition occurs for Ni, Cu and Hg complex. Co, Zn and Cd complex may be more stable compared to Ni, Cu and Hg complex. The residue remained after 900^{0}C confirms that after decomposition the Co, Ni, Cu, Zn and Cd complex almost converted to the respective metal oxide. The Hg complex undergone about 98% decomposition at around 200 ^{0}C. The mercury oxide formed may be further decomposed. This is reasonable since HgO decomposes on exposure to light or on heating producing mercury fumes and oxygen. The Differential Scanning Calorimetry (DSC) curve of the complexes is sharp endothermic. Therefore, the weight changes monitored by thermogravimetry involved absorption of energy [100].

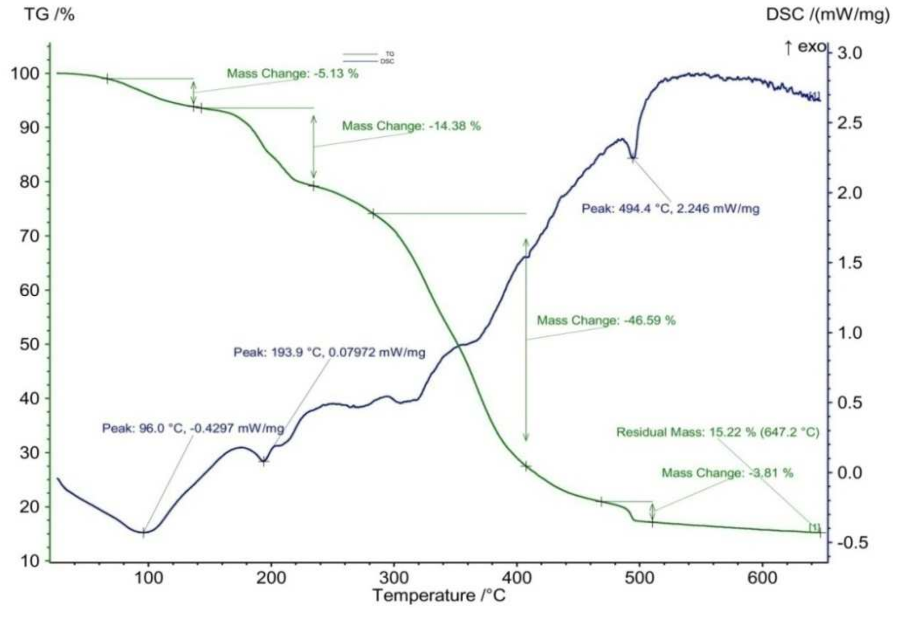

Fig. 3.93: TG and DSC curves of $Co(C_6H_{12}NO_2)_2.2H_2O$

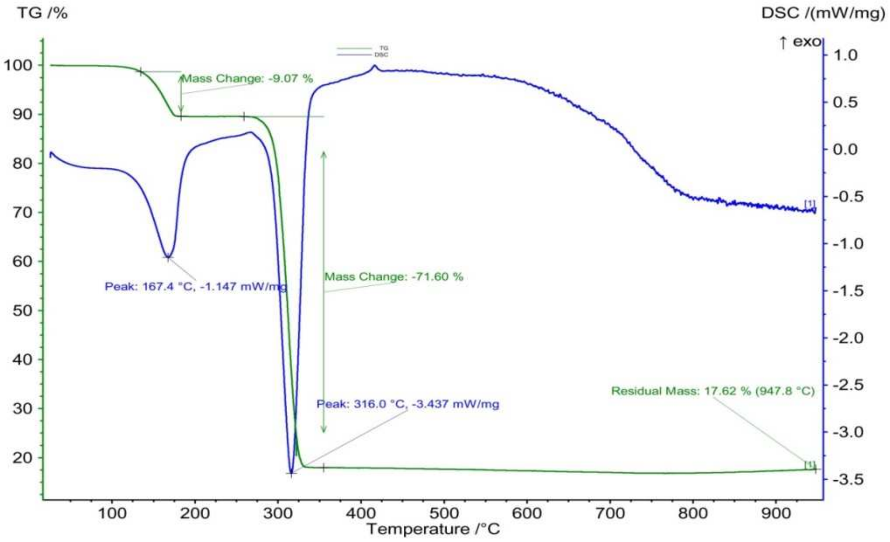

Fig. 3.94: TG and DSC curves of $Ni(C_6H_{12}NO_2)_2.2H_2O$

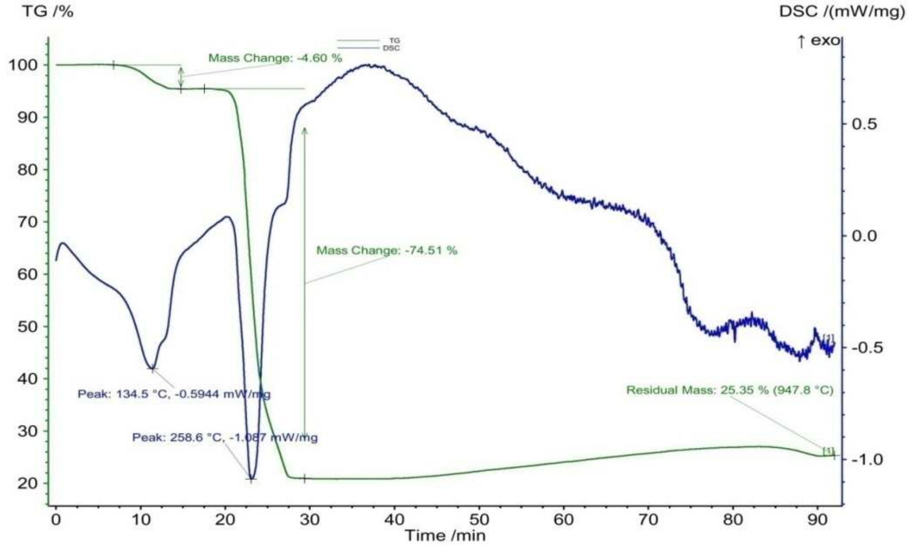

Fig. 3.95: TG and DSC curves of $Cu(C_6H_{12}NO_2)_2.H_2O$

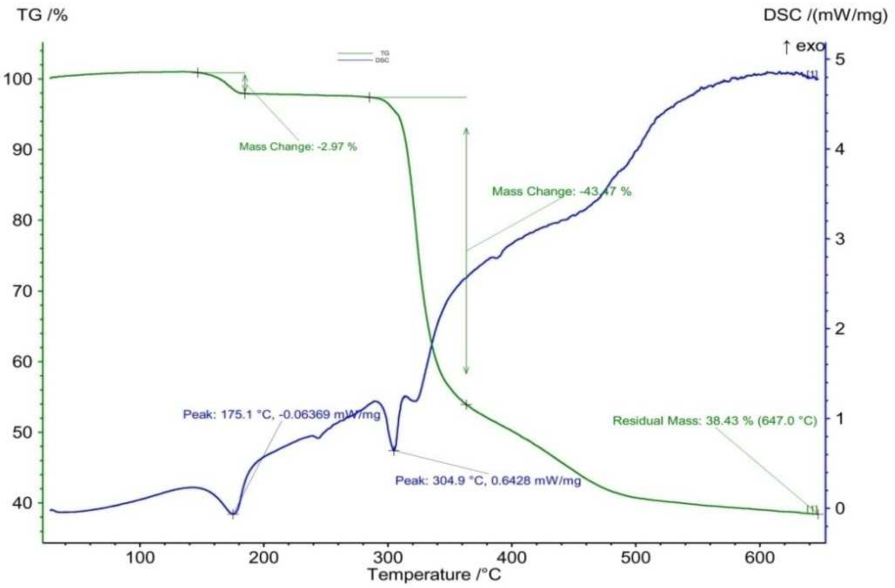

Fig. 3.96: TG and DSC curves of $Zn(C_6H_{12}NO_2)_2.½ H_2O$

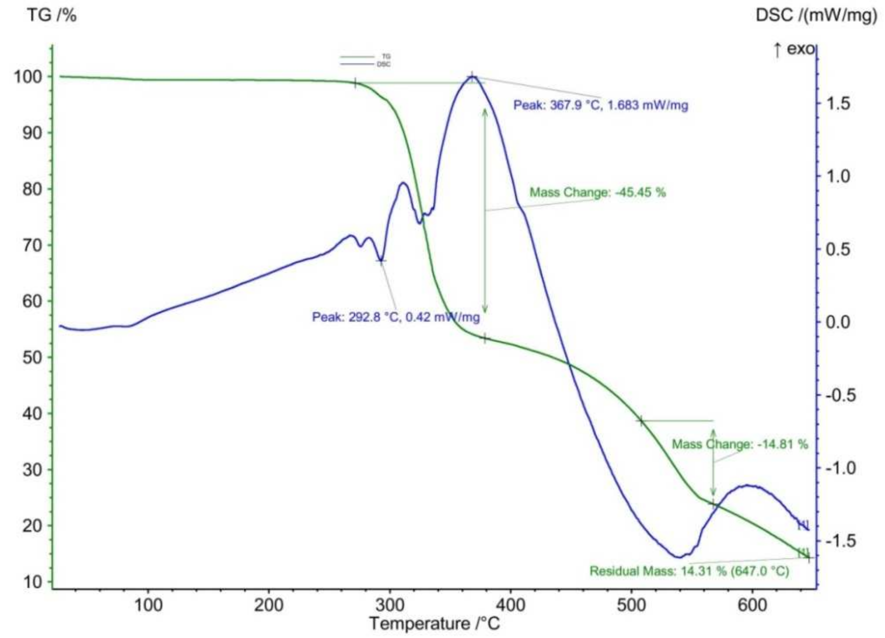

Fig. 3.97: TG and DSC curves of $Cd(C_6H_{12}NO_2)_2$

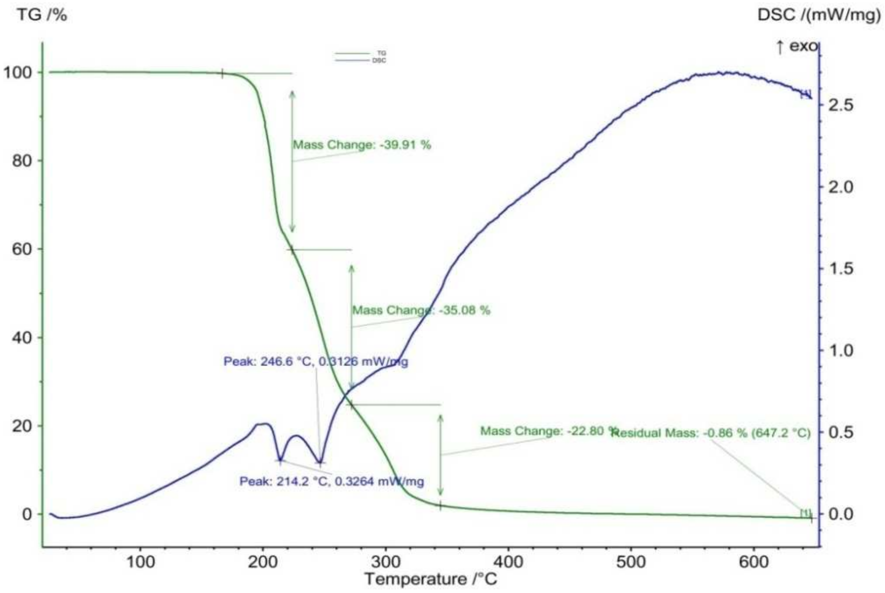

Fig. 3.98: TG and DSC curves of Hg($C_6H_{12}NO_2$)$_2$

Table 3.42: Weight loss at different stages of TG analysis of isoleucine and its complexes

Compound	Temperature range	Mass change	Inference
Isoleucine ($C_6H_{13}NO_2$)	0 ^{0}C- 200 ^{0}C	0%	No moisture
	200 ^{0}C – 300 ^{0}C	94 %	Total decomposition
	947 ^{0}C	0.08 %	Residue
Co($C_6H_{12}NO_2$)$_2$.2H_2O	0 ^{0}C – 100 ^{0}C	5 %	Moisture and two water molecule may be lost
	100 ^{0}C – 200 ^{0}C	14 %	
	200 ^{0}C – 500 ^{0}C	50 %	The weight loss may be due to loss of NH_3, CO_2, CH_4
	647 ^{0}C	15 %	May be cobalt oxide
Ni($C_6H_{12}NO_2$)$_2$.2H_2O	0 ^{0}C – 100 ^{0}C	0 %	No moisture
	100 ^{0}C – 170 ^{0}C	9 %	Two water molecule may be lost
	300 ^{0}C – 320 ^{0}C	72 %	The weight loss may be due to loss of NH_3, CO_2, CH_4
	947 ^{0}C	18 %	May be nickel oxide
Cu($C_6H_{12}NO_2$)$_2$.H_2O	0 ^{0}C- 100 ^{0}C	0%	No moisture
	100 ^{0}C – 140 ^{0}C	5%	One water molecule may be lost
	150 ^{0}C – 270 ^{0}C	75 %	The weight loss may be due to loss of NH_3, CO_2, CH_4
	947 ^{0}C	25 %	May be copper oxide

Compound	Temperature range	Mass change	Inference
$Zn(C_6H_{12}NO_2)_2.½ H_2O$	0 ^{0}C- 170 ^{0}C	0%	No moisture or chemically bound water
	170 ^{0}C – 180 ^{0}C	3%	half water molecule may be lost
	280 ^{0}C – 500 ^{0}C	60 %	The weight loss may be due to loss of NH_3, CO_2, CH_4
	647 ^{0}C	38 %	May be zinc oxide
$Cd(C_6H_{12}NO_2)_2$	0 ^{0}C – 280 ^{0}C	0 %	No moisture or chemically bound water
	280 ^{0}C – 350 ^{0}C	45 %	The weight loss may be due to loss of NH_3, CO_2, CH_4
	350 ^{0}C – 600 ^{0}C	35%	Rest of the organic part may be lost
	647 ^{0}C	14 %	May be cadmium oxide
$Hg(C_6H_{12}NO_2)_2$	0 ^{0}C – 180 ^{0}C	0 %	No moisture or chemically bound water
	180 ^{0}C – 350 ^{0}C	98 %	The weight loss may be due to loss of NH_3, CO_2, CH_4
	647 ^{0}C	0.86 %	The mercury oxide has also decomposed.

3.3.2.7 Magnetic properties

An interesting characteristic of transition metals is their ability to form magnets. Metal complexes that have unpaired electrons are magnetic. Since the last electrons reside in the d orbitals, this magnetism must be due to having unpaired d electrons. Considering only monometallic complexes, unpaired electrons arise because the complex has an odd number of electrons or because electron pairing is destabilized. When an electron in an atom or ion is unpaired, the magnetic moment due to its spin makes the entire atom or ion paramagnetic**.** The size of the magnetic moment of a system containing unpaired electrons is related directly to the number of such electrons: the greater the number of unpaired electrons, the larger the magnetic moment. Magnetic susceptibility measures the force experienced by a substance in a magnetic field.

Specimen calculation:

Sample ID: $[Co(C_6H_{12}NO_2)_2.2H_2O]$

The balance calibration constant,

$C_{Bal} = C_{tube} / (R_s – R_0) = 1090 / (1060 + 33) = 0.9972$

where R_s = reading for standard sample tube.

The molar susceptibility,

$$\chi_A = \frac{C_{Bal} * l * (R - R_0)}{10^9 * m} * MW$$

$$= \frac{0.9972 * 2 * (1724 + 32)}{10^9 * 0.11} \times 354.93$$

$$= 1.13 * 10^{-2} \text{ cgs}$$

Here,

$R = 1724$
$R_0 = -32$
$l = 2$cm
$m = 0.11$ g
$C_{Bal} = 0.9972$

The magnetic moment, $\mu_{eff} = 2.828 \sqrt{(T * \chi_A)} = 2.828 \sqrt{(300 * 1.13 * 10^{-2})} = 5.2$ BM

From the result found we may decided the number of unpaired electron n = 3

The magnetic properties of the complexes of isoleucine were examined by magnetic susceptibility balance and are tabulated in Table 3.43. From the experimental results, we get the following information's about the magnetic properties of the complexes.

Table 3.43: Magnetic properties of the complexes of isoleucine

Compound	χ_A (cgs) x 10^{-3}	μ_{eff} BM (at 300K)		No. of unpaired electron (n)	Config.	Inference
		Found	Theo.			
$Co(C_6H_{12}NO_2)_2.2H_2O$	11.3	5.2	4.3-5.2	3	d^7	Paramagnetic
$Ni(C_6H_{12}NO_2)_2.2H_2O$	4.0	3.1	3.0-3.3	2	d^8	Paramagnetic
$Cu(C_6H_{12}NO_2)_2.H_2O$	1.35	1.8	1.8-2.1	1	d^9	Paramagnetic
$Zn(C_6H_{12}NO_2)_2$.½ H_2O	negative	0*		0	d^{10}	Diamagnetic
$Cd(C_6H_{12}NO_2)_2$	negative	0*		0	d^{10}	Diamagnetic
$Hg(C_6H_{12}NO_2)_2$	negative	0*		0	d^{10}	Diamagnetic

Theo. = Theoretical values [112] *The negative value of χ_A indicates that the tube and sample have a net diamagnetism. In that case μ_{eff} can be considered as zero.

$Co(C_6H_{12}NO_2)_2.2H_2O$: Experimentally observed magnetic moment of Co(II)-complex is 5.2, which implies in the complex Co exists as Co^{2+} ion with three unpaired electrons, d^7 (t_{2g}^5 e_g^2). The experimental magnetic moment quite agrees with the theoretical value (4.3-5.2 BM).

$Ni(C_6H_{12}NO_2)_2.2H_2O$: Experimentally observed magnetic moment of Ni(II)-complex is 3.1, which implies in the complex Ni exists as Ni^{2+} ion with two unpaired electrons, d^8 (t_{2g}^6 e_g^2). This magnetic moment quite agree with the theoretical value (3.0-3.3 BM).

$Cu(C_6H_{12}NO_2)_2.H_2O$: Experimentally observed magnetic moment of Cu(II)-complex is 1.8, which implies in the complex Cu exists as Cu^{2+} ion with one unpaired electrons, d^9 (t_{2g}^6 e_g^3). This magnetic moment quite agree with the theoretical value (1.8-2.1 BM).

$Zn(C_6H_{12}NO_2)_2$. ½ H_2O, $Cd(C_6H_{12}NO_2)_2$ and $Hg(C_6H_{12}NO_2)_2$: The magnetic susceptibility of Zn(II), Cd(II) and Hg(II) complex shows that they has no unpaired electron i.e. they possess d^{10} configuration with diamagnetic character [112].

3.3.2.8 Theoretical studies

All calculations were performed with the Gaussian 09 software package. Gas phase equilibrium geometries of the complexes were fully optimized and then vibrational frequencies were calculated at density functional theory (B3LYP) using 6-31 G(d) and SDD basis set. After computing the optimized structure and vibrational frequencies molecular orbital calculations were conducted with all compounds using same level of theory for analyzing the transition metal effects on the HOMO-LUMO energies. For calculating the excited state properties of the complexes, time dependent density functional theory (TD-DFT) is employed with CAM-B3LYP/6-31 +G (d,p) and B3LYP/SDD [59, 113-117].

3.3.2.8.1 Optimized structure: The optimized structure of isoleucine and its complexes are shown in Fig. 3.99 to Fig. 3.105. The calculated bond distances and angles are listed in Table 3.44 and Table 3.45.

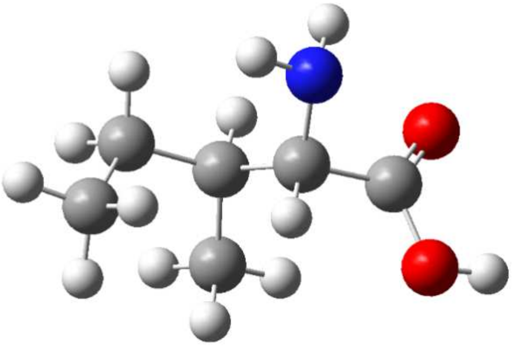

Fig. 3.99: Optimized structure of isoleucine calculated at B3LYP/SDD level of theory

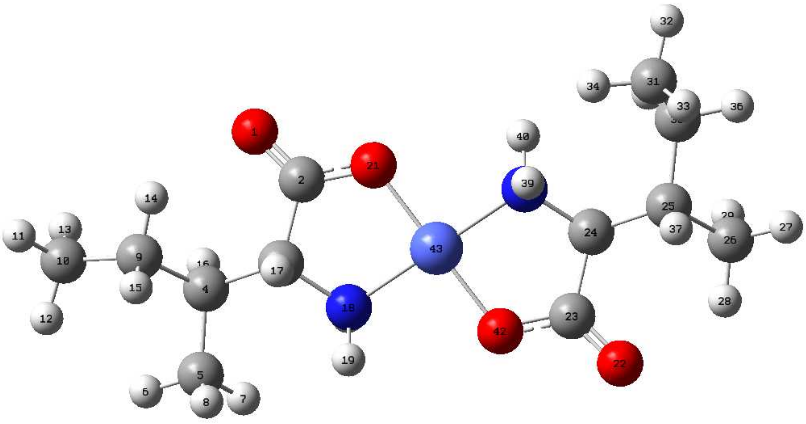

Fig. 3.100: Optimized structure of Co(ile)$_2$ calculated at B3LYP/SDD level of theory

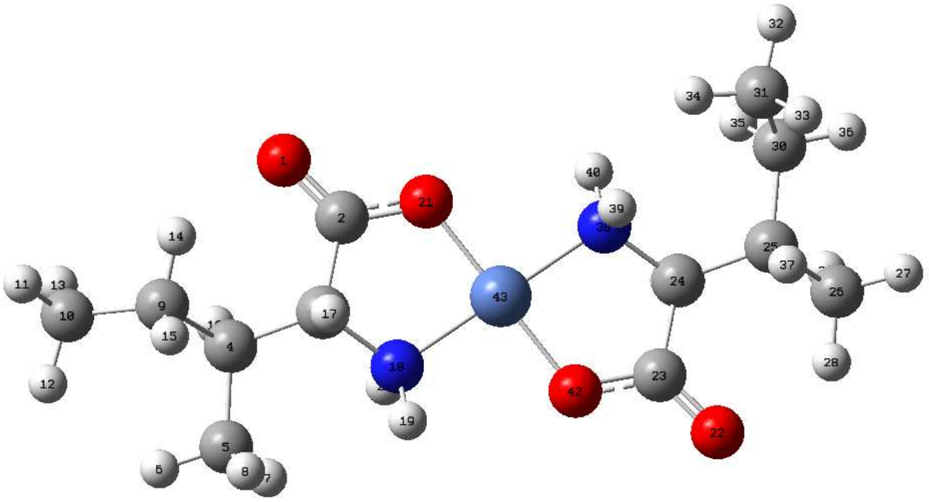

Fig. 3.101: Optimized structure of Ni(ile)$_2$ calculated at B3LYP/SDD level of theory

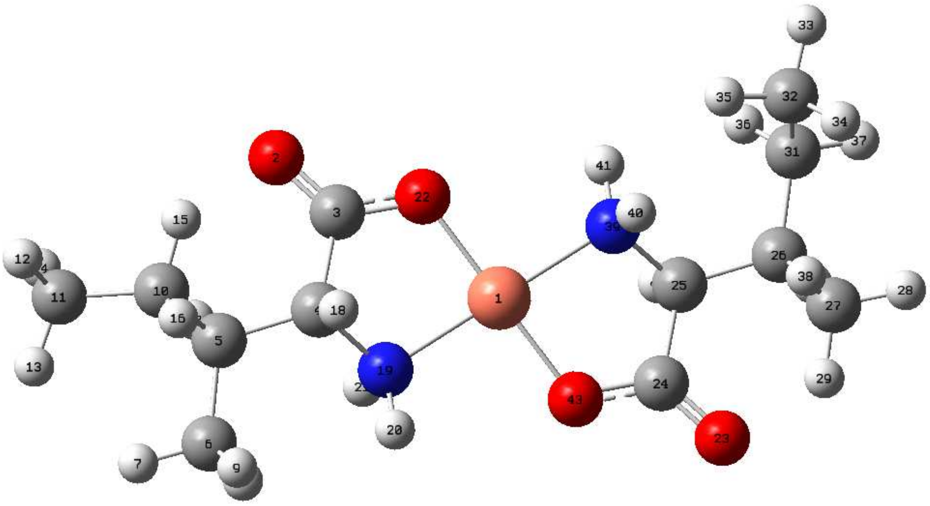

Fig. 3.102: Optimized structure of Cu(ile)$_2$ calculated at B3LYP/SDD level of theory

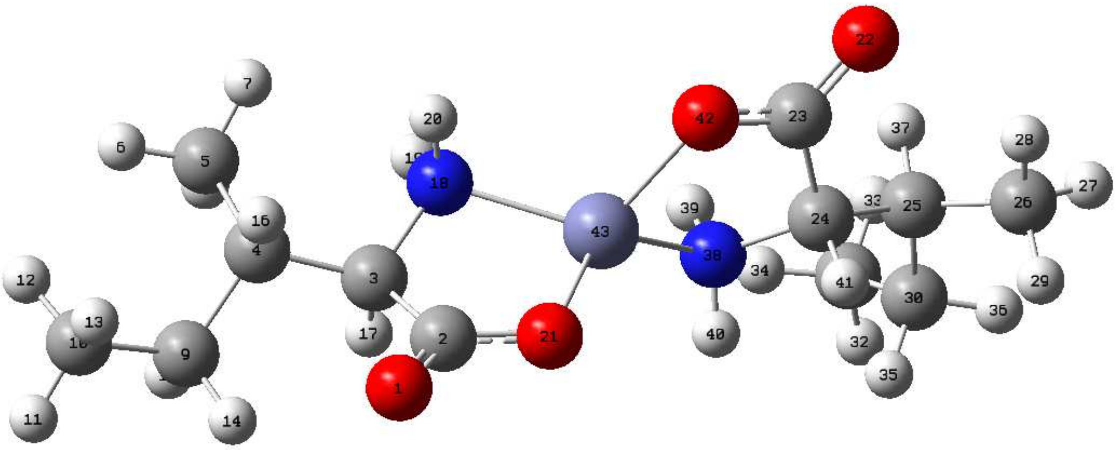

Fig. 3.103: Optimized structure of Zn(ile)$_2$ calculated at B3LYP/SDD level of theory

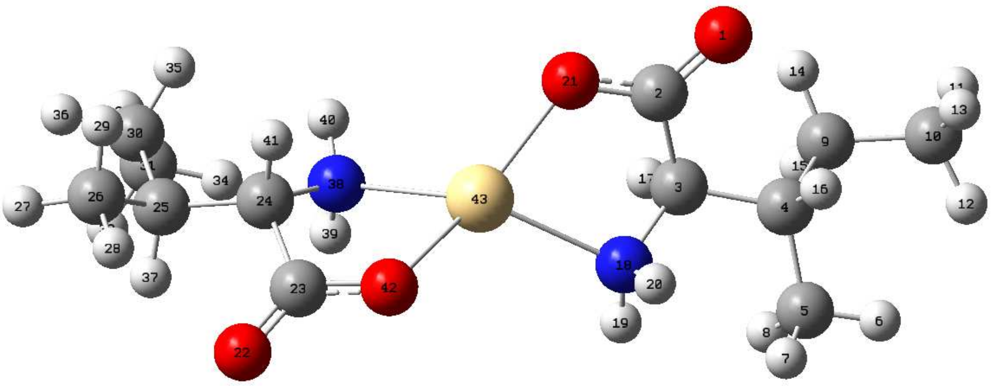

Fig. 3.104: Optimized structure of Cd(ile)$_2$ calculated at B3LYP/SDD level of theory

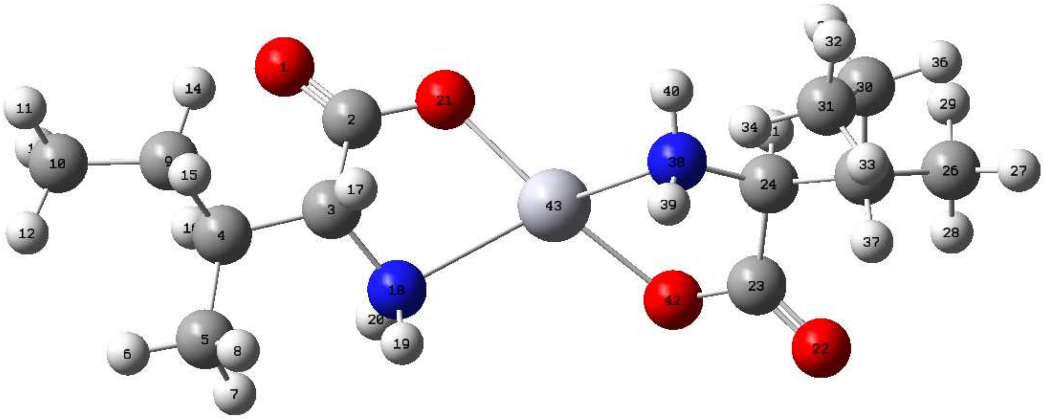

Fig. 3.105: Optimized structure of Hg(ile)$_2$ calculated at B3LYP/SDD level of theory

Table 3.44: Selected bond distances (Å) and angles of isoleucine

Assignment	Isoleucine
C=O	1.214
C–O	1.353
C–N	1.465
O–H	0.973
N–H	1.017
O–C–O	122.6
C–O–H	107.1
C–C–N	105.6

The C-O and C-N bond distances have deviated in the complexes compared to the ligand. This may be due to the complex formation with the metal ion. The N-M-O bond angles of the Co, Ni and Cu complexes are close to each other. Therefore they forms square planner structure. The difference in N-M-O bond angles indicates that the Zn, Cd and Hg complexes form distorted tetrahedral structure [59, 113-117].

Table 3.45: Selected bond distances (Å) and angles of the metal-isoleucine complexes

	Co(ile)$_2$	Ni(ile)$_2$	Cu(ile)$_2$	Zn(ile)$_2$	Cd(ile)$_2$	Hg(ile)$_2$
M–O	1.856	1.855	1.877	1.992	2.124	2.127
M–O	1.858	1.855	1.877	1.981	2.124	2.125
M–N	1.936	1.921	1.993	2.074	2.340	2.534
M–N	1.936	1.922	1.994	2.079	2.353	2.505
O–C	1.312	1.338	1.310	1.327	1.336	1.349
O–C	1.312	1.339	1.309	1.328	1.337	1.347
N–C	1.496	1.512	1.495	1.512	1.513	1.501
N–C	1.495	1.512	1.495	1.510	1.517	1.499
C–C	1.549	1.553	1.564	1.565	1.577	1.569
C–C	1.550	1.554	1.565	1.566	1.575	1.566
C=O	1.226	1.257	1.219	1.263	1.251	1.248
C=O	1.226	1.257	1.220	1.263	1.250	1.248
N–M–O	85.6	85.9	85.2	83.1	77.091	74.0
N–M–O	85.8	85.8	85.1	83.5	77.219	74.4
N–M–O	94.2	94.1	94.9	128.4	116.1	114.9
N–M–O	94.4	94.1	94.8	114.9	115.2	114.2
M–N–C	107.5	109.2	105.6	106.1	102.6	103.1
M–N–C	106.8	109.1	105.9	106.6	105.5	100.1
M–O–C	116.2	116.6	116.5	115.3	118.8	120.8
M–O–C	116.0	116.6	116.4	115.5	118.6	120.2

The binding energy of the complexes is calculated in terms of gas phase electronic energy, enthalpy and Gibbs free energy. These are summarized in Table 3.46. The positive ΔH and ΔG values indicate that the process of formation of the Ni, Zn, Cd and Hg complexes is endothermic i.e not spontaneous. On the other hand formation of Co and Cu complexes is exothermic i.e spontaneous [59, 113-117].

Table 3.46: Cation-binding energy, enthalpy, Gibbs free energy (Kcal/mol) of the metal-isoleucine complexes calculated at B3LYP/SDD level of theory

	$Co(ile)_2$	$Ni(ile)_2$	$Cu(ile)_2$	$Zn(ile)_2$	$Cd(ile)_2$	$Hg(ile)_2$
ΔE	-1052715.37	696.53	-904755.03	784.39	840.86	891.06
ΔH	-775663.87	696.53	-904755.03	784.39	840.86	891.06
ΔG	-775651.32	709.09	-904742.48	796.94	853.41	903.61

3.3.2.8.2 Vibrational frequencies: The computed IR frequencies of the ligand and the complexes have been visualized and confirmed by Gauss view program. The spectrum is shown in Fig. 3.106 to Fig. 3.112. The IR frequencies and their intensities of the complexes are compared with that of ligand in Table 3.47. The computed IR frequencies are compared with the experimental values in Table 3.48. The experimental IR vibrational frequencies are very consistent with the calculated values.

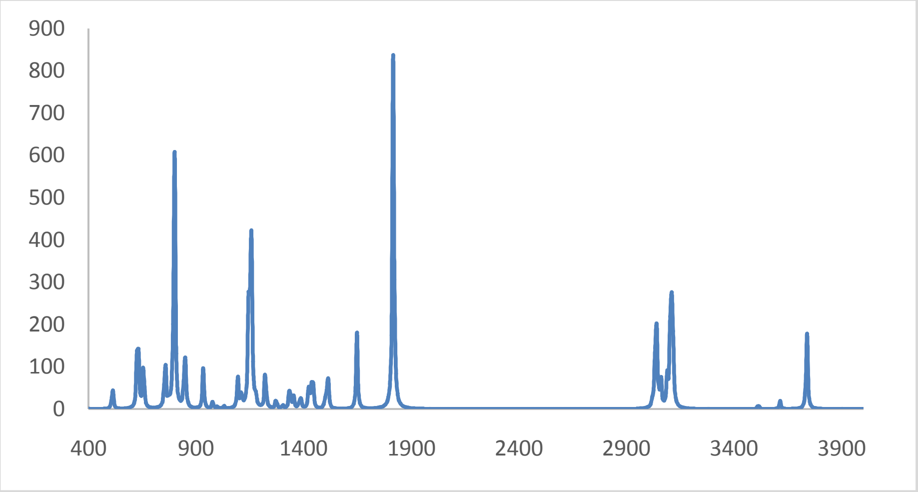

Fig. 3.106: Calculated IR spectrum of isoleucine

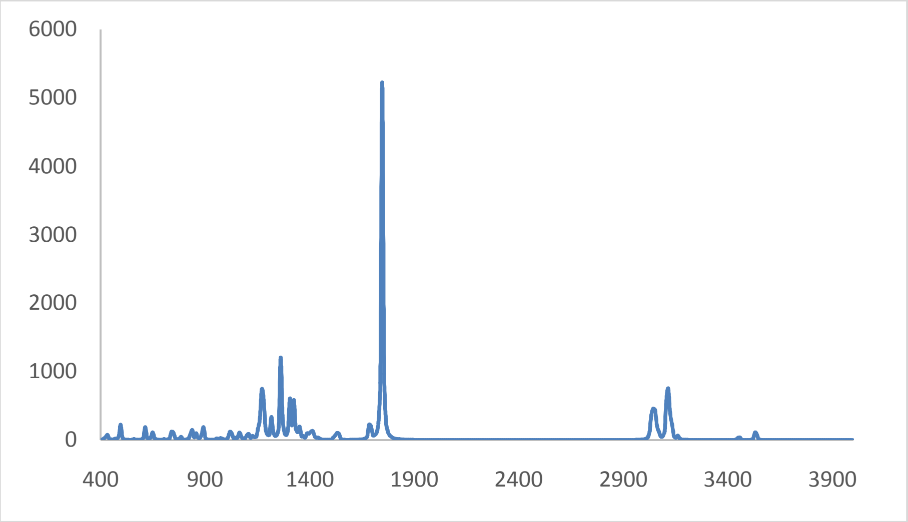

Fig. 3.107: Calculated IR spectrum of $Co(ile)_2$

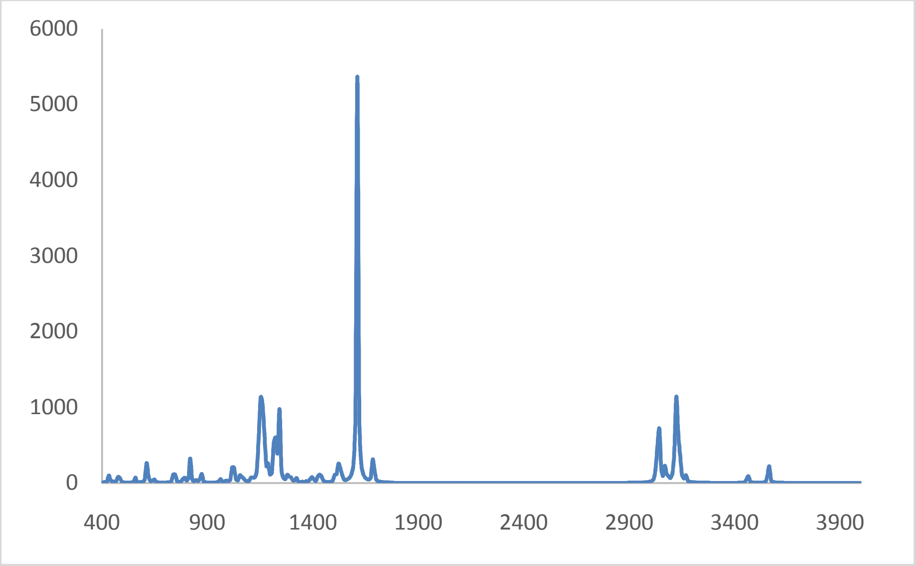

Fig. 3.108: Calculated IR spectrum of Ni(ile)$_2$

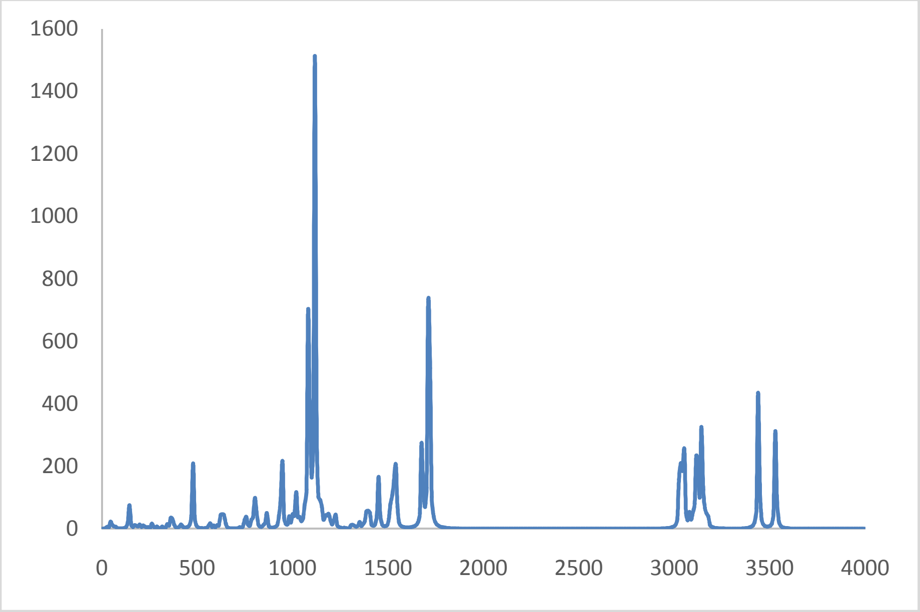

Fig. 3.109: Calculated IR spectrum of Cu(ile)$_2$

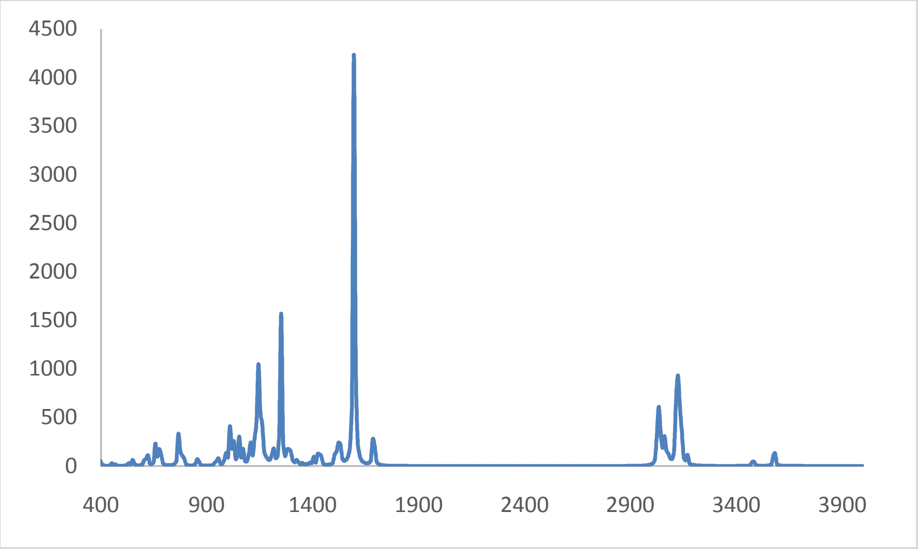

Fig. 3.110: Calculated IR spectrum of Zn(ile)$_2$

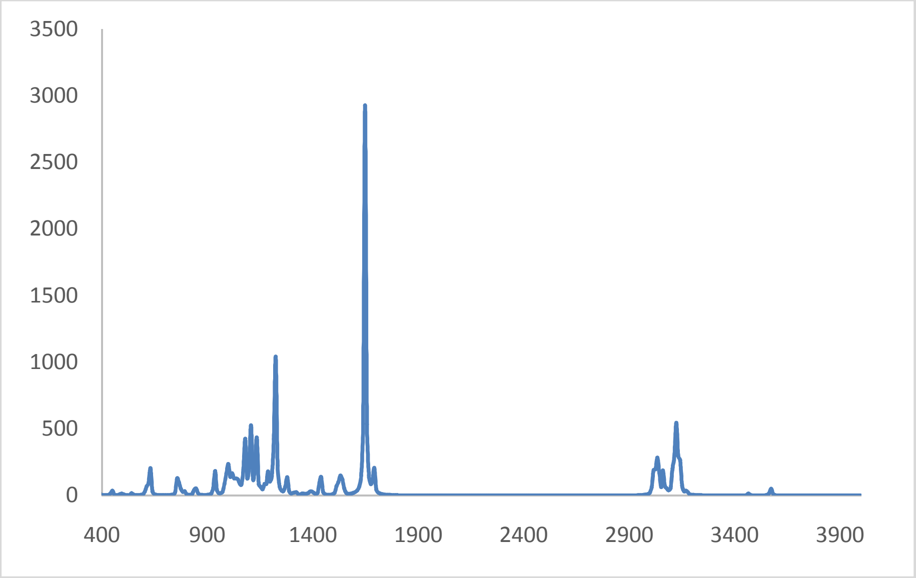

Fig. 3.111: Calculated IR spectrum of Cd(ile)$_2$

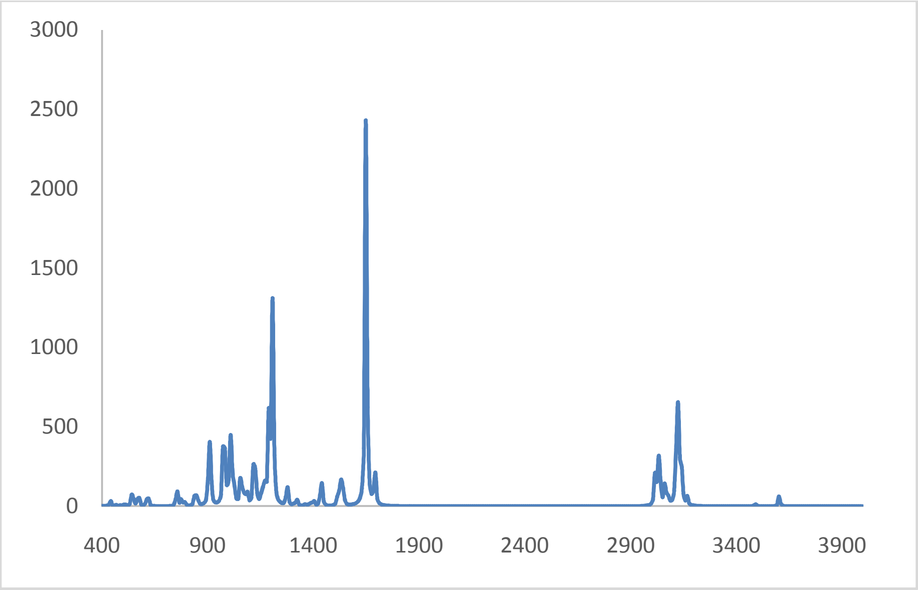

Fig. 3.112: Calculated IR spectrum of Hg(ile)$_2$

Table 3.47: Comparison of calculated IR frequencies and their intensities of the metal-isoleucine complexes (intensities in parentheses)

Compound	N–H str. (asymm)	N–H str. (symm)	C–H str.	C=O str.	N–H bending
Isoleucine	3613(5)	3511(3)	3088(20)	1815(267)	1646(52)
Co(ile)$_2$	3529(27)	3455(10)	3115(95)	1746(1505)	1682(49)
Ni(ile)$_2$	3560(43)	3464(18)	3127(154)	1610(1551)	1688(71)
Cu(ile)$_2$	3530(97)	3439(114)	3119(84)	1713(243)	1676(109)
Zn(ile)$_2$	3579(35)	3476(12)	3126(141)	1593(1154)	1685(69)
Cd(ile)$_2$	3569(11)	3465(3)	3120(128)	1646(851)	1687(39)
Hg(ile)$_2$	3599(11)	3488(4)	3121(113)	1654(46)	1688(37)

Table 3.48: Comparison of the scaled IR frequencies of the metal-isoleucine complexes with the experimental values (experimental values in parentheses)

Compound	N–H str. (asymm)	N–H str. (symm)	C–H str.
Isoleucine	3473 (3125)	3375 (3125)	2968 (2960)
Co(ile)$_2$	3392(3340)	3321(3290)	2994(2960)
Ni(ile)$_2$	3422(3340)	3330(3275)	3006(2960)
Cu(ile)$_2$	3393(3300)	3306(3250)	2998 (2975)
Zn(ile)$_2$	3440(3325)	3341(3260)	3005(2960)
Cd(ile)$_2$	3431(3300)	3331(3260)	2999(2960)
Hg(ile)$_2$	3460(3200)	3353(3100)	3000(2975)

Scaling factor 0.9613 is applied.

3.3.2.8.3 UV-Visible spectral analysis: The UV-Visible spectrum of the complexes were calculated at B3LYP/SDD and B3LYP/6-31+G(d,p) level of theory and are displayed from Fig. 3.113 to Fig. 3.119. The corresponding absorption properties are tabulated from Table 3.49 to Table 3.55. It was observed that the calculated results are very consistent with the experimental results.

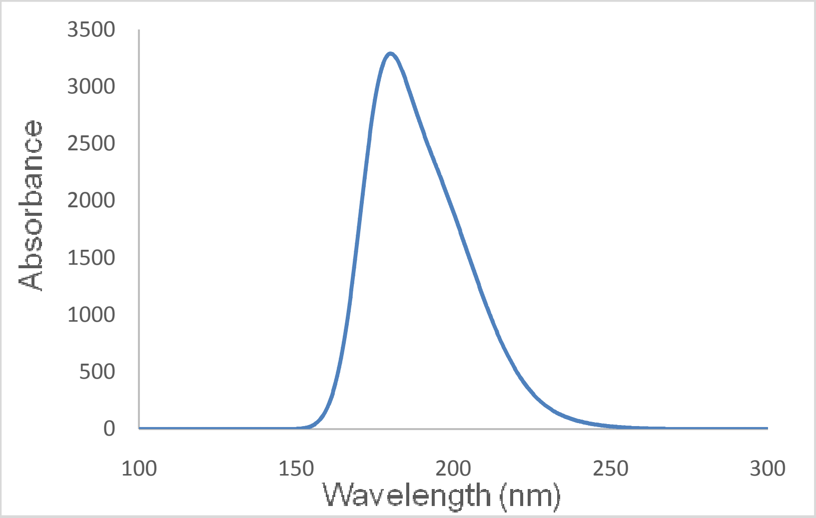

Fig. 3.113: Calculated UV-Vis spectrum of isoleucine

Table 3.49: The absorption properties of isoleucine calculated at CAM- B3LYP/6-31+G(d,p) level of theory

Wavelength	Excitation energies (eV)	Oscillator strengths	MO contribution	Assignments
232	5.34	0.0012	H → L (89.2%)	IL
213	5.81	0.0078	H → L+1 (36.1%) H-1 → L (32.0%)	IL
210	5.90	0.0025	H-1 → L (42.0%) H → L+1 (38.5%)	IL
200	6.19	0.0241	H → L+2 (75.2%) H → L+1 (16.5%)	IL

d-d = d-d transition, CT = charge transfer transition, IL = Intraligand charge transfer

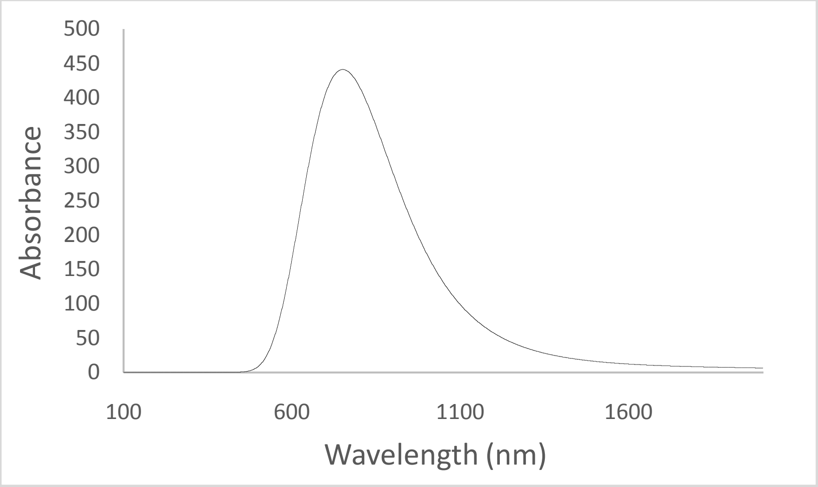

Fig. 3.114: Calculated UV-Vis spectrum of Co(ile)$_2$

Table 3.50: The absorption properties of Co(ile)$_2$ calculated at CAM- B3LYP/6- 31+G(d,p) level of theory

Wavelength	Excitation energies (eV)	Oscillator strengths	MO contribution	Assignments
753	1.64	0.0024	H-4 → L (93.3%)	d-d
742	1.66	0.0016	H-6 → L (23.5%) H-5 → L (53.8%)	d-d
681	1.81	0	H-6 → L (45.1%) H-5 → L (34.8%)	d-d

d-d = d-d transition, CT = charge transfer transition, IL = Intraligand charge transfer

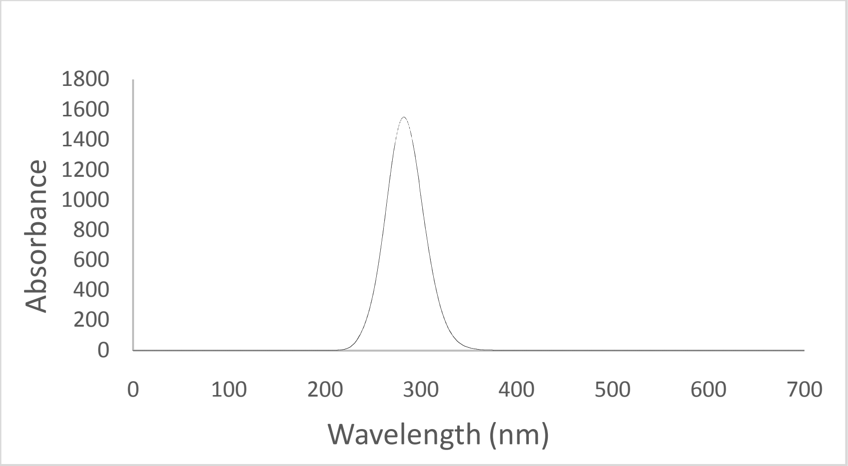

Fig. 3.115: Calculated UV-Vis spectrum of Ni(ile)$_2$

Table 3.51: The absorption properties of Ni(ile)$_2$ calculated at CAM- B3LYP/6 31+G(d,p) level of theory

Wavelength	Excitation energies (eV)	Oscillator strengths	MO contribution	Assignments
597	2.07	0	H → L (83.1%)	d-d
563	2.20	0	H-3 → L (64.2%)	d-d
479	2.58	0	H-4 → L (88.4%)	CT
466	2.65	0	H-7 → L (45.8%)	CT
282	4.38	0.0373	H-1 → L (95.4%)	IL
271	4.57	0	H-2 → L (53.4%)	IL
253	4.88	0.0041	H-5 → L (83.3%)	IL
251	4.94	0.0005	H-1 → L+2 (25.8%)	IL
248	4.99	0.0001	H → L+2 (80.2%)	IL

d-d = d-d transition, CT = charge transfer transition, IL = Intraligand charge transfer

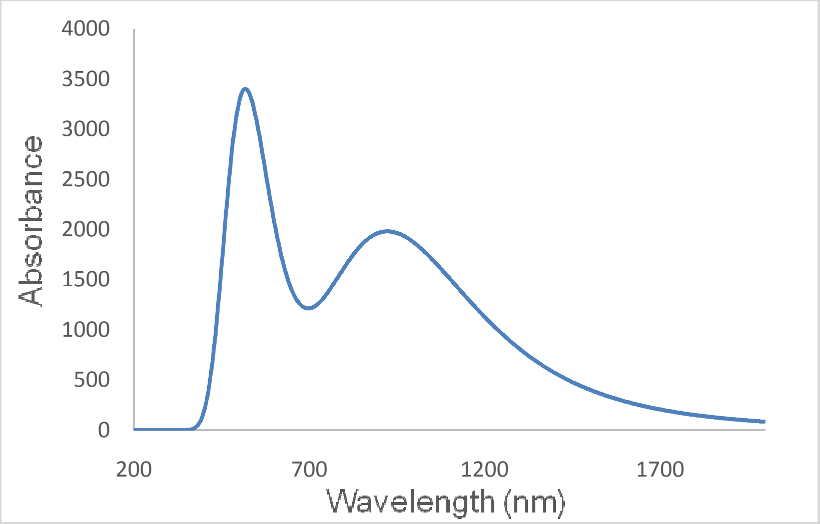

Fig. 3.116: Calculated UV-Vis spectrum of $Cu(ile)_2$

Table 3.52: **The absorption properties of $Cu(ile)_2$ calculated at CAM- B3LYP/6 31+G(d,p) level of theory**

Wavelength	Excitation energies (eV)	Oscillator strengths	MO contribution	Assignments
804	1.54	0.0001	H-6 → L (48.5%)	d-d
638	1.94	0.0091	H-2 → L (57.1%)	d-d
614	2.01	0.0002	H-3 → L (41.9%)	d-d
577	2.15	0.0053	H-3 → L (37.5%)	CT
549	2.25	0.0047	H-4 → L (43.4%)	CT
513	2.41	0.0483	H-5 → L (66.2%)	CT
512	2.42	0.0033	H-8 → L (60.0%)	CT
500	2.47	0.0230	H-7 → L (43.8%)	CT

d-d = d-d transition, CT = charge transfer transition, IL = Intraligand charge transfer

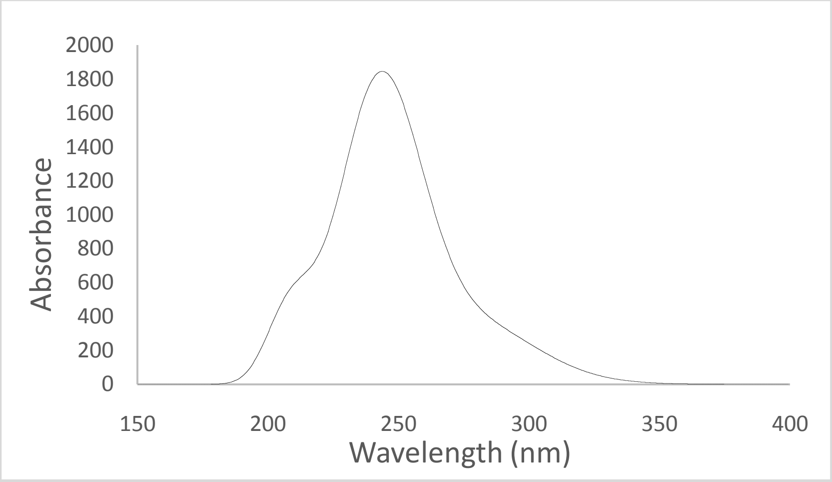

Fig. 3.117: Calculated UV-Vis spectrum of Zn(ile)$_2$

Table 3.53: The absorption properties of Zn(ile)$_2$ calculated at CAM- B3LYP/6 31+G(d,p) level of theory

Wavelength	Excitation energies (eV)	Oscillator strengths	MO contribution	Assignments
288	4.30	0.0056	H-1 → L (45.4%)	IL
285	4.34	0.0011	H → L (47.7%)	IL
253	4.89	0.0037	H-2 → L (42.8%)	IL
251	4.92	0.0033	H-2 → L (47.2%)	IL
249	4.96	0.0191	H-3 → L (93.0%)	IL
243	5.09	0.0027	H-1 → L+2 (40.9%)	IL
237	5.22	0.0142	H-4 → L (95.1%)	IL
233	5.30	0.0091	H-5 → L (95.4%)	IL
210	5.89	0.0118	H-1 → L+1 (43.7%)	IL
206	6.00	0.0011	H-4 → L+1 (31.8%)	IL

d-d = d-d transition, CT = charge transfer transition, IL = Intraligand charge transfer

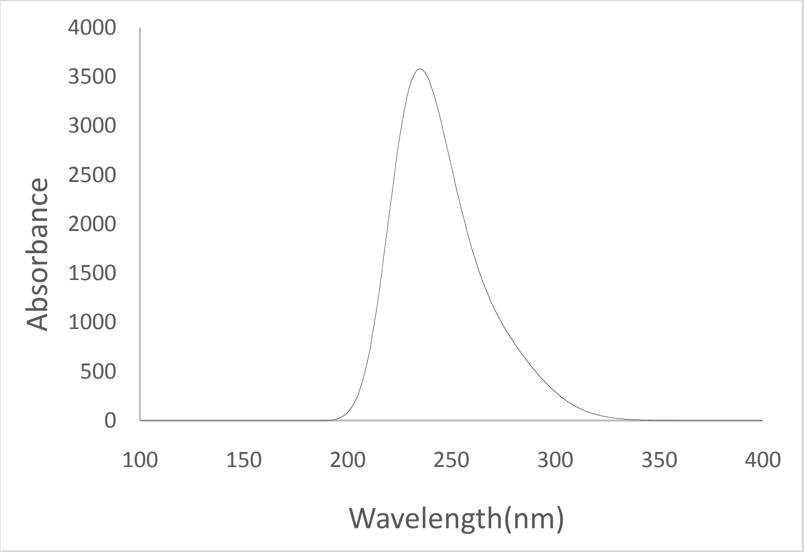

Fig. 3.118: Calculated UV-Vis spectrum of $Cd(ile)_2$

Table 3.54: The absorption properties of $Cd(ile)_2$ calculated at CAM- B3LYP/6 31+G(d,p) level of theory

Wavelength	Excitation energies (eV)	Oscillator strengths	MO contribution	Assignments
279	4.44	0.0048	H → L (90.5%)	IL
276	4.49	0.0089	H-1 → L (91.3%)	IL
253	4.90	0.0008	H-1 → L-2 (38.6%)	IL
251	4.92	0.0084	H-2 → L (35.3%)	IL
250	4.94	0.0089	H-2 → L (54.6%)	IL
249	4.97	0.0125	H-3 → L (93.4%)	IL
238	5.19	0.0023	H-4 → L (92.8%)	IL
232	5.33	0.0615	H-5 → L (90.0%)	IL
223	5.54	0.0130	H-1 → L+1 (53.3%)	IL
218	5.68	0.0039	H → L+2 (71.3%)	IL

d-d = d-d transition, CT = charge transfer transition, IL = Intraligand charge transfer

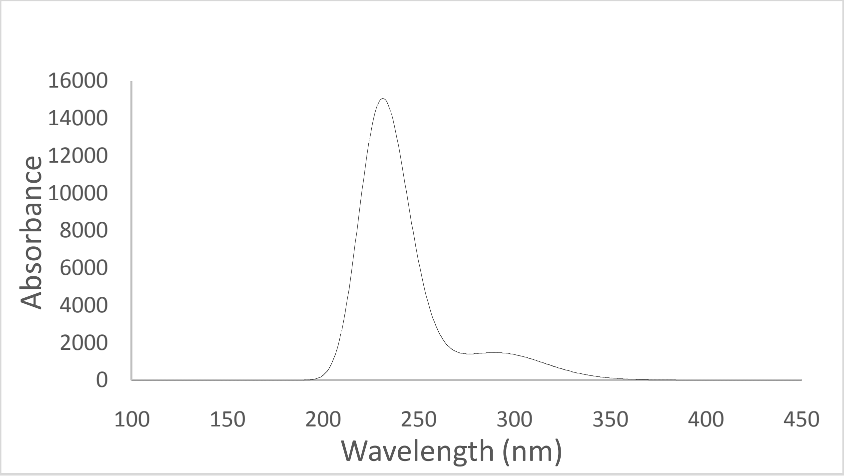

Fig. 3.119: Calculated UV-Vis spectrum of Hg(ile)$_2$

Table 3.55: The absorption properties of Hg(ile)$_2$ calculated at CAM- B3LYP/6-31+G(d,p) level of theory

Wavelength	Excitation energies (eV)	Oscillator strengths	MO contribution	Assignments
308	4.02	0.0014	H → L (96.2%)	IL
299	4.14	0.0250	H → L (94.0%)	IL
279	4.44	0.0057	H-2 → L (62.5%)	IL
274	4.52	0.0110	H-3 → L (68.5%)	IL
258	4.79	0.0010	H-4 → L (46.8%)	IL
256	4.83	0	H-4 → L (38.2%)	IL
254	4.88	0.0002	H-1 → L+2 (45.1%)	IL
237	5.23	0.1183	H-5 → L (70.7%)	IL
229	5.40	0.1929	H → L+1 (46.0%)	IL
226	5.46	0.0796	H → L+1 (36.3%)	IL

d-d = d-d transition, CT = charge transfer transition, IL = Intraligand charge transfer

UV–Visible spectral studies reveal that Co, Ni and Cu complex demonstrate characteristic metal to ligand charge transfer (MLCT) or ligand to metal charge transfer (LMCT) and d–d transition bands. On the other hand Zn, Cd and Hg complex only demonstrate intraligand charge transfer (IL). This is reasonable since the respective metal ions in the later case have d^{10} configuration [59, 113-117].

3.3.2.8.4 Frontier molecular orbital: Selected frontier molecular orbital of isoleucine and its complexes is displayed from Fig. 3.120 to Fig. 3.126 and the corresponding molecular orbital energy is listed in Table 3.56 and 3.57.

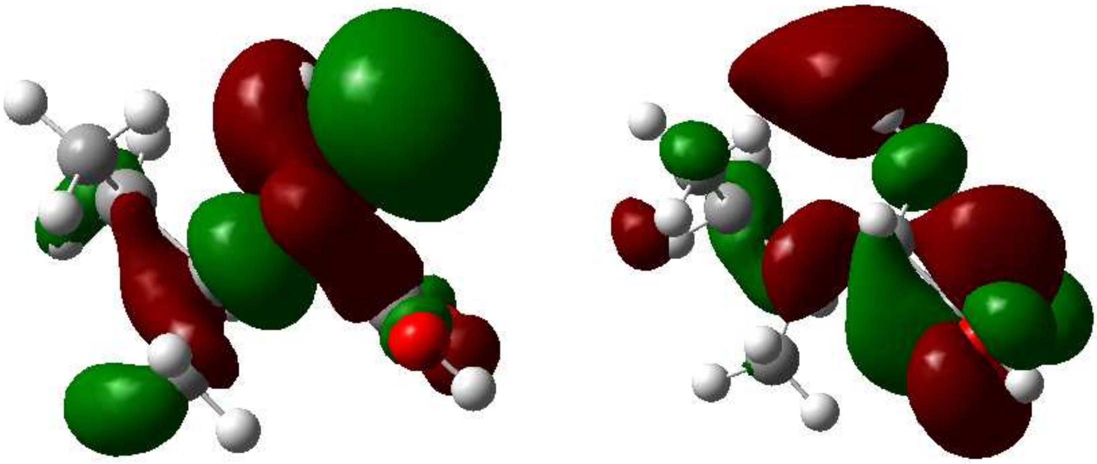

HOMO LUMO

Fig. 3.120: HOMO and LUMO of isoleucine

Table 3.56: Energies (Hartree) of HOMO and LUMO orbital's, HOMO-LUMO gaps are calculated at B3LYP/SDD level of theory for isoleucine

HOMO-5	-0.43	LUMO+5	0.02	
HOMO-4	-0.43	LUMO+4	0.02	
HOMO-3	-0.42	LUMO+3	0.01	
HOMO-2	-0.38	LUMO+2	0.00	
HOMO-1	-0.36	LUMO+1	-0.03	
HOMO	-0.34	LUMO	-0.12	0.22

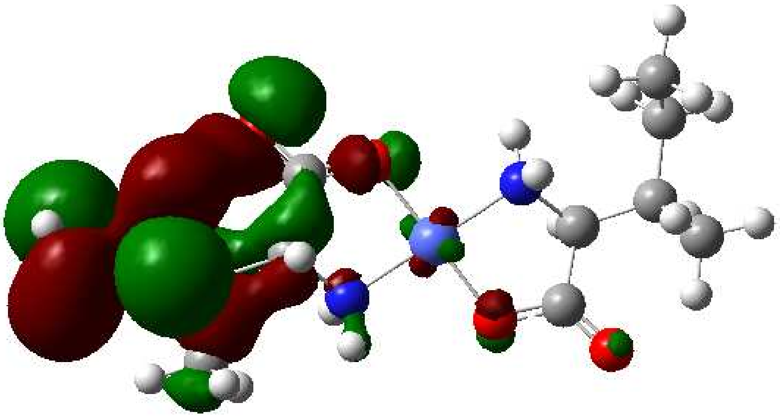

Co(ile)$_2$: HOMO-3

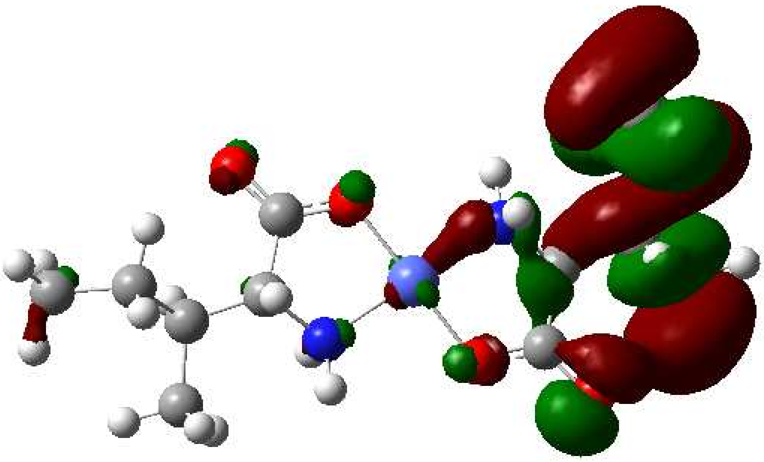

Co(ile)$_2$: HOMO-4

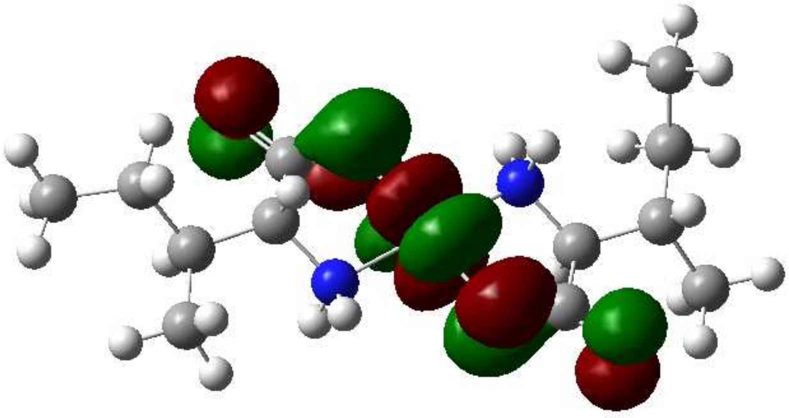

Co(ile)$_2$: LUMO

Fig. 3.121: HOMO and LUMO of Co(ile)$_2$

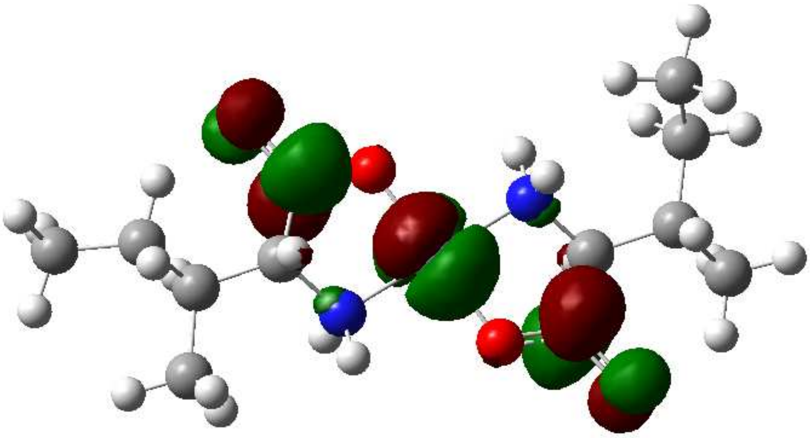

Ni(ile)$_2$: HOMO

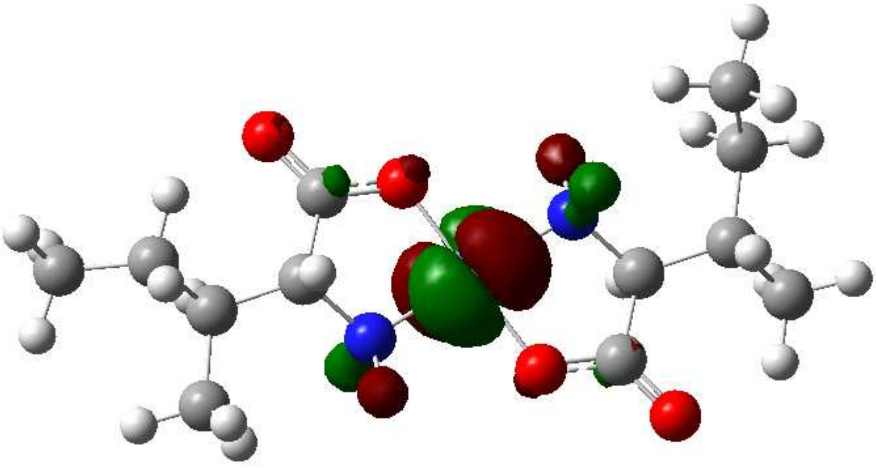

Ni(ile)$_2$: HOMO-1

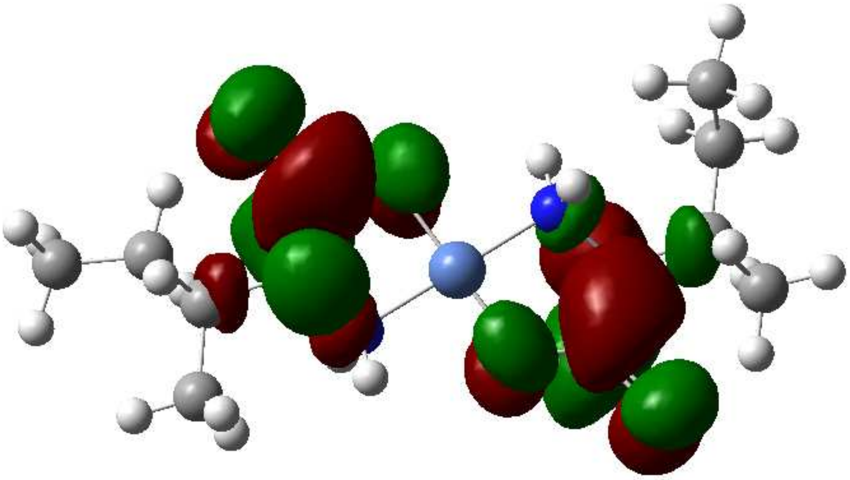

Ni(ile)$_2$: LUMO

Fig. 3.122: HOMO and LUMO of Ni(ile)$_2$

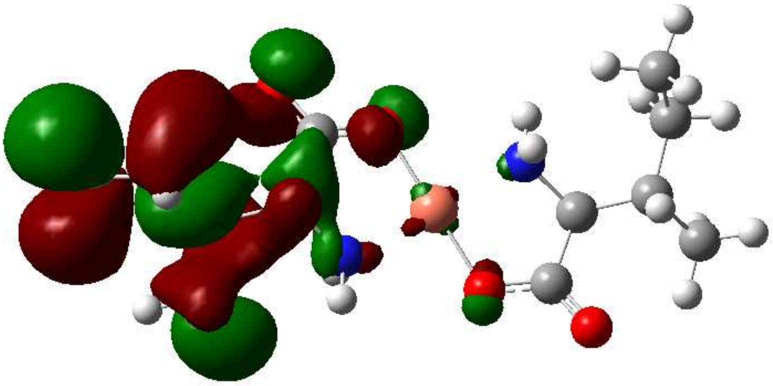

Cu(ile)$_2$: HOMO-3

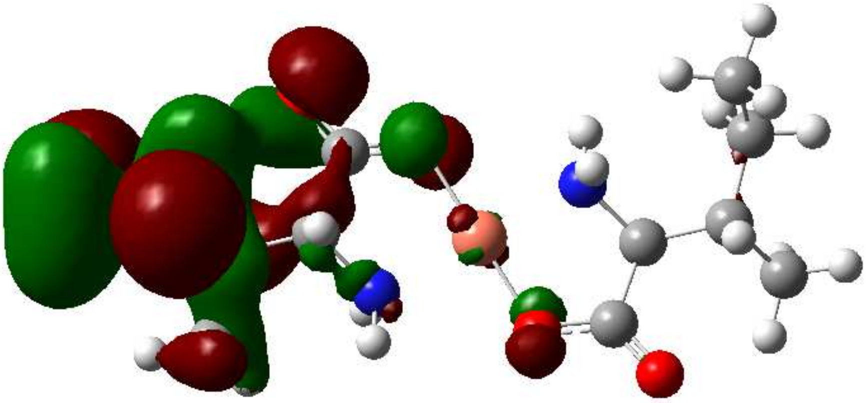

Cu(ile)$_2$: HOMO-4

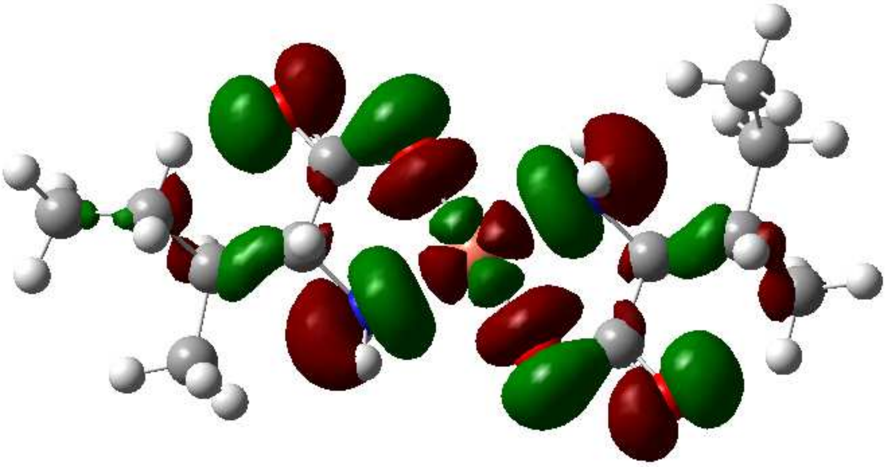

Cu(ile)$_2$: LUMO

Fig. 3.123: HOMO and LUMO of Cu(ile)$_2$

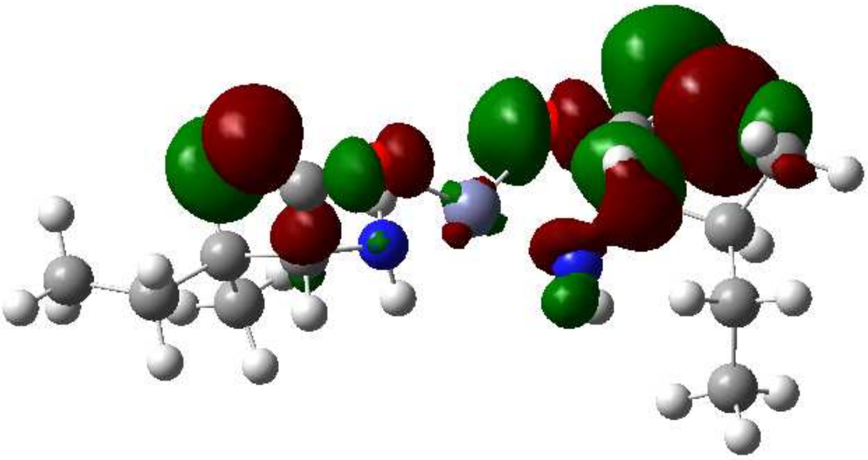

Zn(ile)$_2$: HOMO

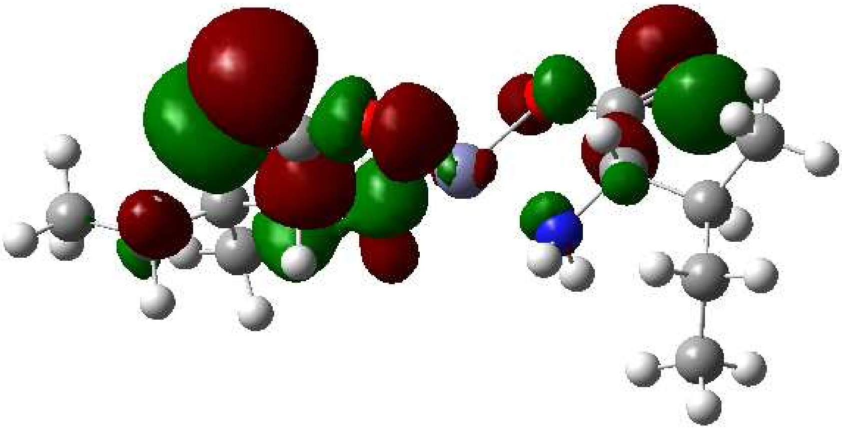

Zn(ile)$_2$: HOMO-1

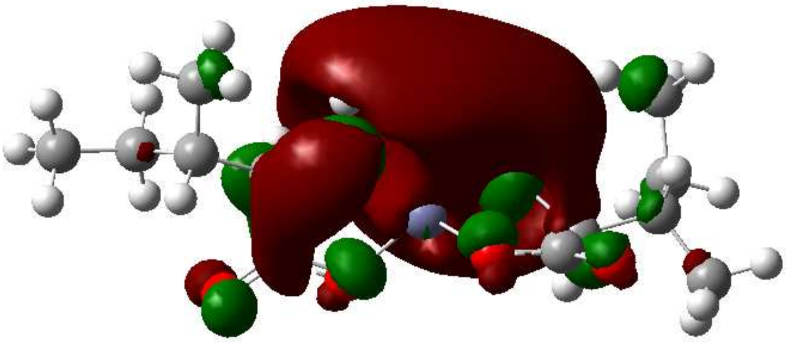

Zn(ile)$_2$: LUMO

Fig. 3.124: HOMO and LUMO of Zn(ile)$_2$

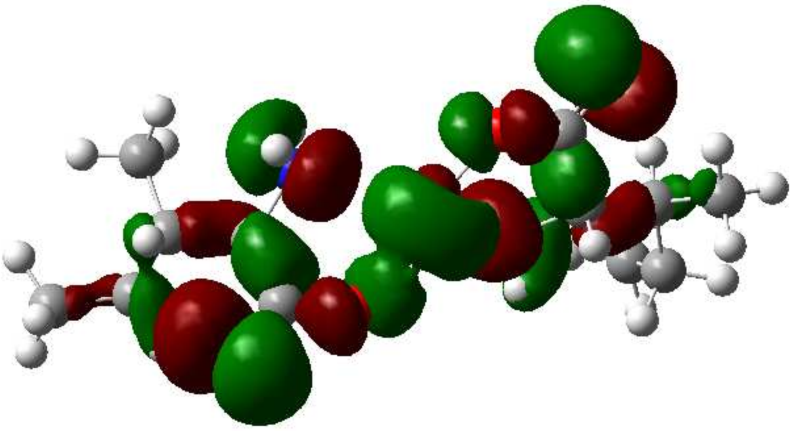

Hg(ile)$_2$: HOMO

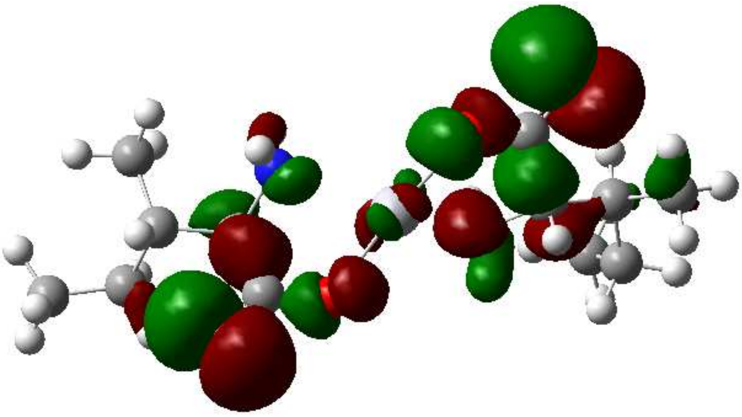

Hg(ile)$_2$: HOMO-1

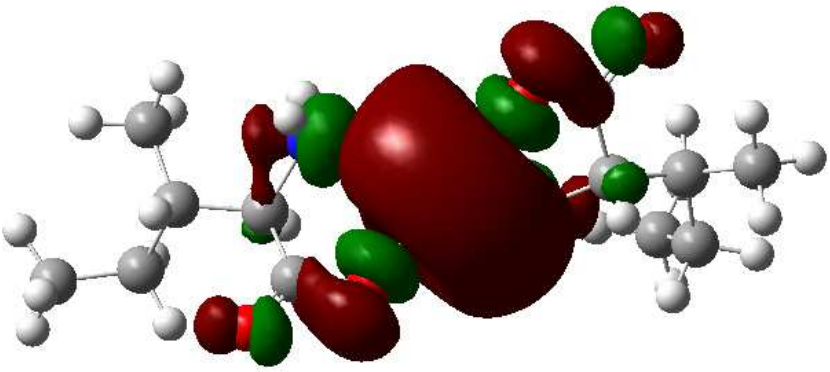

Hg(ile)$_2$: LUMO

Fig. 3.125: HOMO and LUMO of Hg(ile)$_2$

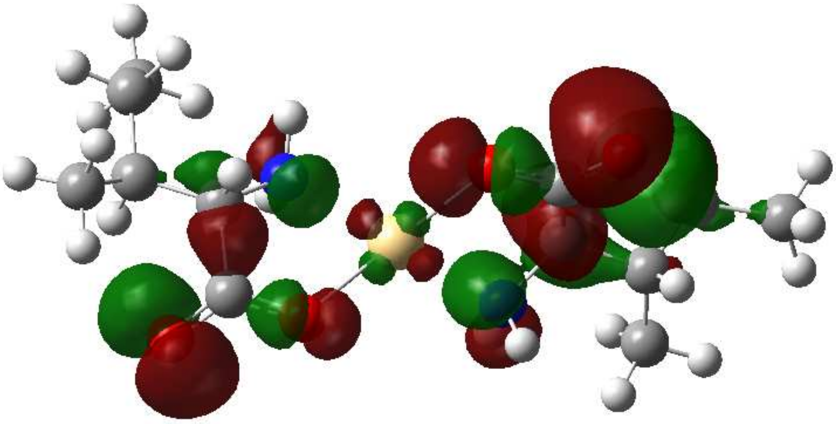

Cd(ile)$_2$: HOMO

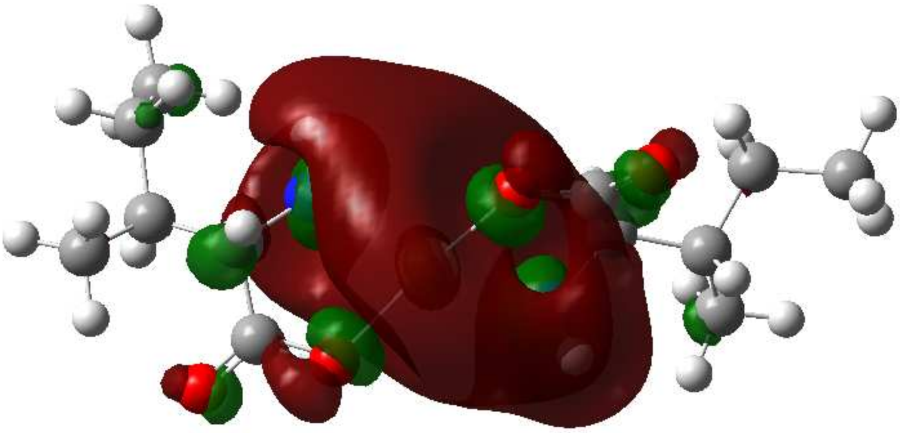

Cd(ile)$_2$: LUMO

Fig. 3.126: HOMO and LUMO of Cd(ile)$_2$

Table 3.57: Energies (Hartree) of HOMO and LUMO orbital's, HOMO-LUMO gaps are calculated at B3LYP/SDD level of theory for all metal-isoeucine complexes

Molecular Orbital	Co(ile)$_2$	Ni(ile)$_2$	Cu(ile)$_2$	Zn(ile)$_2$	Cd(ile)$_2$	Hg(ile)$_2$
HOMO-5	-0.45	-0.36	-0.45	-0.28	-0.28	-0.29
HOMO-4	-0.45	-0.36	-0.44	-0.28	-0.28	-0.29
HOMO-3	-0.44	-0.35	-0.44	-0.26	-0.27	-0.28
HOMO-2	-0.44	-0.18	-0.44	-0.26	-0.27	-0.27
HOMO-1	-0.42	-0.16	-0.42	-0.24	-0.25	-0.26
HOMO	-0.42	-0.15	-0.41	-0.24	-0.25	-0.25
LUMO	-0.36	-0.14	-0.32	-0.05	-0.06	-0.08
LUMO+1	-0.26	-0.12	-0.17	-0.01	-0.02	-0.03
LUMO+2	-0.17	-0.11	-0.17	0.01	-0.02	-0.02
LUMO+3	-0.17	-0.09	-0.15	0.01	0.00	0.00
LUMO+4	-0.14	-0.06	-0.13	0.02	0.02	0.01
LUMO+5	-0.14	-0.05	-0.12	0.04	0.03	0.02
GAP	0.06	0.01	0.09	0.19	0.19	0.17

The HOMO-LUMO gap of the complexes is decreased from the parent isoleucine. Therefore metal has a noticeable effect on the frontier molecular orbital energies [59, 113-117].

3.3.2.9 Antimicrobial activity: Attempt was taken to study the antimicrobial activity of the complexes. The complexes are insoluble in water. Therefore it was not possible to get any information in this field.

SUMMARY

4.1 Metal-ligand interaction in solution

The electrochemical study demonstrates that the metal ion interacts with both the zwitterionic and anionic form of the ligand. But the metal-anionic ligand interaction is more pronounced over metal-zwitterionic ligand interaction. Maximum interaction occurs in 1:2 mole ratios. The phenomenon that the peak current changes almost linearly with square root of scan rate, the peak potential separation is much larger and the peak current ratio is greater than unity indicates that the redox process of the respective metal ion may be quasi-reversible and coupled with some chemical reaction. The interaction of Cd(II) with leucine and isoleucine is compared in Fig. 4.1 to Fig. 4.4.

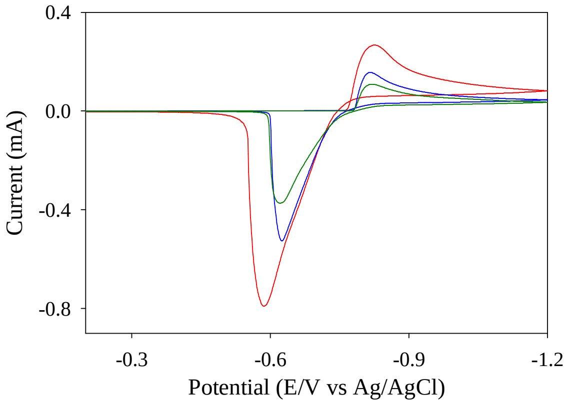

Fig. 4.1: CV's of free Cd(II) (red), Cd(II) in presence of z. leu (blue) and Cd(II) in presence of a. leu (green)

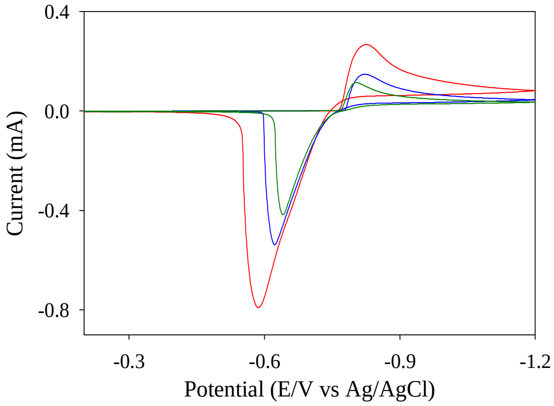

Fig. 4.2: CV's of free Cd(II) (red), Cd(II) in presence of z. ile (blue) and Cd(II) in presence of a. ile (green)

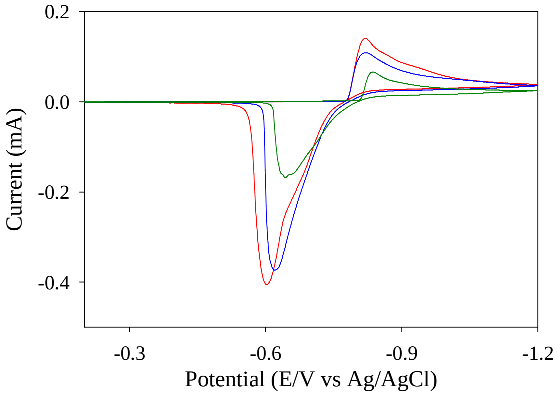

Fig. 4.3: CV's of Cd(II) in presence of a. leu at 1:0.5 (red), 1:1 (blue) and 1:2 (green) mole ratio

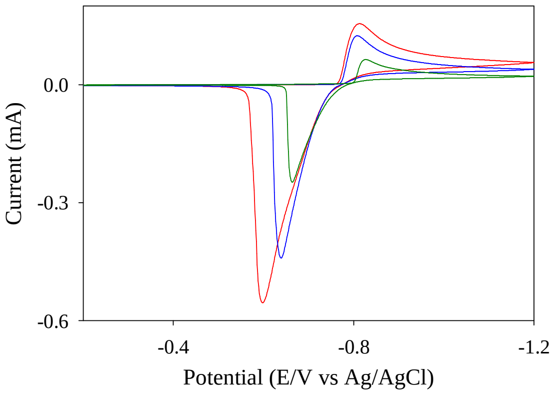

Fig. 4.4: CV's of Cd(II) in presence of a. ile at 1:0.5 (red), 1:1 (blue) and 1:2 (green) mole ratio

The chronoamperometric and chronocoulometric analysis suggests adsorption of reactant or products occurring at the electrode while electrolysis. The current response, charge response and the Anson plot for the Zn(II)-anionic leucine and Zn(II)-anionic isoleucine system are displayed in Fig. 4.5 – Fig. 4.10.

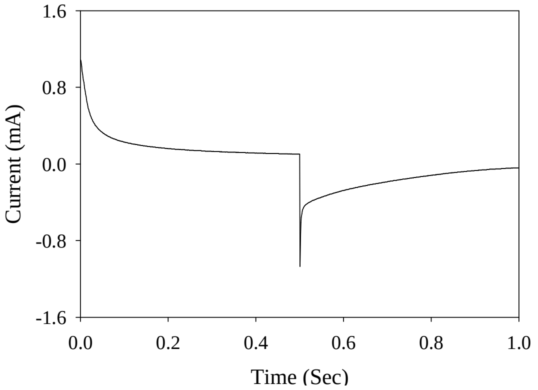

Fig. 4.5: **Current vs time plot for Zn(II) in presence of a. leu**

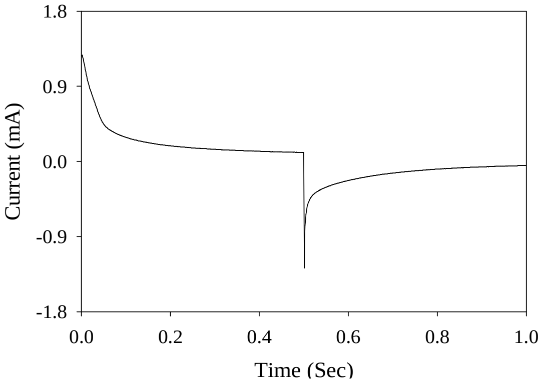

Fig. 4.6: **Current vs time plot for Zn(II) in presence of a. ile**

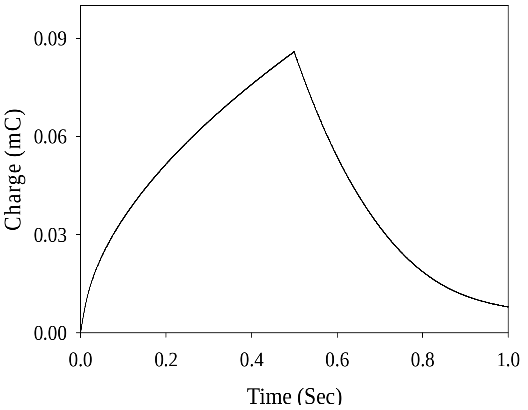

Fig. 4.7: **Charge vs time plot for Zn(II) in presence of a. leu**

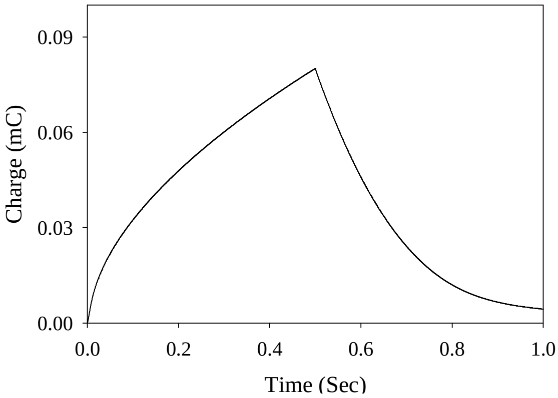

Fig. 4.8: **Charge vs time plot for Zn(II) in presence of a. ile**

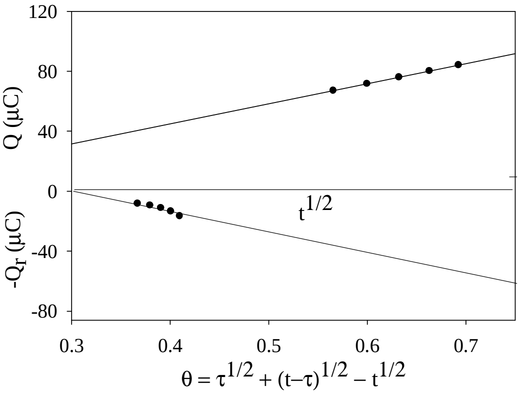

Fig. 4.9: **Plots of Q vs $t^{1/2}$ and $-Q_r$ vs θ for Zn(II) in presence of a. leu**

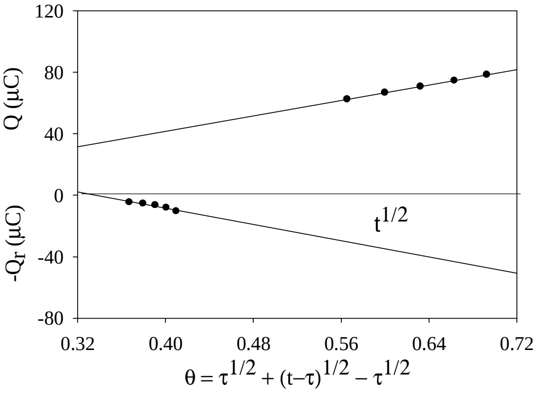

Fig. 4.10: **Plots of Q vs $t^{1/2}$ and $-Q_r$ vs θ for Zn(II) in presence of a. ile**

4.2 Metal-ligand interaction in solid state

Leucine and isoleucine both forms 1:2 complexes with metal. The complexes were prepared in aqueous medium by direct reaction between the metal salt and anionic ligand. The reaction scheme is shown below. The precipitate formed was then filtered, washed and dried over silica gel.

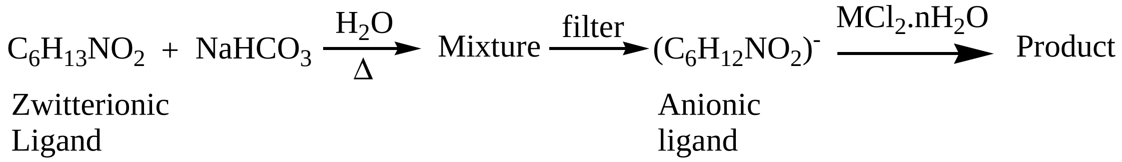

$$C_6H_{13}NO_2 + NaHCO_3 \xrightarrow[\Delta]{H_2O} \text{Mixture} \xrightarrow{\text{filter}} (C_6H_{12}NO_2)^- \xrightarrow{MCl_2.nH_2O} \text{Product}$$

The formulation of the prepared complexes were done by comparing the elemental (C, H and N) and metal analysis data and the calculated values. Comparing all the experimental and theoretical data for C, H, N and M, the proposed empirical formula of the complexes are,

Co-leucine complex	$Co(C_6H_{12}NO_2)_2.2H_2O$	Co-isoleucine complex	$Co(C_6H_{12}NO_2)_2.2H_2O$
Ni-leucine complex	$Ni(C_6H_{12}NO_2)_2.2H_2O$	Ni-isoleucine complex	$Ni(C_6H_{12}NO_2)_2.2H_2O$
Cu-leucine complex	$Cu(C_6H_{12}NO_2)_2$	Cu-isoleucine complex	$Cu(C_6H_{12}NO_2)_2.H_2O$
Zn-leucine complex	$Zn(C_6H_{12}NO_2)_2$	Zn-isoleucine complex	$Zn(C_6H_{12}NO_2)_2.½ H_2O$
Cd-leucine complex	$Cd(C_6H_{12}NO_2)_2$	Cd-isoleucine complex	$Cd(C_6H_{12}NO_2)_2$
Hg-leucine complex	$Hg(C_6H_{12}NO_2)_2$	Hg-isoleucine complex	$Hg(C_6H_{12}NO_2)_2$

Table 4.1: Percent composition of C, H, N and metal in the leucine complexes

Compound	% C		% H		% N		% Metal		% Yield based on metal
	Fnd.	Cal.	Fnd.	Cal.	Fnd.	Cal.	Fnd.	Cal.	
$Co(C_6H_{12}NO_2)_2.2H_2O$	40.45	40.57	8.07	7.89	7.90	7.89	16.50	16.60	54
$Ni(C_6H_{12}NO_2)_2.2H_2O$	40.34	40.60	7.98	7.89	7.80	7.89	15.65	16.55	50
$Cu(C_6H_{12}NO_2)_2$	43.35	44.51	7.16	7.42	8.45	8.65	17.92	19.63	67
$Zn(C_6H_{12}NO_2)_2$	43.88	44.25	7.56	7.37	8.56	8.60	19.11	20.10	81
$Cd(C_6H_{12}NO_2)_2$	37.52	38.67	5.95	6.44	7.10	7.52	28.23	30.18	65
$Hg(C_6H_{12}NO_2)_2$	30.96	31.26	5.10	5.21	5.90	6.08	42.60	43.55	55
$Pb(C_6H_{12}NO_2)_2$	1.58	30.82	0.77	5.14	3.10	5.99	-	44.35	-

Cal. = Calculated, Fnd. = Found

Table 4.2: Percent composition of C, H, N and metal in the isoleucine complexes

Compound	% C		% H		% N		% Metal		% Yield based on metal
	Fnd.	Cal.	Fnd.	Cal.	Fnd.	Cal.	Fnd.	Cal.	
$Co(C_6H_{12}NO_2)_2.2H_2O$	41.21	40.56	7.94	7.89	7.91	7.89	15.50	16.62	55
$Ni(C_6H_{12}NO_2)_2.2H_2O$	40.42	40.60	8.08	7.89	7.89	7.89	15.55	16.55	52
$Cu(C_6H_{12}NO_2)_2. H_2O$	42.37	42.17	7.84	7.61	8.20	8.20	17.45	18.59	60
$Zn(C_6H_{12}NO_2)_2.½ H_2O$	36.42	43.11	6.72	7.49	7.06	8.38	18.34	19.46	46
$Cd(C_6H_{12}NO_2)_2$	36.89	38.67	6.12	6.44	7.16	7.52	28.90	30.18	48
$Hg(C_6H_{12}NO_2)_2$	30.10	31.26	4.98	5.21	5.82	6.08	42.89	43.55	50
$Pb(C_6H_{12}NO_2)_2$	4.10	30.82	0.69	5.14	0.79	5.99	-	44.35	-

Cal. = Calculated, Fnd. = Found

Thermal analysis ensures that the Co and Ni complex of both leucine and isoleucine contains two molecules of water of crystallization. The Cu complex of isoleucine contains one molecule and the Zn complex of isoleucine contains half molecule of water of crystallization. The other complexes do not contain any water of crystallization.

The complexes are insoluble in the most common solvent with few exceptions. The Ni-leucine, Co-isoleucine, Ni-isoleucine and Cu-isoleucine complexes are soluble in methanol. The melting temperature of all the complexes is more than 200 ^{0}C.

Table 4.3: Solubility of the prepared metal-leucine complexes

Compound	Appearance	Soluble in	Insoluble in
$Co(C_6H_{12}NO_2)_2.2H_2O$	Pink	-	H_2O, CH_3OH, C_2H_5OH, CH_3COCH_3, DMSO
$Ni(C_6H_{12}NO_2)_2.2H_2O$	Sky blue	CH_3OH	H_2O, C_2H_5OH, CH_3COCH_3, DMSO
$Cu(C_6H_{12}NO_2)_2$	Blue	-	H_2O, CH_3OH, C_2H_5OH, CH_3COCH_3, DMSO
$Zn(C_6H_{12}NO_2)_2$	Colorless	-	H_2O, CH_3OH, C_2H_5OH, CH_3COCH_3, DMSO
$Cd(C_6H_{12}NO_2)_2$	Colorless	-	H_2O, CH_3OH, C_2H_5OH, CH_3COCH_3, DMSO
$Hg(C_6H_{12}NO_2)_2$	Colorless	-	H_2O, CH_3OH, C_2H_5OH, CH_3COCH_3, DMSO

Table 4.4: Solubility of the prepared metal-isoleucine complexes

Compound	Appearance	Soluble in	Insoluble in
$Co(C_6H_{12}NO_2)_2.2H_2O$	Pink	CH_3OH	H_2O, C_2H_5OH, CH_3COCH_3, DMSO
$Ni(C_6H_{12}NO_2)_2.2H_2O$	Sky blue	CH_3OH	H_2O, C_2H_5OH, CH_3COCH_3, DMSO
$Cu(C_6H_{12}NO_2)_2. H_2O$	Blue	CH_3OH	H_2O, C_2H_5OH, CH_3COCH_3, DMSO
$Zn(C_6H_{12}NO_2)_2.½ H_2O$	Colorless	-	H_2O, CH_3OH, C_2H_5OH, CH_3COCH_3, DMSO
$Cd(C_6H_{12}NO_2)_2$	Colorless	-	H_2O, CH_3OH, C_2H_5OH, CH_3COCH_3, DMSO
$Hg(C_6H_{12}NO_2)_2$	Colorless	-	H_2O, CH_3OH, C_2H_5OH, CH_3COCH_3, DMSO

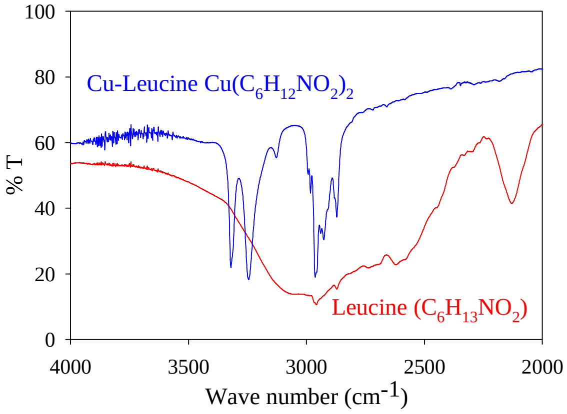

Fig. 4.11: Comparison of IR spectrum of leucine and Cu-leucine complex

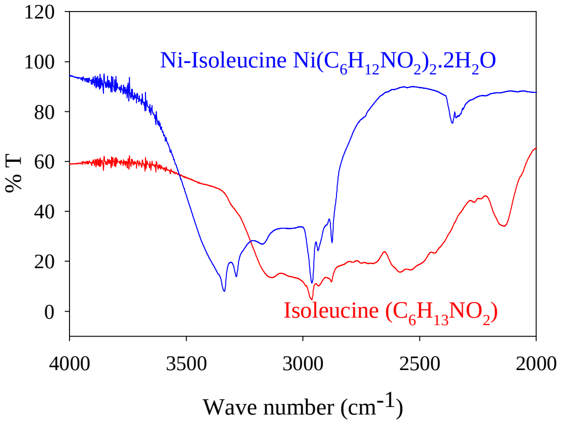

Fig. 4.12: Comparison of IR spectrum of isoleucine and Ni-isoleucine complex

The IR spectrum of leucine and isoleucine is compared with their complex in Fig. 4.11 and Fig. 4.12. The comparison of IR bands of leucine and isoleucine with their complexes are given in Table 4.5 and Table 4.6. Leucine and isoleucine both show a weak and broad peak at around 3100 cm^{-1} due to NH_3^+ stretching. But the complexes show two sharp bands between 3100-3350 cm^{-1} due to asymmetric and symmetric stretching of the free $-NH_2$ groups. Asymmetric and symmetric stretching for carboxyl group (COO^-) occurs at around 1575 and 1400 cm^{-1} for both ligand and the complex. The ligand and its complexes exhibit two bands for N-H bending near 1600 and 1475 cm^{-1}. The C-H and C-N stretching occurs at around 2960 and 1100 cm^{-1} respectively. The change in position and intensity of the bands in the complex compare to that of ligand confirms the complex formation.

Table 4.5: Comparison of IR bands of leucine and its complexes

Compound	υ(N-H) assym. str. cm^{-1}	υ(N-H) sym. str. cm^{-1}	υ(C-H) str. cm^{-1}	υ (NH) asym. bending cm^{-1}	υ(COO^-) asym. str. cm^{-1}	υ (NH) sym. bending cm^{-1}	υ(COO^-) sym. str. cm^{-1}	υ (CN) str. cm^{-1}
Leucine ($C_6H_{13}NO_2$)	3070		2960	1610	1575	1510	1400	1080
$Co(C_6H_{12}NO_2)_2.2H_2O$	3360	3300	2950	1625		1475	1400	1100
$Ni(C_6H_{12}NO_2)_2.2H_2O$	3360	3300	2950	1640	1580	1475	1410	1100
$Cu(C_6H_{12}NO_2)_2$	3325	3250	2975	1625	1575	1480	1400	1120
$Zn(C_6H_{12}NO_2)_2$	3325	3260	2960	1625		1475	1410	1110
$Cd(C_6H_{12}NO_2)_2$	3350	3250	2960	1600	1560	1400		1080
$Hg(C_6H_{12}NO_2)_2$	3150	3100	2960	1600	1575	1475	1400	1150

Table 4.6: Comparison of IR bands of isoleucine and its complexes

Compound	υ(N-H) assym. str. cm^{-1}	υ(N-H) sym. str. cm^{-1}	υ(C-H) str. cm^{-1}	υ (NH) asym. bending cm^{-1}	υ(COO^-) asym. str. cm^{-1}	υ (NH) sym. bending cm^{-1}	υ(COO^-) sym. Str. cm^{-1}	υ (CN) str. cm^{-1}
Isoleucine($C_6H_{13}NO_2$)	3125		2960	1590	1500	1450	1410	1140
$Co(C_6H_{12}NO_2)_2.2H_2O$	3340	3290	2960	1650	1590	1460	1400	1075
$Ni(C_6H_{12}NO_2)_2.2H_2O$	3340	3285	2960	1650	1580	1475	1410	1080
$Cu(C_6H_{12}NO_2)_2.H_2O$	3300	3250	2975	1610	1600	1460	1400	1125
$Zn(C_6H_{12}NO_2)_2$. ½ H_2O	3325	3260	2960	1600		1475	1400	1100
$Cd(C_6H_{12}NO_2)_2$	3300	3260	2960	1620	1575	1460	1400	1120
$Hg(C_6H_{12}NO_2)_2$	3200	3100	2975	1600	1575	1460	1400	1175

The comparison of IR spectrum of Ni-leucine and Ni-isoleucine complex is shown in Fig. 4.13. The figure shows that the pattern of the IR spectrum of the complexes is almost similar with each other with a few exceptions, which indicates that all the complexes have similar bonding pattern and composition.

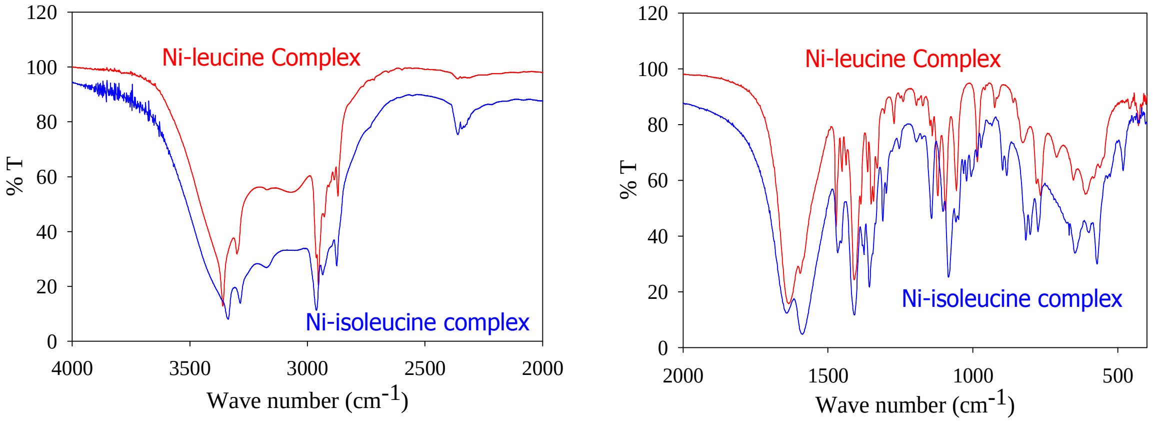

Fig. 4.13: Comparison of IR spectrum of Ni-leucine and Ni-isoleucine complex

The UV-Visible spectrum of ligand and their metal complexes are shown in the Fig. 4.14 - Fig. 4.17. The comparison of absorption bands are given in Table 4.7. The presence of characteristic metal-ligand charge transfer bands and d-d transition bands in the Co, Ni and Cu complex indicate the probability of forming M←L coordination bonds.

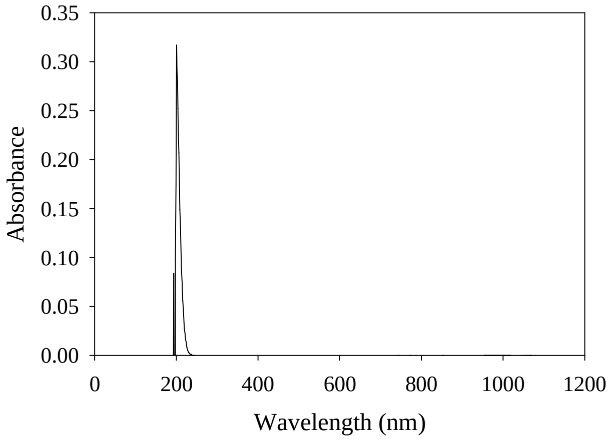

Fig. 4.14: UV-Vis spectrum of leucine ($C_6H_{13}NO_2$)

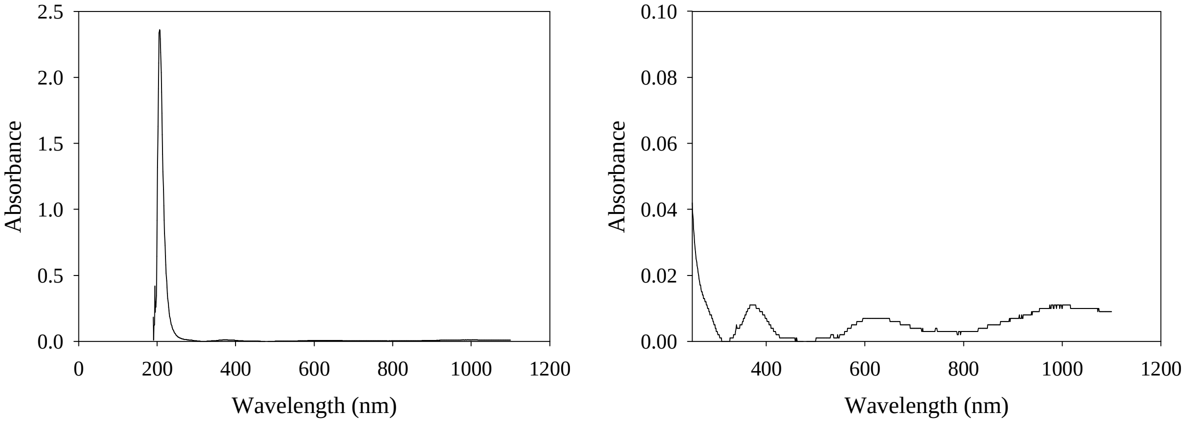

Fig. 4.15: UV-Vis spectrum of Ni-leucine complex [Ni($C_6H_{12}NO_2$)$_2$.2H_2O]

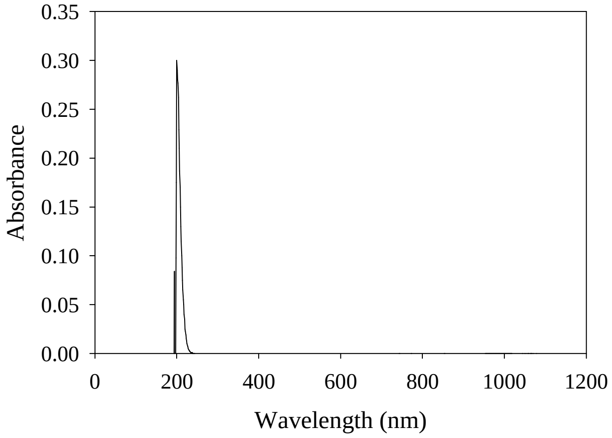

Fig. 4.16: UV-Vis spectrum of isoleucine ($C_6H_{13}NO_2$)

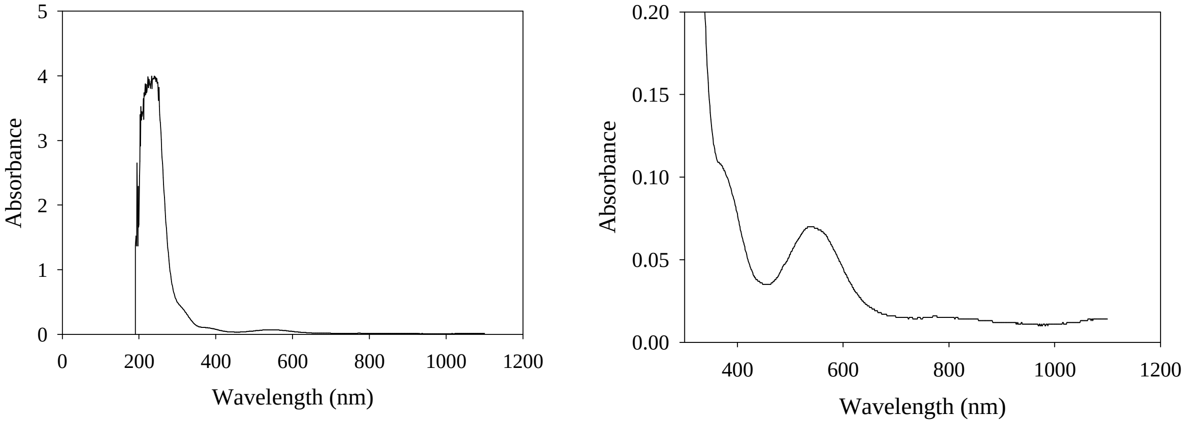

Fig. 4.17: UV-Vis spectrum of Co-isoleucine complex [Co($C_6H_{12}NO_2$)$_2$.2H_2O]

Table 4.7: Absorption bands of ligand and its complexes

Compound	Absorption band		
	d - d	CT	IL
Leucine ($C_6H_{13}NO_2$)	-	-	201
Ni-leucine complex [$Ni(C_6H_{12}NO_2)_2.2H_2O$]	620	370	206
Isoleucine ($C_6H_{13}NO_2$)	-	-	200
Co-isoleucine complex [$Co(C_6H_{12}NO_2)_2.2H_2O$]	535	-	240
Ni-isoleucine complex [$Ni(C_6H_{12}NO_2)_2.2H_2O$]	625	380	208
Cu-isoleucine complex [$Cu(C_6H_{12}NO_2)_2.H_2O$]	605	-	240

d-d = d-d transition, CT = charge transfer transition, IL = Intraligand charge transfer

The reflectance spectrum and the corresponding energy function of ligand and the complexes are displayed in Fig. 4.18 to Fig. 4.21 respectively. The determined band gap energy of the complexes is reported in Table 4.8. The complexes may be good conductor because of having low band gap energy.

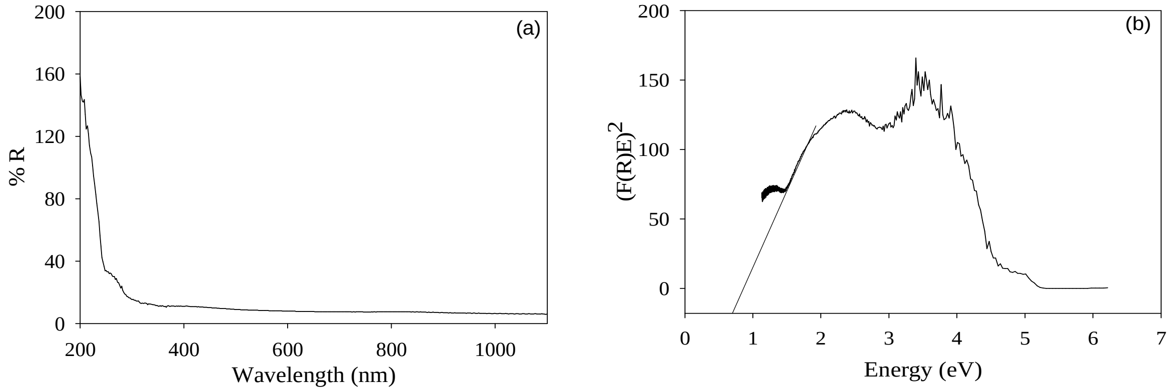

Fig. 4.18: (a) Reflectance spectrum and (b) $(F(R)E)^2$ vs E plot for leucine ($C_6H_{13}NO_2$)

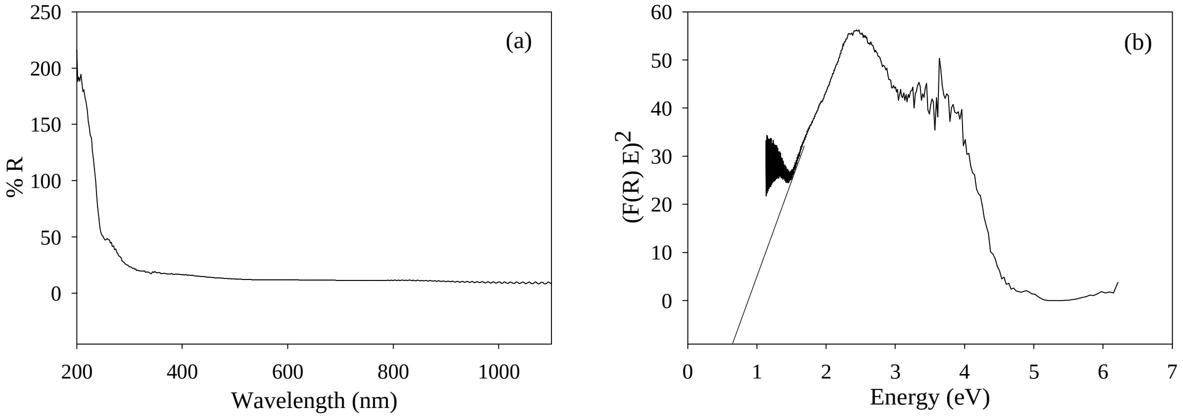

Fig. 4.19: (a) Reflectance spectrum and (b) $(F(R)E)^2$ vs E plot for Co-leucine complex [$Co(C_6H_{12}NO_2)_2.2H_2O$]

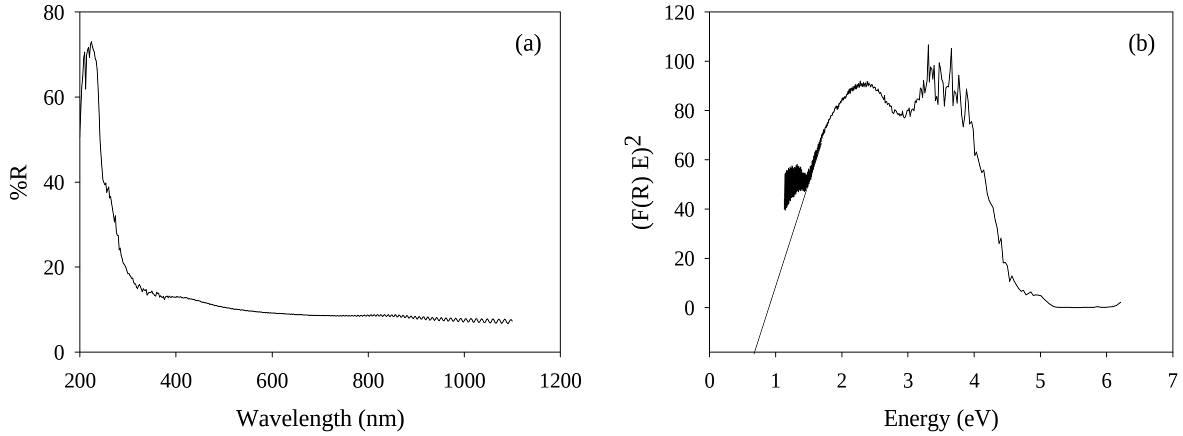

Fig. 4.20: (a) Reflectance spectrum and (b) $(F(R)E)^2$ vs E plot for isoleucine ($C_6H_{13}NO_2$)

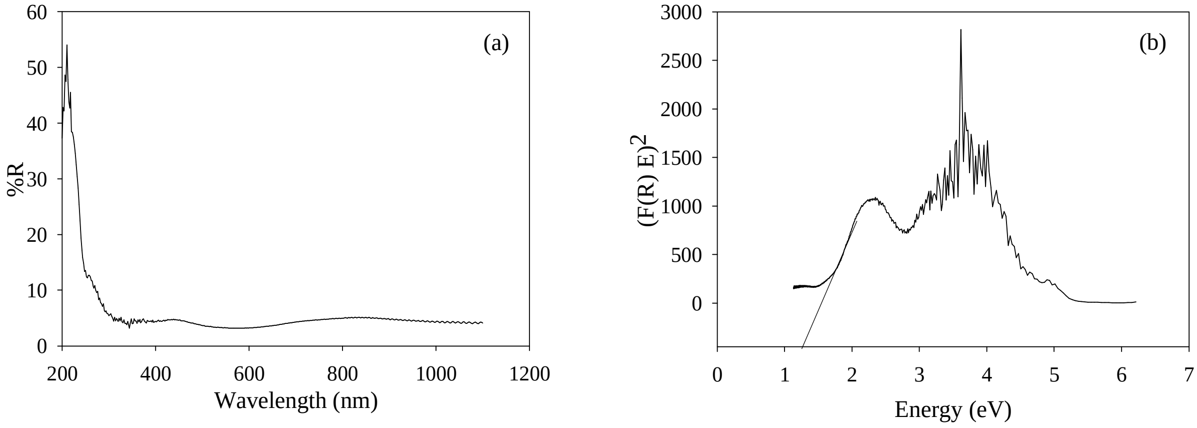

Fig. 4.21: (a) Reflectance spectrum and (b) $(F(R)E)^2$ vs E plot for Co-isoleucine complex $[Co(C_6H_{12}NO_2)_2.2H_2O]$

Table 4.8: The calculated band gap energy for the complexes

Leucine complex	Band gap energy (eV)	Isoleucine complex	Band gap energy (eV)
Leucine ($C_6H_{13}NO_2$)	0.7	Isoleucine ($C_6H_{13}NO_2$)	0.7
$Co(C_6H_{12}NO_2)_2.2H_2O$	0.8	$Co(C_6H_{12}NO_2)_2.2H_2O$	1.2
$Ni(C_6H_{12}NO_2)_2.2H_2O$	0.2	$Ni(C_6H_{12}NO_2)_2.2H_2O$	0.8
$Cu(C_6H_{12}NO_2)_2$	0.7	$Cu(C_6H_{12}NO_2)_2.H_2O$	0.9
$Zn(C_6H_{12}NO_2)_2$	0.7	$Zn(C_6H_{12}NO_2)_2.½ H_2O$	0.1
$Cd(C_6H_{12}NO_2)_2$	0.5	$Cd(C_6H_{12}NO_2)_2$	0.6
$Hg(C_6H_{12}NO_2)_2$	0.7	$Hg(C_6H_{12}NO_2)_2$	0.6

The nuclear magnetic resonance (NMR) spectral analysis demonstrated that the protons overlap with each other. A peak for –COOH proton appears in the ligand but in the complex it is not seen. This may be due to complexation of ligand with the metal. The position of the other peaks in the complex is consistent with that of ligand. The NMR spectrum of ligand and some complexes are displayed in Fig. 4.22 to Fig. 4.27.

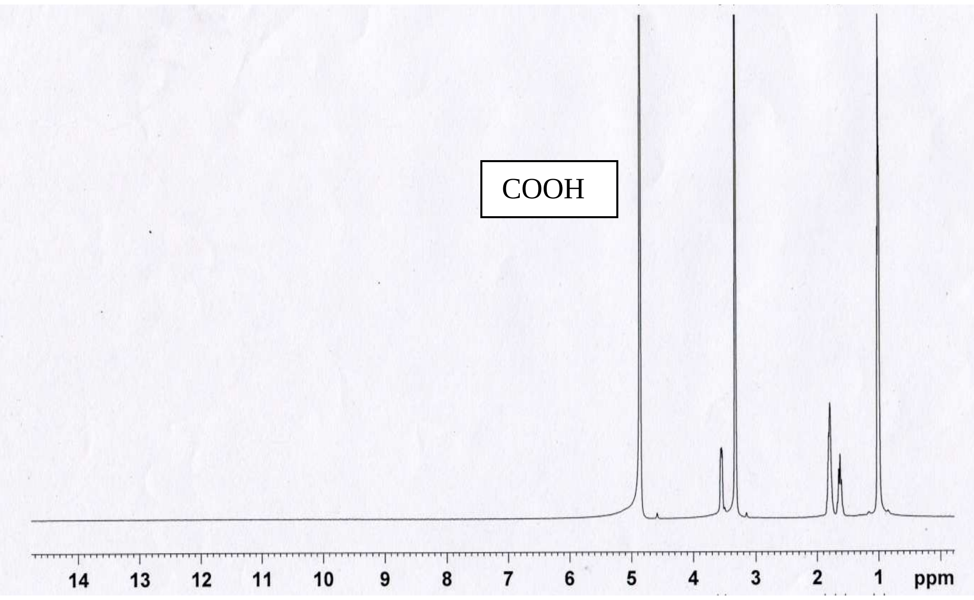

Fig. 4.22: NMR spectrum of leucine ($C_6H_{13}NO_2$)

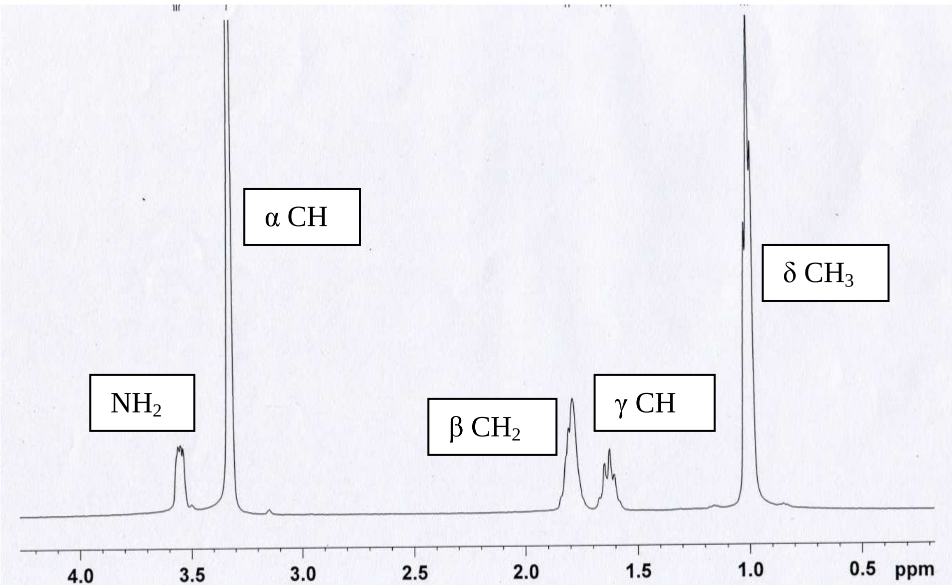

Fig. 4.23: NMR spectrum of leucine ($C_6H_{13}NO_2$)

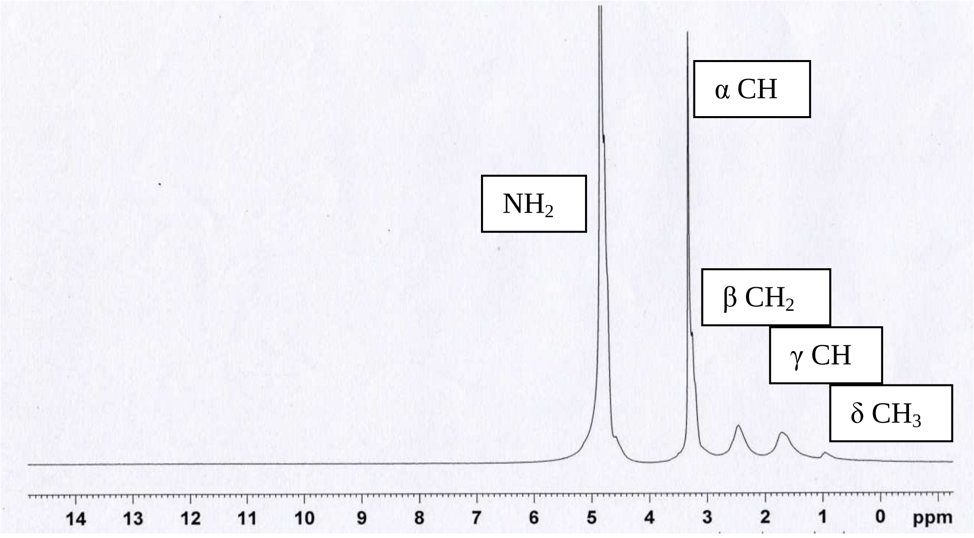

Fig. 4.24: NMR spectrum of Ni-leucine complex [Ni($C_6H_{12}NO_2$)$_2$ .2H_2O]

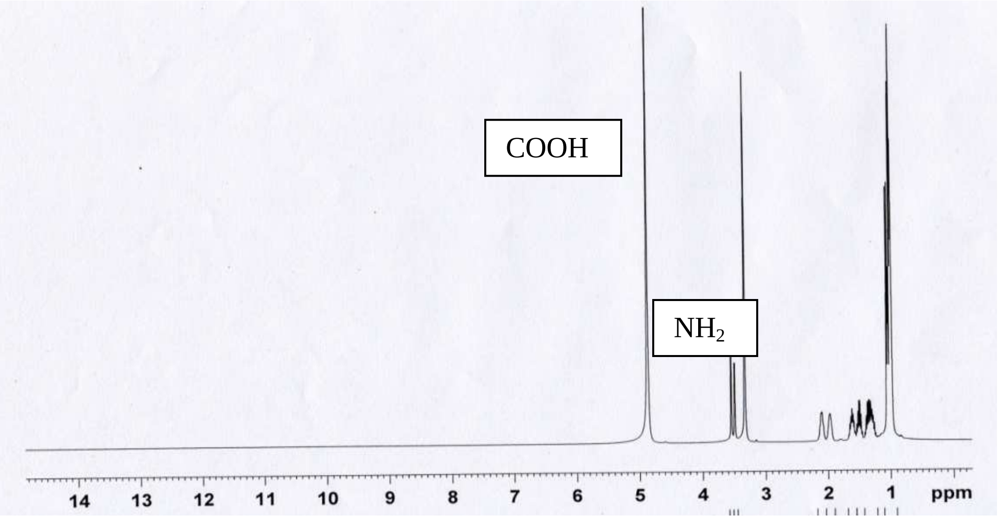

Fig. 4.25: NMR spectrum of isoleucine ($C_6H_{13}NO_2$)

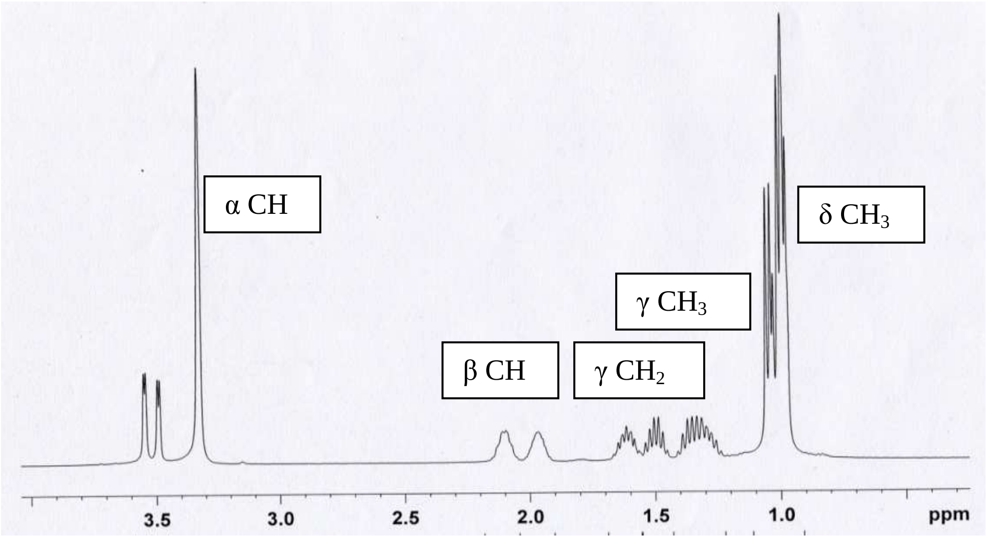

Fig. 4.26: NMR spectrum of isoleucine ($C_6H_{13}NO_2$)

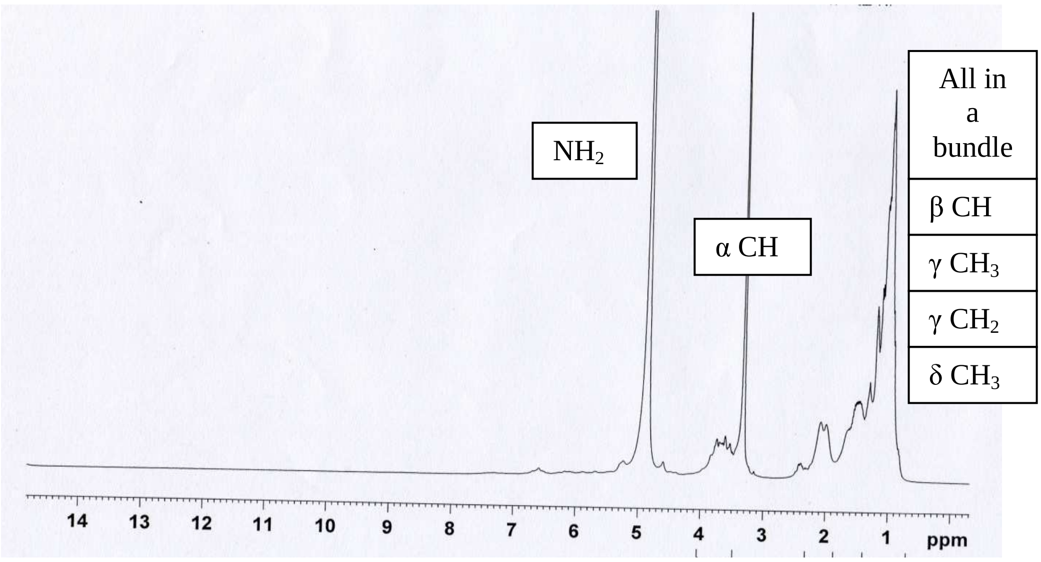

Fig. 4.27: NMR spectrum of Co-isoleucine complex [$Co(C_6H_{12}NO_2)_2.2H_2O$]

The Differential Scanning Calorimetry (DSC) curve of the complexes is sharp endothermic. Therefore, the weight changes monitored by thermogravimetry involved absorption of energy. The TG and DSC curves of ligand and the complexes are presented in Fig. 4.28 to Fig. 4.31.

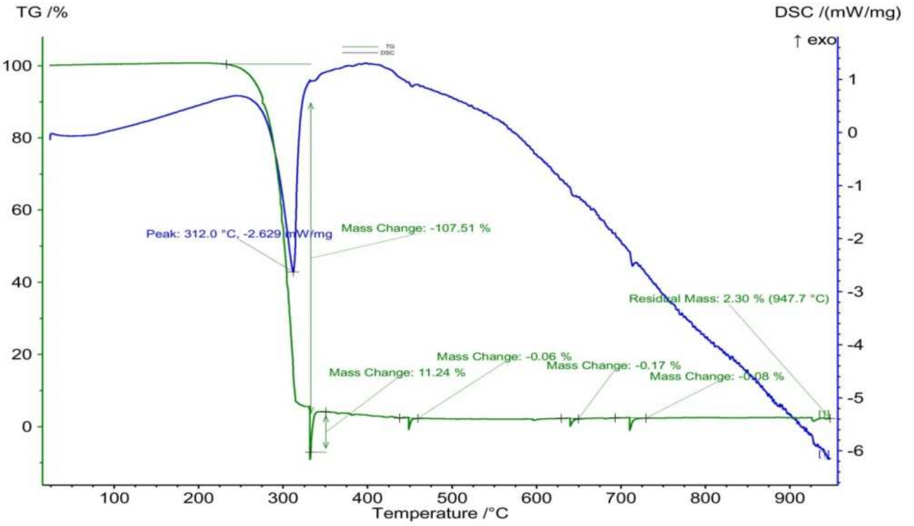

Fig. 4.28: TG and DSC curves of leucine ($C_6H_{13}NO_2$)

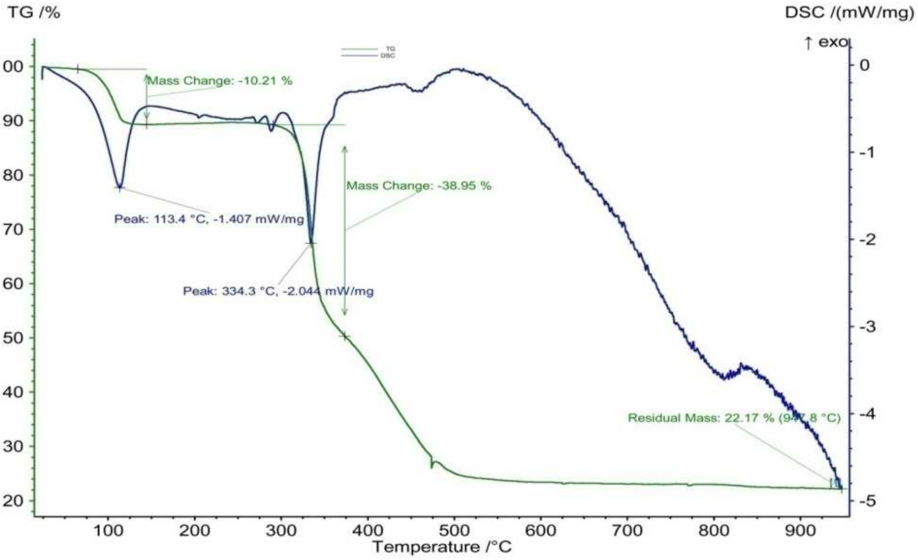

Fig. 4.29: TG and DSC curves of Co-leucine complex [$Co(C_6H_{12}NO_2)_2.2H_2O$]

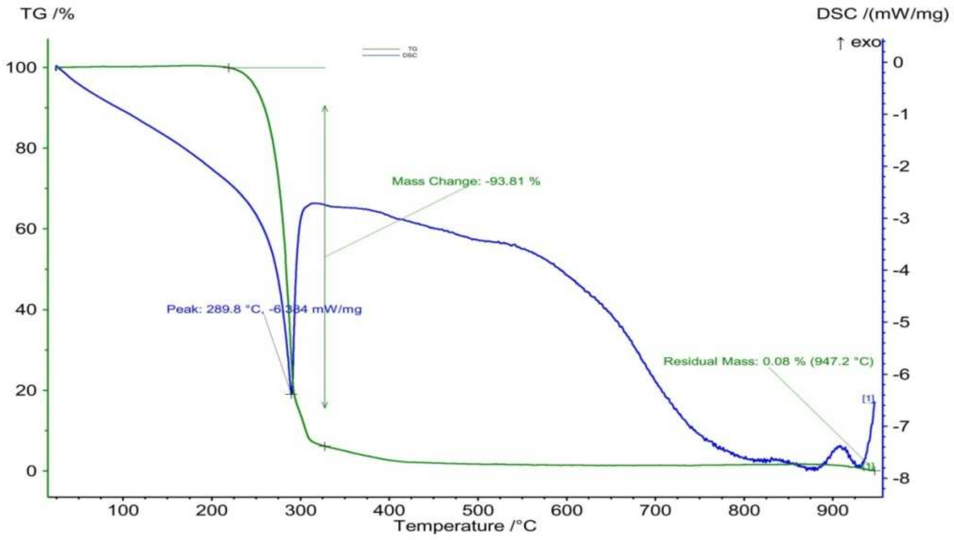

Fig. 4.30: TG and DSC curves of isoleucine ($C_6H_{13}NO_2$)

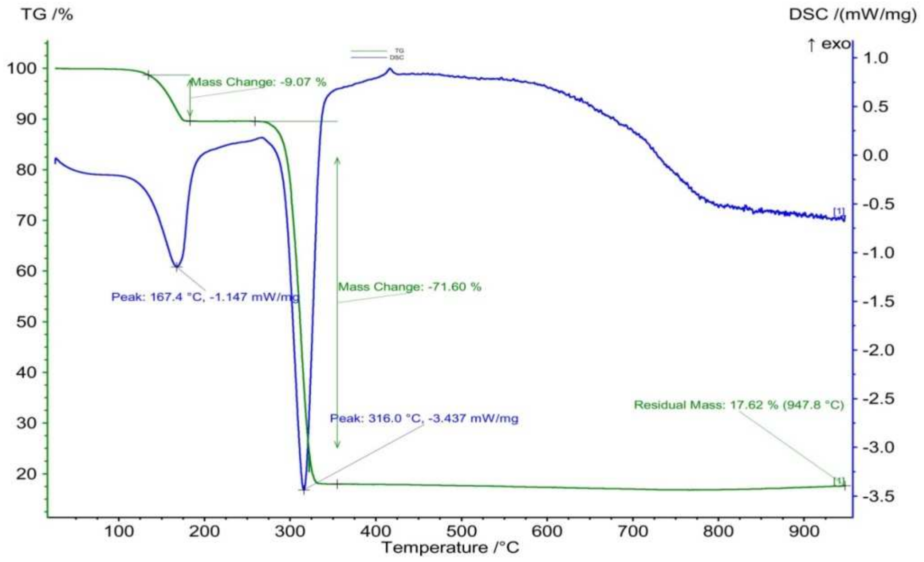

Fig. 4.31: TG and DSC curves of Ni-isoleucine complex [$Ni(C_6H_{12}NO_2)_2.2H_2O$]

Magnetic susceptibility data of the complexes conclude that all of them are high spin paramagnetic complex excluding Zn, Cd and Hg which are diamagnetic. The magnetic properties of the complexes of ligand are summarized in Table 4.9 and Table 4.10.

Table 4.9: Magnetic properties of the complexes of leucine

Compound	χ_A (cgs) x 10^{-3}	μ_{eff} BM (at 300K) Found	μ_{eff} BM (at 300K) Theo.	No. of unpaired electron (n)	Config.	Inference
$Co(C_6H_{12}NO_2)_2.2H_2O$	7.4	4.2	4.3-5.2	3	d^7	Paramagnetic
$Ni(C_6H_{12}NO_2)_2.2H_2O$	4.7	3.3	3.0-3.3	2	d^8	Paramagnetic
$Cu(C_6H_{12}NO_2)_2$	1.5	1.9	1.8-2.1	1	d^9	Paramagnetic
$Zn(C_6H_{12}NO_2)_2$	negative	0*		0	d^{10}	Diamagnetic
$Cd(C_6H_{12}NO_2)_2$	negative	0*		0	d^{10}	Diamagnetic
$Hg(C_6H_{12}NO_2)_2$	negative	0*		0	d^{10}	Diamagnetic

Theo. = Theoretical values. *The negative value of χ_A indicates that the tube and sample have a net diamagnetism. In that case μ_{eff} can be considered as zero.

Table 4.10: Magnetic properties of the complexes of isoleucine

Compound	χ_A (cgs) x 10^{-3}	μ_{eff} BM (at 300K) Found	μ_{eff} BM (at 300K) Theo.	No. of unpaired electron (n)	Config.	Inference
$Co(C_6H_{12}NO_2)_2.2H_2O$	11.3	5.2	4.3-5.2	3	d^7	Paramagnetic
$Ni(C_6H_{12}NO_2)_2.2H_2O$	4.0	3.1	3.0-3.3	2	d^8	Paramagnetic
$Cu(C_6H_{12}NO_2)_2.H_2O$	1.35	1.8	1.8-2.1	1	d^9	Paramagnetic
$Zn(C_6H_{12}NO_2)_2.½ H_2O$	negative	0*		0	d^{10}	Diamagnetic
$Cd(C_6H_{12}NO_2)_2$	negative	0*		0	d^{10}	Diamagnetic
$Hg(C_6H_{12}NO_2)_2$	negative	0*		0	d^{10}	Diamagnetic

Theo. = Theoretical values. *The negative value of χ_A indicates that the tube and sample have a net diamagnetism. In that case μ_{eff} can be considered as zero.

Theoretical calculations ensures that the Co, Ni and Cu complexes forms square planner structure while the Zn, Cd and Hg complexes form distorted tetrahedral structure. The optimized structure of ligand and the complexes are displayed in Fig. 4.32 – Fig. 4.37.

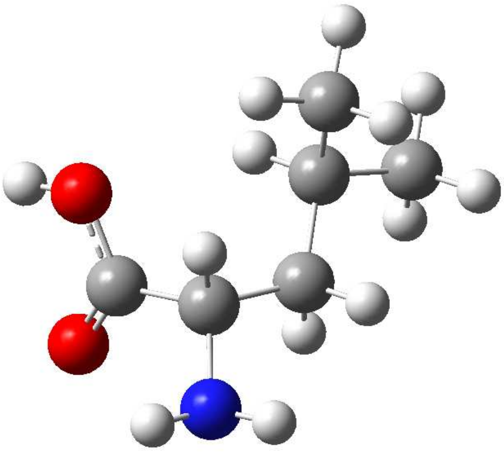

Fig. 4.32: Optimized structure of leucine calculated at B3LYP/SDD level of theory

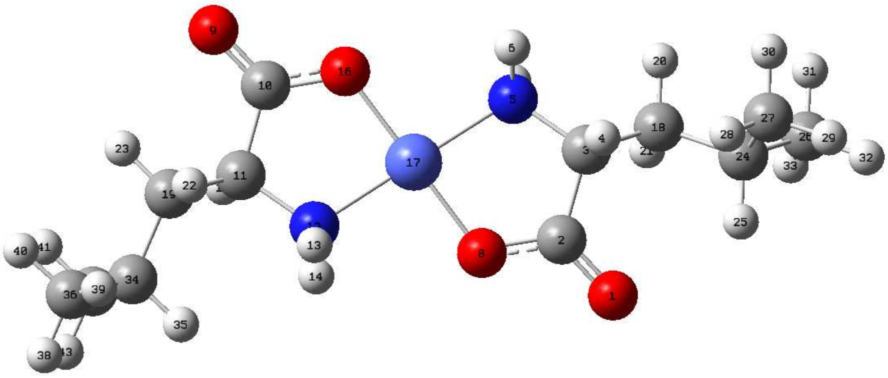

Fig. 4.33: Optimized structure of Co(leu)$_2$ calculated at B3LYP/SDD level of theory

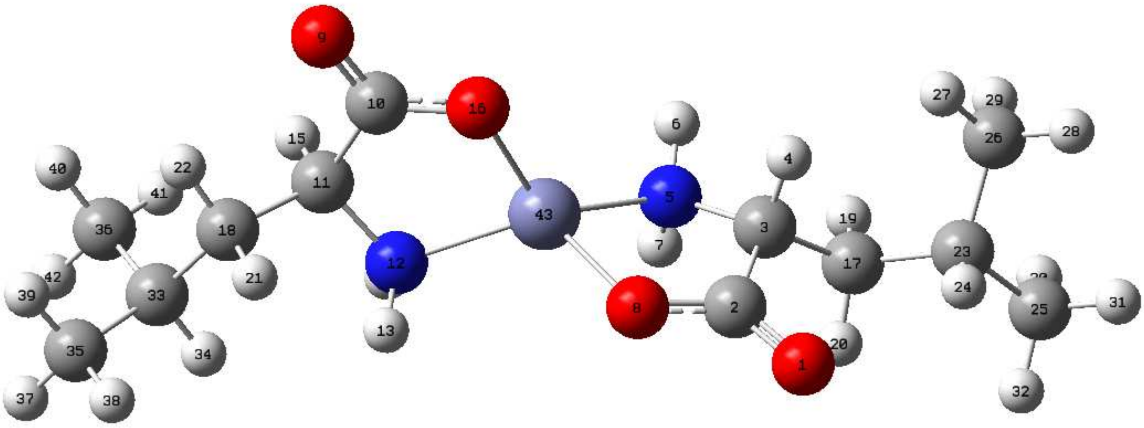

Fig. 4.34: Optimized structure of Zn(leu)$_2$ calculated at B3LYP/SDD level of theory

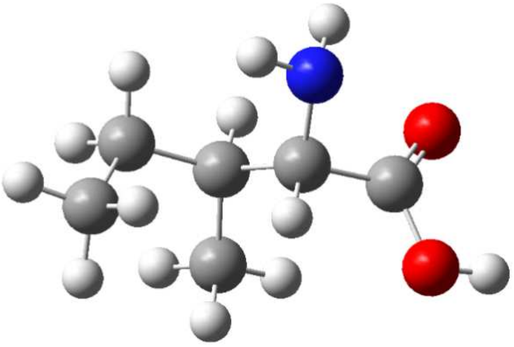

Fig. 4.35: Optimized structure of isoleucine calculated at B3LYP/SDD level of theory

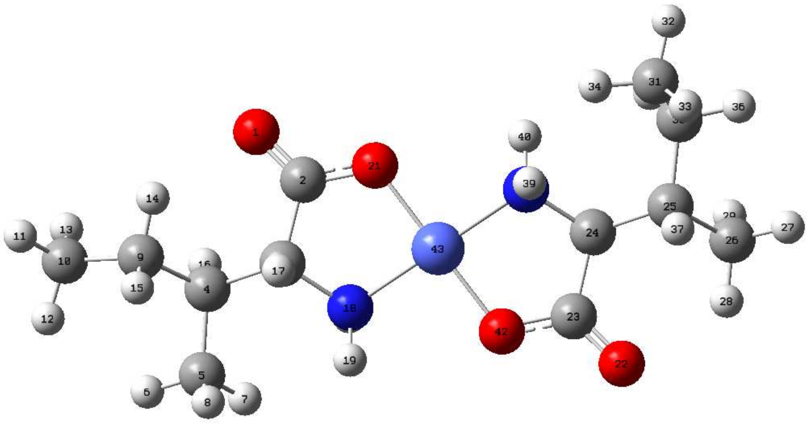

Fig. 4.36: Optimized structure of Co(ile)$_2$ calculated at B3LYP/SDD level of theory

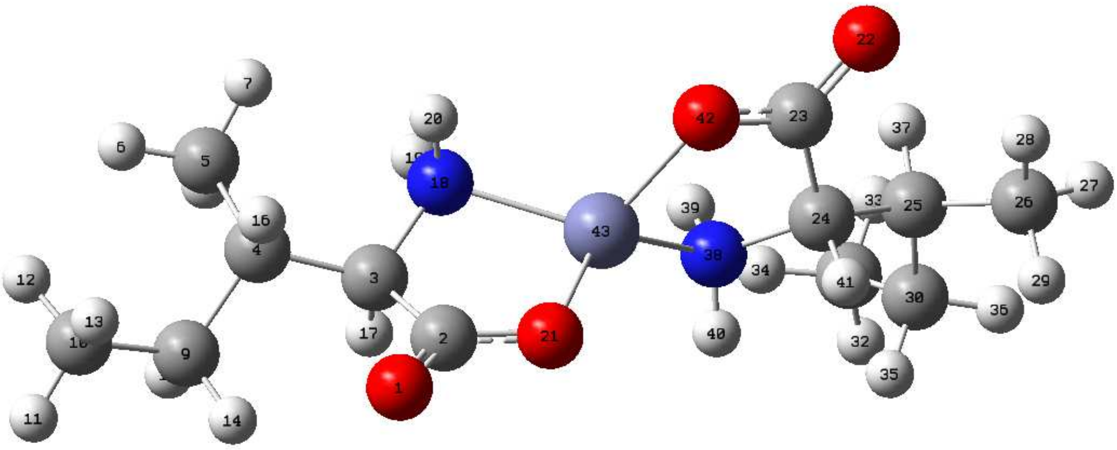

Fig. 4.37: Optimized structure of Zn(ile)$_2$ calculated at B3LYP/SDD level of theory

The experimental IR vibrational frequencies and the absorption properties are very consistent with the calculated values. The computed IR frequencies are compared with the experimental values in Table 4.11 and Table 4.12. The absorption properties of leucine and the Ni(leu)$_2$ are tabulated min Table 4.13 – Table 4.16. The UV–Visible studies reveal that Co, Ni and Cu complex demonstrate characteristic metal to ligand charge transfer (MLCT) or ligand to metal charge transfer (LMCT) and d–d transitions bands. On the other hand Zn, Cd and Hg complex does not show any charge transfer or d-d transition bands because of their d^{10} configuration.

Table 4.11: Comparison of the scaled IR frequencies of the metal-leucine complexes with the experimental values (the experimental values is in parentheses)

Compound	N–H str. (asymm)	N–H str. (symm)	C–H str.
Leucine	3482 (3070)	3403 (3070)	2949 (2960)
Co(leu)$_2$	3424(3360)	3329(3300)	3006(2950)
Ni(leu)$_2$	3424(3360)	3325(3300)	3005(2950)
Cu(leu)$_2$	3399(3325)	3310(3250)	2891 (2975)
Zn(leu)$_2$	3444(3325)	3351(3260)	3004(2960)
Cd(leu)$_2$	3438(3350)	3339(3250)	3012(2960)
Hg(leu)$_2$	3467(3150)	3362(3100)	3012(2960)

Scaling factor 0.9613 is applied.

Table 4.12: Comparison of the scaled IR frequencies of the metal-isoleucine complexes with the experimental values (the experimental values is in parentheses)

Compound	N–H str. (asymm)	N–H str. (symm)	C–H str.
Isoleucine	3473 (3125)	3375 (3125)	2968 (2960)
Co(ile)$_2$	3392(3340)	3321(3290)	2994(2960)
Ni(ile)$_2$	3422(3340)	3330(3275)	3006(2960)
Cu(ile)$_2$	3393(3300)	3306(3250)	2998 (2975)
Zn(ile)$_2$	3440(3325)	3341(3260)	3005(2960)
Cd(ile)$_2$	3431(3300)	3331(3260)	2999(2960)
Hg(ile)$_2$	3460(3200)	3353(3100)	3000(2975)

Scaling factor 0.9613 is applied.

Table 4.13: The absorption properties of leucine calculated at CAM-B3LYP/6 31+G(d,p) level of theory

Wavelength	Excitation energies (eV)	Oscillator strengths	MO contribution	Assignments
224	5.51	0.0051	H-1 → L (13.3%)	
			H → L (83.2%)	IL
219	5.64	0.0035	H-1 → L (73.9%)	IL
			H → L (15.0%)	
214	5.78	0.0090	H → L+1 (72.2%)	IL
			H → L+2 (21.6%)	

d-d = d-d transition, CT = charge transfer transition, IL = Intraligand charge transfer

Table 4.14: The absorption properties of $Ni(leu)_2$ calculated at CAM-B3LYP/6 31+G(d,p) level of theory

Wavelength	Excitation energies (eV)	Oscillator strengths	MO contribution	Assignments
604	2.05	0	H → L (82.8%)	d-d
569	2.18	0	H-3 → L (69.9%)	d-d
482	2.57	0	H-5 → L (91.4%)	CT
470	2.64	0	H-7 → L (47.2%)	CT
285	4.34	0.0435	H-1 → L (90.1%)	IL
273	4.54	0	H-2 → L (55.9%)	IL
256	4.83	0.0012	H-4 → L (94.7%)	IL
249	4.96	0	H → L+1 (42.0%)	IL
248	4.99	0.0005	H → L+1 (46.6%)	IL
245	5.06	0.0002	H-1 → L+2 (24.1%)	IL

d-d = d-d transition, CT = charge transfer transition, IL = Intraligand charge transfer

Table 4.15: The absorption properties of isoleucine calculated at CAM-B3LYP/6-31+G(d,p) level of theory

Wavelength	Excitation energies (eV)	Oscillator strengths	MO contribution	Assignments
232	5.34	0.0012	H → L (89.2%)	IL
213	5.81	0.0078	H → L+1 (36.1%) H-1 → L (32.0%)	IL
210	5.90	0.0025	H-1 → L (42.0%) H → L+1 (38.5%)	IL
200	6.19	0.0241	H → L+2 (75.2%) H → L+1 (16.5%)	IL

d-d = d-d transition, CT = charge transfer transition, IL = Intraligand charge transfer

Table 4.16: The absorption properties of Ni(ile)$_2$ calculated at CAM-B3LYP/6 31+G(d,p) level of theory

Wavelength	Excitation energies (eV)	Oscillator strengths	MO contribution	Assignments
597	2.07	0	H → L (83.1%)	d-d
563	2.20	0	H-3 → L (64.2%)	d-d
479	2.58	0	H-4 → L (88.4%)	CT
466	2.65	0	H-7 → L (45.8%)	CT
282	4.38	0.0373	H-1 → L (95.4%)	IL
271	4.57	0	H-2 → L (53.4%)	IL
253	4.88	0.0041	H-5 → L (83.3%)	IL
251	4.94	0.0005	H-1 → L+2 (25.8%)	IL
248	4.99	0.0001	H → L+2 (80.2%)	IL

d-d = d-d transition, CT = charge transfer transition, IL = Intraligand charge transfer

Selected frontier molecular orbital of ligand and their complexes is displayed from Fig. 3.38 to Fig. 3.41. The HOMO-LUMO gap of the complexes is decreased from the parent ligand. Therefore metal has a noticeable effect on the frontier molecular orbital energies.

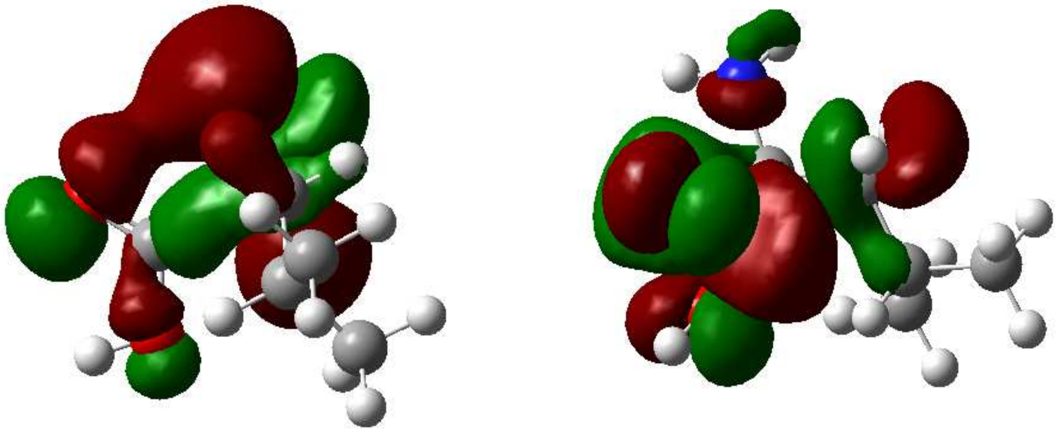

HOMO LUMO

Fig. 4.38: HOMO and LUMO of leucine

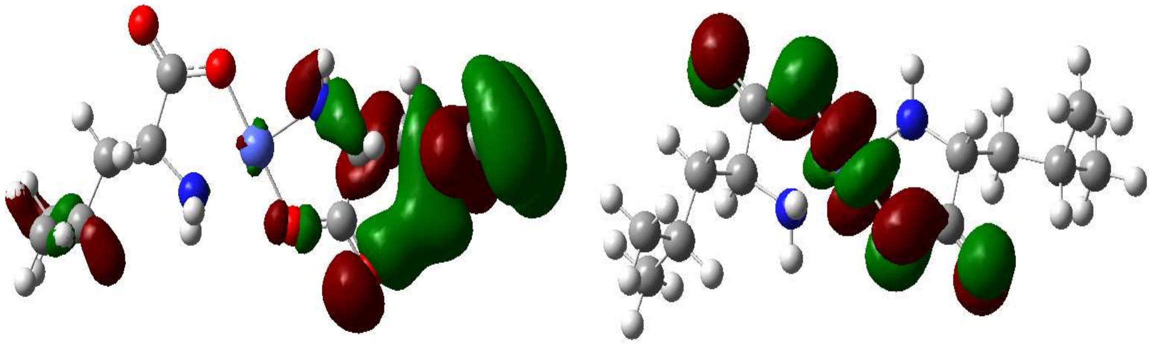

HOMO LUMO

Fig. 4.39: HOMO and LUMO of Co(leu)$_2$

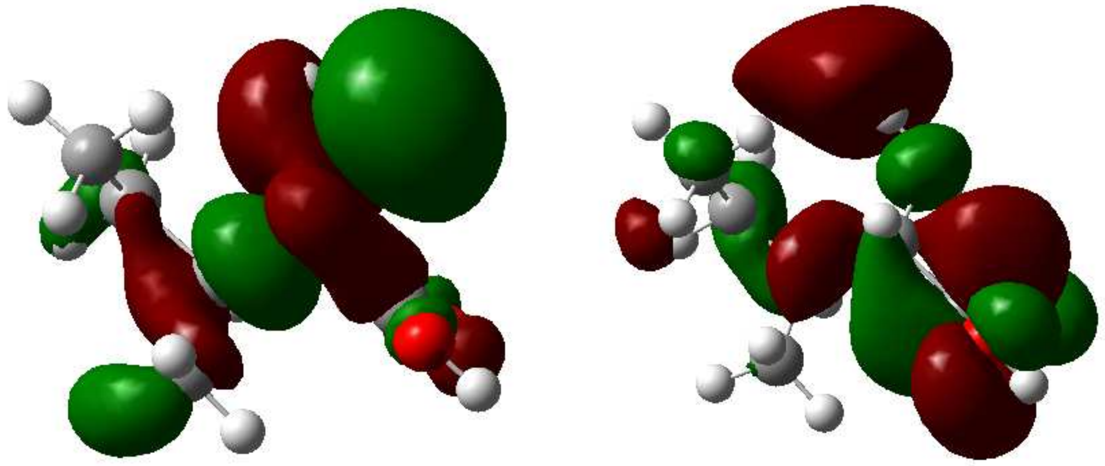

HOMO LUMO

Fig. 4.40: HOMO and LUMO of isoleucine

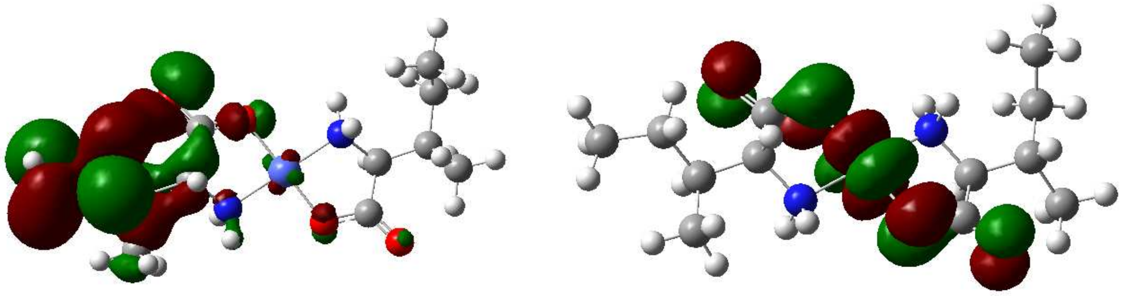

HOMO LUMO

Fig. 4.41: HOMO and LUMO of Co(ile)$_2$

So, leucine forms 1:2 complexes with transition metals and the following common structural formula can be proposed for the new species:

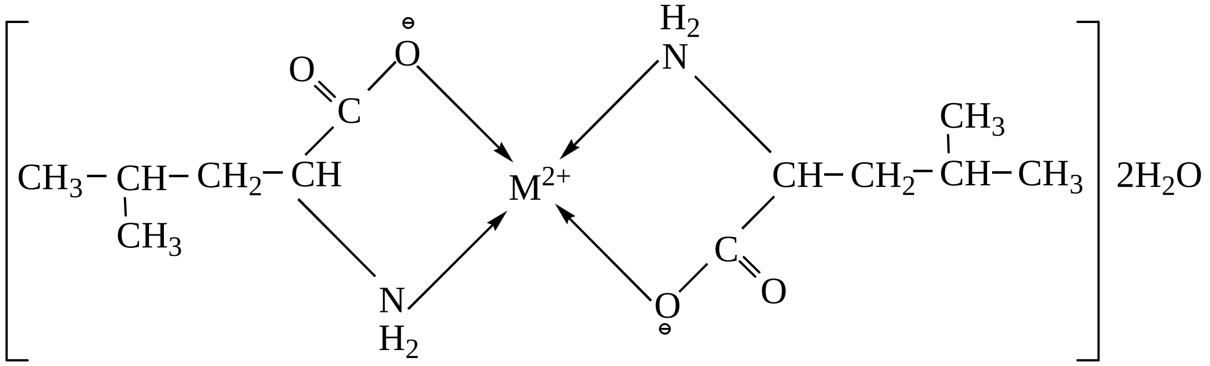

Square planner structure for $M^{2+} = Co^{2+}, Ni^{2+}$

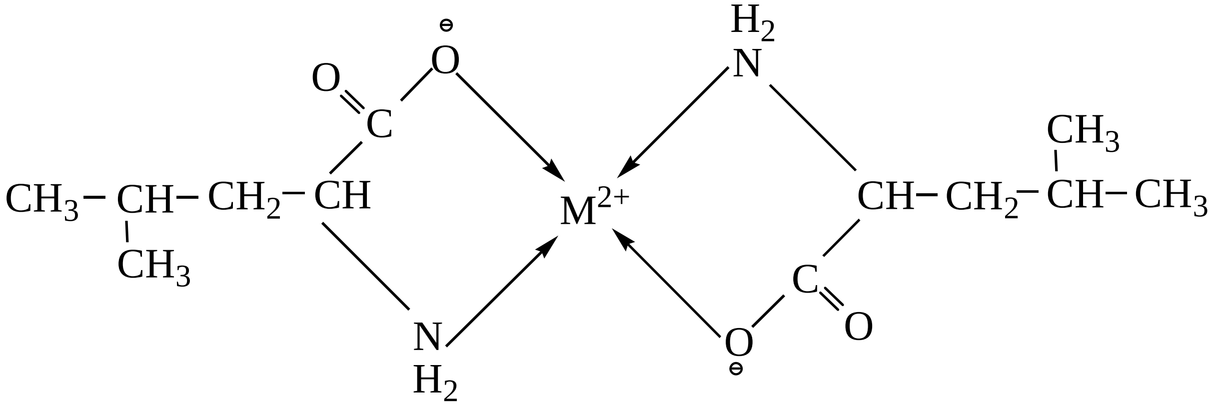

Square planner structure for $M^{2+} = Cu^{2+}$

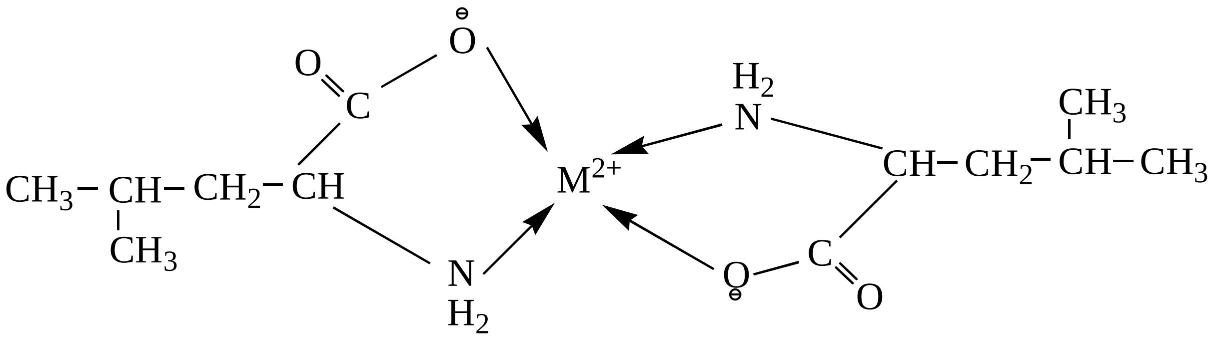

Distorted tetrahedral structure for $M^{2+} = Zn^{2+}, Cd^{2+}, Hg^{2+}$

Isoleucine forms 1:2 complexes with transition metals and the following common structural formula can be proposed for the new species:

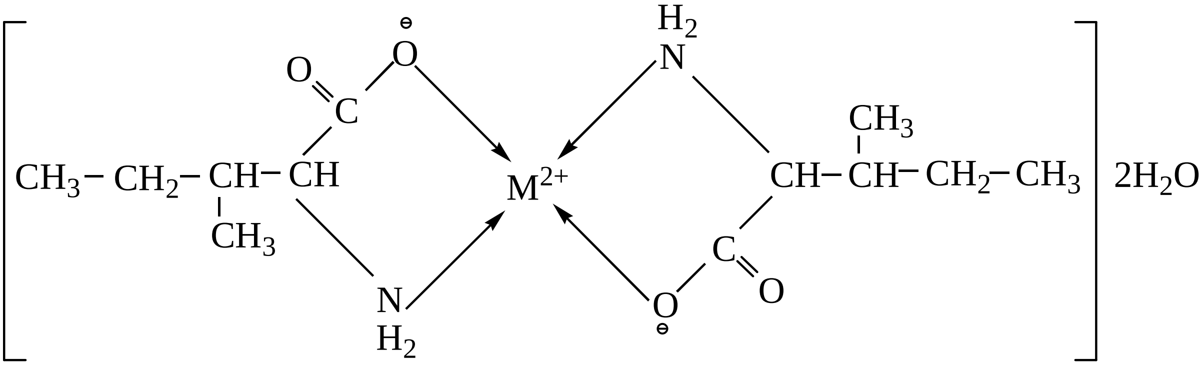

Square planner structure $M^{2+} = Co^{2+}, Ni^{2+}$

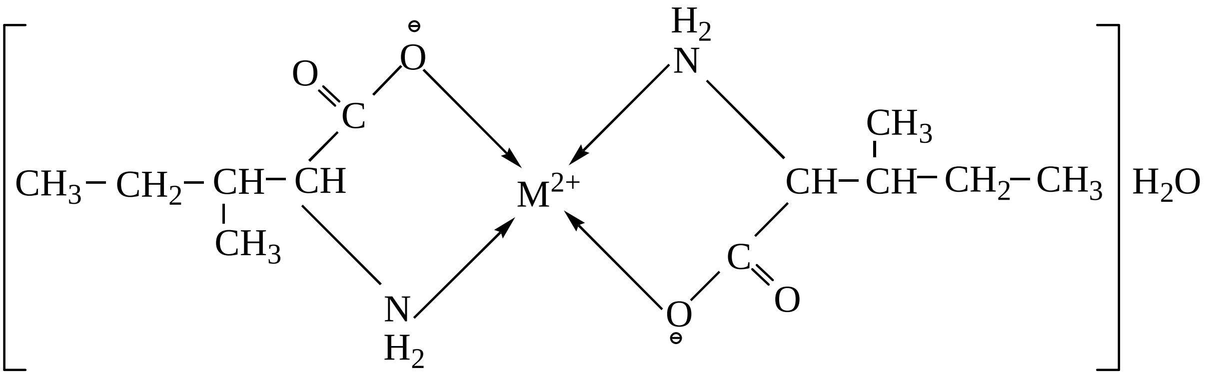

Square planner structure $M^{2+} = Cu^{2+}$

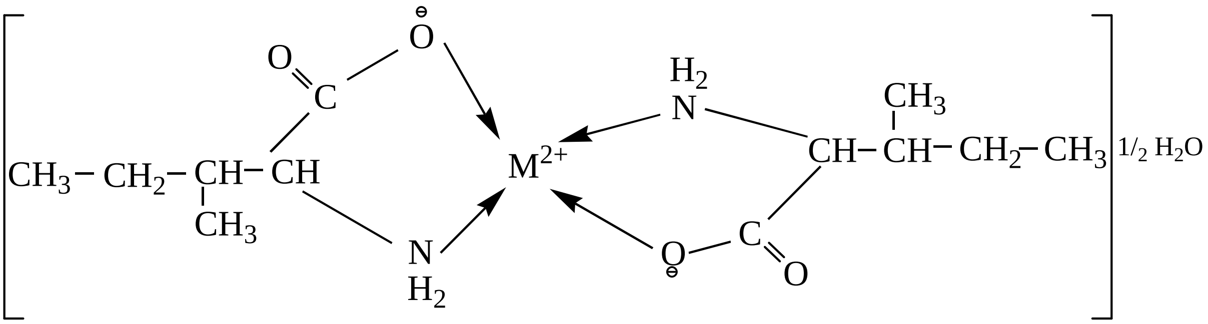

Distorted tetrahedral structure for $M^{2+} = Zn^{2+}$

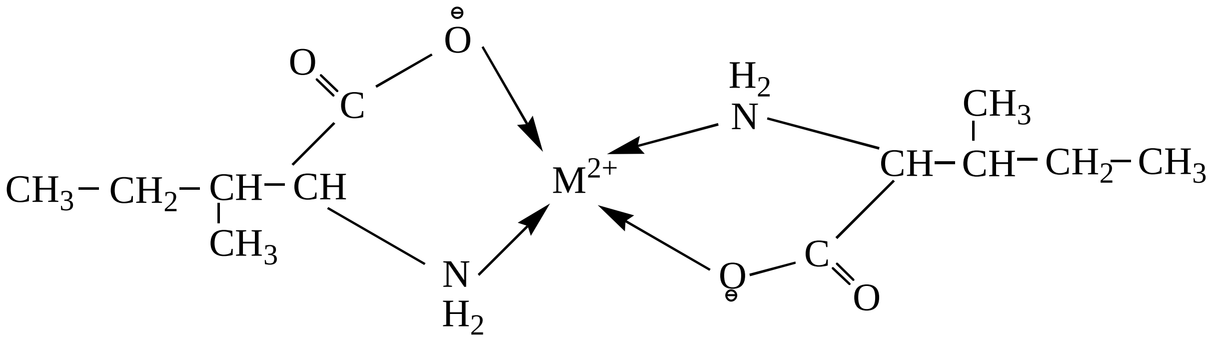

Distorted tetrahedral structure for $M^{2+} = Cd^{2+}$, Hg^{2+}

CONCLUSION

The electrochemical study concludes that the metal ion interacts with both the zwitterionic and anionic form of the ligand. But the metal-anionic ligand interaction is more pronounced over metal-zwitterionic ligand interaction. Maximum interaction occurs in 1:2 mol ratios. The redox behavior of the respective metal ion in absence and presence of the ligand was quasi-reversible and coupled with some chemical reaction. Chronoamperometry and chronocoulometric study concludes that adsorption of reactant and product occurs at the electrode surface in all cases.

The solid products were isolated from the reaction of the metal ions, Co(II), Ni(II), Cu(II), Zn(II), Cd(II) and Hg(II) with the anionic ligand. Both leucine and isoleucine forms 1:2 complexes with metal ion, which is confirmed by the elemental and metal analysis. Thermal analysis ensures that the Co and Ni complex of both leucine and isoleucine contains two molecules of crystalline water. The Cu complex of isoleucine contains one molecule and the Zn complex of isoleucine contains half molecule of crystalline water. The other complexes do not contain any water of crystallization. The compounds have high melting temperature and are mostly insoluble in the common solvents. But the Ni-leucine, Co-isoleucine, Ni-isoleucine and Cu-isoleucine complexes are soluble in methanol.

The IR spectral data of the complexes indicate that the metal-ligand bonding occurs through nitrogen atom of NH_2 group and oxygen atom of COO^- group. All the complexes have similar bonding pattern. The shifting of the absorption bands, appearing of d-d transitions and charge transfer bands in the UV-Visible absorption spectrum also indicates the probability of forming M←L coordination bonds in the complexes. The complexes may be good conductor because of having low band gap energy. The NMR peaks of the complexes overlaps with each other. A peak for –COOH proton appears in the ligand but in the complex it is not seen. This may be due to complexation of ligand with metal ion.

The Differential Scanning Calorimetry (DSC) curve of the complexes is sharp endothermic. Therefore, the weight changes monitored by thermogravimetry involved absorption of energy. Magnetic susceptibility data of the complexes conclude that all of them are high spin paramagnetic complex excluding Zn, Cd and Hg complexes which are diamagnetic.

Density functional theory (DFT) calculation confirms that Co, Ni and Cu complexes form square planar structure whereas Zn, Cd and Hg adopt distorted tetrahedral structure. Cation-binding energy, enthalpy and Gibbs free energy value indicates that these complexes are thermodynamically stable. The experimental IR vibrational frequencies and the absorption properties of the complexes are very consistent with the calculated values. Metal has a noticeable effect on the frontier molecular orbital energies.

Both leucine and isoleucine forms 1:2 complexes with transition metals and the following common structural formula can be proposed for all the new species:

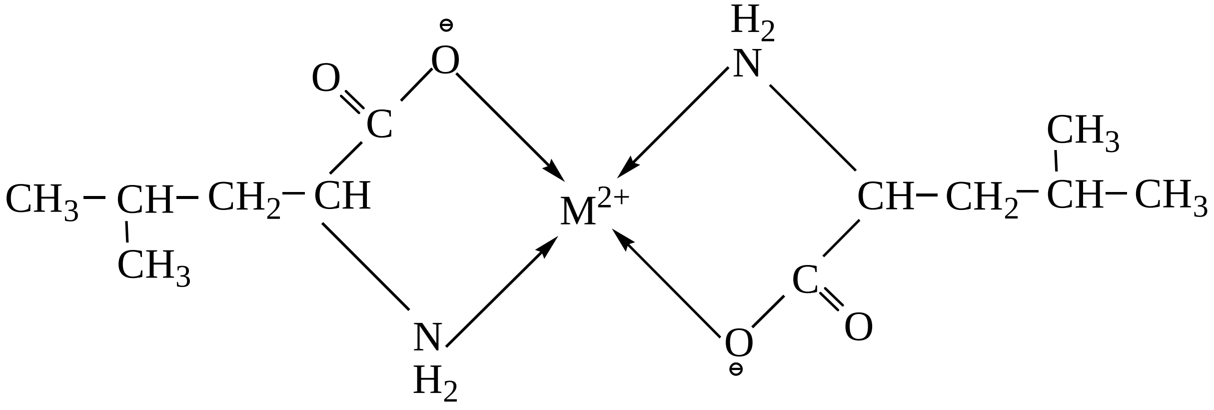

Leucine complexes

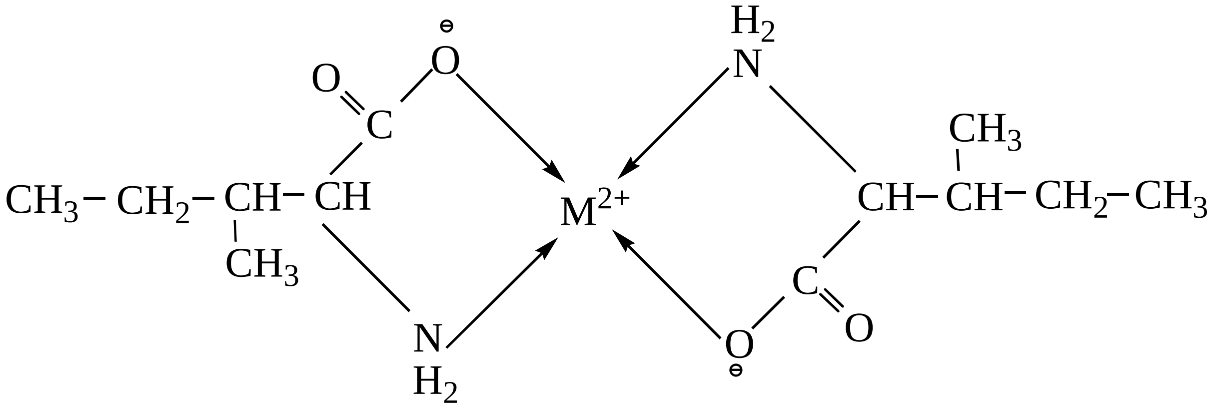

Isoleucine complexes

REFERENCES

01 M. C. Latham, “Human Nutrition in the Developing World, FAO Food and Nutrition Series”, No. 29, 1997.

02 D. L. Nelson and M. M. Cox, “Lehninger Principles of Biochemistry”, 3rd ed., Worth Publishing, New York, 2000.

03 W. Sakami and H. Harrington, “Amino acid metabolism”, *Annu. Rev. Biochem.*, **32(1)**, 355–398, 1963.

04 M. Swaminathan, “Essentials of Food and Nutrition”, Volume 1, 2nd ed., The Bangalore Printing and Publishing Co. Ltd., 1985.

05 B. Rosenberg, L. Vancamp, J. E. Trosko and V. H. Mansour, “Platinum compounds: a new class of potent antitumour agents”, *Nature,* **222**, 385–386, 1969.

06 K. G. Taylor and K. O. Konhauser, “Iron in earth surface systems: a major player in chemical and biological processes”, *Elements*, **7(2)**, 83–88, 2011.

07 R. J. P. Williams, “Zinc in evolution”, *J. Inorg. Biochem.*, **111,** 104–109, 2012.

08 C. Andreini, I. Bertini, G. Cavallaro, G. L. Holliday and J. M. Thornton, “Metal ions in biological catalysis: from enzyme databases to general principles”, *J. Biol. Inorg. Chem.*, **13(8)**, 1205–1218, 2008.

09 Ochiai and Ei-Ichiro, “Copper and the biological evolution”, *Biosystems*, **16(2)**, 81–86, 1983.

10 C. Garza, “Dietary Reference Intakes for Energy, Carbohydrates, Fiber, Fat, Fatty Acids, Cholesterol, Protein and Amino Acids”, Institute of Medicine of the National Academies, The National Academies Press, Washington DC, 2002.

11 M. U. Hossain, M. T. Rahman and M. Q. Ehsan, “Simultaneous detection and estimation of catechol, hydroquinone and resorcinol in binary and ternary mixtures using electrochemical techniques”, *Int. J. Anal. Chem.,* **2015**, 1-8, 2015.

12 M. T. Rahman, M. U. Hossain and M. Q. Ehsan, “Electrochemical behavior of dihydroxybenzene isomers at glassy carbon electrode in different electrolytic media”, *J. Bangladesh Acad. Sci.,* **39(2)**, 135-146, 2015.

13 G. J. Islam, E. Hossain, M. Hasan and M. Q. Ehsan, “Study of the interaction of Zn(II) ion with metronidazole drug in aqueous medium using electrochemical techniques”, *J. Asiat. Soc. Bangladesh, Sci.,* **41(2)**, 193-201, 2015.

14 G. J. Islam, S. Zannah and M. Q. Ehsan, “Study of the redox behavior of biologically important metal ion (Cu^{2+}) and its interaction with metronidazole drug in aqueous solution”, *J. Eng. Sci.*, **5(1)**, 61-67, 2014.

15 M. T. Rahman, M. E. Hossain and M. Q. Ehsan, “Spectrophotometric and cyclic voltammetric study of interaction of Fe(III) with Vitamin B_3 and Vitamin B_6”, *J. Bangladesh Acad. Sci.*, **38(2)**, 143-153, 2014.

16 M. M. Hasan, M. E. Hossain, M. A. Mamun and M. Q. Ehsan, “Study of redox behavior of Cd(II) and interaction of Cd(II) with proline in the aqueous medium using cyclic voltammetry”, *J. Saudi Chem. Soc.,* **16**, 145-151, 2012.

17 M. E. Hossain, M. M. Hasan, M. A. Mamun and M. Q. Ehsan, “Study of interaction between Zinc(II) and aspartic acid using cyclic voltammetry”, *Pak. J. Sci. Ind. Res. Ser. A: Phys. Sci.*, **55(2)**, 72-79, 2012.

18 M. A. Jabbar, K. Kaium, S. Salahuddin, R. A. Chowdhury and M. Q. Ehsan, “Voltammetric and spectrophotometric evidences for the complexation between ascorbic acid and iron in aqueous media and its applications”, *Bangladesh J. Sci. Res.,* **24(1)**, 1-14, 2011.

19 M. Laiju, H. M. N. Akhtar, M. A. Mamun, M. A. Jabbar and M. Q. Ehsan, “Cyclic voltammetric study on the effect of the introduction of secondary ligands on the redox behavior of the copper-saccharin complex”, *J. Natn. Sci. Foundation Sri Lanka*, **38(2)**, 91-99, 2010.

20 G. J. Islam, H. M. N. Akhtar, M. A. Mamun and M. Q. Ehsan, “Investigations on the redox behavior of manganese in manganese(II)-saccharin and manganese(II)-saccharin-1,10-phenanthroline complex”, *J. Saudi Chem. Soc.,* **13**, 177-183, 2009.

21 H. M. N. Akhtar, A. A. Sheikh and M. Q. Ehsan, “Cyclic voltammetric study of the redox behavior of Fe(II)/Fe(III) systems forming during the oxidation of Fe(II) complexes with saccharin and with saccharin and 1,10-phenanthroline”, *Russ. J. Electrochem.,* **44(12)**, 1403-1408, 2008.

22 M. S. Rahman, H. M. N. Akhtar, P. K. Bakshi and M. Q. Ehsan, “Studies on redox behavior of Mn(II)/Mn(IV) system and interaction of Mn(II) with aspartic acid”, *J. Saudi Chem. Soc.,* **11(2)**, 277-286, 2007.

23 A. A. Sheikh, M. Begum, A. H. Khan, and M. Q. Ehsan, “Cyclic voltammetric studies of the redox behavior of iron(III)-Vitamin B_6 complex at carbon paste electrode”, *Russ. J. Electrochem.,* **42(6)**, 620-625, 2006.

24 A. A. Sheikh, S. N. Afzal, A. H. Khan and M. Q. Ehsan, “Electrochemical study on redox reaction of iodide and bromide in presence of benzoylacetone at carbon electrodes”, *J. Saudi Chem. Soc.,* **9(2)**, 279-286, 2005.

25 *I.* Ara, A. A. Sheikh, M. Q. Ehsan and A. H. Khan, “Electrochemical behavior of copper-aspartic acid complex at glassy carbon electrode”, *J. Saudi Chem. Soc.,* **7(1)**, 129-138, 2003.

26 M. Pervaiz, I. Ahmad, M. Yousaf, S. Kirn, A. Munawar, Z. Saeed, A. Adnan, T. Gulzar, T. Kamal, A. Ahmad and A. Rashid, “Synthesis, spectral and antimicrobial studies of amino acid derivative Schiff base metal (Co, Mn, Cu, and Cd) complexes”, *Spectrochim. Acta A*, **206**, 642-649, 2019.

27 M. M. Salama, S. G. Ahmed and S. S. Hassan, “Synthesis, characterizations, biological, and molecular docking studies of some amino acid Schiff bases with their cobalt(II) complexes”, *Adv. Biol. Chem.,* **7**, 182-194, 2017.

28 A. Angoso, J. M. M. Llorente, J. L. Manzano and M. Martin, “Preparation and study of amino acid (DL-leucine, L-isoleucine, L-histidine) Schiff bases with ethyl-α-ketocyclopentylcarboxylate and the corresponding copper(II) complexes”, *Inorg. Chim. Acta*, **195(1)**, 45-49, 1992.

29 V. J. Tonoyan, S. H. Ghazaryan, S. Minasyam and F. Greenaway, “Synthesis, characterization and measurement of antioxidant reactivity of salicylidene-D,L-tyrosine ethyl ester and copper(II)(salicylidene-D,L-tyrosine ethyl ester)2 in a linoleic acid peroxidation reaction system”, *Synth. React. Inorg. M.,* **36(5)**, 425-434, 2006.

30 G. S. Grigoryan, M. G. Harutyunyan and S. K. Grigoryan, “Catalytic activity of cobalt(II) ion and isoleucine complex on decay of cumene hydroperoxide in aqueous solution”, *Proc. YSU Chem. Biol.,* **2014(1)**, 15–19, 2014.

31 G. A. Thakur and M. M. Sheikh, "Synthesis, characterization, antibacterial and cytotoxicity studies on some mixed ligand Th(IV) complexes", *Acta Pol. Pharm.*, **63(2)**, 95-100, 2006.

32 S. S. Patil, G. A. Thakur and V. R. Patil, "Synthesis, spectral and biological studies on some mixed ligand Ni(II) complexes", *Acta Pol. Pharm.*, **66(3)**, 271-277, 2009.

33 F. Khan and A. Khanam, "Investigation of electrode kinetics and thermodynamics of [Zn–L-amino acidate–Vitamin B_7] complexes by voltammetric technique". *Chemija*, **20(3)**, 154–161, 2009.

34 R. Rao, A. K. Patra and P. R. Chetana, "Synthesis, structure, DNA binding and oxidative cleavage activity of ternary (L-leucine/isoleucine) copper(II) complexes of heterocyclic bases", *Polyhedron*, **27**, 1343–1352, 2008.

35 F. Khan and A. Khanam, "Study of complexes of cadmium with some L-amino acids and Vitamin-c by voltammetric technique", *Ecl. Quím.*, **33(2)**, 29-36, 2008.

36 F. M. Elzawawy, "Complex formation constants and thermodynamic parameters for La(III) and Y(III) L-serine complexes", *Monatsh. Chem.*, **122**, 921-925, 1991.

37 S. S. Khaloo, M. K. Amini, S. Tangestaninejad, S. Shahrokhian and R. Kia, "Voltammetric and potentiometric study of cysteine at Cobalt(II) phthalocyanine modified carbon-paste electrode", *J. Iran. Chem. Soc.*, **1(2)**, 128-135, 2004.

38 M. S. Islam and M. A. Salam, "Preparation and characterization of copper isoleucine complex and structure determination by computational calculation", *Int. J. Sci. Eng. Res.*, **8(11)**, 563-577, 2017.

39 F. H. A. A. Jeboori, T. A. M. A. Shimiesawi and O. M. N. Jassim, "Synthesis and characterization of some essential amino acid metal complexes having biological activity", *J. Chem. Pharm. Res.*, **5(10)**, 172-176, 2013.

40 B. B. Tewari, "Studies on biologically significant copper(II) / manganese(II) / uranyl(II)–isoleucine binary complexes", *J. Mex. Chem. Soc.*, **52(3)**, 219-223, 2008.

41 C. W. Child, "Calcium(I1) and magnesium(I1) binding by L-serine orthophosphate in aqueous solutions", *Can. J. Chem.*, **49**, 2359-2364, 1971.

42 A. Adam, S. Verma and G. Seth, "Stability constants of mixed ligand complexes of Cu(II) and Ni(II) with some amino acids and phosphates", *e-J. Chem.*, **8(S1)**, S404-S408, 2011.

43 A. T. Kabbani, H. Ramadan, H. H. Hammud, A. M. Ghannoum and Y. Mouneimne, "Synthesis of some metal complexes of N-[(benzoylamino)-thioxomethyl]-aminoacid (HL)", *J. Univ. Chem. Technol. Metallurgy*, **40(4)**, 339-344, 2005.

44 L. A. Kochergina and O. M. Drobilova, "The thermochemical characteristics of complex formation reactions between 3*d* transition metal ions and L-serine in aqueous solution", *Russ. J. Phys. Chem. A.*, **83(11)**, 1842-1849, 2009.

45 M. Watabe, M. Kai, K. Goto, H. Ohmuro, S. Furukawa, N. Chikaraishi, T. Takayama and Y. Koike, "Preparation of platinum(II) complexes with L-serine using KI. X-ray crystal structure, HPLC and ^{195}Pt NMR spectra", *J. Inorg. Biochem.*, **97(2)**, 240-248, 2003.

46 M. A. Qadir, M. Ahmed, A. Ahmad, S. Naz, S. A. A. S. Tirmazi, R. Khan, I. Hussain and R. Waseem, "Synthesis of metal complexes with amino acids for animal nutrition", *Glob. Vet.*, **12(6)**, 858-861, 2014.

47 A. C. Massabni, P. P. Corbi, P. Melnikov, M. A. Zacharias and H. R. Rechenberg, "Four new metal complexes with the amino acid deoxyalliin", *J. Braz. Chem. Soc.*, **16(4)**, 718-722, 2005.

48 I. P. Tripathi and A. Kamal, "Synthesis, characterization of some complexes of copper(II) with L-asparginine, L-histidine, L-lysine", *Am. J. Adv. Drug Deliv.*, **3(1)**, 95-103, 2015.

49 U. Dhusiya, S. Gautam, S. Chandra and S. Agrawal, "Unsymmetrical mixed ligand (with 2, 3- dihydroxypyridine and some amino acids) on complxation with metal ions Hg(II) and UO_2(II): syntesis, spectral characterization and antifungal activity", *J. Pharm. Chem. Biol. Sci.*, **4(1)**, 1-12, 2016.

50 S. M. H. Obaid, H. A. S. A. Naemi and A. A. S. A. Hamdani, "Synthesis, spectroscopic and antimicrobial studies of mixed ligand metal (II) complexes with three amino acids", *Res. J. Pharm. Biol. Chem. Sci.*, **9(6)**, 1560-1571, 2018.

51 T. O. Aiyelabola, I. A. Ojo, A. C. Adebajo, G. O. Ogunlusi, O. Oyetunji, E. O. Akinkunmi and A. O. Adeoye, "Synthesis, characterization and antimicrobial activities of some metal(II) amino acids complexes", *Adv. Biol. Chem.*, **2**, 268-273, 2012.

52 Y. Z. Hamada, N. Makoni and H. Hamada, "Cu^{2+} Complexes with the simplest amino acid glycine (Gly)", *J. Nanomed. Res.*, **5(4)**, 1-6, 2017.

53 C. Rîmbu, R. Danac and A. Pui, "Antibacterial activity of Pd(II) complexes with salicylaldehyde-amino acids Schiff bases ligands", *Chem. Pharm. Bull*, **62(1)**, 12–15, 2014.

54 A. Stanila, C. Braicu, S. Stanila and R. M. Pop, "Antibacterial activity of copper and cobalt amino acids complexes", *Not. Bot. Hort. Agrobot. Cluj*, **39(2)**, 124-129, 2011.

55 S. F. Mohammed, "Synthesis and characterization of some N-protected amino acid complexes", *J. Am. Sci.*, **6(10)**, 1032-1043, 2010.

56 D. Boruah, "Interaction of cobalt(II) and nickel(II) ions with amino acids in aqueous solution: a spectrophotometric study", *Int. J. Sci. Res. Pub.*, **2(8)**, 1-4, 2012.

57 J. Bhattacharjee, "Synthesis and characterization of peroxo vananidium (V) complexes with amino acids as ligands", *Int. J. Interdiscip. Multidiscip. Stud.*, **2(2)**, 7-17, 2016.

58 E. K. Efthimiadou, A. Karaliota and G. Psomas, "Mononuclear metal complexes of the second-generation quinolone antibacterial agent enrofloxacin: Synthesis, structure antimicrobial activity and interaction with DNA", *Polyhedron*, **27**, 1749-1738, 2008.

59 M. E. Hossain, M. M. Hasan, M. E. Halim, M. Q. Ehsan and M. A. Halim "Interaction between transition metals and phenylalanine: a combined experimental and computational study", *Spectrochim. Acta A*, **138**, 499–508, 2015.

60 T. A. Tanvir, M. E. Hossain, M. A. Mamun and M. Q. Ehsan, "Preparation and characterization of iron(III) complex of saccharin", *J. Bangladesh Acad. Sci.*, **37(2)**, 195-203, 2013.

61 M. Q. Ehsan, S. S. Shammi, A. A. Sheikh and S. M. S. Islam, "Preparation, characterization and molecular models of some transition metal complexes of tren[tren = tris(2-aminoethyl)amine]", *Malaysian J. Chem.*, **7(1)**, 38-45, 2005.

62 M. Q. Ehsan, S. M. Begum and S. M. S. Islam, “Preparation and characterization of pyridoxine complexes of Fe(III), Mo(VI), Cd(II), Hg(II) and U(VI)”, *J. Saudi Chem. Soc.*, **8(2)**, 251-256, 2004.

63 M. Q. Ehsan, M. H. Rashid and S. M. S. Islam, “Preparation, characterization and molecular models of the complexes of quadridentate tripodal ligand tren [tren = tris(2-aminoethyl)amine] with Ag(I), Cd(II), Hg(II), Zr(IV) and U(VI)”, *Pak. J. Sci. Ind. Res.*, **46(5)**, 317-322, 2003.

64 M. Q. Ehsan, M. A. Islam, M. A. Quyser and S. M. S. Islam, “Preparation, characterization and molecular models of mixed ligand complexes of saccharine and 4,4′-bipyridyl with Co(II), Ni(II), Cu(II) and Zn(II)”, *Dhaka Univ. J. Sci.*, **50(2)**, 151-157, 2002.

65 M. Q. Ehsan and M. A. Quyser, “Preparation and characterization of copper complexes β-N-oxalyl-α,β-diamino propionic acid”, *J. Saudi Chem. Soc.*, **6(2)**, 231-236, 2002.

66 M. Q. Ehsan, S. Khatun and M. A. Quyser, “Preparation and characterization of pyridoxine complexes of Mn(II), Co(II), Ni(II), Cu(II) and Zn(II)”, *J. Saudi Chem. Soc.*, **5(1)**; 59-66, 2001.

67 M. Q. Ehsan, A. Rudaba and M. A. Quyser, “Studies of mixed ligand complexes of metal aspartates with 2,2′-bipyridyl”, *J. Nepal Chem. Soc.*, **20**, 41-48, 2001.

68 M. Q. Ehsan and S. M. S. Islam, “Preparation and characterization of complexes of quadridentate tripodal ligand tren [tren = tris(2-aminoethyl)amine] with trivalent metal ions Cr(III) and Fe(III)”, *Dhaka Univ. J. Sci.*, **48(2)**, 125-128, 2000.

69 M. Q. Ehsan, “Preparation and characterization of first row transition metal complexes with quadridentate tripodal ligand tren [tren = tris(2-aminoethyl)amine]”, *Pak. J. Sci. Ind. Res.*, **43(5)**, 271-274, 2000.

70 M. Q. Ehsan, M. Jebin, E. Ahmed, and M. A. Quyser, “Synthesis and characterization of manganese(II), cobalt(II), nickel(II) and palladium(II) complexes of DL-aspartic acid”, *Ind. J. Chem.*, **38(A)**, 826-828, 1999.

71 M. Q. Ehsan, “Preparation and characterization of mixed ligand complexes M(asp)(L).H_2O. M=Hg(II) and Pb(II), Asp = DL-aspartic acid, L = 2,2′-bipyridyl and 1,10-phenanthroline”, *Dhaka Univ. J. Sci.*, **47(2)**, 263-265, 1999.

72 M. Q. Ehsan, Rudaba and M. A. Quyser, "Studies of mixed ligand complexes of metal aspartates with 1,10-phenanthroline", *J. Bangladesh Chem. Soc.*, **12(1)**, 75-81, 1999.

73 K. M. A. Malik, M. B. Hursthouse, P. K. Bakshi, A. A. Bhuiyan, M. Q. Ehsan and S.Z. Haider, "Structural characterization of a metal-thiamine compound $Hg_3Cl_8(C_{12}H_{18}N_4OS)$ containing direct Hg-O and Hg-N bonds", *J. Bangladesh Chem. Soc.*, **12(2)**, 193-205, 1999.

74 M. Q. Ehsan, Y. Ohba, S. Yamauchi and M. Iwaizumi, "EPR and ^{14}N ENDOOR studies of the trigonal bipyramidal copper complexes with sulphur and nitrogen donor quadridentate tripodal ligands", *J. Bangladesh Chem. Soc.*, **11(1&2)**, 1-8, 1998.

75 M. Q. Ehsan, J. M. A. Rahman and M. A. Quyser, "Interactions of DL-aspartic acid with metal ions. part V preparation, characterization and properties of DL-aspartic acid complexes of trivalent metal ions Cr(III) and Fe(III)", *J. Bangladesh Chem. Soc.*, **10(2)**, 195-201, 1997.

76 M. Q. Ehsan, M. Jebin, M. A. Quyser, E. Ahmed, K. M. A. Malik and S. Z. Haider, "Interactions of DL-aspartic acid with metal ions. part IV preparation, characterization and properties of DL-aspartic acid complexes of Zr(IV), Ru(III), Pt(IV) and U(VI)", *J. Bangladesh Chem. Soc.*, **10(1)**, 31-37, 1997.

77 M. Q. Ehsan, J. M. A. Rahman and M. A. Quyser, "Preparation, characterization and properties of L-glutamic acid complexes $M(C_5H_7NO_4).2H_2O$ [M = Co(II), Ni(II), Cu(II) and Zn(II)]", *J. Bangladesh Chem. Soc.*, **10(2)**, 187–193, 1997.

78 M. Q. Ehsan, "Identification and characterization of the proton ENDOR signals of the trigonal bipyramidal copper complexes, $[Cu(tren)(NH_3)](ClO_4)_2$ and [Cu(tren)(NCS)](SCN) [tren = tris(2-aminoethyl) amine", *J. Bangladesh Acad. Sci.*, **21(2)**, 207-211, 1997.

79 M. Q. Ehsan, K. M. A. Malik and S. Z. Haider, "Preparation, characterization and properties of L-prolinato complexes of Cd(II) and Hg(II)", *J. Bangladesh Acad. Sci.*, **20(2)**, 175-181, 1996.

80 M. Q. Ehsan, S. Z. Haider, K. M. A. Malik, M. S. Khan, R. J. Quddus and M. B. Hursthous, “Interactions of DL aspartic acid with metal ions. part II. preparation, characterization and properties of DL-aspartic acid complexes of Zn(II), Mo(VI), Hg(II) and Pb(II), *Dhaka Univ. Stud.*, **B 35(2)**, 153-160, 1986.

81 S. Z. Haider, K. M. A. Malik, M. Q. Ehsan, P. K. Bakshi and M. S. Khan, “Interactions of DL-aspartic acid with metal ions. part I. preparation, characterization and properties of DL-aspartic acid complexes of Cu(II), Cd(II), and Hg(II), *J. Bangladesh Acad. Sci.*, **10(1)**, 85-92, 1986.

82 S. Z. Haider, K. M. A. Malik, L. S. Ahmed, P. K. Bakshi, M. Q. Ehsan, M. S. Khan and T. Wadsten, “Preparation and properties of 8-hydroxyquinoline compounds of some heavy metals”, *Dhaka Univ. Stud.*, **B 34(2)**, 239-246, 1986.

83 M. M. Hasan, M. E. Hossain, M. E. Halim and M. Q. Ehsan, “Preparation and characterization of some transition metal complexes of niacinamide (Vitamin B_3)”, *Pak. J. Sci. Ind. Res. Ser. A: Phys. Sci.*, **58(2)**, 59-65, 2015.

84 S. Sarker and M. Q. Ehsan, “Preparation and characterization of toxic metal complexes of nicotinamide and nicotinic acid”, *J. Bangladesh Acad. Sci.*, **41(1)**, 37-45, 2017.

85 K. L. Rahman, M. A. Mamun and M. Q. Ehsan, “Preparation of metal niacin complexes and characterization using spectroscopic and electrochemical techniques”, *Russ. J. Inorg. Chem.*, **56(9)**, 1436-1442, 2011.

86 M. A. Mamun, O. Ahmed, P. K. Bakshi, S. Yamauchi and M. Q. Ehsan, “Synthesis and characterization of some metal complexes of cystene: $[M(C_6H_{10}N_2O_4S_2)]$; where M^{II} = Mn(II), Co(II), Ni(II), Cu(II), Zn(II), Cd(II), Hg(II) and Pb(II)”, *Russ. J. Inorg. Chem.*, **56(12)**, 1972-1980, 2011.

87 M. A. Mamun, O. Ahmed, P. K. Bakshi and M. Q. Ehsan, “Synthesis and spectroscopic, magnetic and cyclic voltammetric characterization of some metal complexes of methionine: $[(C_5H_{10}NO_2S)_2M^{II}]$; M^{II} = Mn(II), Co(II), Ni(II), Cu(II), Zn(II), Cd(II), Hg(II)”, *J. Saudi Chem. Soc.*, **14**, 23-31, 2010.

88 S. S. Shammi, A. A. Sheikh, S. M. S. Islam and M. Q. Ehsan, “Preparation, characterization, molecular models and cyclic voltammetric study of tren complexes of Cu(II) and Zn(II)”, *Malaysian J. Chem.*, **10(1)**, 9-14, 2008.

89 M. Q. Ehsan, M. M. Hossain and S. M. S. Islam, “Preparation, characterization and molecular models of the complexes of triethylenetetramine with Cr(III) and Fe(III)”, *Malaysian J. Chem.*, **9(1)**, 67-72, 2007.

90 M. Q. Ehsan, M. M. Hossain, O. Ahmed and S. M. S. Islam, “Preparation, characterization and molecular models of the Co(II), Ni(II) and Cu(II) complexes of tetradentate ligand triethylenetetramine”, *J. Saudi Chem. Soc.*, **11(1)**, 25-30, 2007.

91 A. J. Bard and L. R. Faulkner, “Electrochemical Methods, Fundamentals and Applications", 2nd ed., John Wiley and Sons, Inc., New York, 2001.

92 C. M. A. Brett and A. M. O. Brett, “Electrochemistry Principles, Methods and Applications”, Oxford University Press, Inc., New York, 1993.

93 P. Kissinger and W. R. Heineman, “Laboratory Techniques in Electroanalytical Chemistry”, 2nd ed., CRC Press, USA, 1996.

94 F. Scholz, “Electroanalytical Methods: Guide to Experiments and Applications”, 2nd ed., Springer-Verlag Berlin Heidelberg, 2010.

95 J. Wang, “Analytical Electrochemistry”, 3rd ed., John Wiley & Sons, Inc., New York, 2006.

96 N. Elgrishi, K. J. Rountree, B. D. McCarthy, E. S. Rountree, T. T. Eisenhart and J. L. Dempsey, “A practical beginner’s guide to cyclic voltammetry”, *J. Chem. Educ.* **95**, 197−206, 2018.

97 E. A. Gomaa, A. Negm, R. M. A. Qarn, “Cyclic voltammetry of cobalt chloride with L-carrageenan using glassy carbon electrode”, *Iran. J. Chem. Eng.,* **14(4)**, 90-99, 2017.

98 P. S. Joshi and D. S. Sutrave, “A brief study of cyclic voltammetry and electrochemical analysis”, *Int. J. ChemTech Res.,* **11(09)**, 77-88, 2018.

99 C. Cofan and C. Radovan, “Simultaneous chronoamperometric sensing of ascorbic acid and acetaminophen at a boron-doped diamond electrode”, *Sensors,* **8**, 3952-3969, 2008.

100 J. Mendham, R. C. Denney, J. D. Barnes, and M. Thomas, “Vogel’s Textbook of Quantitative Chemical Analysis”, 6th ed., Pearson Education Ltd., 2000.

101 G. D. Christian, “Analytical Chemistry”, 5th ed., John Willey & Sons. Inc., 1994.

102 C. N. Banwell and Elaine M. McCash, "Fundamentals of Molecular Spectroscopy", 4th ed., McGraw-Hill International Ltd., UK, 2003.

103 D. L. Pavia, G. M. Lampman and G. S. Kriz, "Introduction to Spectroscopy", 3rd ed., Harcourt College Publishers, 2001.

104 R. M. Silverstein, F. X. Webster and D. J. Kiemle, "Spectroscopic Identification of Organic Compounds", 7th ed., John Wiley and Sons. Inc., New York, 2005.

105 A. B. P. Lever, "Inorganic Electronic Spectroscopy", 1st ed., Elsevier Publishing Company, 1968.

106 D. Sutton, "Electronic Spectra of Transition Metal Complexes", 1st ed., McGraw Hill, New York, 1968.

107 R. Lopez and R. Gomez, "Band-gap energy estimation from diffuse reflectance measurements on sol–gel and commercial TiO_2: a comparative study", *J Sol-Gel Sci Technol*, **61**, 1-7, 2012.

108 A. Earnshaw, "Introduction of Magnetochemistry", 1st ed., Academic. Press, London, 1968.

109 B. N. Figgis and J. Lewis, "Modern Coordination Chemistry", 1st ed., Interscience Publisher, New York, 1960.

110 M. Gerloch, "Magnetism and Ligand-field Analysis", 1st ed., Cambridge University Press, UK, 1984.

111 P. W. Selwood, "Magnetochemistry", 2nd ed., Interscience Publisher, New York, 1956.

112 "Magway MSB Mk1 Magnetic Susceptibility Balance Instrumental Manual" Sherwood Scientific Ltd, Cambridge, England.

113 A. Rahman, M. T. Ali, M. M. A. K. Shawan, M. G. Sarwar, M. A. K. Khan and M. A. Halim, "Halogen-directed drug design for Alzheimer's disease: a combined density functional and molecular docking study", *Springerplus*, **5(1346)**, 1-14, 2016.

114 A. M. Khan, J. Shawon and M. A. Halim, "Multiple receptor conformers based molecular docking study of fluorine enhanced ethionamide with mycobacterium enoyl ACP reductase (InhA)", *J. Mol. Graphics Model.*, **77**, 386-398, 2017.

115 M. M. Hoque, M. A. Halim, M. M. Rahman, M. I. Hossain and M. W. Khan, "Synthesis and structural insights of substituted 2-iodoacetanilides and 2-iodoanilines", *J. Mol. Struct.*, **1054-1055**, 367-374, 2013.

116 J. Shawon, A. M. Khan, A. Rahman, M. M. Hoque, M. A. K. Khan, M. G. Sarwar and M. A. Halim, "Molecular recognition of azelaic acid and related molecules with DNA polymerase I investigated by molecular modeling calculations", *Interdiscip. Sci.*, **10(3)**, 525-537, 2018.

117 M. A. Saleh, M. Solayman, M. M. Hoque, M. A. K. Khan, M. G. Sarwar and M. A. Halim, "Inhibition of DNA topoisomerase type IIα (TOP2A) by mitoxantrone and its halogenated derivetives: a combined density functional and molecular docking study", *BioMed. Res. Int.*, **2016**, 1-12, 2016